Signals and Communication Technology

Shiban Kishen Koul
Karthikeya G. S.

Antenna Architectures for Future Wireless Devices

Springer

Signals and Communication Technology

This series is devoted to fundamentals and applications of modern methods of signal processing and cutting-edge communication technologies. The main topics are information and signal theory, acoustical signal processing, image processing and multimedia systems, mobile and wireless communications, and computer and communication networks. Volumes in the series address researchers in academia and industrial R&D departments. The series is application-oriented. The level of presentation of each individual volume, however, depends on the subject and can range from practical to scientific.

Indexing: All books in "Signals and Communication Technology" are indexed by Scopus and zbMATH

For general information about this book series, comments or suggestions, please contact Mary James at mary.james@springer.com or Ramesh Nath Premnath at ramesh.premnath@springer.com.

More information about this series at https://link.springer.com/bookseries/4748

Shiban Kishen Koul · Karthikeya G. S.

Antenna Architectures for Future Wireless Devices

Springer

Shiban Kishen Koul
Centre for Applied Research in Electronics
Indian Institute of Technology Delhi
New Delhi, India

Karthikeya G. S.
Centre for Antennas and Radio Frequency Systems
Ramaiah Institute of Technology
Bangalore, India

ISSN 1860-4862 ISSN 1860-4870 (electronic)
Signals and Communication Technology
ISBN 978-981-16-7782-3 ISBN 978-981-16-7783-0 (eBook)
https://doi.org/10.1007/978-981-16-7783-0

Dedicated to

The unfulfilled dreams of Jeevan

Preface

Due to massive hike in smartphone users and their respective data consumption, experts believe that future wireless devices need to be built at mmWave frequencies. To realize this makeover, the entire cellular hardware infrastructure must be revamped, which includes the devices involved in the communication link. Antennas are probably one of the most critical pieces of the wireless device design puzzle. Often, antenna design decides the integrity of the data link. Traditional antenna designs for commercial wireless devices are well-known and have established design principles, but integration of antennas for mmWave-based transceiver radios is a topic of active research across the globe.

This book introduces the readers to the reality of millimetre wave links and various aspects of the communication link design. Special emphasis on the role of antennas in a mmWave link is illustrated comprehensively. Design requirements of antenna integration for modern commercial devices such as smartphones, dongles, and access points are elaborated in this book. Practical use-case scenarios of smartphone and the design process of the antenna system for the same are introduced. Several design examples with experimental results are also included. The feasibility of scaling up sub-6 GHz to mmWave antennas is also discussed in detail followed by a plethora of design examples which could be panel mounted to modern-day commercial smartphones. The unique requirement of gain switchability is introduced in this book, with feasible practical antenna designs. High-efficiency antennas for 5G base stations are introduced along with a design example on planar all-metallic antenna. Beam switchability requirement for base station is illustrated with a couple of compact antenna system examples. Variety of feeding techniques for mmWave antennas is elaborated next. Low-cost antenna designs for future wireless devices are also illustrated in this book.

New Delhi, India — Shiban Kishen Koul
Bangalore, India — Karthikeya G. S.

Contents

About the Authors

Shiban Kishen Koul (*Life Fellow, IEEE*) received the B.E. degree in electrical engineering from Regional Engineering College, Srinagar, India, in 1977, and the M.Tech. and Ph.D. degrees in microwave engineering from the Indian Institute of Technology Delhi, New Delhi, India, in 1979 and 1983, respectively. He is an emeritus professor with the Indian Institute of Technology, Delhi, since 2019 and mentor deputy director (strategy and planning, international affairs) with IIT Jammu, J&K, India, since 2018. He served as a deputy director (strategy and planning) with IIT Delhi from 2012–2016. He also served as the chairman of Astra Microwave Products Limited, Hyderabad, from 2009–2019, and Dr. R. P. Shenoy Astra Microwave Chair Professor at IIT Delhi from 2014–2019. His research interests include RF MEMS, high-frequency wireless communication, microwave engineering, microwave passive and active circuits, device modelling, millimetre and sub-millimetre wave IC design, body area networks, flexible and wearable antennas, medical applications of sub-terahertz waves, and reconfigurable microwave circuits including miniaturized antennas. He has successfully completed 38 major sponsored projects, 52 consultancy projects, and 61 technology development projects. He has authored/co-authored 526 research papers, 16 state-of-the-art books, four book chapters, and two e-books. He holds 25 patents, six copyrights, and one trademark. He has guided 26 Ph.D. theses and more than 120 master's theses.

Dr. Koul is a Fellow of the Indian National Academy of Engineering, India, and the Institution of Electronics and Telecommunication Engineers (IETE), India. He served as a Distinguished Microwave Lecturer of IEEE MTT-S from 2012 to 2014. He was a recipient of numerous awards including the Indian National Science Academy (INSA) Young Scientist Award, in 1986, the Top Invention Award of the National Research Development Council for his contributions to the indigenous development of ferrite phase shifter technology, in 1991, the VASVIK Award for the development of Ka-band components and phase shifters, in 1994, Ram Lal Wadhwa Gold Medal from the Institution of Electronics and Communication Engineers (IETE), in 1995, the Academic Excellence Award from the Indian Government for his pioneering contributions to phase control modules for Rajendra Radar, in 1998, the Shri Om Prakash Bhasin Award in the field of Electronics and Information Technology, in 2009, the VASVIK Award for the contributions made to the area of Information, Communication Technology (ICT), in 2012, the Teaching Excellence Award from IIT Delhi, in 2012, the M. N. Saha Memorial Award from IETE, in 2013, and the IEEE MTT Society Distinguished Educator Award, in 2014. He is the Chief Editor of *IETE Journal of Research* and an Associate Editor of the *International Journal of Microwave and Wireless Technologies*, Cambridge University Press.

Karthikeya G. S. (Member, IEEE) received his undergraduate degree in electronics and communication engineering, with distinction, in the year 2010 from Visvesvaraya Technological University, Belgaum. He received his Master's degree, with distinction, in Microwave engineering from the University of Kerala in 2012. He worked as an assistant professor in Visvesvaraya Technological University from 2013 to 2016, where he established the Antenna Architects' laboratory. He joined the Centre for Applied Research in Electronics, IIT Delhi, as a PhD student in 2017 and defended his thesis in 2019. He served as an event secretary of IEEE MTT-S branch at IIT Delhi. He worked as a project scientist at Foundation for Innovation and Technology Transfer (FITT) in association with Synergy Microwave Corporation from 2019 to 2021. Currently, he serves as the

chief coordinator of the Centre for Antennas and Radio Frequency Systems (CARFS), Department of Electronics and Telecommunication Engineering, Ramaiah Institute of Technology, Bangalore. He has authored or co-authored more than 60 articles in peer-reviewed journals and international conference proceedings. He has also filed four Indian patents and two US patents. He has co-authored two state-of-the-art books and a chapter. He also holds a copyright on 5G antenna module design. One of his articles was featured as a cover page feature in *Microwave Journal*, an industry leading magazine. His research interests include metamaterials, EBG structures, mmWave antennas for mobile terminals and base stations. He is a member of IEEE-Antenna Propagation Society and Antenna Test and Measurement Society. He serves as the reviewer of several IEEE and John Wiley journals. He has actively participated in more than fifteen workshops on antennas in India and abroad. He is a recipient of Dr. N. Vasudevan Nair Memorial Award (2011) and Research Excellence Travel Award (2019).

Abbreviations

1G	First generation
2G	Second generation
3G	Third generation
4G	Fourth generation
5G	Fifth generation
ACS	Asymmetric coplanar stripline
AM	Additive manufacturing
CAD	Computer-aided design
CMOS	Complementary metal oxide semiconductor
CNC	Computer numerically controlled
CPS	Coplanar stripline
CPW	Coplanar waveguide
CST	Computer simulation technology
DC	Direct current
DMLS	Direct metal laser sintering
ECC	Envelope correlation coefficient
EDM	Electrical discharge machining
EMI	Electromagnetic interference
ENZ	Epsilon near zero
FPC	Fabry–Pérot cavity
FTBR	Front to back ratio
GCPW	Grounded coplanar waveguide
GPS	Global positioning system
HFSS	High-frequency structure simulator
LCD	Liquid crystal display
LTE	Long-term evolution
LWA	Leaky wave antenna
MIMO	Multiple input multiple output
mmWave	Millimetre wave
MTM	Metamaterial
MWS	Microwave studio

NR	New radio
OPD	Orthogonal pattern diversity
PC	Personal computer
PCB	Printed circuit board
PD	Pattern diversity
PET	Polyethylene terephthalate
PLA	Polylactic acid
PRG	Printed ridge gap
RF	Radio frequency
RFIC	Radio frequency integrated circuit
RMS	Root mean square
RSSI	Received signal strength indicator
SAR	Specific absorption rate
SIW	Substrate integrated waveguide
SLM	Selective laser melting
SLS	Selective laser sintering
SMA	Sub-miniature A
SMP	Sub-miniature push-on
SoC	System on chip
SP3T	Single pole triple throw
SPDT	Single pole double throw
Tx/Rx	Transmitter/receiver
VNA	Vector network analyzer
VoIP	Voice over Internet protocol
VR	Virtual reality
VSWR	Voltage standing wave ratio
WiFi	Wireless fidelity
WPAN	Wireless personal area network

Chapter 1
Introduction to Future Wireless Devices

1.1 Introduction

The explosive growth of data consumption in the internet accessible devices across the globe has inspired researchers to look out for more sustainable technologies to satisfy the ever-increasing demand for the same. According to Cisco's predictions, 66% of global population will have internet access in a couple of years [1]. This volume includes both the wired devices and the wireless ones. The wireless component of this chink of devices is significant and needs closer examination to accommodate the expected spike in demand soon. Future hardware needs to support and sustain this demand, in addition to this, technologies of the future must also enhance the overall experience of the device with the user.

Future wireless devices also need to maintain a reliable link with the base stations or access points for extended periods of time, given the nature of data consumption of the individual user. With the recent Covid-19 pandemic, most of the white collared jobs relied heavily on the wireless cellular infrastructure to keep the economic clockwork in motion. All these arguments suggest that the dependence on wireless networks is expected to rise in the near future and might continue for the decades, if not centuries, to come. As the penetration and dependence on wireless networks increase, it is imperative for the designers and architects to design wireless devices for the future. These devices must also be compatible with the current generation and that of the previous generations. Designing future-proof wireless systems would be an ideal strategy for sure-fire in the market; but this is more of a speculation than reality. A better off strategy is to design devices and cellular layouts for the carrier frequencies currently allocated for future generations prior to the standardization.

It is also speculated by the analysts that 70% of global population would have mobile connectivity by 2023 [1]. Well, these predictions must be consumed with a pinch of salt, given the myriad number of uncertainties surrounding the policy makers and the industry behavior.

S. K. Koul and K. G. S., *Antenna Architectures for Future Wireless Devices*,
Signals and Communication Technology,
https://doi.org/10.1007/978-981-16-7783-0_1

Nevertheless, 5G would be an important technology in the upcoming decade. Millions of devices would be hooked up online through the 5G route; hence it is critical for the hardware and system architects to design meaningful systems with reasonable performance metrics for these upcoming devices. Spectral allotments for 5G wireless standards across major economies also confirm the eagerness of various countries for early adoption of 5G cellular system [2].

A vague classification of the bands for 5G could be: sub-6 GHz and millimeter wave bands. The wireless hardware design and implementation for sub-6 GHz has been in the industry for more than a couple of decades, which means that realization of hardware in the microwave domain is a straight-forward task. Designing millimeter wave systems centered around 28 GHz or 38 GHz or even 60 GHz is not new for researchers in the space and defense sectors [3, 4]. But mapping these high frequency designs for commercial applications such as smartphones, is a whole new ball game, which lays the groundwork for this book. It must be noted that most of the defense oriented millimeter wave systems use high power and high gain antennas, which may or may not be applicable to consumer products of 5G cellular communication systems.

A few companies have already launched smartphone models, which are compliant with the sub-6 GHz and mmWave (millimeter wave) 5G bands. The examples include Apple® iPhone® 12, Samsung® Galaxy Note® 20 Ultra 5G, Google® Pixel® 5 etc. they operate in the 5G NR (New Radio standard) mmWave bands, mostly in and around 28 GHz. The sub-6 GHz antenna and back-end electronics design would be an extrapolation of the 4G LTE (Long Term Evolution) design strategies. On the other hand, design, and placement of mmWave antennas is challenging due to the electrical length of the deployable antennas. It must also be noted that the location of millimeter wave antennas is equally important as the design of these antennas [5–7]. The antennas for older generations' wireless chipsets could be integrated at any convenient location within the motherboard of the smartphone. This logic would significantly reduce the feasibility of a data link at 28 GHz and beyond. The reasons for this strategy would be discussed in subsequent Chapters of this book.

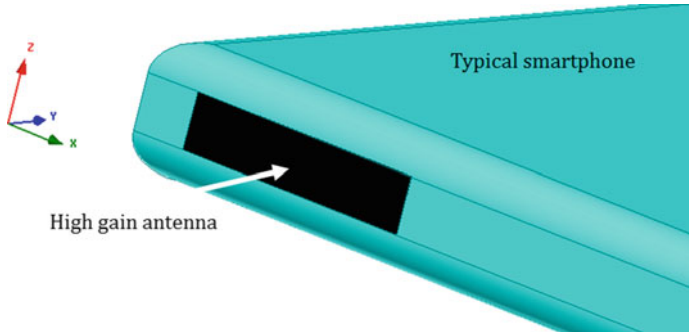

Fig. 1.1 Typical placement of high gain antenna for 5G smart phones

A typical placement of a high gain antenna system is illustrated in Fig. 1.1, which is explored in [8]. It is a phased array operating at 28 GHz, which is mounted along the panel of the smartphone. Two identical modules are integrated within the phone. Even though smartphone manufacturing companies claim to have designed mmWave antenna systems for the latest commercially available phones, the long-term test reports in an actual urban and semi-urban geographies are yet to be published or released. Also, several carrier networks have deployed 5G networks mostly in the sub-6 GHz spectrum rather than the 28 GHz band. As per the data available in the public domain, scalability of 28 GHz chipsets and radios is yet to be seen.

1.2 Taxonomy of Wireless Devices in the Market

In the highly competitive consumer electronics industry, there are several companies fighting for a decent market share. Some of the examples of wireless devices include smartphones, tablets, laptops, modems, dongles, VR (Virtual Reality) headsets, wearable electronics, or radios etc.

This book is focused on devices which would be necessary for the core 5G cellular networks, mainly smartphones and base stations or access points. Wearable devices are currently beyond the scope of this book, but some of the design principles discussed in the forthcoming Chapters could be applied to wearable 5G devices as well, without any loss of generality. Most of the afore-mentioned devices have been in the market since a decade or two, but they must be accommodated with the upcoming millimeter wave systems without any compromise in the performance metrics. Some commonly observed consumer devices are shown in Fig. 1.2. The assumed dimensions for these devices are typical values flicked from some of the popular device's data sheets. The dimensions are primarily mentioned in electrical lengths, wherein λ_{28} denotes the free space wavelength at 28 GHz. As observed from the schematics, most of the real estate of the devices, is a healthy multiple of the wavelength indicating ample space for antenna design. This is only part of the story, current devices have many boards, components and battery jam-packed into a very limited space. Antenna systems or modules for these devices operating in the mmWave 5G must fit in with an electrically small footprint. The details of the antenna requirements for various devices would be discussed in Chap. 2.

1.3 Evolution of Carrier Frequencies

The present 5G cellular infrastructure is centered around higher carrier frequencies. The historical pathway for higher carrier frequencies would be presented in this section. With Hertz's demonstration of transmission of the ultra-wideband spark, wireless technology as we know it today was born. Even though Hertz proved that intelligence could be in-principle transmitted through air, the setup itself was massive

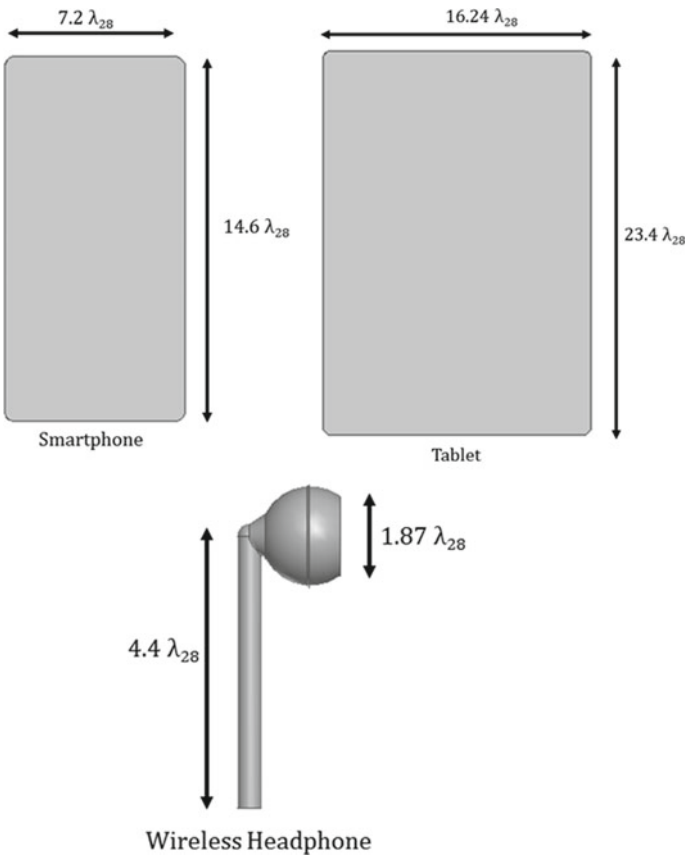

Fig. 1.2 Commonly used wireless devices

and not scalable. Then came Marconi who demonstrated the first trans-Atlantic wireless signal transmission in the kHz range. Naturally, the antennas used for transmission and reception were a fraction of wavelength with extremely high power pumped into the antennas. If Marconi had chosen ultra-wideband spark, then the signal might have been dispersed into thin air without any reception. Hence the concept of specific high carrier frequency came into place. Fast forward to the 1950s, analog modulation schemes were the means for data transmission which had a severe restriction with the amount.

of signal or intelligence transmissible for a specific period. With the onset of digital modulation and digital transmissions, the wireless industry adopted this mode of communication quickly.

The first generation (1G) cellular communication was analogous transmissions and receptions. The antennas were straight-forward to design, the transmitter antennas were standard quarter-wavelength monopoles with narrow band, decided by the then operating frequency allotted to the carrier by the regulatory agency. The

cellphone on the other hand, electrically small telescopic helical antennas had to be mounted with the mobile devices, which were in fact bulky and cumbersome to carry around. After almost a decade of 1G, 2G (Second generation) came into the market around 1992. 2G infrastructure was built around digital telephony which meant that higher data rates could be transacted, which in turn meant that the user would be engaged with the mobile device much more than their 1G counterpart. The digital modulation schemes ensured that the signals were transmission-friendly which means that the digitally encoded data would be embedded on to an analog sinusoid. The antenna to be designed with 2G systems had to accommodate specific bandwidth centered around a carrier frequency dictated by the mobile phone carriers and spectra allotting agencies. Typically, this would be a minute fraction of the operating carrier frequency. Hence bandwidth was not a major issue when designing these antennas. The base station antenna for broadcasting would have a reasonably high gain design overlooking the ground, most of the time. Also, the power pattern of the base station antennas would be unidirectional as there's no need of transmission towards the sky. The antenna on the device, on the other hand, would be electrically small and radiating omni-directionally.

As time progressed, the carrier frequencies also progressed in conjunction with the progress in the RFIC (Radio Frequency Integrated Circuits) industry. This meant that higher data rate could be achieved at the user's terminal. With the development of concepts and techniques such as SoC (System on Chip), a different set of wireless radios could also coexist with the primary cellular service. For instance, WiFi (Wireless Fidelity), Bluetooth and GPS (Global Positioning System) transceivers were added along with the voice service of 2G. This also meant that separate antennas had to be designed, for the coexisting setup to work. In some cases, a cleverly designed multiband antenna would do the trick.

Most of these wireless services were sub-6 GHz bands and placed close to each other, which meant that the antenna design would be much smaller than its 1G counterpart. Two possibilities could be thought out to solve the antenna problem. The first solution is to design a super wideband antenna which works from 1 to 30 GHz, such as the ones reported in [9, 10]. The advantage with this topology is that any band, irrespective of the wireless generation, would be operative. The problem is that all the frequency channels would be open for data link, which may or may not be a good option as the interference from the neighboring channels have a high probability of signal deterioration or co-channel interference. Moreover, the pattern integrity would be compromised at higher frequencies.

The second option is to design a simple telescopic antenna covering 1–30 GHz. Even if we assume a quarter-wavelength monopole, the length varies from 37.5 to 2.7 mm which means a length variation of 13.4:1, which would be impractical to design and integrate, especially given the consumers' preference for compact and sleek devices. Even if this was designed and implemented, patterns would be degraded as the frequency of operation is increased or altered.

What must be observed is that, with the onset of 2G services, antennas within a mobile device migrated from wire antennas to PCB (Printed Circuit Board) antennas, which could be manufactured by the industrially viable chemical etching technique

used for RF (Radio Frequency) boards. These antennas would be a modified version of a printed monopole with parasitic coupling to create the desired resonances based on the requirements of the local carriers.

A large system ground is also integrated beneath the keypad and the LCD (liquid–crystal display) panel. The expected pattern from a 2G antenna, irrespective of the specific band, which is activated, would be omnidirectional. This is an expected phenomenon from an electrically small radiator embedded within a mobile device, hence no design jugglery required from the antenna designer. Also, free space path loss is manageable for low gain antennas to be involved in the data link.

Also, radiation efficiency of these antennas of embedded 2G antennas would be poor, this metric does not contribute to the data link. The characteristics of 2G antennas cannot be extrapolated to mmWave 5G antenna systems for a lot of reasons, which will be explored in Chap. 2.

After a decade of 2G, 3G came into the market with a promise of higher data rates. The data rate was also augmented by the improvements in the hardware and operating systems, which boosted the user experience. The antenna design was a simple extrapolation of the 2G designs. Also, with the arrival of 3G mobile devices, the issue of backward compatibility was an important aspect of design. This meant that the antennas or antenna systems also had to be compliant with multiple wireless standards, which is a norm even today. This trend might continue in future as well. The reason is that the investments of previous generations would have a revenue generating mechanism even with the onset of newer wireless generations.

The story of 4G is also like that of 3G, except for the introduction of MIMO (Multiple Input Multiple Output) systems into mobile handsets, which meant that higher number of antenna elements had to be crammed into minimal space within the handset. The data rate also improved phenomenally with the introduction of 4G cellular systems. 5G would be a healthy mixture of sub-6 GHz and mmWave systems. Detailed discussions would be available in the subsequent Chapters. Figure 1.3 gives a glimpse of mobile devices in the span of 1989–2004. The external antennas of older generation are clear. The internal antennas are implied in the photograph.

1.4 Why Millimeter Waves Hold the Key to the Future?

As illustrated in the previous sections, most of the sub-6 GHz bands intended for cellular communications are congested; and it's a logical guess to assume that to maintain the current user experience with the anticipated growth rate might be difficult to attain. A simple solution is to double or quadruple the spectral efficiency, which works well on paper and not in reality. Another alternative is to design multiple types of diversity systems to enhance throughput of the overall wireless system. For instance, pattern diversity could be augmented with polarization diversity at the mobile terminal level. As the number of radios for a given wireless service increases, the controlling circuitry also becomes complex leading to higher probability of error and might not strongly correlate with the expected data rate.

Fig. 1.3 Sample antennas from previous generations [16]

One of the logical solutions to ease spectral congestion is to operate with multiple higher frequency bands. One of them being millimeter waves. If researchers assume that millimeter wave could deliver at least five-fold increase in the data-rate, then why not design systems beyond 100 GHz or 1000 GHz, the primary hindrance for scaling frequencies to these high values is that free space path loss also increases exponentially, which means that the number of antenna towers would increase by at least a 100-fold for a given cell to maintain a similar angular coverage compared to the commercial 4G systems. Also, circuits and components beyond 100 GHz are not very efficient [11, 12], which means that higher power must be pumped at both the tower and the terminal to maintain a reasonable link budget.

In conclusion, millimeter waves seem to be a viable solution given the feasibility and expected data rate growth. It must be noted that atmospheric absorption in the 60 GHz is close to 20 dB/km, which means that 60 GHz suffers from both higher path loss and absorption loss, severely degrading the signal strength, so designers prefer 60 GHz for WPAN (wireless personal area network) applications [13, 14]. The 28 GHz band has an atmospheric absorption close to 7 dB/km even during heavy rainfall, which is an indicator that there's a possibility of building mmWave 5G in and around this frequency.

1.5 Feasibility of Millimeter Waves for Data Links: A Reality Check

As mentioned in the preceding sections, the free space path loss or power loss beyond 20 GHz is higher than the sub-6 GHz carrier frequencies. Not to forget the penetration losses of common building materials of urban and suburban construction found across the globe. For the sake of simplicity, assume a mobile device is receiving signal from a single base station, which is not at all true but helps us understand better. Consider the famous Friis transmission formula [15] recreated below:

$$P_{MT} = \left(P_{BT} G_{MT} G_{BT} \lambda_c^2\right) / \left(16\pi^2 R^2\right) \tag{1.1}$$

In this equation, P_{MT} is the received power at the mobile terminal when a base station located at R distance with a transmitted power of P_{BT}. The gains of the antennas involved in mobile terminal and base station are G_{MT} and G_{BT} respectively. λ_c is the free space wavelength at the carrier frequency of operation. Imagine the frequency of operation to be 2 GHz with G_{MT} and G_{BT} to be 0 dBi, which means that simple omnidirectional monopoles are installed on the antenna tower and the mobile terminal. Assume the distance between the radios is 1 W, then the received power on the mobile phone is 142 μW (or −8.46 dBm), which is well above the receiver sensitivity of the mobile device. On the other hand, if the frequency is raised to 28 GHz for this setup, received power decreases to 0.726 μW (or −31.4 dBm), a decrement of 23 dB, which must be compensated for by some other means to establish a reliable link. Of course, the actual values of transmitted power and the distance would be much higher, but the amount of decrement in free space path loss would be maintained. The above equation works well in geographies which are devoid of obstacles and could be considered close to free space within some specific locality of operation. Nevertheless, (1.1) serves as a benchmark for designing data link beyond 20 GHz. Figure 1.4 illustrates the variation of free space path loss against frequency at 200 m between the radios. The mmWave band has at least 20 dB higher path loss compared to the sub-6 GHz bands, which means that this value of 20 dB has to be compensated by the P_{BT}, G_{MT} and G_{BT} parameters of (1.1), these parameters would be explored in detail in subsequent sections. Ground reflections and diffraction from a myriad of entities in an urban area, would complicate the business of designing these high frequency data links. Diffraction effects would be more rampant at higher frequencies as the size of the physical objects would be in the vicinity of the wavelength of operation.

1.6 Remedies for Establishing the mmWave Data Link

Even though the values for a link budget seems to be unreasonable and discouraging, several remedial measures could be investigated to realize the same.

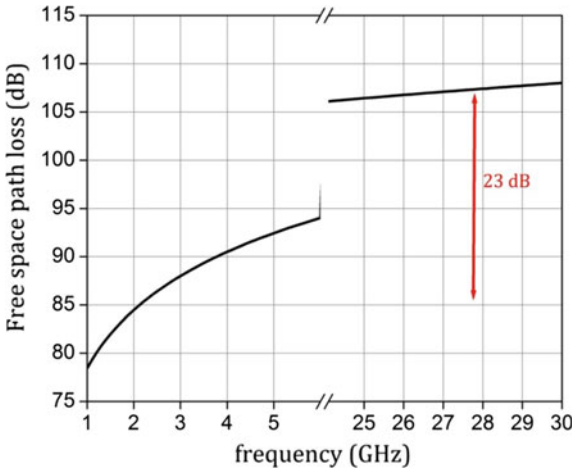

Fig. 1.4 Free space path loss at 200 m

1.6.1 Power Constraints

Power at the base station for a commercial 4G LTE would be in the range of 10–15 W. the insertion losses of the feeding cables at the antenna towers would be in the range of 3–5 dB. If the same logic is translated to 28 GHz, then high efficiency transmitters must be designed. Not to forget the heating effects of these systems and an effective method to dissipate the same would also be necessary. It must also be noted that losses in the precision cables rising from the control electronics to the antenna systems would be in the range of 5 dB/m. if an antenna is mounted at a height of 10 m, then the feeding cable loss itself would be 30 dB, that is assuming a perfectly straight installation of the cable, but reality has much more losses than imagined theoretically.

A more elegant solution is to install an appropriate waveguide to drastically reduce the feeding losses. The problem with waveguides is that temperature variations of the ambience would deteriorate the mode integrity of the waveguide leading to a compromise in the power pumped into the antenna system. Also, transition from the power amplifier to the antenna's feeding network might create losses in the spectrum of our interest.

In consideration of all the afore-mentioned points, pundits in the industry opine that low power base station or access points with lower power would be the future. It would be similar to WiFi network; wherein numerous low power access points would be beaming high data rate to the subscribers through 5G network. With the incorporation of low power systems, sustainable and reliable access points could be easily built even at such high frequencies. The downside with this argument is that the number of access points would increase exponentially compared to its 4G towers' counterpart.

The aspect which could be explored is to jack up the power transmitted by the mobile terminal. The typical 4G smartphone transmits power in the range of 0.5–2 W.

if the same is to be mapped to 28 GHz, it would be challenging to accomplish, given the efficiencies of the power amplifiers to be integrated with smartphones.

Some designers might also argue that the receiver sensitivity of the mobile terminal could be increased. To achieve the same, the signal's noise floor will need to be reduced from −110 dBm to at least −140 dBm, which needs the intervention of cryogenics or the use of superconductors, the research for commercialization might be decades away.

Hence, a low transmitting power at the base station would be a preferable choice in addition to a reasonable value of the transmit power at the mobile terminal like that of 4G or WiFi devices. It must also be noted that the received power at the radios must be well above the signal's noise floor.

1.6.2 Gains of the Antennas Integrated in Radios

Probably, the only feasible solution to the antenna puzzle of millimeter wave systems is to tweak the gain values of (1.1) the free space path loss is at least 23 dB higher than the sub-6 GHz bands. This translates to a requirement of 23 dB higher collective gains of the antennas deployed on base stations and mobile terminals. Various strategies could be employed for the collective gains to reach 23 dB. In other words, $G_{MT} + G_{BT} = 23$ dBi, the first way is to design 23 dBi + 0 dBi, which means that current base station antennas (4G base station antennas have a typical gain of 10 dBi) to be increased by 23 dB, so the new 5G base station antenna's gain would be 33 dBi, meaning a pencil beam with a significant compromise in the angular coverage. A pencil beam would mean that higher scanning rate of the concerned area of operation. The scanning also gets complicated with users' mobility. The second strategy is to design 0 dBi (base station) + 23 dBi (mobile terminal) which means that the base station would have an actual gain of 0 + 8 = 8 dBi, meaning a unidirectional beam directed towards the subscribers, which seems to be a logical and reasonable value. But a 23 dBi antenna on the mobile terminal means a pencil beam when the mobile device is activated. A pencil beam on the mobile device means high probability of missing the signal from the base station. It must also be noted that the angular coverage would be highly sensitive to the orientation of the smartphone with respect to the user's axis. Hence a compromise would be 15 dBi (base station) + 8 dBi (mobile terminal). Translating to 8 dBi + 15 dBi = 23 dBi at the base station and 0 dBi + 8 dBi = 8 dBi at the mobile terminal. A 23 dBi antenna's radiation pattern would be wide enough to accommodate 10–15 users but narrow enough to deliver high gain for additional path loss compensation. An 8 dBi gain on the mobile terminal would simply mean a unidirectional beam with high front to back ratio, this indirectly benefits the reliability of the data link by minimizing radiation towards the user. The realization of mobile terminal antennas would be discussed in detail in subsequent Chapters.

1.6.3 Distance Between the Radios

Distance between the transceivers is another important and critical factor for deployment of mmWave 5G links. A conventional commercial 4G cellular network would have its base stations at least 1 km from each other. This layout is reliable even in various types of terrains, due to the path loss phenomenon presented earlier. The same 4G layout cannot be mapped to mmWave 5G as the data link would have an outage beyond the 200 m boundary.

For the sake of comparison, consider a 4 km $\times$ 4 km hypothetical geography to provide 4G connectivity. In this area, 16 antenna towers would suffice. On the other hand, to maintain a similar connectivity, 100 base station towers would be necessary for mmWave 5G network, translating to 6.25 times increase. This would also mean that the capital investment and operating costs for 5G base stations also would rise exponentially. A typical cellular layout for 5G network is illustrated in Fig. 1.5. This line of reasoning, however, is for an obstruction free environment.

If we bring in realistic parameters such as: buildings, trees, concrete roads (which influences signal bouncing off the ground), density of users with variable data consumption, dynamic vehicular movement etc., then the layout would be much denser at higher traffic areas and less sparse at lower density zones. The distance between the antenna tower and its cellular boundary is expected to be 200 m. most of the commercial companies would design wireless infrastructure based on this value.

The claims by multitude of reports claiming multi-Gbps 5G links would be due to high power pumped from the mock-up mobile base stations (more than + 30 dBm) attached with these base stations were high gain antennas (more than + 20 dBi).

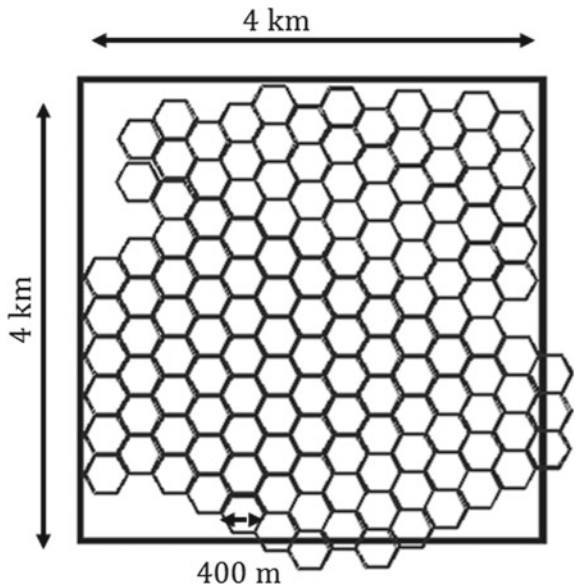

Fig. 1.5 Typical layout of 5G network

In addition to these unrealistic parameters, the tests would be purely in an outdoor context with lesser obstacles in the test site. All these indicate that a full-fledged 5G network in the 28 GHz band might take a few more iterations to be functional. The testing campaigns run by research group at New York University also experimented with the 28 GHz link with high transmission power with pencil beam to prove the feasibility of 28 GHz as a carrier frequency [16].

1.6.4 Optimal Recipe for mmWave 5G: A Case Study

A case study of the communication link budget is presented in this section for outdoor and indoor scenarios. The assumption is for data transmission, which requires higher bandwidth and hence pencil beams emanating from the base station tower.

A. ***Outdoor Scenario***

Consider a typical outdoor communication link using the proposed millimetre wave 28 GHz link as shown in Fig. 1.6. The base station antenna would be mounted on a mast at a height of 3 m from the ground level. There is lot of controversy regarding the optimal height of the base station antenna, but 3 m seems to be a reasonable assumption for millimetre wave links. Gain of the base station could be assumed to be 20 dBi without any loss of generality. Transmitted power for commercial 4G base stations is in the range + 30 to + 40 dBm, a similar assumption could be extended for the 5G link. If the gain of the antenna integrated on the mobile device is assumed to be 10 dBi and the receiver sensitivity would be -70 dBm. The distance d_2 could be as high as 5 km, assuming an obstacle free zone. In rural areas which has minimal contaminants of the signal strength, distance of close to 2 km could achieved.

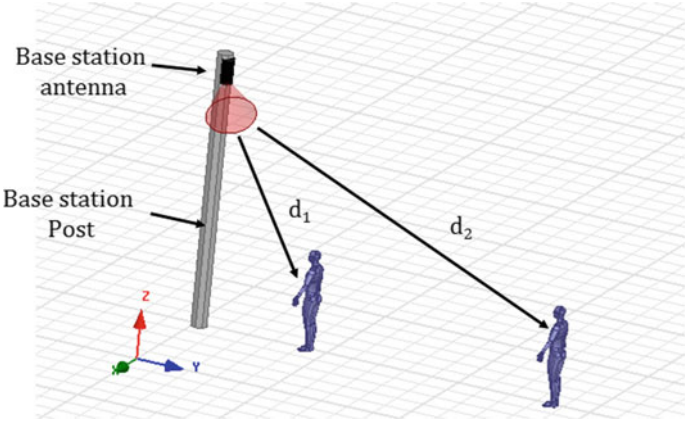

Fig. 1.6 Schematic for outdoor mmWave 5G link

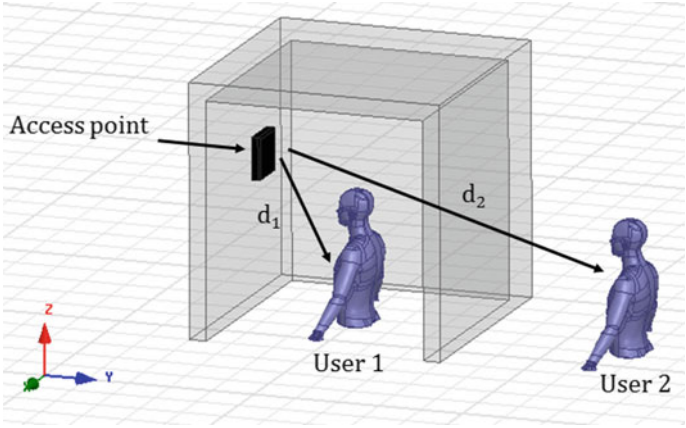

Fig. 1.7 Schematic for Indoor mmWave 5G link

B. ***Indoor Scenario***

Figure 1.7 illustrates a typical scenario of an indoor communication link. The access point is usually wall or ceiling mounted with relatively lower gain compared to the outdoor base station to avoid complexity of the multi-beam and to keep the costs to a minimum. Also, the transmitted power would be significantly lower compared to its outdoor counterpart. The antenna at the access point could have a gain of 10 dBi, which could be easily achieved with compact size leading to a hemispherical coverage and front to back ratio of greater than 10 dB. The transmitted power of the access point could be safely assumed to be + 20 dBm. The gain of the mobile device would be invariant of whether the user is indoor or outdoor, hence the gain of the mobile device would be 10 dBi, the associated receiver sensitivity is -70 dBm. For these constraints the maximum distance within the walls could be as high as 30 m But, when the access point is being used beyond the wall, let's say in adjacent room then the distance is severely restricted by the attenuation of the concrete or wooden walls.

1.7 Outline of the Book

Chapter 2 gives a detailed introduction to antenna design requirements. The antennas of previous generations are discussed in detail to get some perspectives on design evolution followed by breakout of a typical modern-day smartphones. All the physical dimensions are discussed in terms of antenna design and placement. Typical requirements for wireless dongle, wearable devices and access points are also explained.

Chapter 3 presents antenna architectures for the typical data modes of a smartphone usage. Initially, the idea of orthogonal modes is presented, followed by the

desired characteristics of the antenna system for the same. The failure of phased array in this context is also presented, followed by design examples.

The principle of backward compatibility is also an important feature of antenna designs for future devices, Chap. 4 addresses this issue. Desired characteristics of antenna systems for this application is explained followed by a couple of design examples to illustrate co-design architecture.

The need for gain switchability for data modes and broadcast applications is illustrated in Chap. 5. Two design examples to achieve the same is also included in this chapter with exhaustive simulated and experimental results.

Base stations are equally important in deployment of millimeter wave 5G network. Hence Chaps. 6 and 7 are dedicated to base station antenna design. High efficiency antennas with design examples are discussed in Chap. 6 and beam switching modules in Chap. 7. Various feeding techniques for Ka-band antennas are explained in Chap. 8. Fabrication technology for realizing low-cost antennas is discussed in Chap. 9, followed by a couple of design examples.

References

1. Cisco, U.: Cisco Annual Internet Report (2018–2023) White Paper (2020)
2. Dahlman, E., Parkvall, S., Skold, J.: 4G, LTE-advanced Pro and the Road to 5G. Academic Press (2016)
3. Cooley, M.: Phased array fed reflector (PAFR) antenna architectures for space-based sensors. In 2015 IEEE Aerospace Conference, pp. 1–11. IEEE (2015)
4. Huang, J., Rascoe, D., Riley, A.L., Lubecke, V., Duffy, L.: A Ka-band MMIC phased array antenna. In Digest on Antennas and Propagation Society International Symposium, pp. 1212–1215. IEEE (1989)
5. Syrytsin, I., Zhang, S., Pedersen, G.F., Zhao, K., Bolin, T., Ying, Z.: Statistical investigation of the user effects on mobile terminal antennas for 5G applications. IEEE Trans. Antennas Propag. **65**(12), 6596–6605 (2017)
6. Gandhi, O.P., Riazi, A.: Absorption of millimeter waves by human beings and its biological implications. IEEE Trans. Microw. Theory Tech. **34**(2), 228–235 (1986)
7. Andersen, J.B., Nielsen, J.Ø., Pedersen, G.F.: Absorption related to hand-held devices in data mode. IEEE Trans. Electromagn. Compat. **58**(1), 47–53 (2015)
8. Huo, Y., Dong, X., Xu, W.: 5G cellular user equipment: from theory to practical hardware design. IEEE Access **5**, 13992–14010 (2017)
9. Chen, K.R., Row, J.S.: A compact monopole antenna for super wideband applications. IEEE Anten. Wirel. Propag. Lett. **10**, 488–491 (2011)
10. Azari, A.: A new super wideband fractal microstrip antenna. IEEE Trans. Antennas Propag. **59**(5), 1724–1727 (2011)
11. Kallfass, I., Dan, I., Rey, S., Harati, P., Antes, J., Tessmann, A., et al.: Towards MMIC-based 300GHz indoor wireless communication systems. IEICE Trans. Electron. **98**(12), 1081–1090 (2015)
12. Kobayashi, K.W., McCleary, Y.Z.: Baseband to 140-GHz SiGe HBT and 100-GHz InP DHBT broadband triple-Stacked distributed amplifiers with active bias terminations. IEEE J. Solid-State Circuits **55**(9), 2336–2344 (2020)
13. Jaiswal, A., Abegaonkar, M.P., Koul, S.K.: Highly efficient, wideband microstrip patch antenna with recessed ground at 60 GHz. IEEE Trans. Antennas Propag. **67**(4), 2280–2288 (2019)

14. Jaiswal, A., Dey, S., Abegaonkar, M.P., Koul, S.K.: Design and development of 60 GHz antenna integrated with RF MEMS SPDT switch for transceiver modules. In 2018 IEEE International Symposium on Radio-Frequency Integration Technology (RFIT), pp. 1–3. IEEE (2018)
15. Friis, H.T.: A note on a simple transmission formula. Proc. IRE **34**(5), 254–256 (1946)
16. https://commons.wikimedia.org/wiki/File:Mobile_phone_evolution.jpg

Chapter 2
Antenna Design Requirements

2.1 Introduction

One of the important parameters to understand and appreciate for antennas is the design requirements for the application at hand. In the present context, various wireless devices are the target applications, for which antennas need to be designed. This means that the designers must fully comprehend the application at hand from an antennas' perspective. Understanding of the application would enhance the researchers' chances of landing up with a better antenna topology or architecture, hence it is important to spend some time on the desired characteristics of antennas for commercial wireless devices, especially at higher frequencies.

The design requirements for specific models might change over the course of time, but the generic requirements for a certain class of device would remain nearly the same. The design requirements that shall be discussed in this Chapter are generic in nature and might require some tweaking when designing for an actual commercial device or a product. It is important for the designer to understand the form factor and the constraints with respect to the wavelength of the operating frequency. The design requirements would be for the antenna itself, which means that these design requirements would work for an antenna in free space without any metallic or non-metallic interferences nearby. However, antenna in free space gives an idea about the expected characteristics of the antenna post-integration with the intended device. Initially, expected characteristics of the antennas in free space namely: impedance behavior, dominant polarization, radiation pattern, gain etc. would be discussed in detail followed by comments on post-integration with the specific device under consideration.

If the antennas have an electrically large ground, which could be shared or integrated with that of the back-end electronics or radiating devices then most of the antenna characteristics of the stand-alone element would be retained even in an integrated environment. The antenna requirements post integration with the device is an intricate problem, as there are numerous aspects which deteriorate or detune the

S. K. Koul and K. G. S., *Antenna Architectures for Future Wireless Devices*,
Signals and Communication Technology,
https://doi.org/10.1007/978-981-16-7783-0_2

antenna's behavior. For instance, the injection moulded plastic casing might reduce the gain of the antenna as these dielectrics are built upon low-cost, industrially viable materials which have quite high dielectric loss tangent. The hands of the user acts as an attenuator for mmWave (millimetre wave) signals, hence placement of antennas which has higher exposure to the user's hands must be kept in mind. Hence the designers must also optimize the placement of the antennas or antenna systems for better transmission and reception to ensure reliability of the data link.

The antennas integrated within a wireless device would also suffer from other nearby objects when the device is in use. For instance, if the device is placed near an electrically large (several multiples of the operating wavelength) object then the patterns might get specular and lead to multipath interference at the receiving terminal [1]. This phenomenon could happen inside a vehicle or within an elevator. These effects would be prominent for millimetre wave carrier frequencies than its sub-6 GHz counterparts.

Generic antenna designs of previous generations is discussed in Sect. 2.2, followed by discussion on the breakout of a typical smartphone in Sect. 2.3. Antenna requirements for wireless dongle, common wearable devices and base stations are explained in Sects. 2.4, 2.5 and 2.6 respectively.

2.2 Antennas of the Previous Generations of Wireless Devices

With the onset of consumer devices which offered numerous wireless services, antennas which could fit within the constraints of the device in question was necessary [2]. But the concept of miniaturization and planar antennas were not popular during the 1980s. So, telescopic antennas or aerials were incorporated with the prevalent mobile devices. A sample telescopic antenna is illustrated in Fig. 2.1 [3]. The overall length of the antenna in the figure shows Xλ, the value of X usually depends on the form factor and the least carrier frequency of operation. For instance, if the operating frequency range is 1–2 GHz then the highest free space wavelength is 300 mm (as the least frequency of operation is 1 GHz), a scaling factor of 0.2 would mean that the overall length of the telescopic antenna is 0.2 λ or 60 mm. Often, the carrier frequencies would be much lesser than these values, but the scaling factor typically remains the same, the idea is that the extension of monopole would support lower frequencies. The mechanical sturdiness would be compromised when the frequency is decreased. It must be noted that these antennas had to extended for better reception during a telephonic conversation.

With the evolution of wireless devices, printed antennas were introduced with commercial devices, especially the mobile devices. A generic stand-alone antenna intended for mobile device is shown in Fig. 2.2 [4–6]. The illustration shows only the metallic portion of the antenna, a suitable commercially viable dielectric substrate is assumed to be beneath this antenna geometry. Usually, the antenna would be

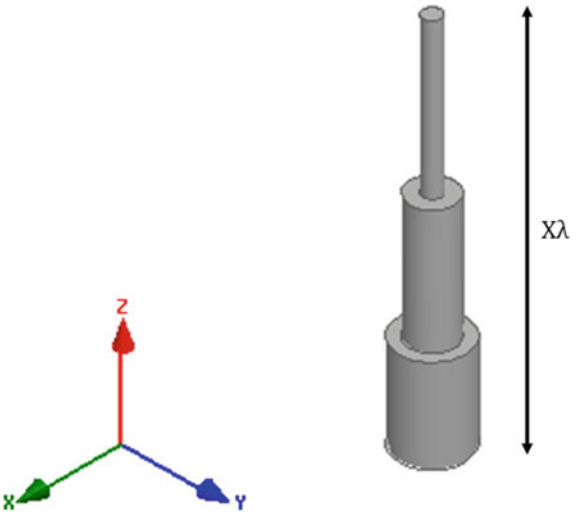

Fig. 2.1 Schematic of a telescopic antenna

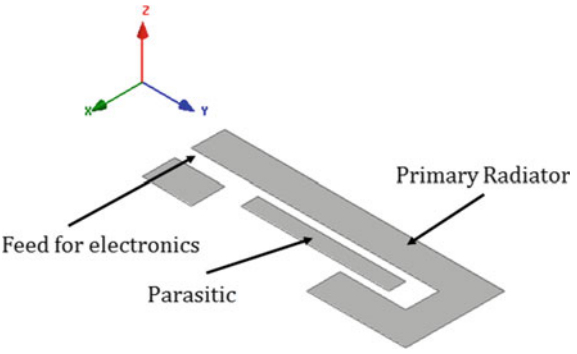

Fig. 2.2 A generic multiband printed mobile antenna

integrated at the edge of the motherboard of the mobile device. The back-end RF (Radio frequency) electronics would be beneath this antenna element. Multi-layer PCB (Printed Circuit Board) would be integrated with the radiator through suitable impedance matching networks. In this current schematic, a CPS (Coplanar Stripline) feeding network is displayed, which would be fed by coaxial pins [7].

The feeding network might also have an in-series RF switch to activate the given antenna. A switch would prevent unintentional interference from neighboring antennas, which also would be operating at frequencies very close to the activated antenna. The primary radiator would be some form of a modified meandered line. The meandering is introduced to reduce the size of the radiator. Some of the mobile antennas might also use integrated passive inductors for miniaturization [8]. Some of the designers might cleverly integrate varicaps for tuning the primary radiator to accommodate the necessary bands. A meandered primary radiator would usually

create a couple of bands, to incorporate higher number of bands as required by the manufacturer, parasitics would be introduced like the generic antenna of Fig. 2.2.

The purpose of parasitics is to achieve additional resonances below that of the primary radiator. In 4G LTE (Long Term Evolution) devices, antennas like the generic example presented here, would be integrated with multiple copies of the same antenna to achieve higher throughput using MIMO (Multiple Input Multiple Output) architecture [9, 10].

The afore-mentioned concept might not be translated to mmWave 5G. the reason being, electrically small antennas would have an almost omnidirectional radiation with poor radiation efficiency [11], 5G antennas need directional beams with high radiation efficiency for a sustainable data link. Co-design of antennas of different wireless standards would be discussed in Chap. 4.

2.3 Breakout of a Typical Smartphone

As smartphones have become ubiquitous, it is important for the designers to comprehend the challenges of designing antennas for smartphones. A generic illustration of a smartphone is presented in Fig. 2.3a. The assumed dimensions are typical values found in commercial smartphones. As evident from the illustration, battery occupies maximum space within the device. The next high space occupying element is the back-end electronics and its associated paraphernalia. The back-end electronics also houses the switches and signal source to the antennas. The back-end electronics would be shielded by an electrically large ground plane to prevent EMI (Electromagnetic Interference) from wireless signals from nearby sources. The effect of this ground plane must be considered while designing the antennas. It must be noted that the generic design presented in the figure works in the stand-alone mode. The effects of user's hands and that of the heterogeneous environment would further complicate the design business. Most of the antenna designs discussed in this book would be for the stand-alone case. The performance metrics would be slightly compromised post integration in the real-world.

The space available for antenna design is exclusively demonstrated in Fig. 2.3b. The space available is along the perpendicular edges of the smartphone. The designers might also accommodate a few antennas on the other side of the longer edge. The figure also illustrates the electrical lengths of the space for various bands like 4G (0.7–2.7 GHz), sub-6 GHz 5G (3.5 GHz) and mmWave 5G (28 GHz). It must be noted that antennas of the current and previous generations must be crammed into this space, which is complicated ordeal in itself, in addition to these requirements, mmWave 5G antennas have specific metrics, which must be met for a reliable data link. Panel mountable antennas just beneath the mobile phone panel is the most common technique for antenna integration; this aspect shall be explored thoroughly in the forthcoming chapters. As evident from the illustration, the electrical space for sub-6 GHz is low compared to its mmWave 5G counterpart, which indicates

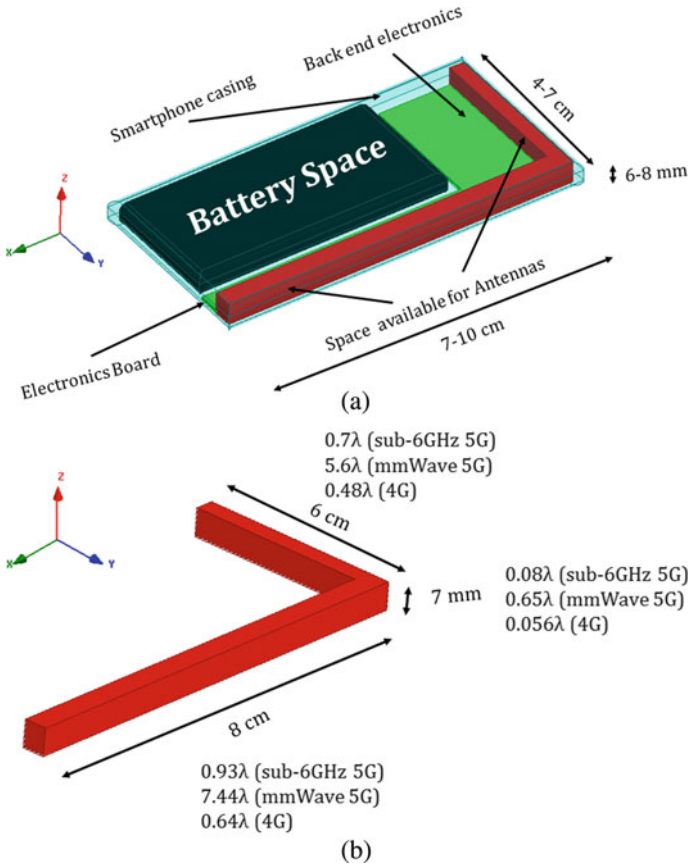

Fig. 2.3 **a** Breakout of a typical commercial smartphone **b** Exclusive space available for antenna integration

that high gain, unidirectional beams for 5G could be realized with a corresponding compromise in the metrics of the sub-6 GHz antenna system.

2.3.1 Detailed Characteristics of Antennas for Smartphones

The performance metrics, which are desirable for antennas integrated with smartphone specifically for the mmWave 5G purpose in discussed in this subsection. One of the most fundamental parameters of an antenna is the radiation pattern when activated. For older wireless standards, omnidirectional patterns would be ideal, the same logic would diminish the feasibility of a 5G link from the mobile terminal to base station. The radiation pattern for a mmWave 5G antenna must be unidirectional, which means that the patterns in the operating band must have a front to back ratio of

at least 10 dB, which makes sure that the power level of the backward radiation is at least 10 dB lower than the forward radiation levels. The radiation from the activated 5G antenna should be directed towards the base station and away from the user. The beamwidth should be in such a way as to achieve high gain at the mobile terminal but wide enough to ensure a successful data link with the base station or access point. An example for the expected radiation pattern when the mobile device is held vertically is illustrated in Fig. 2.4. A unidirectional antenna such as an electrically compact inset fed patch antenna could be integrated on the top panel, the expected 3D radiation pattern demonstrates the desirable pattern.

Even though lot of researchers [12–15] opine that high gain antennas on mobile devices is necessary to establish a decent communication link, the angular coverage is often neglected in this argument. Hence a reasonably high gain value such as 8–12 dBi would suffice for 5G mobile terminals' application. The form factor of the mobile device also must be considered to realize the gain necessary. As illustrated before, the panel height of most modern smartphones is 7 mm or 0.65 λ (calculated at 28 GHz in free space), indicating an electrically compact space to realize high gain. A unidirectional beam with hemispherical coverage itself would mean a gain of at least 6–7 dBi, if two elements of this radiator could be fed in-phase, a forward gain of 9–10 dBi could be achieved. Realizing high gain in an electrically compact environment would be discussed in Chap. 3.

Radiation efficiency beyond 90% is readily feasible with adequately wide antennas designed on low-loss substrate if the back-end electronics and the switches are properly matched to the radiating element, high radiation efficiency can be achieved. A wide impedance bandwidth (beyond 10%) would be preferred to support multiple bands centered around a specific carrier frequency, techniques to achieve wide bandwidth would be discussed in subsequent Chapters with design examples. The specific

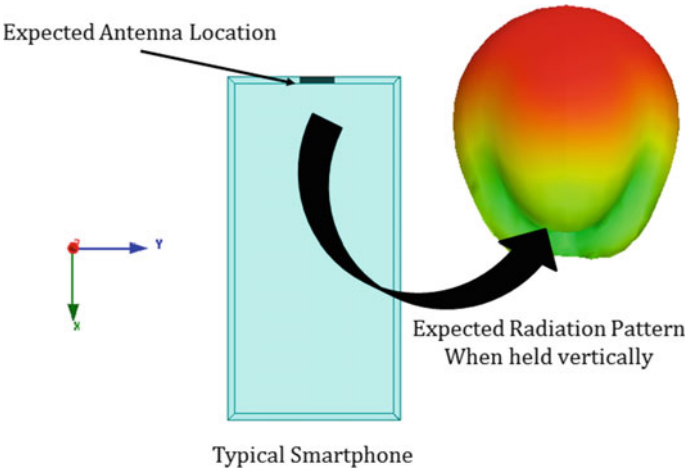

Fig. 2.4 Antenna placement example for a 5G device

absorption rate (SAR) is not at all a critical parameter for design of 5G antenna systems. The primary reason for this argument is that, as 5G services would be used for data usage, the distance between the user's head and the source of radiation would be electrically large, which indicates poor signal transmission into the user's head, when the antenna is activated.

Polarization is another important aspect of consideration while designing 5G antenna systems. Both horizontal and vertical polarization could be achieved within the constraints of the panel height of a typical smartphone. The polarization requirement should be backed by rigorous testing campaigns pertaining to both the polarizations. Polarization is important for indoor applications, as different polarizations result in different multipath effects, leading to variation in the received signal in the indoor space. Thus, experimental reports must be analyzed before deciding upon the polarization of the antenna system within a 5G mobile device.

2.3.2 Smartphone Usage Modes

Any user typically engages with the smartphone either in data mode or voice mode. In the data mode, the user is busy with data consumption, which in turn means that the higher data rate link is activated. In the voice mode on the other hand, lower data rate link is activated as voice services need substantially lesser data rate than its data counterpart. With this assumption, it can be inferred that the older wireless services such as 2G to 4G would be used for voice mode and the mmWave 5G would be exclusively used for data transmission and reception. Some researchers might argue that voice also could be transmitted through data services (VoIP: Voice over Internet Protocol), but that would mean that 5G would be wasted for low data rate applications. Statistically speaking, when the user is engaged with data consumption, the user would be staring at the screen of the mobile device, as illustrated in Fig. 2.5. We might assume that the smartphone would be at angle of roughly 30º with respect to the horizontal. This illustration suggests that the expected radiation for 5G must be away from the user, which could be achieved by panel mountable end-fire antenna or an electrically small broadside antenna. The expected radiation pattern is also demonstrated in Fig. 2.5. the logistics of realizing antenna systems to meet this criterion would be discussed in subsequent Chapters. It must be noted that the dynamism of the smartphone being handled by the user is neglected here on purpose, as the link would still be established if the antenna has a unidirectional, hemispherical beam. Some of the antennas or phased array antennas with boresight axis radiation might be unsuitable, but a fixed beam tilt of let's say 30º–45º might be a compromise between the form factor and the data link establishment.

The user when engaged in data mode might use the mobile device in vertical mode, when scrolling down Gmail® or Instagram®, for instance. The user might also be immersed with data in horizontal mode, when watching a movie or playing a game, such as Call of Duty®. The generic usage scenarios for both these use-cases

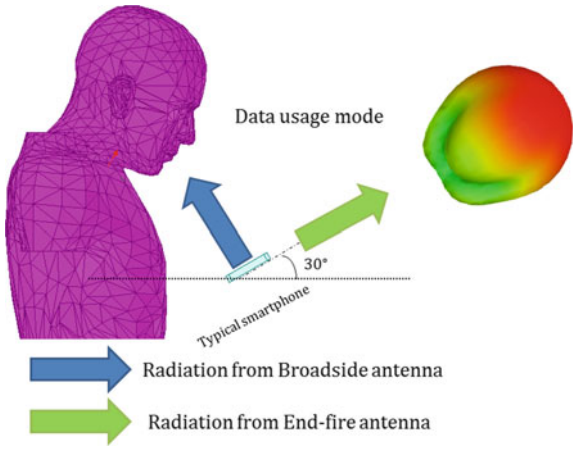

Fig. 2.5 Typical smartphone usage for data consumption

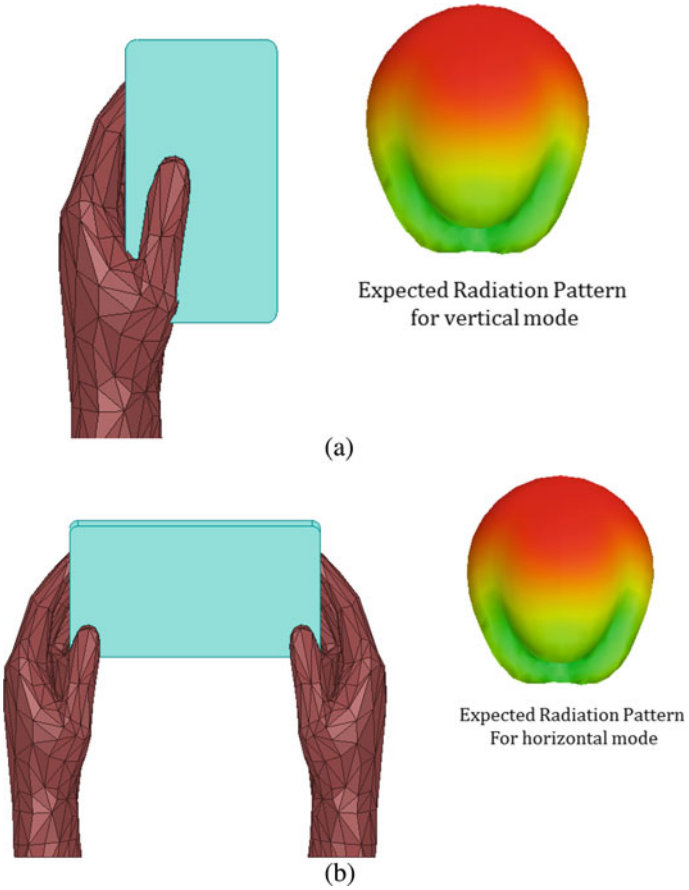

Fig. 2.6 Modes of smartphone data usage, **a** vertical mode, **b** horizontal mode

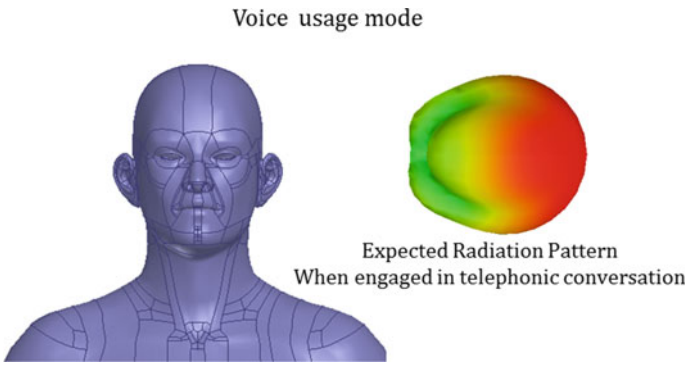

Fig. 2.7 Expected radiation pattern for voice usage

are illustrated in Figs. 2.6a, b. The expected radiation pattern must be like the aforementioned cases for both the data modes. In other words, the antenna system must radiate orthogonally when a particular mode is activated. This is a unique problem to the mmWave 5G antenna design, since both the modes do not hamper the performance of the sub-6 GHz wireless transmissions. Hence placement of antennas with respect to the orientation, is an important task too. One might assume that the simplest and most competent solution to this problem is to design a conductor backed wrapped around antenna at one of the corners of the mobile device, given the electrical size requirements of the antenna, it might not be a feasible solution.

The other usage mode is the voice mode, wherein the user is engaged in a telephonic conversation with the mobile device closer to the user's head. A typical use case scenario for voice mode is illustrated in Fig. 2.7. The expected radiation pattern would be away from the head to prevent heavy attenuation due to the head; this argument is applicable to the mmWave carrier frequencies alone. It is assumed that in case 5G is used for voice mode, this is the expected pattern, which could be easily realized by plugging the mobile device with a broadside radiator beneath the LCD (Liquid Crystal Display) panel. But most of the time, the older wireless generation(s) would be engaged in voice activities, which means that the expected pattern would never be feasible given the radiating physics of the electrically small antennas.

2.4 Antenna Requirements of a Wireless Dongle

The other important class of wireless device in the current consumer market is the wireless dongle. These dongles provide connectivity to the cellular network when connected to the PC (Personal Computer) or a laptop. Typically, a wireless dongle is like a pen drive in appearance and might match the form factor as well. These dongles also have a motherboard with integrated antenna. Like smartphones, the sub-6 GHz antennas of dongles would have an omni-directional pattern but might be

inappropriate for a 5G antenna. A generic wireless dongle along with its electrical dimensions is illustrated in Fig. 2.8. The inside electronics and the metallic ports are not shown in the figure, but implied. As evident from the illustration, the dongle provides ample electrical space to design and integrate mmWave 5G antennas at the edges. Coexistence with sub-6 GHz antennas, necessary for older wireless cellular standards, would not be very challenging to design due to the electrical real estate available in the dongle.

The user's hands would have very little effect on the performance of the antennas within the dongle. A popular use case for the wireless dongle is sketched in Fig. 2.9. The wireless dongle would be plugged onto a laptop, which means that the environment is mostly static, and dynamic beam scanning would be unnecessary.

The expected radiation pattern must be unidirectional with high front to back ratio. In this application, the backward radiation towards the laptop should be minimal to avoid specular radiation pattern due to the electrically large metallic parts within the laptop. As the user would be engaged with the laptop directly, radiation from the dongle should be minimal towards the user as well, like the argument of Fig. 2.5. hence the only logical solution of radiation which is both away from the user and that of the laptop is the orthogonal direction, or along –ve Y axis, with reference to Fig. 2.9. vertically mounted end-fire antennas would serve this purpose. A forward gain of 5–6 dBi would suffice as these antennas would be engineered for indoor applications,

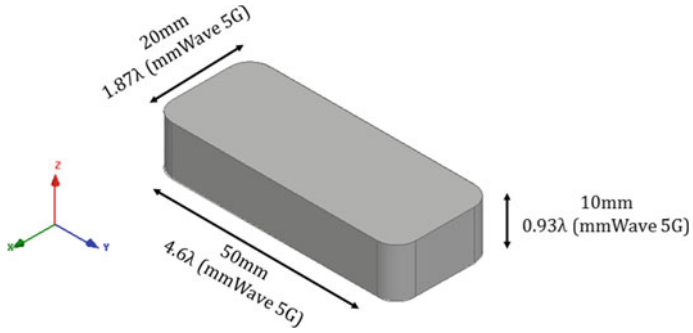

Fig. 2.8 Typical wireless dongle

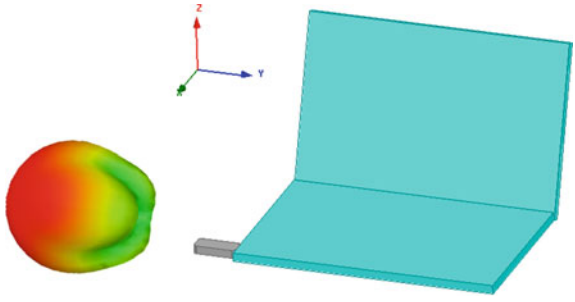

Fig. 2.9 Wireless dongle connected to a commercial laptop

which means that unidirectional hemispherical pattern would be desirable which dictates the values of the gains. Higher gain would mean narrow beamwidth and the possibility of losing the signal. It must also be noted that as these dongles are intended for low-power indoor applications, the indoor base stations also would have low gain antennas hence relaxing the need for high gain antennas. Radiation efficiency higher than 90% is readily feasible given the form factor of the device. The 10-dB impedance bandwidth must accommodate the promised bands like that of its smartphone counterpart. An integrated harmonic filter might be essential to suppress out of band signals. The SAR values are not relevant in this application for two reasons: first, the distance between the radiating 5G antenna and the user's head is typically over 1 m, significantly reducing the signal strength at the user's head. Second, radiating power is mostly directed orthogonally away from the user further decreasing the radiation exposure to the user.

2.5 Antenna Requirements for Wearable Devices

In the past decade, numerous wearable devices with wireless connectivity have been introduced in the consumer market. Sample wearable devices and their antenna requirements would be discussed in this section. Wearable devices include but not limited to smart watches, wireless earphones, Virtual reality headsets, smart goggles, health monitoring devices etc., invariably have low power and low range connectivity. It is speculated that these wearable devices would also be hooked on to mmWave 5G, which means that the antenna designers must accommodate 5G antennas with these devices.

Consider a generic smart watch illustrated in Fig. 2.10a, here the primary console is at the center with strap-on belts on either side of the console. Even though it appears that an electrically huge real estate is available to integrate the antenna system, the space is overloaded with LCD panel and the display electronics. This statement suggests that the effective space for antennas is much smaller than that of its smartphone counterpart.

Radiation must be directed away from the user and away from the user's hand to mitigate the attenuation effects. Hence the only logical space for realization of the antenna is to mount it perpendicular to that of the user's axis, when staring at the smart device. The contour of the radiation pattern is not very stringent as wearable applications deal with low power radios. Broadside panel mountable antennas could be designed for 5G applications without significant degradation of the performance metrics of the antennas.

The impedance bandwidth and gain requirements are like that of the wireless dongle. SAR might be relevant in this application due to the proximity of the radiating source and the user's head.

Another important class of wearable device popular in the recent times is the wireless earphone. A typical use case scenario of the wireless earphone is illustrated in Fig. 2.10b. Here the protruding element is close to 4 λ (free space wavelength

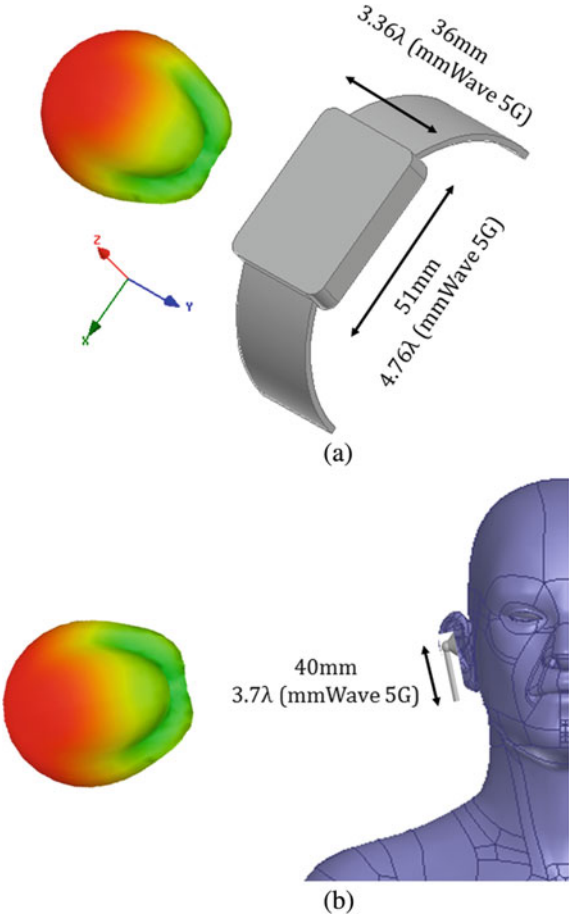

Fig. 2.10 Wearable devices: **a** Generic smartwatch. **b** Wireless earphone in use

computed at 28 GHz), but the actual module integrated with the audio processor and the speaker could have a diameter less than 10 mm (or 1 λ at 28 GHz). The expected radiation pattern should be strictly away from the user's head to avoid high SAR values and heavy attenuation. The antenna could be electrically small broadside element with coaxial feeding and high front to back ratio (at least greater than 15 dB). The speaker module of the earphone must have an electrically large system ground plane to ensure high front to back ratio. The other characteristics are like that of a smart watch.

2.6 Antenna Requirements for Base Stations and Access Points

Base stations are another important component of the cellular infrastructure. The older wireless standards had base stations mounted on metallic towers, typically 10–15 m tall. The same logic might not workout for mmWave 5G base stations. The primary reason being high free space power loss which indicates that taller base stations would unnecessarily decrease the received power. Also, base stations must be densely packed as discussed in Sect. 1.6.3. It is also speculated that 5G infrastructure would be a mixture of outdoor links and indoor links due to the high penetration loss of common building materials. Hence the design requirements for outdoor links would be different from that of the indoor links, as the number of users and the power requirements are different for both the cases.

Consider a typical ceiling mounted access point within a room as demonstrated in Fig. 2.11. These are like WiFi modems operating at 2.4 GHz except that these 5G access points operate in the 28 GHz band. As the distance between the radios is manageable, low power transmission would suffice for establishing and maintaining a data link. The pattern must be unidirectional as power towards the ceiling would be wasted. Hemispherical pattern ensures maximum angular coverage in an indoor environment. The antennas within access points need not have wide bandwidth since achieving wide bandwidth with high radiation efficiency would be difficult.

The radiation efficiency must be as high as possible that could be achieved by the chosen manufacturing process. Several design examples to achieve high radiation efficiency would be explained in Chap. 6.

The base stations for outdoor links have a different set of requirements. A sample base station mounted on an antenna mast is sketched in Fig. 2.12. The expected patterns are also shown in the same illustration. The antennas or antenna system

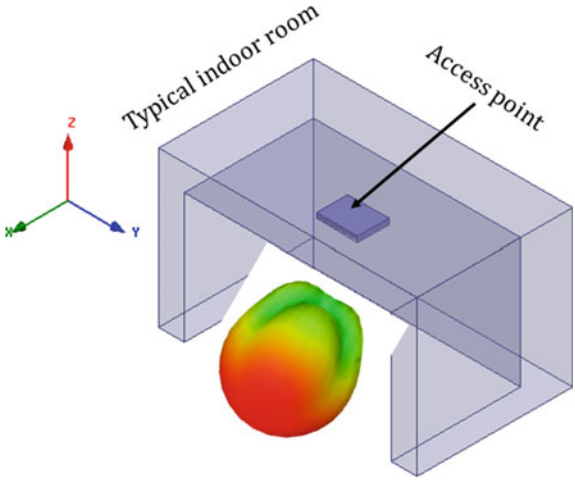

Fig. 2.11 Access point in an indoor context

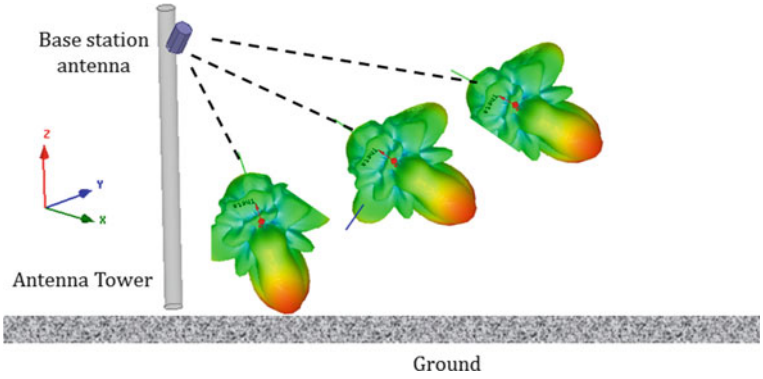

Fig. 2.12 Base station in an outdoor context

must radiate toward the ground, which has the highest density of subscribers. The gain must be high, as the expected area of coverage is higher than the indoor access points. The base station module needs to be tilted with respect to the axis of the antenna tower, to maximize coverage. It must also be noted that beam scanning is necessary to have a wider outreach for a given base station module. In some cases, beam switchability might be the preferred choice over phased array systems. The radiation efficiency also must be as high as the technology permits. Radiation efficiency is a critical parameter, as the base station would be activated much longer compared to the antennas on the mobile handsets. The base station antennas must be rugged and sturdy as they would be exposed to harsh environments [16]. Design examples to illustrate these criteria would be discussed in Chap. 7.

2.7 Conclusion

Antenna design requirements for wireless devices is an important topic of discussion. Generic antennas for previous wireless standards are explained followed by the detailed breakout of a commercial smartphone. The antenna requirements for the smartphone also were discussed in detail. The data usage modes and the voice usage mode were explained with respect to antenna requirements. Antenna requirements for common wireless devices such as dongles, wearable devices and access points were also described in this Chapter. This Chapter serves as a guide for the designs presented later in this book.

References

1. Rappaport, T.S.: Wireless Communications: Principles and Practice, vol. 2. Prentice Hall PTR, New Jersey (1996)
2. Huo, Y., Dong, X., Xu, W.: 5G cellular user equipment: from theory to practical hardware design. IEEE Access **5**, 13992–14010 (2017)
3. Egashira, Y.: Telescopic antenna for portable telephones. U.S. Patent 5,546,094, issued August 13, 1996
4. Rowell, C., Lam, E.Y.: Mobile-phone antenna design. IEEE Antennas Propag. Mag. **54**(4), 14–34 (2012)
5. Tarvas, S., Isohatala, A.: An internal dual-band mobile phone antenna. In: IEEE Antennas and Propagation Society International Symposium. Transmitting Waves of Progress to the Next Millennium. 2000 Digest. Held in conjunction with: USNC/URSI National Radio Science Meeting, vol. 1, pp. 266–269. IEEE (2000, July)
6. Wong, K.L., Kang, T.W., Tu, M.F.: Internal mobile phone antenna array for LTE/WWAN and LTE MIMO operations. Microw. Opt. Technol. Lett. **53**(7), 1569–1573 (2011)
7. Ban, Y.L., Li, C., Wu, G., Wong, K.L.: 4G/5G multiple antennas for future multi-mode smartphone applications. IEEE Access **4**, 2981–2988 (2016)
8. Wong, K.L., Chen, S.C.: Printed single-strip monopole using a chip inductor for penta-band WWAN operation in the mobile phone. IEEE Trans. Antennas Propag. **58**(3), 1011–1014 (2009)
9. Sun, L., Huang, W., Sun, B., Sun, Q., Fan, J.: Two-port pattern diversity antenna for 3G and 4G MIMO indoor applications. IEEE Antennas Wirel. Propag. Lett. **13**, 1573–1576 (2014)
10. Malik, J., Patnaik, A., Kartikeyan, M.V.: Novel printed MIMO antenna with pattern and polarization diversity. IEEE Antennas Wirel. Propag. Lett. **14**, 739–742 (2014)
11. Masoodi, I.S., Ishteyaq, I., Muzaffar, K., Magray, M.I.: Low cost substrate based compact antennas for 4g/5g side-edge panel smartphone applications. Progr. Electromagn. Res. Lett. **91**, 145–152 (2020)
12. Ta, S.X., Choo, H., Park, I.: Broadband printed-dipole antenna and its arrays for 5G applications. IEEE Antennas Wirel. Propag. Lett. **16**, 2183–2186 (2017)
13. Bang, J., Choi, J.: A SAR reduced mm-wave beam-steerable array antenna with dual-mode operation for fully metal-covered 5G cellular handsets. IEEE Antennas Wirel. Propag. Lett. **17**(6), 1118–1122 (2018)
14. Hwang, I.J., Ahn, B., Chae, S.C., Yu, J.W., Lee, W.W.: Quasi-Yagi antenna array with modified folded dipole driver for mmWave 5G cellular devices. IEEE Antennas Wirel. Propag. Lett. **18**(5), 971–975 (2019)
15. Di Paola, C., Zhao, K., Zhang, S., Pedersen, G.F.: SIW multibeam antenna array at 30 GHz for 5G mobile devices. IEEE Access **7**, 73157–73164 (2019)
16. Chen, Z.N., Luk, K.M.: Antennas for Base Stations in Wireless Communications. McGraw-Hill Education (2009)

Chapter 3
Antenna Systems for Smartphones

3.1 Introduction

Several recent reports strongly suggest that data consumption on mobile devices would see a surge in the coming years. It must be carefully noted that the voice demand growth in the coming future would be minimal compared to the data consumption growth. A typical voice channel needs a couple of kHz bandwidth, on the other hand a high-speed data channel would require a couple of MHz bandwidth. If these data channels are to be scaled up for 5G and 6G consumers, then the current data channels need to re-engineered [1]. One of the options to improve the data throughput in the communication system is to increase the spectral efficiency, but this method has its own limitations as suggested by numerous communication engineers in the past. There are only certain number of subscribers who could be accommodated at any given time within a prescribed allotted bandwidth. As the spectral efficiency is limited, the data throughput available to the user would also be limited. The other alternative is to rethink about the entire cellular ecosystem by shifting the carrier frequencies to millimetre wave frequencies. Several variants of testing campaigns have testified the feasibility of using millimetre waves as carrier frequencies for outdoor communication links [2, 3]. The reported testing campaigns have limited range, typically in the range of 100–200 m. Several commercial carriers have already deployed mmWave networks in North America, Europe, and Asia.

Even though, millimetre wave spectrum has been popularized as the future carrier frequency, designing communication links and radio transceivers is challenging due to the high free space path loss and high penetration loss [1]. Free space path loss could be mitigated by increasing the gains of the antennas on base station and mobile device respectively. Gain of the antenna is decided by the physical aperture of the antenna [4]. Researchers argue that as the carrier frequency is shifted to millimetre waves, the antenna size would automatically shrink, hence increasing the number of elements would enhance gain for the same physical footprint [3]. Several antennas need to be controlled individually via appropriate controllers. Alternate design strategies are

S. K. Koul and K. G. S., *Antenna Architectures for Future Wireless Devices*,
Signals and Communication Technology,
https://doi.org/10.1007/978-981-16-7783-0_3

needed to realize reliable antenna systems on the smartphone. A couple of design examples are discussed in this Chapter.

Commercial smartphones have very limited space for antenna integration, as seen in Chap. 2 [5–8]. Several topologies for 5G smartphones have been reported in the recent years [9–22]. Only a few antenna designs operating in the 28 GHz band are compliant with commercial smartphone dimensions. The practical implementational aspects of the antenna system is often ignored in the literature. A couple of antenna systems, along with the integration on to a smartphone platform are discussed in this chapter.

3.2 Data Modes of a Typical Mobile Device

The most common ways of handling a mobile device in data mode is shown in Fig. 3.1a, b. In data mode-1, the elongated side of the mobile device is parallel to the hands and in data mode-2, it is perpendicular to the hands. The expected radiation patterns at 28 GHz for both the modes are also illustrated in Fig. 3.1. It is implied that

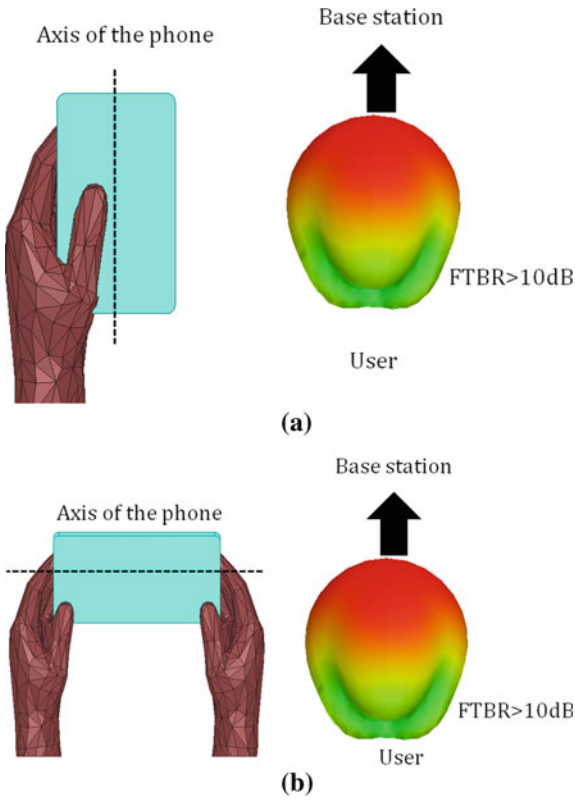

Fig. 3.1 Data modes of smartphone: **a** Data mode-1. **b** Data mode-2

as the user switches between the two modes, a millimetre wave switch would activate the necessary port of the antenna system. Switch design is beyond the scope of this book. Planar high isolation SPDT (Single Pole Double throw) switches at 28 GHz could be designed based on standard design principles. The idea is that the radiation must be directed towards the base station and away from the user, irrespective of the data mode engaged by the user. If the primary beam is directed towards the base station, then the chances of a beam lock between the smartphone and the base station improves. Radiation must be directed away from the user to prevent attenuation by the user. A typical human torso would attenuate the signal by up to 20 dB at 28 GHz.

The antenna system must dynamically switch the antennas according to the orientation of the mobile device. Hence, orthogonal beam switching with high front to back ratio with unidirectional beams for both the data modes would be necessary. This is a unique problem to millimetre wave 5G antenna design, and not necessarily for the sub-6 GHz antenna designs of the previous generations. The reason is that attenuation by users' hands is significantly lower in the sub-6 GHz spectrum, signal propagation would not be disturbed by the users' hands.

3.3 Design Candidates for Beam Switching

One common approach to deal with the afore-mentioned data mode problem is to design a leaky wave antenna (LWA). A typical LWA and its patterns are shown in Fig. 3.2. To scan the beam, frequency must be altered. Frequency of operation is usually fixed by the telecom regulatory authorities and hence this is not a flexible parameter. Also, tweaking the entire cellular infrastructure for variable frequency beam scanning would be extremely complex. The scanning loss is also high in LWA,

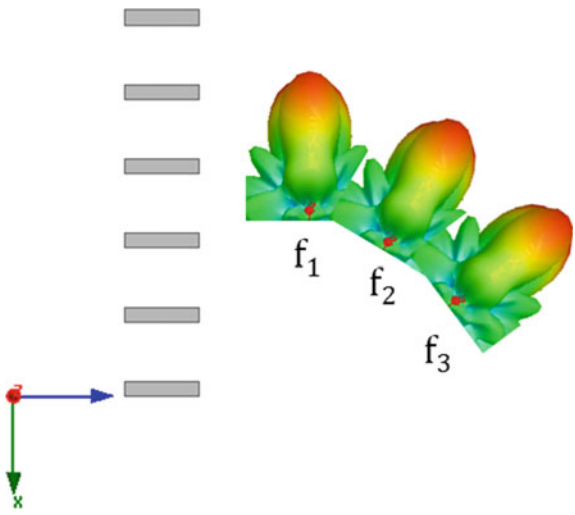

Fig. 3.2 Generic layout of a leaky wave antenna

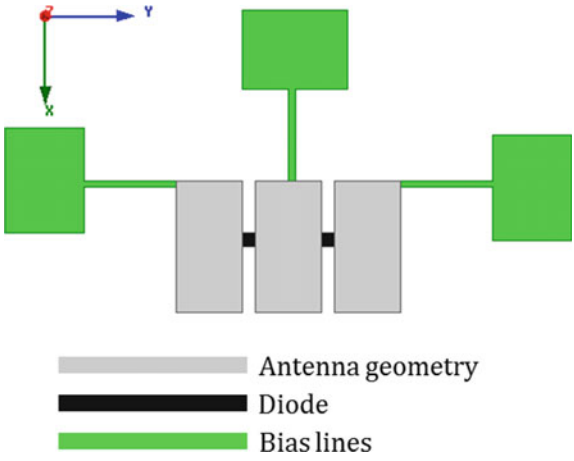

Fig. 3.3 Generic layout of a reconfigurable antenna

which in turn decreases the reliability of the data link. Another point is that LWAs are electrically larger compared to discreet elements, hence might not be integration friendly with a smartphone.

Another approach is to design pattern reconfigurable antenna, which can switch between 0° and 90° beams. A generic pattern reconfigurable antenna is illustrated in Fig. 3.3. Here, as a certain number of diodes are activated, beam is at one angle and the other set of diodes' activation leads to beam at another angle. Achieving orthogonal beams with this method is difficult even at the microwave frequencies. The design problem becomes even more complex when attempting to design a reconfigurable antenna at 28 GHz. As observed in Fig. 3.3, the size of the radiator would be close to 3 mm × 4 mm, the Ka-band diode also would occupy similar dimensions. To achieve two distinct patterns, at least two diodes are essential, making it an impossible constraint. On top of this, the electrically large bias lines also would radiate, leading to poor patterns when the diodes are activated. Fabrication errors also would easily detune the antenna. For all these reasons, reconfigurable antenna systems might be unsuitable for smartphone integration.

The current de-facto standard for designing antennas for mobile devices has been phased arrays [3]. A typical inset fed patch antenna and its four-element array operating at 28 GHz is shown in Fig. 3.4a. The corresponding beam scanning of the phased array in YZ plane is illustrated in Fig. 3.4b, the 3D patterns prove that a typical phased array system would suffer from scanning loss up to 3 dB, when the beam is formed at 45°, beyond this angular scan the patterns become unusable as evident from Fig. 3.4b also observed in [10, 11, 13–17]. If the beam integrity is compromised, phased array would fail to operate when excited for orthogonal beams, which is a requirement for the use-case in consideration as per Fig. 3.1. The scanning behavior is also observed in end-fire phased array systems. Several pattern diversity schemes have been proposed [23–31], but these schemes would be in-operational for orthogonal beams or would not necessarily compactly fit in a commercial smartphone. Hence, compact beam switching antenna modules are investigated in this Chapter.

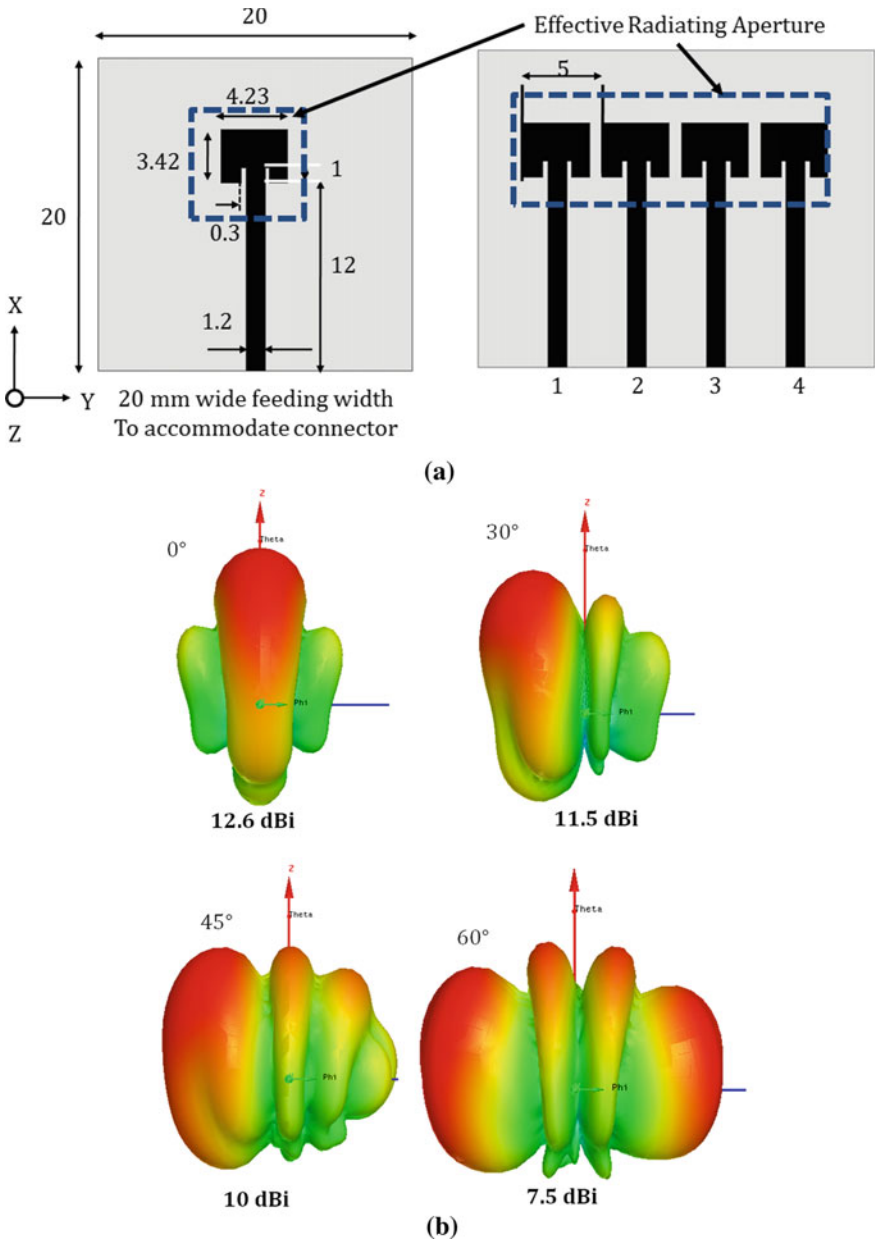

Fig. 3.4 **a** Schematics of inset fed patch antenna and its array. **b** Scanning loss demonstration of 4-elements array

3.4 Shared Ground Conformal Antenna Module

3.4.1 Conformal Array

Planar broadside antennas when integrated with the mobile device would radiate towards the user and cause a noticeable amount of attenuation due to the human tissue and/or torso [11, 13, 15]. On the other hand, a planar end-fire antenna such as a printed dipole or printed Yagi antenna [10, 12, 23, 29, 30] would have high front to back ratio and radiate most of the energy towards the base station. Both the types of antennas would occupy a significantly large footprint as the space near the transmission lines would be unusable. Hence, a conformal unidirectional antenna design is presented in this section.

As there are two modes of smartphone operation, the antennas corresponding to both the modes would be independently designed and integrated together with a shared ground. First, single hand mode is designed. A conformal corporate fed array is proposed. The planar version of the antenna is illustrated in Fig. 3.5a. The antenna is designed on Nelco NY9220 substrate with a dielectric constant in the range 2.18–2.22 and a dielectric loss tangent of 0.0009. Variation of the dielectric constant within the said range does not detune the antenna significantly. Ideally, for high radiation efficiency air should be used as the substrate but designing metallic radiators floating in air would not be feasible [4], more on this coming up in Chap. 6. Also, coaxial feeding is avoided to aid conformity. The proposed antenna is constructed on a 20 mil substrate which is a compromise between flexibility and impedance bandwidth [4]. An all-metallic planar antenna is presented in Sect. 6.8, the same could not be integrated with a smartphone. The feed is a 50 Ω transmission line, which is matched to the impedance of the inset fed patch antenna through a 1×4 power divider.

The proposed antenna when integrated with the panel of the mobile device would not be practical to implement. Hence, a corner bent version of the same shown in Fig. 3.5b is investigated. It is well known that the slots from the fringing fields create radiation from a patch antenna, hence the effective radiating area is decided by the inset fed patch alone and this could be in the orthogonal plane (XY plane) and the transmission line along with the power divider network could be built in the YZ plane, thus reducing additional radiation arising due to discontinuities in the feeding network. As evident from Fig. 3.5b, the radiators are compliant with the smartphone panel height. The corner bent design could be further extended to a conformal version as illustrated in Fig. 3.5c. The corner bent antenna could be conformed onto the curved panel of typical smartphones. As the actual radiating aperture of the antenna is unharmed post conforming, the proposed antenna would deliver desired characteristics. The fabricated prototype is shown in Fig. 3.5d, a 2.92 mm southwest end-launch connector is used for measurements. The radiators are placed at least 1 λ away from the feed plane, which ensures minimal influence of the electrically large connector on the measurements.

This concept of conformal array could be even designed with an aperture coupled feeding technique, without any deterioration in the performance metrics. The input

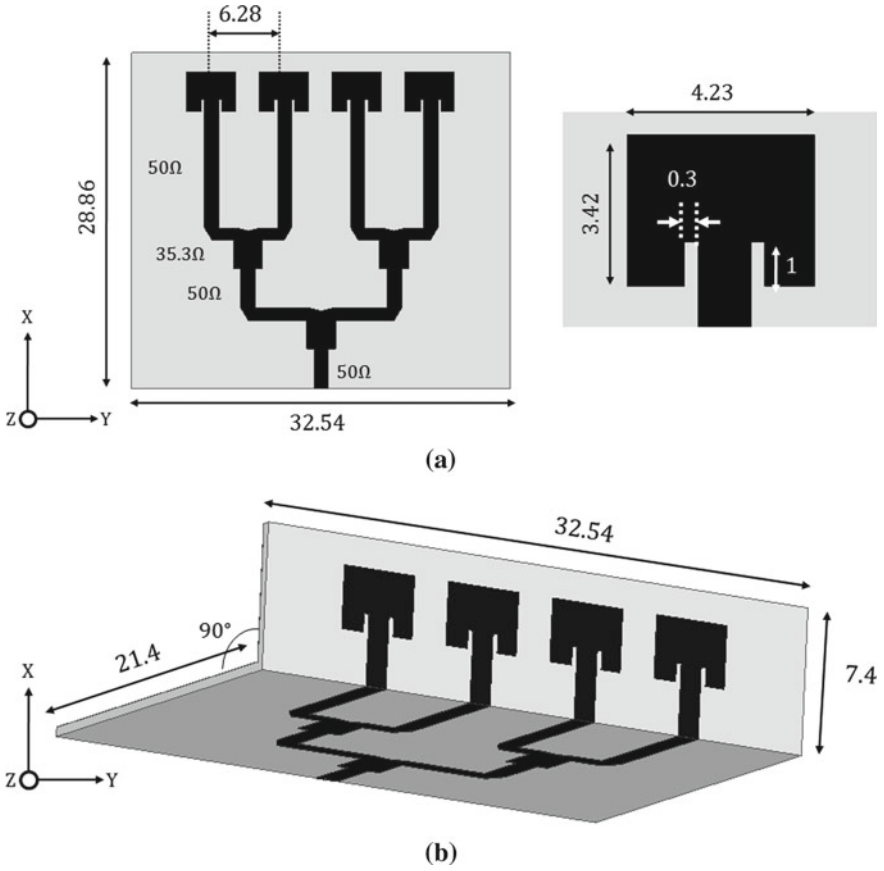

Fig. 3.5 **a** Corporate fed planar array (units: mm). **b** Conformal array (units: mm). **c** Concept of wrapping. **d** Photograph of the prototype

reflection coefficient is shown in Fig. 3.6. The simulated impedance bandwidth is from 26 to 29 GHz translating to 11%. The S-parameter measurement is done with Agilent PNA E3864C. All the simulations were done using Ansys HFSS. The deviation between simulated and measured curves are attributed to lack of soldering between the end-launch connector and the antenna element. The actual connector used for measurement had undergone numerous mating cycles leading to deterioration in the connector to antenna transition. A more expensive approach would be to limit the number of mating cycles for a given connector.

The H-plane or YZ plane patterns are shown in Fig. 3.7. The patterns at 28 and 30 GHz are almost similar, indicating beam integrity across the operational spectrum, which is an expected feature of a wideband corporate fed array. The front to back ratio is more than 20 dB, which means that the power radiated towards the user's hand, or the user would be very minimal and most the radiated power is directed towards a

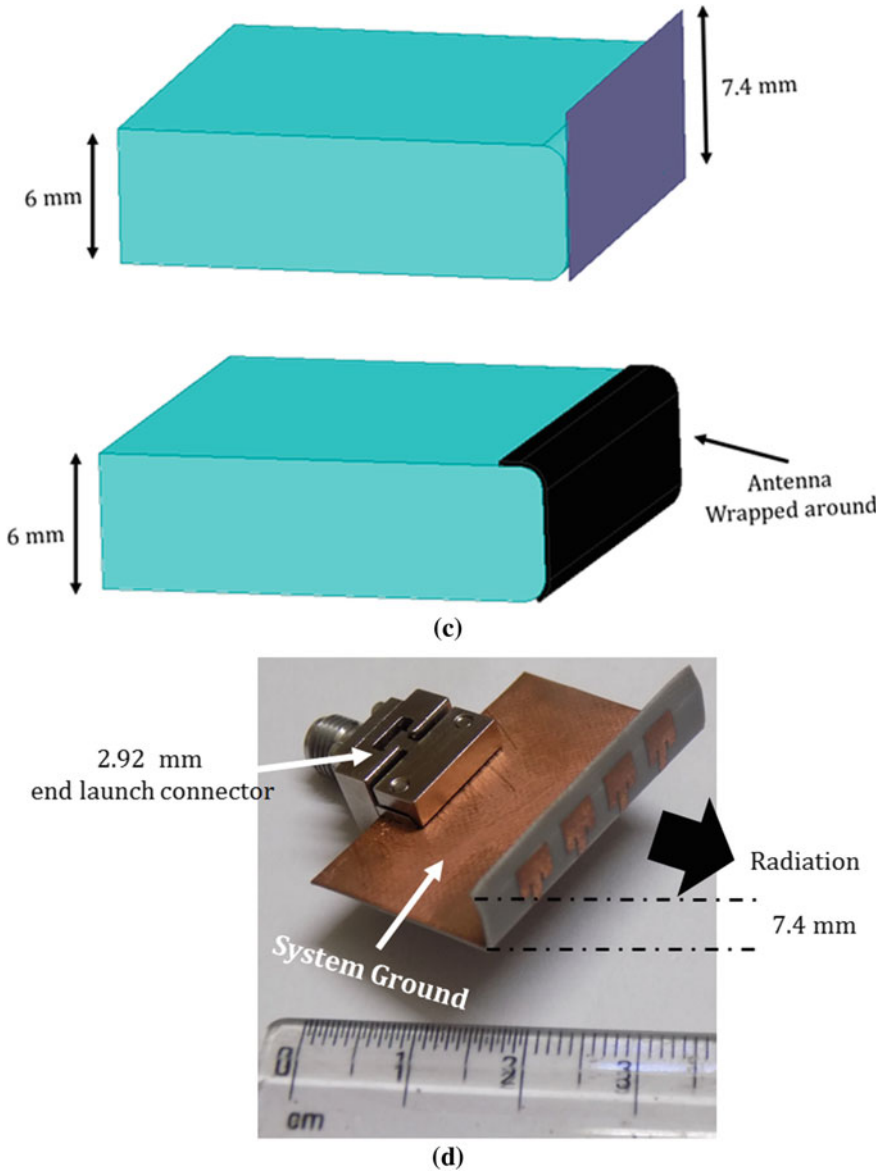

Fig. 3.5 (continued)

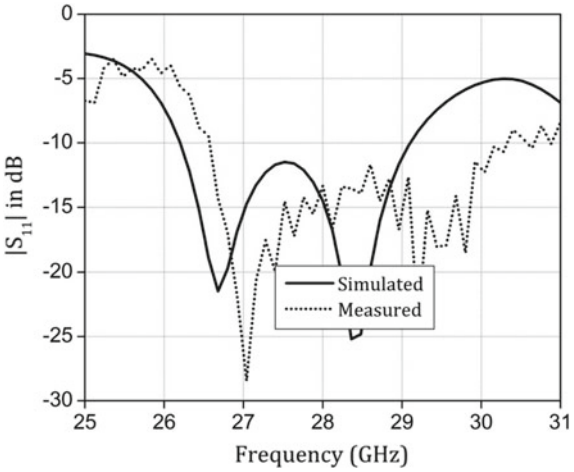

Fig. 3.6 $|S_{11}|$ of the conformal array

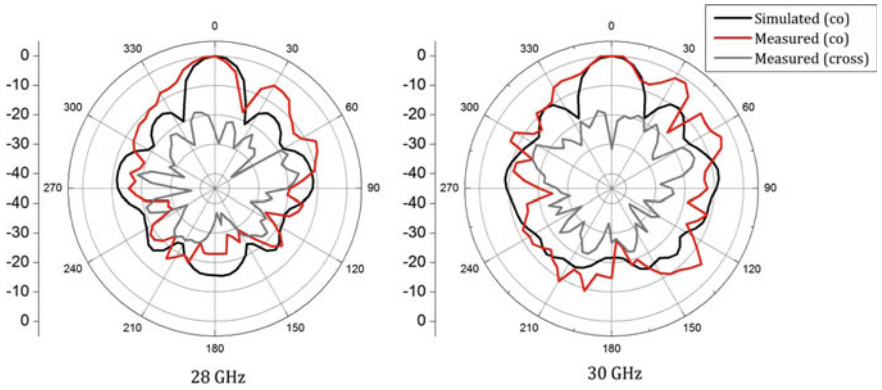

Fig. 3.7 H-plane (YZ plane) patterns of the array

base station or access point. The cross-polarization level is less than 25 dB indicating a high polarization purity of the vertically polarized radiating element. Polarization purity is not really a stringent requirement for a smartphone. The forward gain of the conformal antenna is depicted in Fig. 3.8. The gain is close to 9 dBi at 28 GHz, the gain could have been higher by up to 2 dB, if Wilkinson based power divider was used to design the power divider network. Wilkinson based power divider needs 100 Ω resistor to be soldered between the feed lines. The passive resistor would also bring additional inductances and parasitic capacitances further complicating the design process. Due to fabricational challenges these resistors are avoided in the current design. Standard gain transfer method was used for gain measurement in an anechoic chamber.

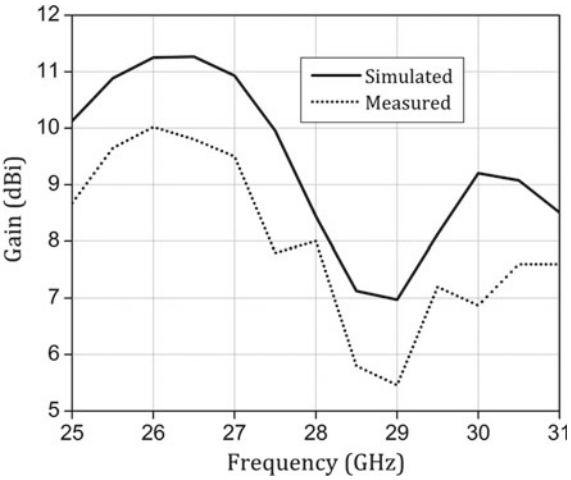

Fig. 3.8 Forward gain of the conformal array

3.4.2 Conformal Printed Yagi Antenna

To design an antenna which works for the dual hand mode of Fig. 3.1, the antenna must radiate orthogonally with respect to the beam of conformal antenna presented in Sect. 3.4.1. The simplest way to realize this is to design either a printed dipole [14] or a planar Vivaldi [12]. The issue with these designs is low gain and non-compliance with the smartphone panel height. Hence, a conformal printed Yagi-Uda antenna is proposed. The planar version of the antenna is illustrated with dimensions in Fig. 3.9a. The agenda of this design is to feed along X axis and get the antenna to radiate along Y axis so that the antenna could be conformed onto the mobile panel. To achieve this objective, an orthogonal printed Yagi antenna is designed. The feed is a standard 50 Ω transmission line feeding the arms of the printed dipole, but a 90° bend is required for this design. A straight-forward approach is to design the transmission line with a bend, but this approach would create additional radiation due to the discontinuity.

Hence, stubs which double up as impedance transformers are used to solve this issue. The stubs are shown in the inset of Fig. 3.9a. The effective radiating aperture is 7.4 mm, hence could be easily integrated onto a mobile panel. The conformal version of the printed Yagi is shown in Fig. 3.9b, the bending does not significantly affect the characteristics of the element. The fabricated prototype along with the mounted end-launch connector is shown in Fig. 3.9c. The input reflection coefficient of the conformal Yagi is shown in Fig. 3.10, which has an input impedance bandwidth of 27–31 GHz, translating to 13.8%.

The H-plane radiation patterns of the antenna are shown in Fig. 3.11, the antenna has a high front to back ratio when conformed, indicating that radiation towards the user would be minimal and satisfy the criteria for the use-case as illustrated in Fig. 3.1. The forward gain is 7 dBi as observed in Fig. 3.12. Gain could be further increased

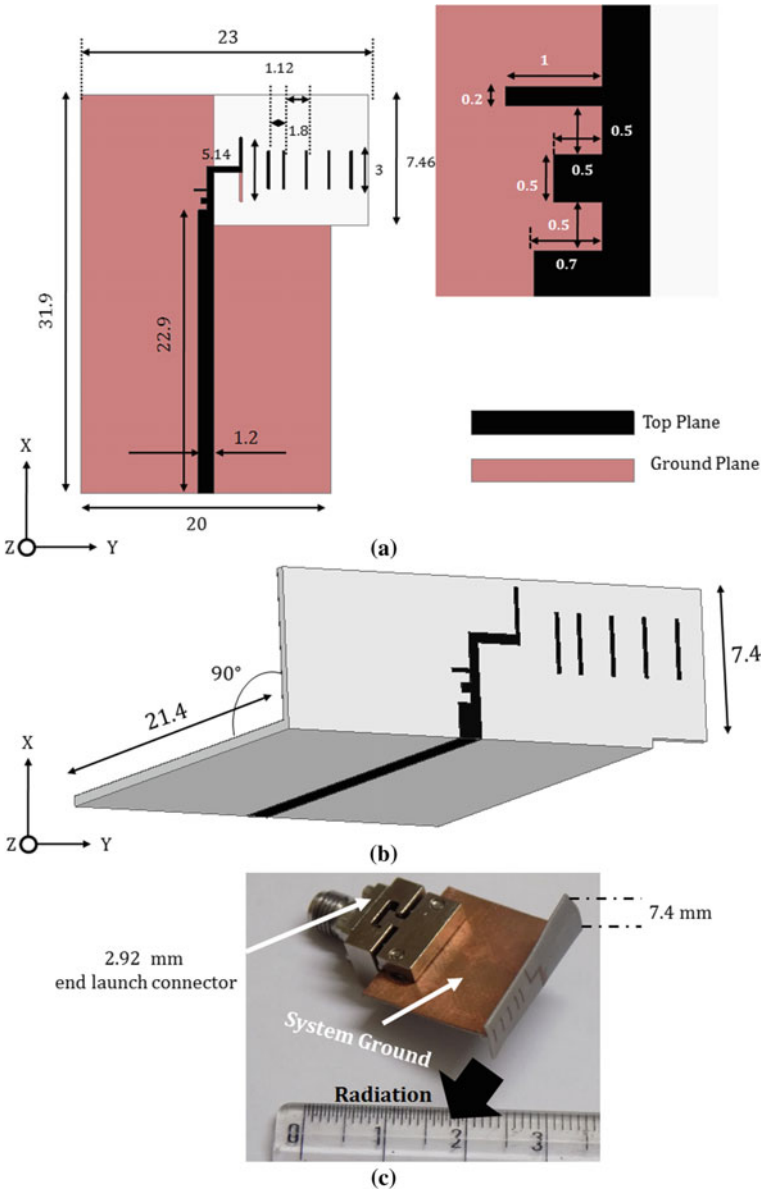

Fig. 3.9 **a** Printed Yagi antenna with orthogonal beam (units: mm), **b** Conformal Yagi antenna (units: mm), **c** Photograph of the fabricated prototype

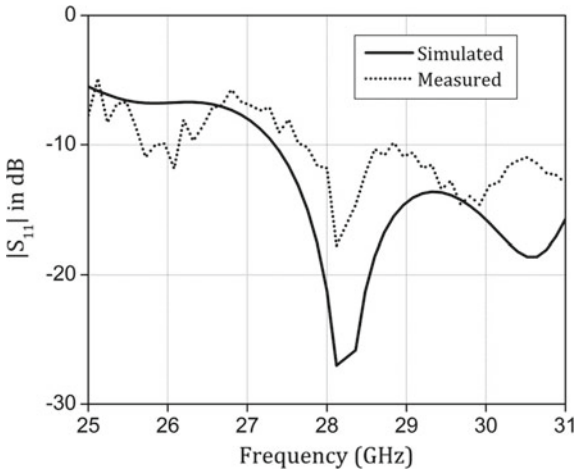

Fig. 3.10 $|S_{11}|$ of the conformal Yagi Uda antenna

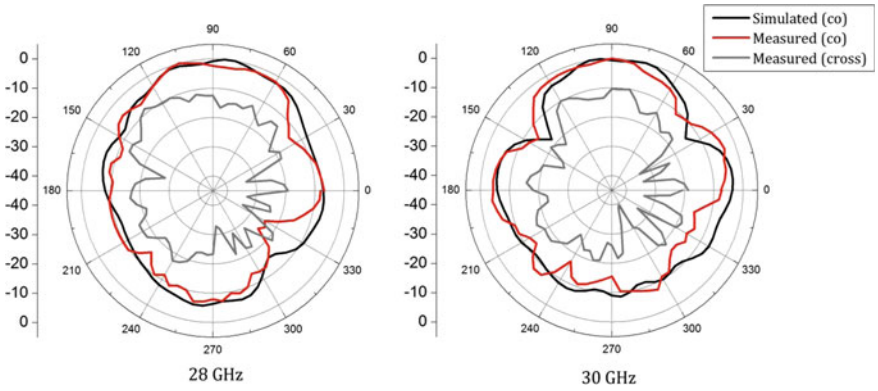

Fig. 3.11 H-plane (YZ plane) patterns of conformal Yagi antenna

by increasing the number of parasitic radiators or by integrating the aperture with appropriate sub-wavelength metamaterial unit cells.

Table 3.1 proves that the proposed concept of conformity yields high gain for minimal physical footprint compared to other reported articles in the 28 GHz band.

3.4.3 Shared Ground Beam Switching Module

The proposed antennas of Sects. 3.4.1 and 3.4.2 must be integrated together to be useful as a beam switching or pattern diversity module. The proposed shared ground is

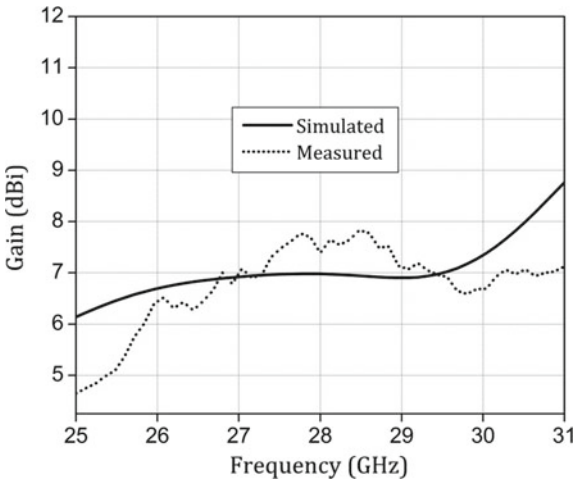

Fig. 3.12 Forward gain of conformal Yagi antenna

Table 3.1 Comparison with reported articles

Ref	Freq	Con	MI	G	ERV
[10]	28	No	No	9	0.138
[14]	28	No	No	6.5	0.207
[23]	28	No	No	11	0.05
[31]	28	No	No	6	0.006
[32]	28	No	Yes	12	0.027
[33]	28	No	Yes	5	0.005
[34]	28	No	Yes	1.5	0.026
[35]	26	No	No	6	0.192
PR1	**28**	**Yes**	**Yes**	**8.5**	**0.099**
PR2	**28**	**Yes**	**Yes**	**7**	**0.07**

Ref Reference, *Freq* Operating Frequency (GHz), *Con* Conformal design, *MI* Mobile integration, *G* Gain (dBi), *ERV* Effective Radiating Volume ($\lambda_0{}^3$), *PR1* Proposed design 1 (Sect. 3.4.1), *PR2* Proposed design 2 (Sect. 3.4.2)

illustrated in Fig. 3.13a, the conformal array and the conformal printed Yagi antennas are designed on the same ground and conformed together. The array is sliced at the non-radiating edge of the element at the edge leading to a compact design without altering radiation characteristics of the conformal array. The distance between the two elements is 1.2 mm translating to 0.11 λ at 28 GHz. It is interesting to note that the orthogonal beam switching module has a shared ground, which means that the RF electronics or the motherboard of the smartphone could be integrated with the module with almost no deterioration in the radiation characteristics of both the

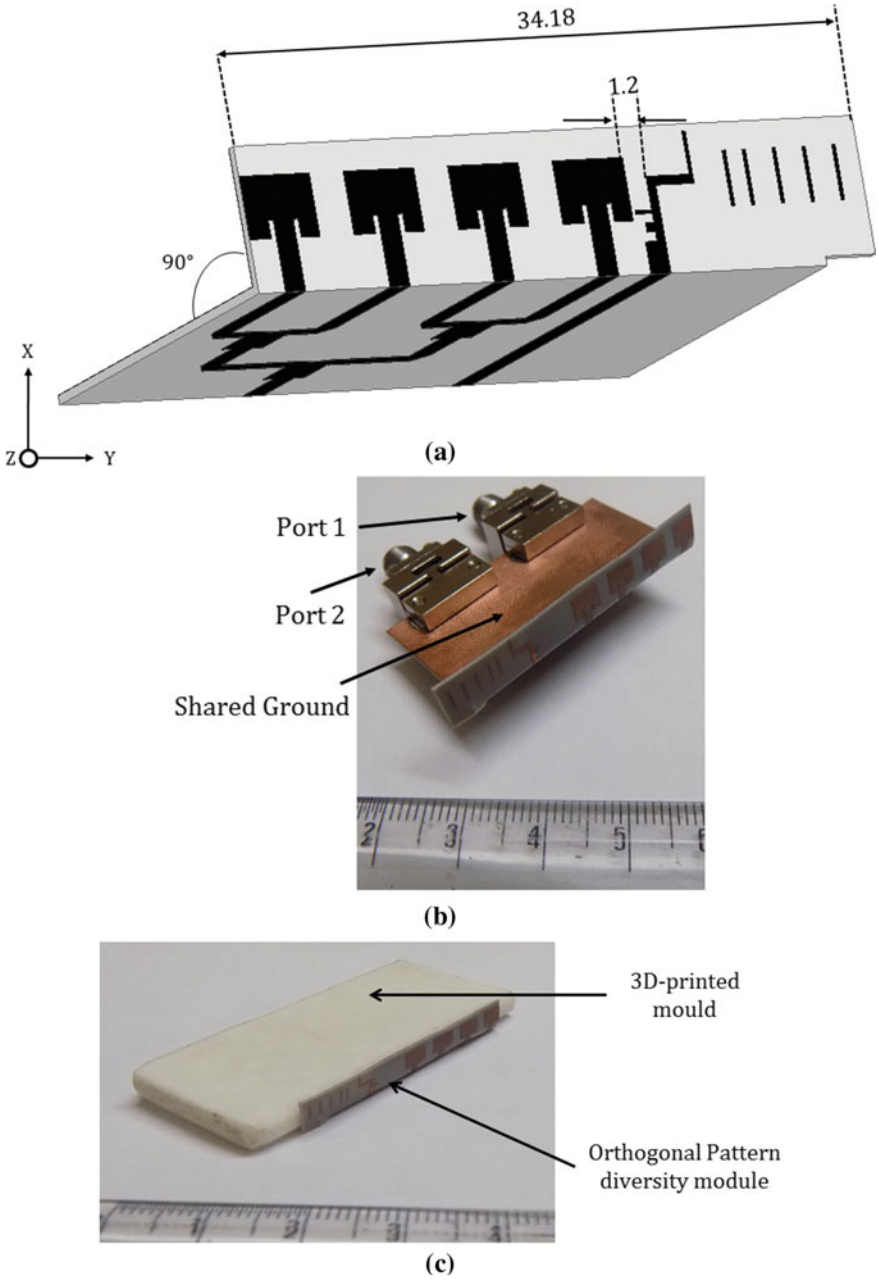

Fig. 3.13 **a** Schematics of the shared ground antenna module (units: mm), **b** Photograph of the prototype, **c** Prototype with a 3D-printed mould, **d** Prototype with a 3D-printed mock-up

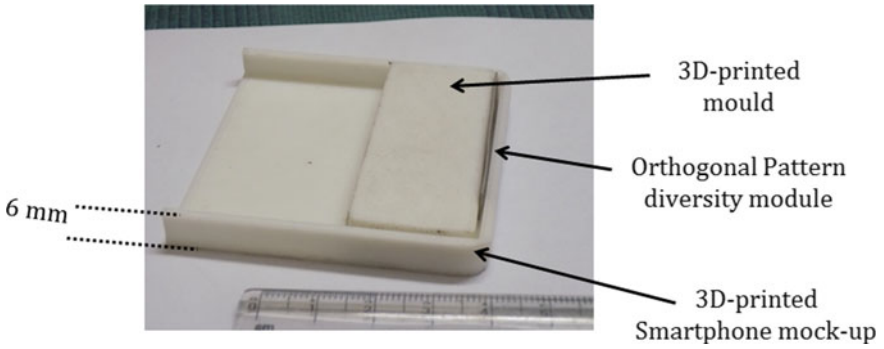

Fig. 3.13 (continued)

antenna elements. Design such as [13] have defected or slotted ground structure which is usually not recommended by the mobile phone industry. Figure 3.13b shows the fabricated prototype with the connectors. The distance between the ports were increased to accommodate the bulky connectors. A 3D-printed mould was designed which mimics commercial smartphone. Fancy curvatures of modern smartphones were also incorporated in the mould design, as evident from Fig. 3.13c, d. The proposed antenna module is mounted to check the compliance of the design and the module has minimal footprint which satisfies both the modes of mobile device operation. The mutual coupling between the ports is less than 20 dB, despite a shared ground and electrical closeness, across the spectrum due to the orthogonal radiation from the respective ports. The antenna of the proposed module has vertical polarization like industry standard designs reported or patented in the recent past.

The radiation patterns of the antenna module are depicted at 28 GHz in Fig. 3.14a and its corresponding 3D patterns is shown in Fig. 3.14b. The patterns are like the individual counterparts indicating a high beam integrity of the antenna module. Table 3.2 indicates that the proposed design is electrically compact with mobile panel integration which has orthogonal beam switching.

3.5 Ultra Compact Vertically Mounted End-Fire Antennas

In the previous Section, shared ground orthogonal beam switching module was explored. In this Section, vertically mounted co-polarized end-fire antenna system is investigated [36].

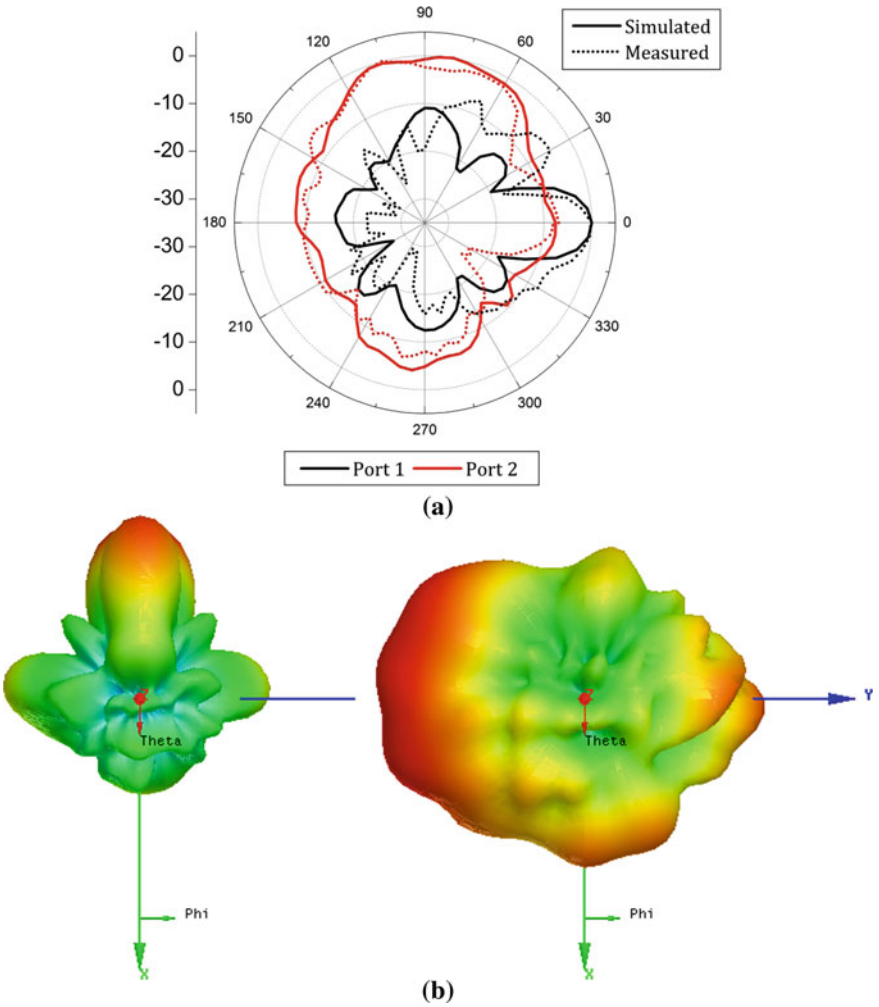

Fig. 3.14 **a** Radiation patterns of the module at 28 GHz, **b** 3D patterns of the module at 28 GHz

3.5.1 Compact Yagi Antenna

To design an electrically compact end-fire antenna, the ground plane requirements of the feeding line is investigated. If microstrip fed end-fire antenna is placed on the XY-plane, then the antenna's width along the X axis must be reduced to achieve maximum compaction of the size. The feeding line reduction is of not much significance as the actual implementation would have a short feeding line. A microstrip transmission line of length 50 mm, along Y axis, and characteristic impedance of 50 Ω on Nelco NY9220 substrate with 20 mil thickness is simulated. The width of the ground plane is varied to understand the variation of insertion loss. The insertion loss for a ground

Table 3.2 Comparison of the module with reported designs

Ref	Freq	G	MC	ERV	MI	PD
[10]	28	9	NA	0.138	No	+40°, −40°
[14]	28	6.5	20	0.207	No	0°, 40°
[23]	28	11	16	0.05	No	0°, +30°, −30°
[31]	28	6	10	0.006	No	0°, +30°
[32]	28	12	NA	0.027	Yes	No
[33]	28	5	NA	0.005	Yes	0°, +30°
[34]	28	1.5	20	0.026	Yes	No
[35]	26	6	10	0.192	No	No
PRW	**28**	**7–9**	**20**	**0.08**	**Yes**	**0°, 90°**

Ref Reference, *Freq* Operating Frequency (GHz), *G* Gain (dBi), *MC* Mutual Coupling (dB), *MI* Mobile integration?, *ERV* Effective Radiating Volume ($\lambda_0{}^3$), *NA* Not Applicable, *PRW* Proposed Work

plane which is at least 10 times the width of the microstrip trace, is close to 0.15 dB. But, when the width of the ground plane is 1 mm the insertion loss increases to 1 dB as observed in the parametric curves of Fig. 3.15. This proves that the feed lines still behave as lossy transmission lines despite the width of the ground plane. Hence, electrically compact transmission line feeding the end-fire antenna could be designed without significant deterioration in the forward gain or impedance matching. This proves that the antenna's size could be reduced along the width, without sacrificing the impedance integrity. The unidirectional beam of the radiator is decided by the radiating aperture and the available ground plane for reflection.

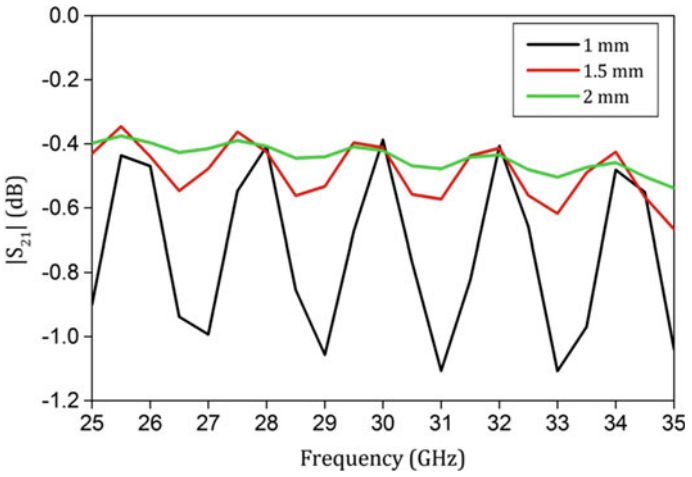

Fig. 3.15 Insertion loss of varying width of ground plane on the chosen substrate (Karthikeya et al. [36], reprinted with permission from John Wiley and Sons)

The schematics of the proposed compact Yagi antenna is depicted in Fig. 3.16a. It is designed on Nelco NY9220 substrate with ε_r is in the range of 2.18–2.22 and a dielectric loss tangent of 0.0009. A low dielectric constant is preferred for the radiator but would compromise the radiation losses from the feed line. A higher dielectric constant would shrink the antenna's size further. The dielectric loss tangent is low indicating minimal losses in the substrate, thus promising maximum gain achievable through a microstrip feeding technique.

The thickness of the substrate is 20 mil, which is essential to maintain an electrically smaller microstrip trace. Electrically thick substrates would yield higher bandwidth at the cost of increased cross-pol radiation, which might be overlooked for a smartphone application, especially when the radiators are placed on different sides of the substrates. Initially, a standard microstrip based dipole antenna is designed as shown in the inset of Fig. 3.16a. The dipole arm length (dip_len) is varied to achieve a strong resonance at a higher band, i.e., at 30.5 GHz for a dipole arm length of 5 mm but the desired band is at 28 GHz as evident from Fig. 3.16b, hence the dipole arms are extended by 0.75 mm on both the planes as observed in Fig. 3.16a, to tune the antenna to 28 GHz.

The parasitics are optimized for gain enhancement of 3 dB in the end-fire. Parasitics could be ignored if gain is not an important criterion. The antenna would still deliver a unidirectional beam without the parasitics. The distance between the parasitics is maintained at 0.2 λ for optimal end-fire gain with minimal physical footprint, which is a standard dimension for printed Yagi design. The dipole antenna is fed by a 1.2 mm wide microstrip line through a quarter wave transformer of width 0.5 mm. The arms of the dipole are 0.25 mm wide to achieve impedance matching with the feed line. The width of the ground plane is maintained at 4.8 mm, which is very well within the limits of commercial smartphones. The width of the ground plane does not hamper the impedance characteristics of the antenna since the insertion loss offered by the electrically compact ground plane is minimal as evident from Fig. 3.15. The width of the ground plane is 20 mm at the feeding edge of the antenna, which is designed for clearance to accommodate the end-launch connector. The radiating arm of the antenna is placed at more than 1.0 λ at 28 GHz to minimize the effects of the electrically large connector during radiation pattern measurements.

One of the most common strategy to design an electrically compact printed dipole is to introduce an angle to radiating arms of the dipole. But the gain of the single element would be compromised. Introducing meandered lines in the radiating arms or miniaturization circuits in the feed line would compromise the impedance bandwidth. Hence, the radiating dipole arms are extended as depicted in Fig. 3.16a. The E-fields of the top and ground plane of the proposed antenna at 27 and 30 GHz are illustrated in Fig. 3.17, indicating that the dipole arm extension indeed contributes to radiation despite the electrically compact ground plane.

The parasitic radiators are optimized for maximum gain in the end-fire which aid in beam collimation in the end-fire as evident from the E-field plots. Gain enhancement techniques such as planar dielectric lens and uniplanar metamaterial integration need electrically larger aperture for substantial gain enhancement, for instance, for a gain

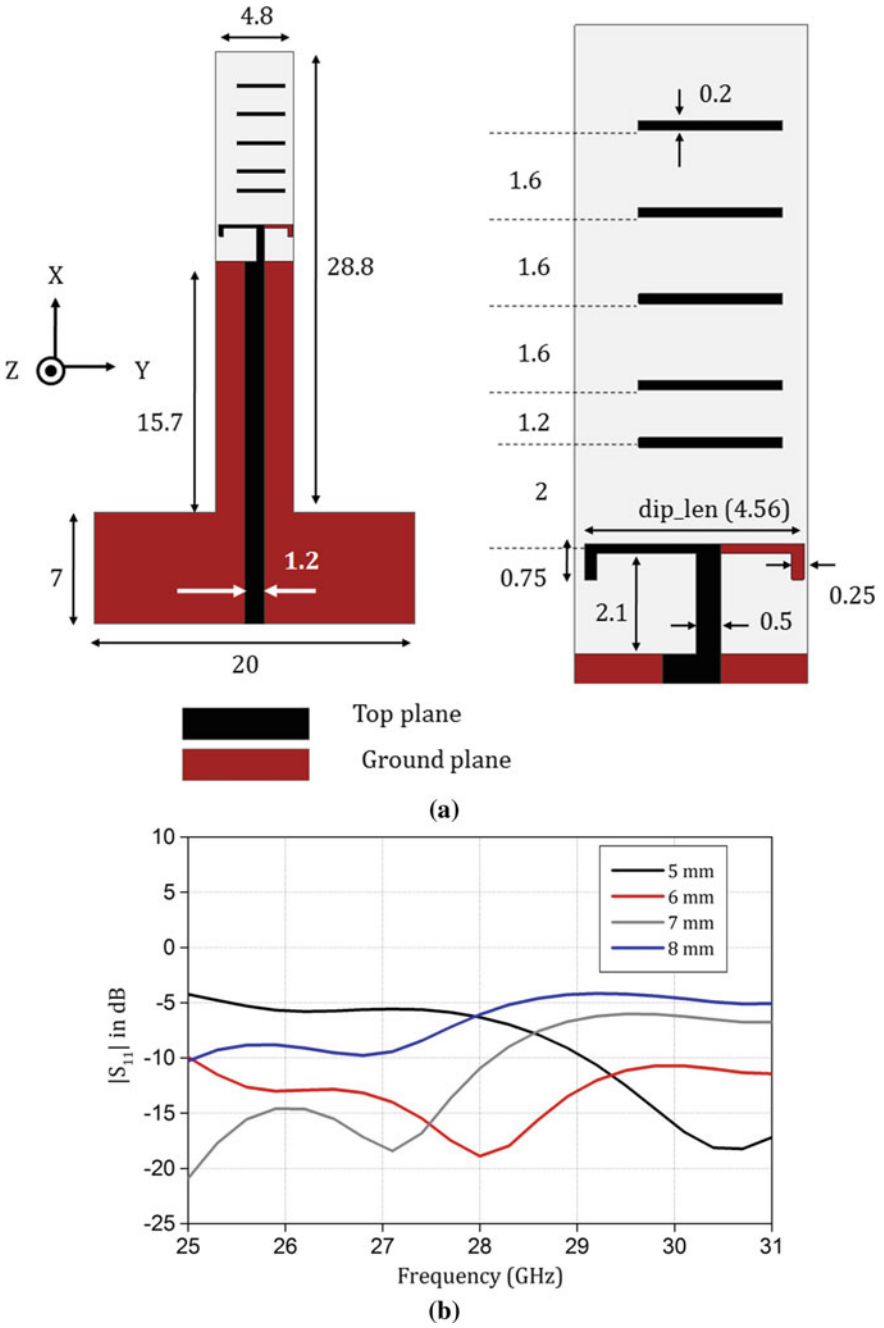

Fig. 3.16 **a** Schematics of the proposed compact Yagi antenna (units: mm), **b** $|S_{11}|$ variation for dipole arm lengths (Karthikeya et al. [36], reprinted with permission from John Wiley and Sons)

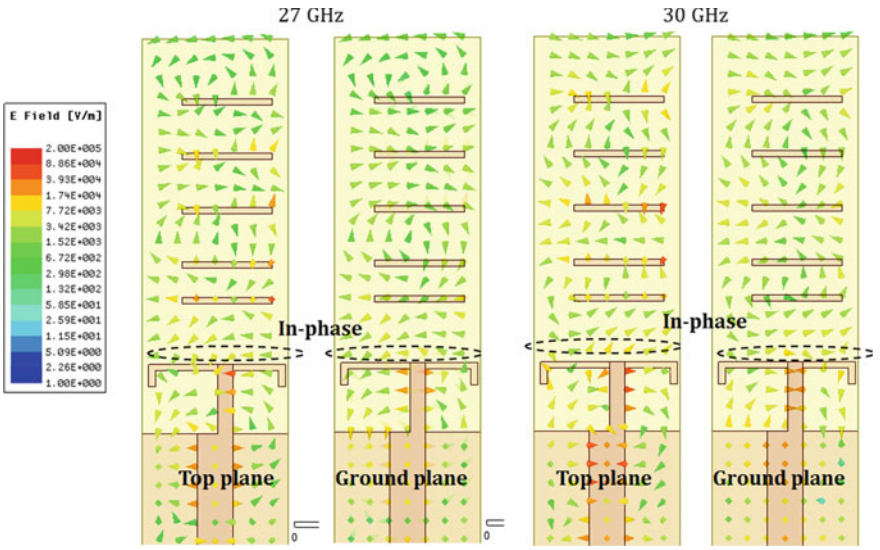

Fig. 3.17 E-field variations of the proposed antenna (Karthikeya et al. [36], reprinted with permission from John Wiley and Sons)

enhancement of 3 dB, an aperture of at least 1λ x 2λ is required. The photograph of the fabricated prototype is shown in Fig. 3.18.

The input reflection coefficient of the antenna is shown in Fig. 3.19. The impedance bandwidth is from 27 to 29.5 GHz, translating to 9%. The wideband is primarily due to the dipole structure with the feeding impedance transformers. All the simulations were performed using ANSYS HFSS. The S-parameter measurements were done using Agilent PNA E8364C. The deviation between simulated and measured curves could be attributed to the solder-less transition used in the fabricated prototype from the end-launch connector to the antenna. Also, the end-launch connector had experienced multiple mating cycles which deteriorates the angle of the trace pin of the connector, leading to a lower quality of transition at the feed plane. The bandwidth could be further increased by using tapered lines or stepped impedance transformers but the parasitic radiators' behavior would alter for a larger bandwidth sacrificing the pattern integrity across the band.

The simulated and measured radiation patterns are depicted in Fig. 3.20. All the measurements were done inside an anechoic chamber using Keysight R281B Ka band horn antenna as the transmitter with 55 cm between the proposed element and transmitter horn. The E-plane (XY plane) patterns at 28 and 30 GHz are illustrated in Fig. 3.20a, b, respectively. The pattern integrity is well maintained at the edges of the operating bandwidth. The beamwidth is 55°.

The front to back ratio is more than 10 dB indicating 90% more power in the forward direction compared to backward direction. This in turn translates to minimal radiation towards the user when integrated in a mobile device. The cross-polarization

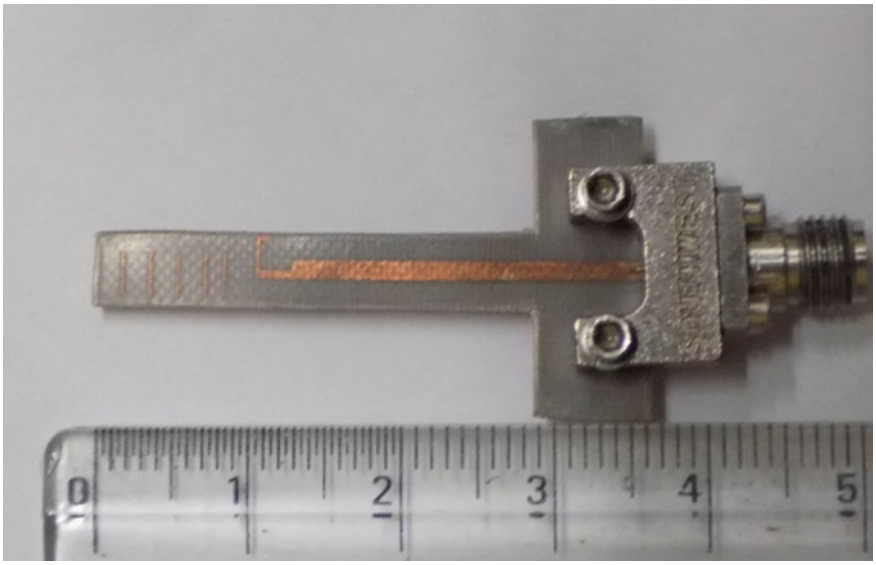

Fig. 3.18 Photograph of the fabricated prototype (Karthikeya et al. [36], reprinted with permission from John Wiley and Sons)

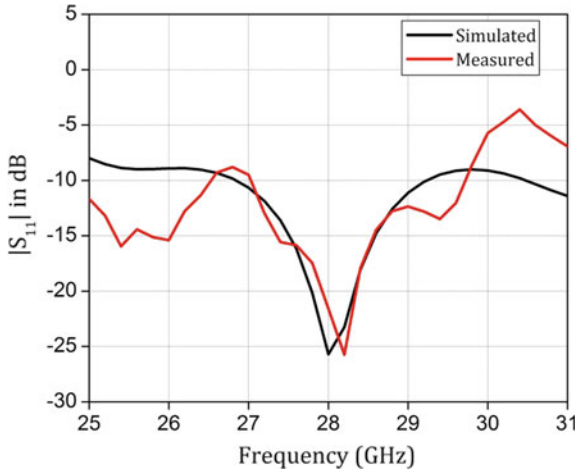

Fig. 3.19 Input reflection coefficient of the proposed antenna (Karthikeya et al. [36], reprinted with permission from John Wiley and Sons)

level is less than 20 dB. The H-plane (XZ plane) patterns are shown in Fig. 3.20c, d. The beamwidth is 67°.

The cross-polarization level is relatively higher compared to the E-plane due to the location of the dipole arms in different sides of the substrate, but since the substrate chosen is electrically thin the cross-pol is less than 10 dB. The patterns indicate a beam in the forward direction with adequate angular coverage to establish a link

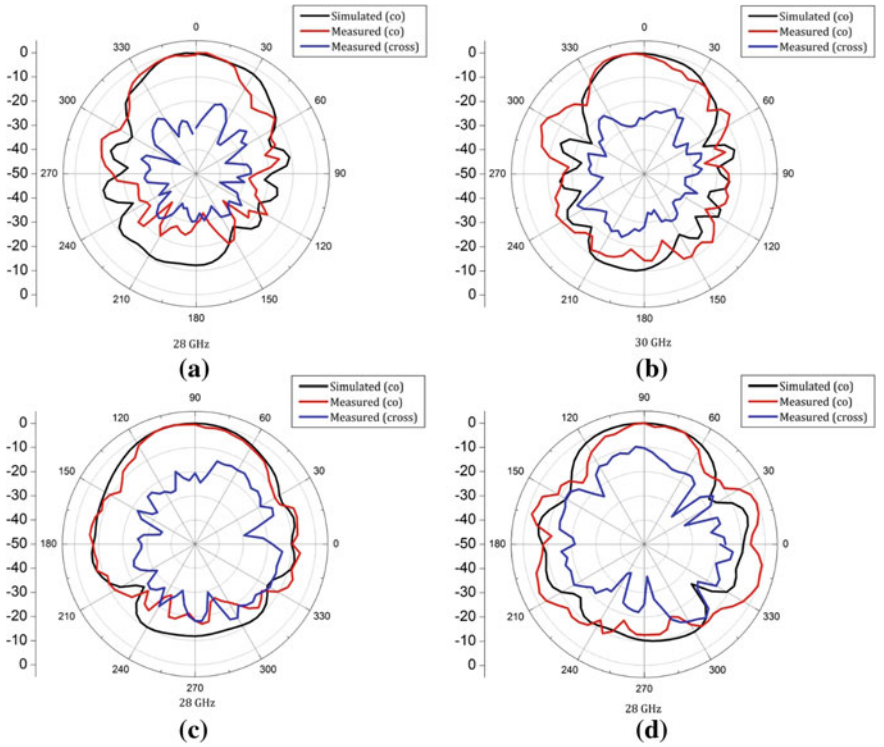

Fig. 3.20 Radiation patterns: E-plane at **a** 28 GHz, **b** 30 GHz, H-plane at **a** 28 GHz, **b** 30 GHz (Karthikeya et al. [36], reprinted with permission from John Wiley and Sons)

with the mobile terminal and base station. The deviation between the simulated and measured results is due to the aperture blockage of the electrically large metallic end launch connector which was not considered in the full-wave simulations.

The forward end-fire gain of the proposed element is depicted in Fig. 3.21. The gain varies from 8 to 10 dBi in the frequency of interest. Gain measurements were performed using two antennae gain transfer method using the vector network analyser. Hence, the deviation between simulated and measured curves is observable especially at the higher end of the spectrum due to polarization mismatch and multipath effects during measurement.

3.5.2 Orthogonal Pattern Diversity Module

To achieve orthogonal beam forming with minimal physical footprint, an orthogonal beam switching module is proposed. The schematic is illustrated in Fig. 3.22. The compact Yagi antenna proposed in Sect. 3.5.1 is placed orthogonally, the antenna

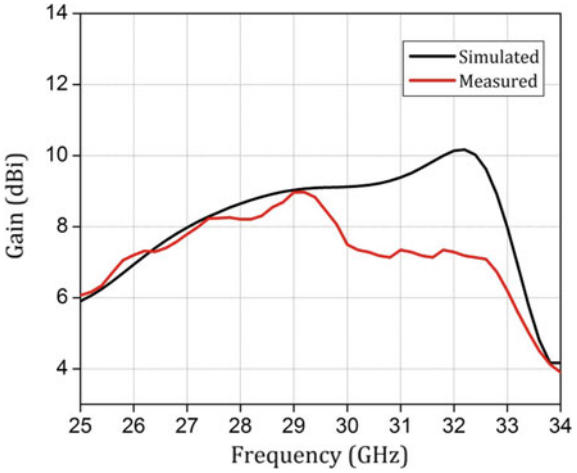

Fig. 3.21 Forward end-fire gain of the proposed antenna (Karthikeya et al. [36], reprinted with permission from John Wiley and Sons)

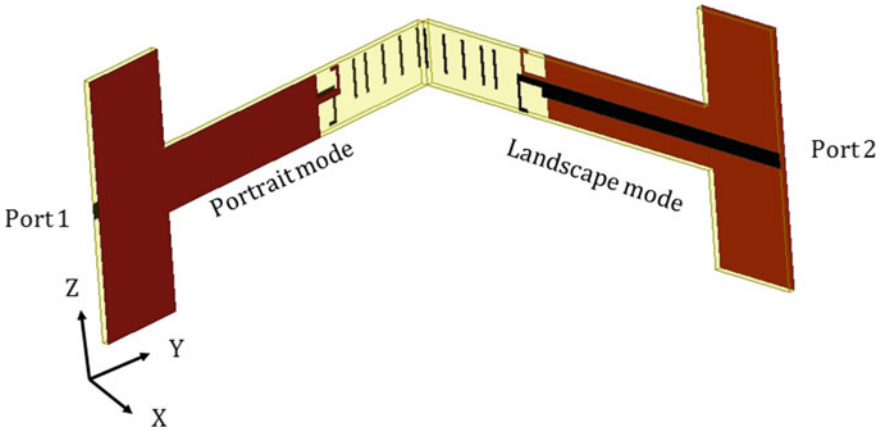

Fig. 3.22 Schematic for Orthogonal pattern diversity module (Karthikeya et al. [36], reprinted with permission from John Wiley and Sons)

corresponding to port 2 is flipped with respect to port 1 to reduce mutual coupling. The height of the antenna corresponds to vertical polarization and is compliant with the height of commercial smartphone. Depending on the mobile usage mode, the corresponding antenna is excited.

To verify the validity of the proposed architecture, a 3D printed corner piece is designed as shown in the photograph of Fig. 3.23. The height of the 3D printed panel is around 6 mm with corner tapering. In actual deployment scenario, the dielectric used in commercial mobile case would alter the radiation pattern and impedance

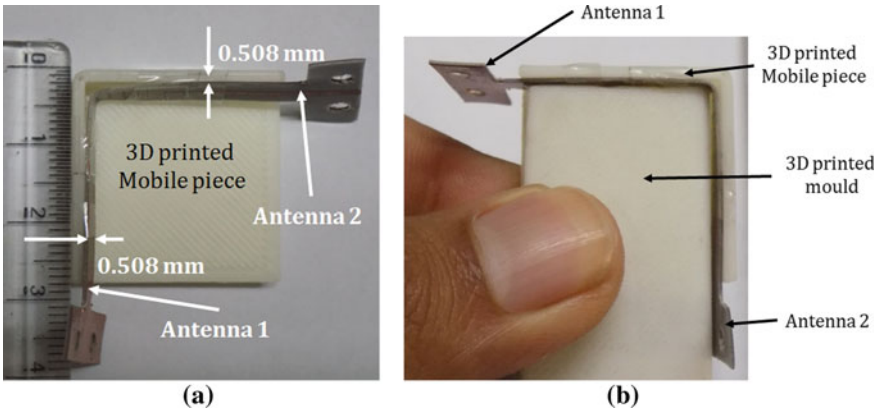

Fig. 3.23 Photograph of the fabricated antenna module: **a** integrated with a mobile corner piece, **b** integrated with a solid 3D-printed mould (Karthikeya et al. [36], reprinted with permission from John Wiley and Sons)

characteristics of the antenna minimally as the dielectric is attached to one side of the radiator. It must also be observed that the thickness of the substrate is 0.508 mm, which leaves ample room for integration with the circuit board and other accessories in a mobile device. Figure 3.23b gives a clear insight into the compactness of the proposed architecture, wherein 3D printed mould is an abstraction for intended electronics circuit board.

The measured mutual coupling between the terminals is illustrated in Fig. 3.24a, the mutual coupling is less than 15 dB across the band despite the antennas being placed electrically close to each other. The primary reason for low mutual coupling is due to the orthogonal placement of the antennas. Antenna corresponding to port 1 radiates in YZ plane whereas antenna corresponding to port 2 radiates in XZ plane.

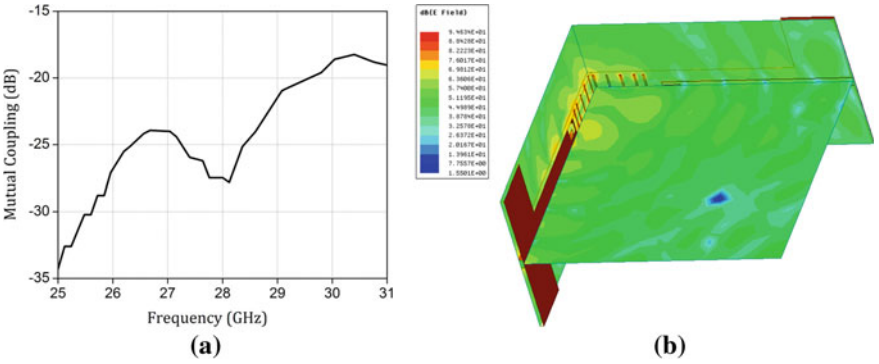

Fig. 3.24 Mutual coupling: **a** Measured mutual coupling, **b** E-field plot of the module at 28 GHz (Karthikeya et al. [36], reprinted with permission from John Wiley and Sons)

The E-fields in the orthogonal planes for the proposed architecture when port 1 is excited, is illustrated in Fig. 3.24b. The transmission line mode and radiation mode are evident in the YZ plane and minimal energy is coupled in the XY plane as the antenna corresponding to port 2 has very low cross-polarization level in the XY plane. Also, the dominant radiating polarization for port 1 is YZ plane and that of port 2 is XZ plane. The E-fields significantly reduce as the wave propagates. The 3D patterns at 28 GHz when the corresponding port is switched on is illustrated in Fig. 3.25. The beams are predominantly in the forward direction, but the pattern becomes specular due to the placement of the second element electrically close to each other. Figure 3.26a. Illustrates the envelope correlation coefficient (ECC) which is well below 0.008 for the operating band. Figure 3.26b. Illustrates the radiation efficiency of the antenna element and it is close to 99.5% at 28 GHz. The losses are

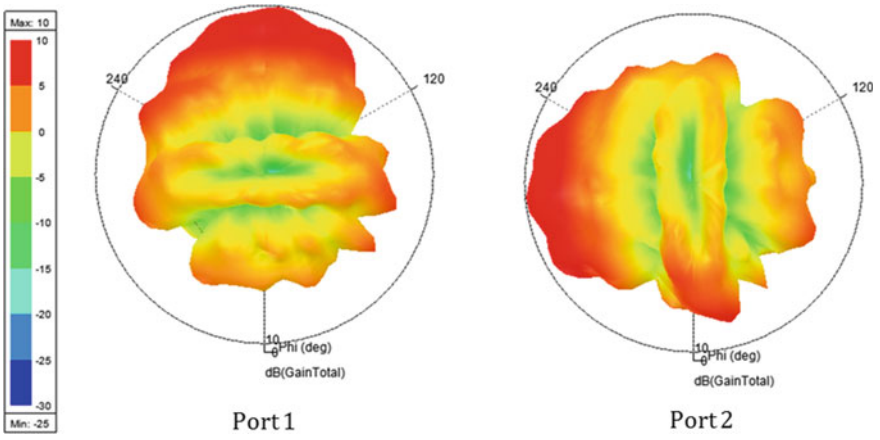

Fig. 3.25 3D radiation patterns when each port is excited (Karthikeya et al. [36], reprinted with permission from John Wiley and Sons)

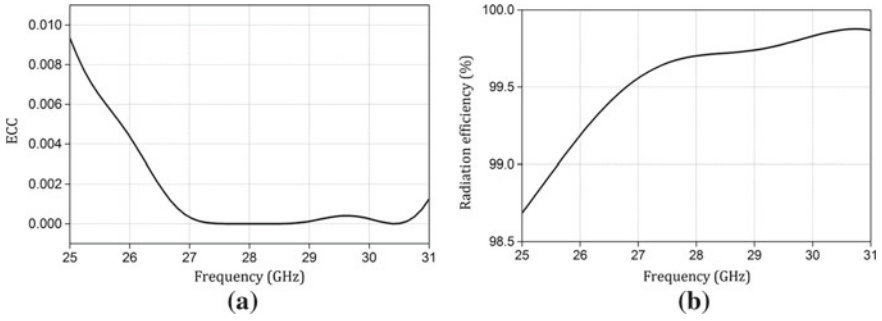

Fig. 3.26 **a** ECC of the proposed module, **b** Radiation efficiency of the proposed antenna (Karthikeya et al. [36], reprinted with permission from John Wiley and Sons)

primarily due to finite conductivity of copper traces and the dielectric loss of the 20-mil substrate.

3.6 Overlapped Shared Ground Module

In this Section, an overlapped shared ground antenna module is explored. It is a two-port system, which can fit in one of the edges of the mobile device.

3.6.1 Compact Wideband Broadside Antenna

An electrically compact wideband broadside antenna centred at 28 GHz is investigated in this Section. To achieve the orthogonal beams of Fig. 3.1, two antennas with orthogonal patterns are required. Hence, the two-port antenna system would have a broadside antenna and an end-fire antenna both of which meets the mobile device's requirements, as observed in the previous Sections. The electrically close placement of these two antennas would be investigated in Sect. 3.6.3. The compact antennas of the system must be co-polarized, hence vertically polarized element is necessary for the design. There is no hard and fast rule for the constituent antennas to be co-polarized. If the antennas are co-polarized, the propagation characteristics of the signals emanating from these antennas would be similar. As the compact antenna would be eventually mounted vertically, polarization of the broadside antenna must be horizontal (specifically X-polarized) when the antenna is initially placed on the XY-plane.

The most obvious solution to achieve this requirement is to design an inset fed patch antenna. If this patch antenna is placed in the XY-plane, the dominant radiating polarization would be oriented along the Y-axis. To solve this problem, the radiating element could be placed orthogonally with respect to the feeding line, which increases the width of the overall antenna due to orthogonal bending and its associated impedance transformers. In addition to these issues, the 10-dB impedance bandwidth would be narrow, 3–5% to be precise, hence proving to be unsuitable for the application in hand.

To solve the afore-mentioned issues, a compact wideband planar antenna with microstrip feeding is proposed as shown in Fig. 3.27. It is designed on F4B substrate with a thickness of 0.508 mm. the dielectric constant is 2.6 ± 0.02 with a corresponding dielectric loss tangent of 0.002. low dielectric constant means lesser surface wave modes, hence higher forward gain for a given radiating aperture, like most of the designs presented in this book. Also, the dielectric loss tangent is lower than that of FR4, thus minimizing losses due to the substrate itself. Any substrate with dielectric constant in the range of 2–3 would serve the purpose. In the present case, F4B was chosen due to its availability.

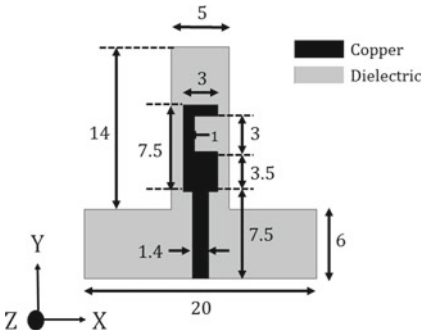

Fig. 3.27 Schematic of the broadside radiator (All dimensions are in mm)

The feeding line is a standard 50 Ω line on the chosen substrate, which happens to be 1.4 mm wide; thus, avoiding spurious radiation from the feed line itself. The radiating portion of the antenna is almost 1 λ away from the feeding plan, to avoid contamination of the pattern integrity due to the end-launch connector. The feeding length could be reduced if mini-SMP connectors could be used. The substrate elongation along the X-axis is also for measurement purposes and need not be included in a commercial deployment or implementation with mobile devices. The 3.5 mm × 3 mm metallic structure connecting the feed line and the radiating aperture acts as an impedance transformer between the two.

The E-fields of the proposed antenna element is illustrated in Fig. 3.28. The dominant radiating E-fields are in-phase at the band edges of the element as seen in the figure, hence creating wide bandwidth. The width of the proposed element is 5 mm or 0.46 λ calculated at 28 GHz, indicating minimal footprint of the wideband broadside element. The proposed antenna is X-polarized as opposed to Y-polarized design of a similar inset fed patch antenna. X-polarized radiation would mean that

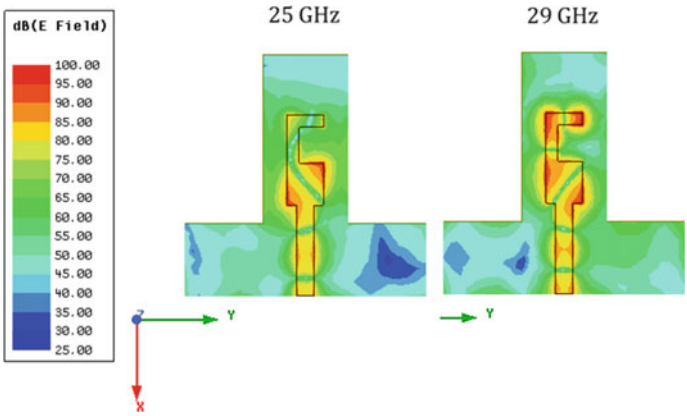

Fig. 3.28 E-fields of broadside radiator

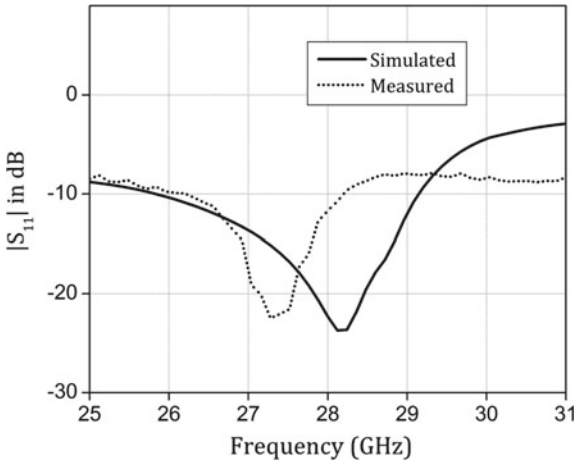

Fig. 3.29 $|S_{11}|$ of the proposed antenna 1

a vertically polarized antenna system could be realized with the proposed radiating element with vertical mounting of the same.

The simulated and measured input reflection coefficients of the proposed antenna are illustrated in Fig. 3.29. All the simulations were carried out using Ansys Electromagnetics Suite version 18.2. All the materials were assumed to be lossy during simulation, with appropriate data from the respective data sheets. The free space radiation box was quarter wavelength from all sides of the planar antenna.

The quarter wavelength was calculated at the least frequency of the sweep, 25 GHz in this case. Electrically large radiation box in simulations would lead to accurate results in the far-field data. All the S-parameter measurements were done using Keysight E8364C. the 10-dB impedance bandwidth is 25.8–29.1 GHz or 12%, which is wideband given the electrically compact width of the broadside antenna. The deviation between simulated and measured $|S_{11}|$ is due to the actual substrate used for fabrication, the frequency shift could be explained by the second decimal variation of the dielectric constant of the sample used for fabrication.

The E-plane (or XZ plane) radiation patterns at 27 and 28 GHz are shown in Fig. 3.30. The beamwidth is 64º at 28 GHz. Front to back ratio is 12 dB at 28 GHz despite the electrically narrow ground plane. The patterns are Y-polarized with reference to Fig. 3.27. The patterns are unidirectional, hence proving to be useful for mobile integration. As the Front to back ratio is greater than 10 dB, it means that radiation would be mostly directed away from the user, when integrated with a mobile device. The deviation between simulated and measured curves could be attributed to the polarization mismatch during measurements. All the measurements were done inside a standard anechoic chamber with R281B as the Ka band standard horn antenna. The Y-polarized forward gain at 28 GHz is close to 7 dBi, which is a reasonable gain for the electrical size of the radiating aperture.

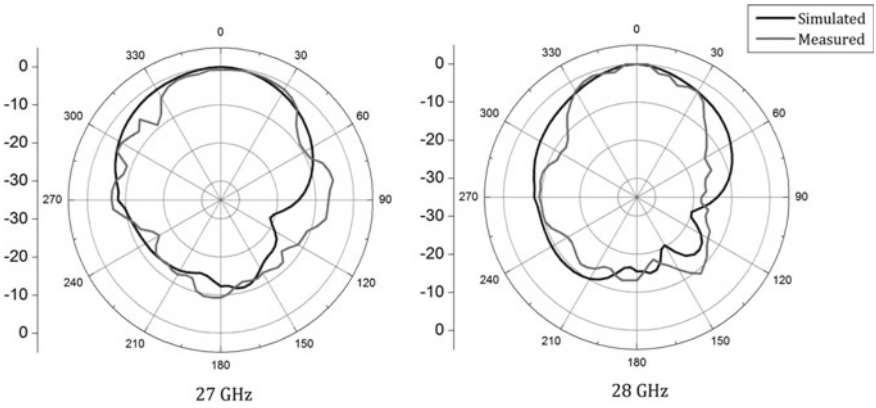

Fig. 3.30 Radiation patterns of the proposed antenna 1

3.6.2 Compact Wideband End-Fire Antenna

To achieve orthogonal beams, leaky wave antennas or phased arrays won't be suitable due to frequency shift or scanning loss, as demonstrated in Sect. 3.2. Hence, an end-fire antenna is necessary to switch the antenna system orthogonal to that of the broadside element presented in Sect. 3.6.1. A compact wideband printed dipole is used to achieve an end-fire unidirectional pattern with low physical footprint. The proposed printed dipole is illustrated in Fig. 3.31. The microstrip fed element is designed on Rogers 5880 substrate with a dielectric constant of 2.2 ± 0.02 and a loss tangent of 0.0009. The thickness of the substrate chosen is 20 mil or 0.508 mm, similar to its broadside counterpart. Electrically thin substrates are better to maintain polarization integrity of end-fire antennas. The substrate used for broadside element

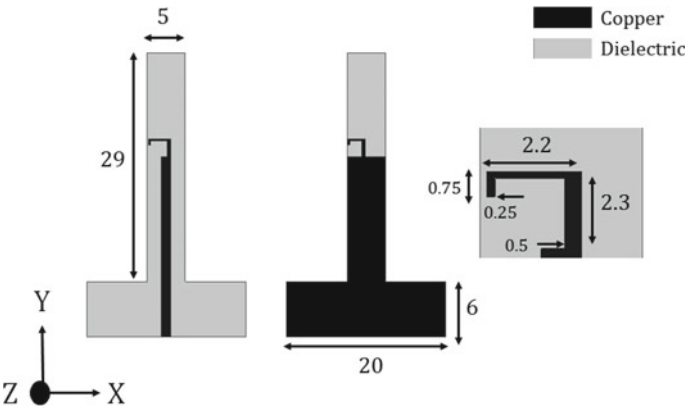

Fig. 3.31 Schematics of compact dipole, (All dimensions are in mm)

could have been used with a reduced length of the dipole arms. The current choice of substrate is purely on the availability of the substrate for fabrication. The reader would observe that this design is identical to the one presented in Sect. 3.5, without the parasitic radiators.

The feed line is a standard 50 Ω line to avoid mismatch between port impedance and that of the antenna. The electrically long feed line is for two reasons: the first is to avoid unnecessary interference from the electrically large end-launch connector and the second reason is to accommodate the broadside element for overlapping, which will be illustrated in Sect. 3.6.3.

The primary radiator is the dipole arms as seen in the inset of Fig. 3.31. The dipole arm length of 2.2 mm is protruded to lower the resonance frequency to 28 GHz. The distance between the dipole arms and the ground plane (along the X axis, with reference to Fig. 3.31) is 2.3 mm to maintain a unidirectional radiation pattern and to achieve a high front to back ratio. The dielectric extension beyond the radiating arms is for slight gain enhancement in the end-fire and could be avoided if the end-fire forward gain could be compromised. Protrusion at the feed is for measurement purposes. E-fields of the printed dipole at 27 and 30 GHz are depicted in Fig. 3.32. The transmission line mode on the feeding line is clearly visible. The radiation along the extended dielectric is also visible. The width of the radiating aperture of the antenna is 5 mm, which is identical to that of the broadside element of Fig. 3.27. To miniaturize the dipole width, the electrical length of the dipole arms could be increased, with a consequent compromise in the beam integrity. Also, a miniaturized dipole might radiate omni-directionally. End-fire gain could be enhanced by techniques such as parasitic radiators, lens integration or sub-wavelength planar metamaterial unit cells, but with a compromise in the electrical width of the element, thus reducing the compliance of the antenna with the panel height of the mobile device.

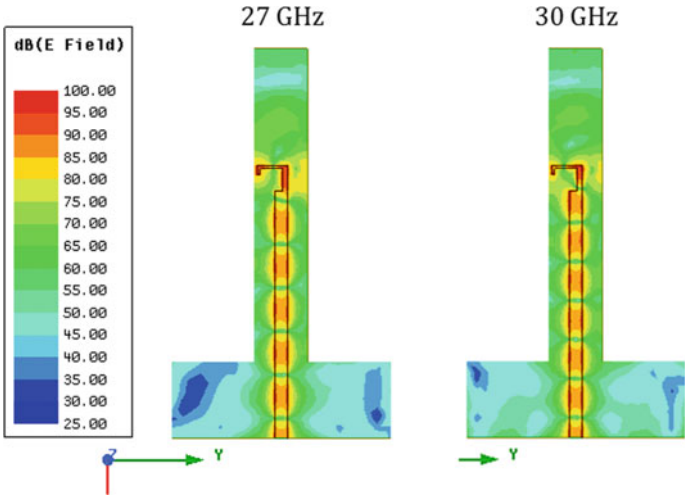

Fig. 3.32 E-fields of the printed dipole antenna

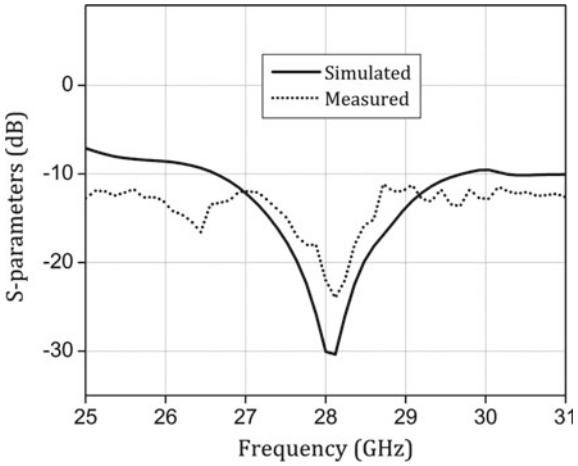

Fig. 3.33 $|S_{11}|$ of proposed antenna 2

The simulated and measured input reflection coefficients for the presented dipole is illustrated in Fig. 3.33. The 10-dB impedance bandwidth is 26.6–31 GHz (or 15.2%) which is a wideband design given the electrically narrow design. Bandwidth could have been further increased by using thicker substrate, wider impedance transformer at the feed line or to widen the width of the radiating dipole arms. All these strategies would hamper the pattern integrity or compromise the physical footprint of the element.

The simulated and measured patterns at 27 and 28 GHz of the printed dipole are illustrated in Fig. 3.34. The co-polarized E-plane (XY-plane with reference to Fig. 3.31) beamwidth at 28 GHz is 41° with FTBR of 11 dB at 28 GHz. The forward end-fire gain is 5.5 dBi at 28 GHz indicating a high gain for electrically low width.

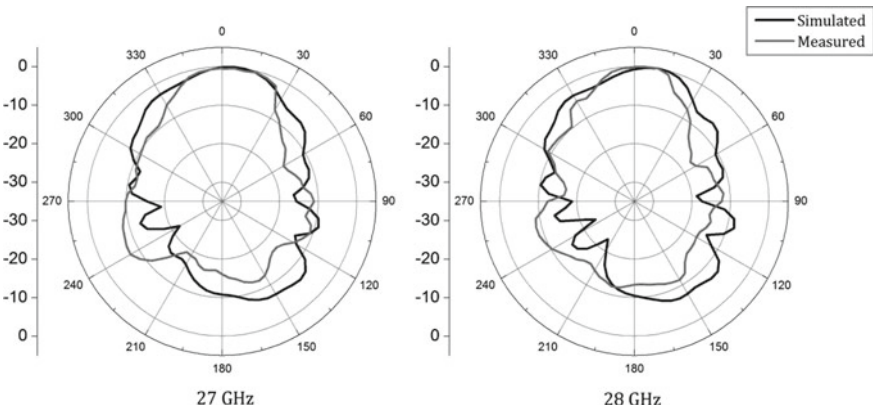

Fig. 3.34 Radiation patterns of antenna 2

3.6.3 Co-Polarized Overlapped Antenna System

Both the proposed antennas of Sects. 3.6.1 and 3.6.2 are X-polarized, which means that if a beam switching module or system is designed, then the radiating polarizations of both the antennas match, hence a co-polarized antenna system could be realized. The proposed co-polarized orthogonal beam switching module is illustrated in Fig. 3.35. The ground plane of the broadside radiator (X-polarized element presented in Sect. 3.6.1) is attached to the ground plane of the end-fire radiator (which is also an X-polarized element presented in Sect. 3.6.2). As observed in the figure, the system has two microstrip fed ports: one port on each side of the module. As the entire antenna system is planar, integrating switches and other allied components would be easy.

The overall thickness of the proposed module is 1 mm or 0.093 λ electrically speaking, indicating minimal space or real estate occupancy would be very low. The longitudinal distance could also be reduced from 29 to20 mm with a slight

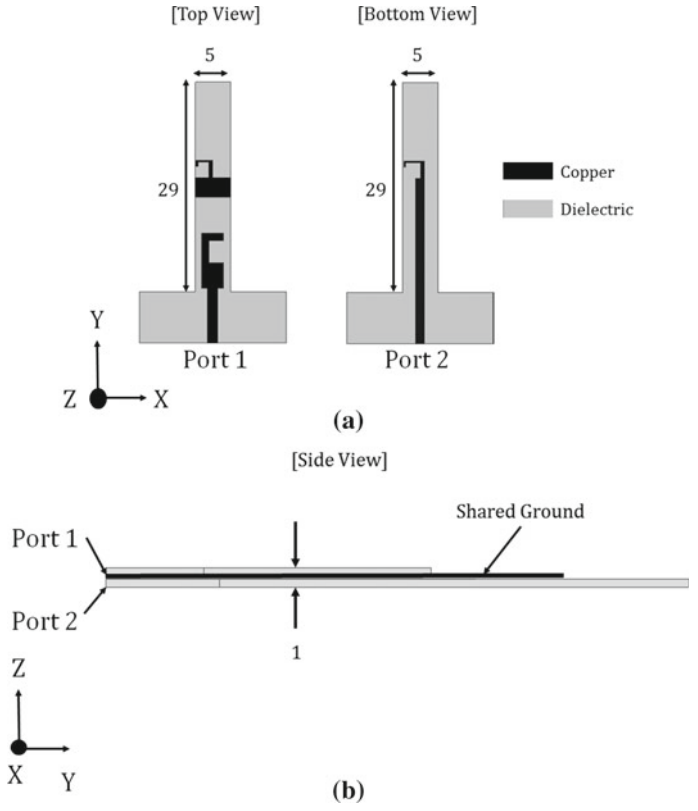

Fig. 3.35 Schematics of the proposed overlapped system (All dimensions are in mm). **a** Top view, **b** Side view

compromise in the forward gains of the respective elements. The distance between the radiating apertures is 12.5 mm. the fabricated prototype of the proposed antenna system is shown in Fig. 3.36. Industry standard chemical etching was used to realize both the antennas. Laser cutting tools were not used to cut along the contour of the design, as the substrates are very thin.

Mutual coupling between the ports is less than 22 dB across the band of operation as seen in Fig. 3.37. The low mutual coupling could be attributed to two reasons: first, the ground plane of the respective antennas acts as an isolating network to prevent strong coupling between the two entities. Second, even though the dominant radiating E-fields for both the ports are co-polarized, radiation is orthogonal to each other.

Mutual coupling could go up to 15 dB when the distance between the active radiating apertures is decreased by 5 mm. A typical placement of the proposed antenna system in a smartphone is demonstrated in Fig. 3.38. The co-polarized or

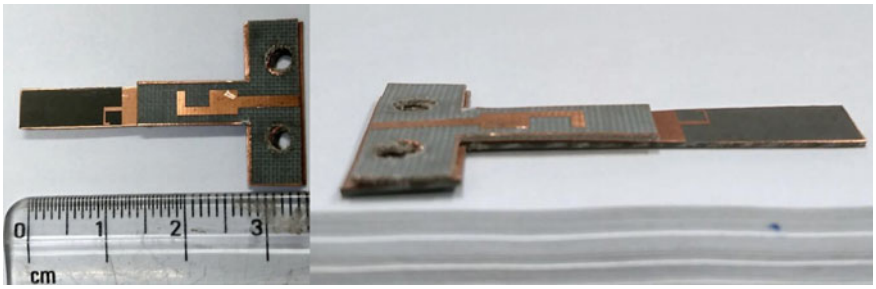

Fig. 3.36 Photographs of the fabricated prototype

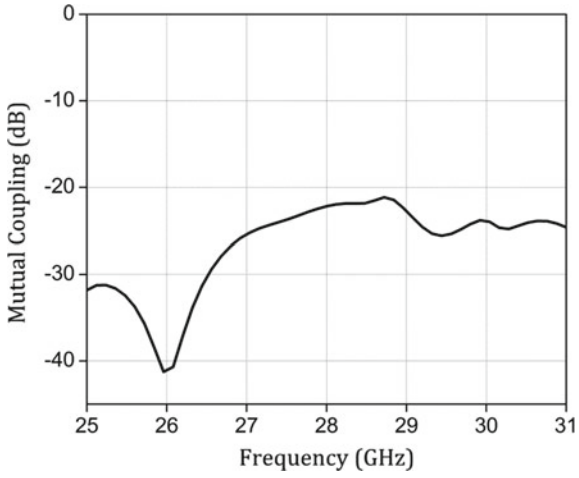

Fig. 3.37 Mutual coupling of the overlapped system

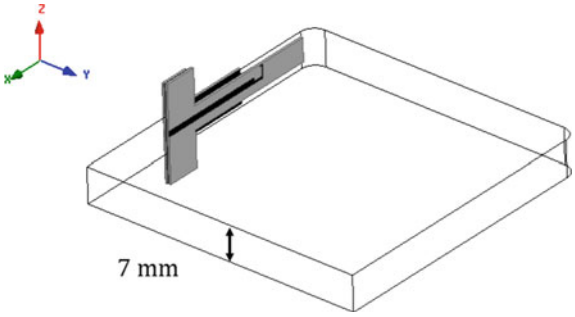

Fig. 3.38 Typical placement of the proposed antenna system within a smartphone mock-up

vertically polarized system would be placed at the corner of the smartphone, wherein an appropriate switch would activate the antenna needed for the corresponding data mode. The proposed antenna system could be placed either on the longer edge (along X axis) or the shorter edge (along Y axis) without any loss of performance metrics of the system. It must be noted that the impedance characteristics and hence the impedance bandwidths remain intact despite the electrically compact nature of the proposed antenna system.

The 3D patterns at 28 GHz for the corresponding ports activation is illustrated in Fig. 3.39. The unidirectional pattern with adequate angular coverage is evident. Forward gains for both the ports are shown in Fig. 3.40. Since the pattern integrities of the respective antenna elements are preserved, gains are also like the independent elements.

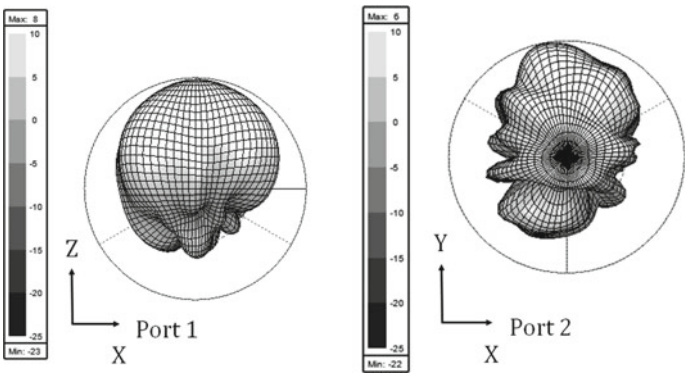

Fig. 3.39 3D patterns when ports are excited at 28 GHz

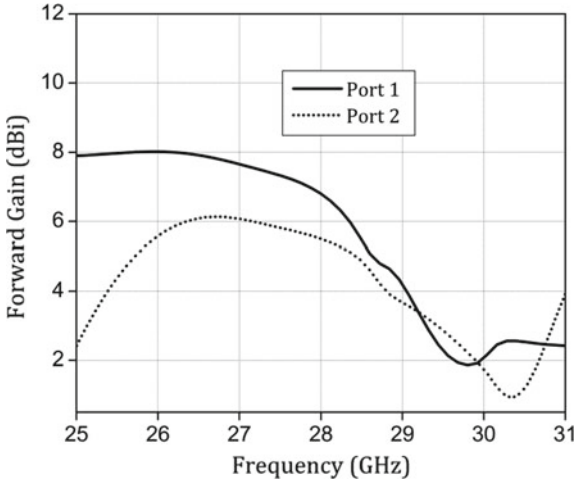

Fig. 3.40 Forward gains of the respective ports of the proposed antenna system

3.7 Design Guidelines

- The primary constraint in designing antenna systems for smartphones is the physical dimensions of the actual smartphone. These dimensions would be specific to a model of the smartphone. Section 2.3 presented a generic overview of these dimensions. Once the overall dimensions are fixed, the space available exclusively for 5G antennas must be understood. This space must be characterized electrically to get a grasp of the feasible electrical dimensions for a given edge of the smartphone. Once the gain requirement is laid down by the network designer, the antenna engineer must optimize the antenna to achieve that value of gain with an additional gain margin. The input impedance requirement would be put up by the active circuits' team, as the antenna must function when integrated with the active back-end circuits, both in the transmission and reception modes. Currently, most of the mmWave 5G standards are narrowband, say 2–5% centred at 28 GHz, hence the impedance matching would not be a major issue.
- Once the gain is fixed, the antenna designer must choose a reasonable radiator topology. The antenna has to radiate with a unidirectional beam across the operating spectrum. The gain bandwidth also must be carefully examined to preserve the pattern integrity of the antenna. if the radiating aperture alone is mounted along the smartphone panel, the pattern integrity would be intact. The ground plane of the antenna should be compatible with the system ground plane. This could be achieved if the ground plane of the antenna has an extended portion, which has minimal influence on the radiating aperture. The feed must be compatible with the transition expected from the back-end electronics.
- Once the radiating element is fixed, placement of the element within the smartphone is as important as the design itself. The obvious choice for antennas is to mount it at the panel edges. The corners would be most preferred real estate

to place the perpendicularly radiating antenna system. The antennas' behavior with the dielectrics of the nearby panel and other electronics must be separately understood. If the nearby dielectrics detune the antenna or the antenna system, the antenna must be redesigned for the panel integrated scenario. Typically, the panel loading and the back-end electronics would detune the antenna by 5–10%, which could be solved by optimization of the primary radiating structure.

- The placement of the orthogonally radiating antennas must be compact enough to meet the spatial criteria of the panel, without compromising the pattern integrity when either antenna element within the antenna system is fired up. Mutual coupling could be as high as 10 dB given the electrically close placement of the radiating elements. A shared ground design would be a favourable choice as the fabrication would be on a single piece of substrate.
- Electrically thin dielectric substrate (say 5–20 mil) would be preferable to have minimal surface wave modes and to enhance polarization purity of the primary beam. Usage of thin substrate would lead to narrow bandwidth, especially when designing broadside radiators. Hence the designer must choose an optimum thickness of the dielectric to maximize gain with an adequate bandwidth.

3.8 Scope for Research

- Shared radiator could be investigated for orthogonal patterns with two feeds. This design could be based on microstrip feed or coaxial feed or a combination of both. The radiating structure must be cleverly designed with appropriate stepped impedance transformers, which also would double up as an isolating network. The design agenda would be to achieve broadside radiation with appropriate unidirectional beam for the first port and endfire-unidirectional beam for the second port. The design must be on the same substrate with simple feeding mechanism. This antenna module would reduce the physical footprint of the antenna by half.
- Reconfigurable antenna system for orthogonal patterns could be explored. In this Chapter, all the antenna systems presented in the previous Sections assumed an inherent RF switch that would fire up the necessary port of the antenna system. An external RF switch would be cumbersome to integrate with a smartphone panel. reconfigurable antenna system with pin diodes would have relatively smaller electrical footprint with higher switching speed. The topologies for broadside and end-fire radiators could be realized with an appropriate pin diode switch to route energy. This would be a single port design with an external DC (Direct Current) switch, which manipulates the state of the pin diode to activate the appropriate radiator. The bias line design and actual implementation of the pin diodes in the feed network of the antenna would be challenging.
- Shared ground antenna system with dual coaxial feed could also be an interesting solution to the orthogonal patterns' problem. Both the feeding ports would have coaxial feeds. One of the ports feed a broadside element and the other one feeds an end-fire element. Coaxial fed broadside radiators have been well understood

in the literature. However, coaxial fed end-fire radiators need to be designed from scratch. The coaxial-fed OPD (Orthogonal Pattern Diversity) system would have minimal influence from the feed network, as the feeds are in the orthogonal plane behind an electrically large metallic ground.

3.9 Conclusion

In this Chapter, the concept of orthogonal data modes in a mobile terminal was introduced. The two modes of operation relate to the users' engagement with the smartphone. The desired characteristics of the antenna system to be integrated within the mobile device have been illustrated with examples. The reason for failure of phased arrays to achieve orthogonal beams has been discussed. The non-feasibility of reconfigurable antennas also has been discussed in this Chapter. Three independent antenna module designs were explained with adequate technical justification.

References

1. Pi, Z., Khan, F.: An introduction to millimetre-wave mobile broadband systems. IEEE Commun. Mag. **49**(6), 101–107 (2011)
2. Rappaport, T.S., Sun, S., Mayzus, R., Zhao, H., Azar, Y., Wang, K., et al.: Millimetre wave mobile communications for 5G cellular: it will work! IEEE Access **1**, 335–349 (2013)
3. Roh, W., Seol, J.Y., Park, J., Lee, B., Lee, J., Kim, Y., et al.: Millimeter-wave beamforming as an enabling technology for 5G cellular communications: theoretical feasibility and prototype results. IEEE Commun. Mag. **52**(2), 106–113 (2014)
4. Garg, R., Bhartia, P., Bahl, I.J., Ittipiboon, A.: Microstrip Antenna Design Handbook. Artech House (2001)
5. Huo, Y., Dong, X., Xu, W.: 5G cellular user equipment: from theory to practical hardware design. IEEE Access **5**, 13992–14010 (2017)
6. Masoodi, I.S., Ishteyaq, I., Muzaffar, K., Magray, M.I.: Low cost substrate based compact antennas for 4g/5g side-edge panel smartphone applications. Progr. Electromagn. Res. Lett. **91**, 145–152 (2020)
7. Magray, M.I., Karthikeya, G.S., Muzaffar, K., Koul, S.K.:. Compact co-design of conformal 4G LTE and mmWave 5G antennas for mobile terminals. IETE J. Res. 1–12 (2019)
8. Kurvinen, J., Kähkönen, H., Lehtovuori, A., Ala-Laurinaho, J., Viikari, V.: Co-designed mm-wave and LTE handset antennas. IEEE Trans. Antennas Propag. **67**(3), 1545–1553 (2018)
9. Zhang, S., Chen, X., Syrytsin, I., Pedersen, G.F.: A planar switchable 3-D-coverage phased array antenna and its user effects for 28-GHz mobile terminal applications. IEEE Trans. Antennas Propag. **65**(12), 6413–6421 (2017)
10. Yang, B., Yu, Z., Dong, Y., Zhou, J., Hong, W.: Compact tapered slot antenna array for 5G millimeter-wave massive MIMO systems. IEEE Trans. Antennas Propag. **65**(12), 6721–6727 (2017)
11. Sorkherizi, M.S., Dadgarpour, A., Kishk, A.A.: Planar high-efficiency antenna array using new printed ridge gap waveguide technology. IEEE Trans. Antennas Propag. **65**(7), 3772–3776 (2017)
12. Dixit, A.S., Kumar, S.: The enhanced gain and cost-effective antipodal Vivaldi antenna for 5G communication applications. Microw. Opt. Technol. Lett. **62**(6), 2365–2374 (2020)

13. Hussain, R., Alreshaid, A.T., Podilchak, S.K., Sharawi, M.S.: Compact 4G MIMO antenna integrated with a 5G array for current and future mobile handsets. IET Microwaves Antennas Propag. **11**(2), 271–279 (2017)
14. Ta, S.X., Choo, H., Park, I.: Broadband printed-dipole antenna and its arrays for 5G applications. IEEE Antennas Wirel. Propag. Lett. **16**, 2183–2186 (2017)
15. Saad, A.A.R., Mohamed, H.A.: Printed millimeter-wave MIMO-based slot antenna arrays for 5G networks. AEU-Int. J. Electron. Commun. **99**, 59–69 (2019)
16. Nouri, M., Abazari Aghdam, S., Jafarieh, A., Bagby, J., Sahebghalam, S.: A wideband millimeter-wave antenna based on quasi-Yagi antenna with MIMO circular array antenna beamforming for 5G wireless networks. Microw. Opt. Technol. Lett. **61**(7), 1810–1814 (2019)
17. Shi, H., Zhang, X., Li, J., Jia, P., Chen, J., Zhang, A.: 3.6-GHz eight-antenna MIMO array for mobile terminal applications. AEU-Int. J. Electron. Commun. **95**, 342–348 (2018)
18. Xi, L.: A wideband planar filtering dipole antenna for 5G communication applications. Microw. Opt. Technol. Lett. **61**(12), 2746–2751 (2019)
19. Ban, Y.L., Li, C., Wu, G., Wong, K.L.: 4G/5G multiple antennas for future multi-mode smartphone applications. IEEE Access **4**, 2981–2988 (2016)
20. Wu, D., Cheung, S.W., Yuk, T.I.: Compact 3D-loop antenna with bandwidth enhancement for WWAN/LTE mobile-phones applications. IET Microwaves Antennas Propag. **11**(2), 240–246 (2017)
21. Desai, A., Upadhyaya, T., Patel, R.: Compact wideband transparent antenna for 5G communication systems. Microw. Opt. Technol. Lett. **61**(3), 781–786 (2019)
22. Sharawi, M.S., Ikram, M., Shamim, A.: A two concentric slot loop based connected array MIMO antenna system for 4G/5G terminals. IEEE Trans. Antennas Propag. **65**(12), 6679–6686 (2017)
23. Wani, Z., Abegaonkar, M.P., Koul, S.K.: Millimeter-wave antenna with wide-scan angle radiation characteristics for MIMO applications. Int. J. RF Microwave Comput. Aided Eng. **29**(5), e21564 (2019)
24. Reddy, G.S., Kamma, A., Kharche, S., Mukherjee, J., Mishra, S.K.: Cross-configured directional UWB antennas for multidirectional pattern diversity characteristics. IEEE Trans. Antennas Propag. **63**(2), 853–858 (2014)
25. Tawk, Y., Costantine, J., Christodoulou, C.G.: An eight-element reconfigurable diversity dipole system. IEEE Trans. Antennas Propag. **66**(2), 572–581 (2017)
26. Sharma, Y., Sarkar, D., Saurav, K., Srivastava, K.V.: Three-element MIMO antenna system with pattern and polarization diversity for WLAN applications. IEEE Antennas Wirel. Propag. Lett. **16**, 1163–1166 (2016)
27. Saurav, K., Mallat, N.K., Antar, Y.M.: A three-port polarization and pattern diversity ring antenna. IEEE Antennas Wirel. Propag. Lett. **17**(7), 1324–1328 (2018)
28. Chaudhary, P., Kumar, A., Yadav, A.: Pattern diversity MIMO 4G AND 5G wideband circularly polarized antenna with integrated LTE band for mobile handset. Progr. Electromagn. Res. **89**, 111–120 (2020)
29. Dadgarpour, A., Zarghooni, B., Virdee, B.S., Denidni, T.A.: One-and two-dimensional beam-switching antenna for millimeter-wave MIMO applications. IEEE Trans. Antennas Propag. **64**(2), 564–573 (2015)
30. Briqech, Z., Sebak, A.R., Denidni, T.A.: Wide-scan MSC-AFTSA array-fed grooved spherical lens antenna for millimeter-wave MIMO applications. IEEE Trans. Antennas Propag. **64**(7), 2971–2980 (2016)
31. Shim, J.Y., Go, J.G., Chung, J.Y.: A 1-D tightly coupled dipole array for broadband mmWave communication. IEEE Access **7**, 8258–8265 (2019)
32. Ikram, M., Al Abbas, E., Nguyen-Trong, N., Sayidmarie, K.H., Abbosh, A.: Integrated frequency-reconfigurable slot antenna and connected slot antenna array for 4G and 5G mobile handsets. IEEE Trans. Antennas Propag. **67**(12), 7225–7233 (2019)
33. Hwang, I.J., Ahn, B., Chae, S.C., Yu, J.W., Lee, W.W.: Quasi-Yagi antenna array with modified folded dipole driver for mmWave 5G cellular devices. IEEE Antennas Wirel. Propag. Lett. **18**(5), 971–975 (2019)

34. Hasan, M.N., Bashir, S., Chu, S.: Dual band omnidirectional millimeter wave antenna for 5G communications. J. Electromagn. Waves Appl. **33**(12), 1581–1590 (2019)
35. Pan, Y.M., Qin, X., Sun, Y.X., Zheng, S.Y.: A simple decoupling method for 5G millimeter-wave MIMO dielectric resonator antennas. IEEE Trans. Antennas Propag. **67**(4), 2224–2234 (2019)
36. Karthikeya, G.S., Koul, S.K., Poddar, A.K., Rohde, U.: Ultra-compact orthogonal pattern diversity antenna module for 5G smartphones. Microw. Opt. Technol. Lett. **63**(8), 2003–2012 (2021)

Chapter 4
Backward Compatible Antenna Systems for Smartphones

4.1 Introduction

Backward compatibility of smartphones would be an essential feature in the future. Gradual migration towards future generation of wireless systems is expected as opposed to sudden and abrupt changes. The infrastructure investments on the previous generations of cellular systems is pretty huge and the return on capital allocated is spread across a decade or so. For instance, 2G serves approximately 300 million subscribers in India, whereas 4G serves almost 700 million subscribers within the same geography. This trend might continue in the near future. This dual existence of multi-frequency cellular systems would mean that future smartphones need to serve the previous wireless generations as well. Hence co-design of microwave and millimeter antennas is an important aspect of future antenna system design. This chapter explores co-design antenna architectures with various design examples. Design of sub-6 GHz or microwave antennas for smartphones has been perfected, as most of the commercial devices in the market have multifunctional antennas for this spectrum. Also, numerous mmWave 5G antenna design variants have been mastered, in the recent past, as observed in the preceding Chapter.

The amalgamation of microwave and mmWave antennas for different generations is not exhaustively investigated in the literature [1–15]. 4G LTE (Long term Evolution) antennas integrated with Antennas on display is explored in [1], here the 4G LTE antennas are mounted on the longer edge of the smartphone and the sub-6 GHz 5G antenna operating in the 3.5 GHz band is placed along the shorter edge. The mmWave phased array, which is integrated with the display is mounted in the orthogonal plane as that of the other elements. Even though the mmWave antenna has a relatively high gain, it radiates towards the user when in use.

An electrically large system ground plane is used as a shared ground between the microwave and the high gain mmWave antenna array in [2]. Even though the design has a shared ground between the microwave antennas, the feeds for microwave and mmWave radiators are in different planes and might not be suitable for integration

S. K. Koul and K. G. S., *Antenna Architectures for Future Wireless Devices*,
Signals and Communication Technology,
https://doi.org/10.1007/978-981-16-7783-0_4

with a commercial smartphone as the presented sub-6 GHz antennas are in the same plane as that of the system ground plane. Usually, the system ground plane would house the back-end electronics and controllers. The microwave antennas would be close to the rim of the smartphone. The presented design must be tweaked a little for smartphone integration. Also, the mmWave antenna radiates from a slot array, leading to a bidirectional radiation pattern, effectively reducing the forward gain, which might not be a favorable design feature as explored in Chap. 2.

An electrically compact design is reported in [3], here the mmWave antennas are end-fire in nature, thus radiating energy away from the user, post integration with the portable device. But the effective occupied physical footprint is higher than the conventional panel mountable broadside radiators. A variant of space saving mmWave end-fire antenna co-designed with a microwave monopole is explored in this Chapter.

Another strategy of co-design is to integrate an electrically small microwave monopole beneath the mmWave end-fire antenna array as demonstrated in [4]. The phased array can also scan the beam, despite the proximity to the microwave monopole antenna. Another variant of the afore-mentioned design principle has been illustrated in [5] as well. The shared ground design of [6] occupies a large physical footprint. Design illustrated in [7] has a compact structure with unidirectional beam in the mmWave domain. The shared aperture design of [8] has complicated feeding network, which might not be readily feasible within a smartphone. A common strategy of shared ground design is illustrated in [9–15].

In this Chapter, the desired characteristics of co-designed antennas is highlighted in Sect. 4.2 followed by discussion on failure of multiband antennas for frequency upscaling. Various design examples of co-design antennas for mobile devices are demonstrated in Sects. 4.4–4.8.

4.2 Desired Characteristics of Co-designed Antennas

The concept of co-designed or co-located antennas would be a trend in the consumer electronics industry for decades to come. As the performance metrics of microwave antenna could be different from that of a millimeter wave antenna, it is important to pay attention to the same. The reader might recall that antenna requirements for smartphones for mmWave frequencies was discussed in Sects. 2.3.1 and 2.3.2, one of the most critical parameters of concern is the form factor, the edge of the smartphone just beneath the panel is the space available for the co-located design. Again, the critical constraining parameter is the panel height of 7 mm, as emphasized in earlier Chapters.

The issue with co-design is that both the antennas for sub-6 GHz and mmWave applications must fit within this form factor. As the gain requirements of the mmWave antenna is stringent, microwave antennas could be placed or mounted beneath the mmWave antenna. The only catch is that the mmWave antenna system would have an electrically large ground which would be restricting radiation from the microwave

antenna. Hence sufficient clearance must be maintained between the two antennas, electrically speaking. Also, panel edges are the only real estate within the smartphone for placing both the types of antennas. Design examples presented in this Chapter will demonstrate the antenna system's constraint of the panel height of 7 mm. The form factor has fractional wavelength for microwave carrier frequencies and multi-wavelength for mmWave antenna; which could be exploited for the design and placement of both the types of antennas.

Radiation patterns of the co-designed antenna system must meet two criteria simultaneously: a unidirectional hemispherical beam with high front to back ratio for mmWave antenna and an omni-directional pattern for the microwave antenna. With an omnidirectional pattern for the microwave antenna, SAR would be high during voice mode. Thus, it is necessary to minimize radiation towards the user's head within the constraints of the available system ground for the microwave antenna. Most of the commercial phones in the market have a quasi-omnidirectional pattern for most of the bands within the sub-6 GHz spectrum.

Techniques to achieve unidirectional beam for mmWave antennas were discussed in the preceding Chapter. The challenge is to introduce electrically small microwave antennas near the previously presented mmWave antennas. In other words, co-design depends not only on the design of compact antennas but also on the strategic placement of the constituent antennas within the antenna system. Co-designing could be categorized as placement analysis of antennas without any loss of generality.

The impedance bandwidths of the constituent antennas of the assembled system must be like that of its stand-alone antenna's impedance characteristics. Due to the electrically (both at microwave and mmWave frequencies) close placement of the antennas, there is a high chance of antennas being detuned from their original stand-alone resonance. Therefore, adequate decoupling networks between the two antennas must be designed. The other way to maintain respective bandwidths for microwave and mmWave antennas is to analyze the characteristics of the antenna system instead of the component stand-alone entities. Mutual coupling between the ports must be less than 20 dB to minimize energy leakage between the ports across the bands.

4.3 Why Multiband Antennas Might Fail for Microwave and mmWave Operations?

The ideal solution for the co-design puzzle is to design an antenna which has quasi-omnidirectional pattern in the microwave spectrum and a unidirectional pattern with adequate gain in the millimeter wave spectrum. The problem is: 28 GHz is 3rd octave of 3.5 GHz, which means the radiator must have a dynamic multimode operation to achieve the above feat. An illustration would prove the problem at hand. Consider an inset fed patch antenna designed on a low dielectric constant substrate, as illustrated in the schematics of Fig. 4.1. The specifics of the substrate, feeding lines and the dimension of the inset feeding is not important for this discussion, hence ignored.

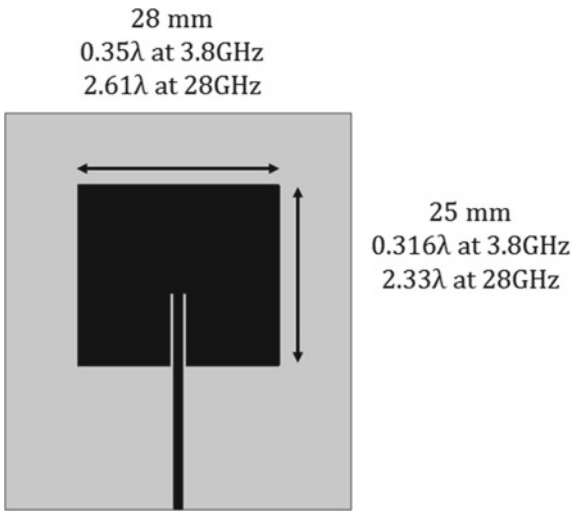

Fig. 4.1 Schematic of a microwave patch antenna

The primary resonance of this radiator is tuned at 3.85 GHz, based on the length and width of the primary radiator. The microwave region of the input reflection coefficient clearly shows the dominant first resonance at 3.85 GHz as evident from Fig. 4.2a the size of the radiator is electrically 0.35 $\lambda \times 0.316\ \lambda$ at 3.85 GHz, which also delivers a clean speckle-free unidirectional broadside beam with a peak gain of about 4dBi, as sketched in the 3.85 GHz pattern of Fig. 4.2b. This is the expected behavior of a dominant mode resonant patch antenna. If the same physical antenna is simulated in the millimeter wave band, i.e., 25–31 GHz, interesting results pop up.

The same antenna gives a strong resonance at 28.5 GHz with the overall magnitude of S_{11} below 5 dB in the higher frequency domain, this just means that the low frequency antenna has an impedance match in the higher frequency as well. The 28 GHz patterns of Fig. 4.2b prove that the element gets overmoded leading to a specular pattern with a peak gain of close to 3dBi. But this pattern would not serve the purpose of any consumer device application.

The physical size of the radiator is also way beyond the expected values of any commercial consumer device. This proves that upscaling of resonant low frequency antenna to work reasonably well in the millimeter wave spectrum might not be feasible. This illustration does not deny the possibility totally but proves the challenge to simultaneously meet the design criteria for microwave and millimeter wave bands. The impedance characteristics could be easily achieved with the frequency upscaling technique, but patterns and hence gain might be compromised at higher band.

The other logical technique to explore is to see whether frequency downscaling could be realized. For this illustration, consider a printed dipole designed on an electrically thin substrate with low dielectric constant. The antenna is like the printed Yagi-Uda design presented in Sect. 3.5.1, without the parasitics. The schematic along with the electrical dimensions for the intended microwave and millimeter wave bands are illustrated in Fig. 4.3.

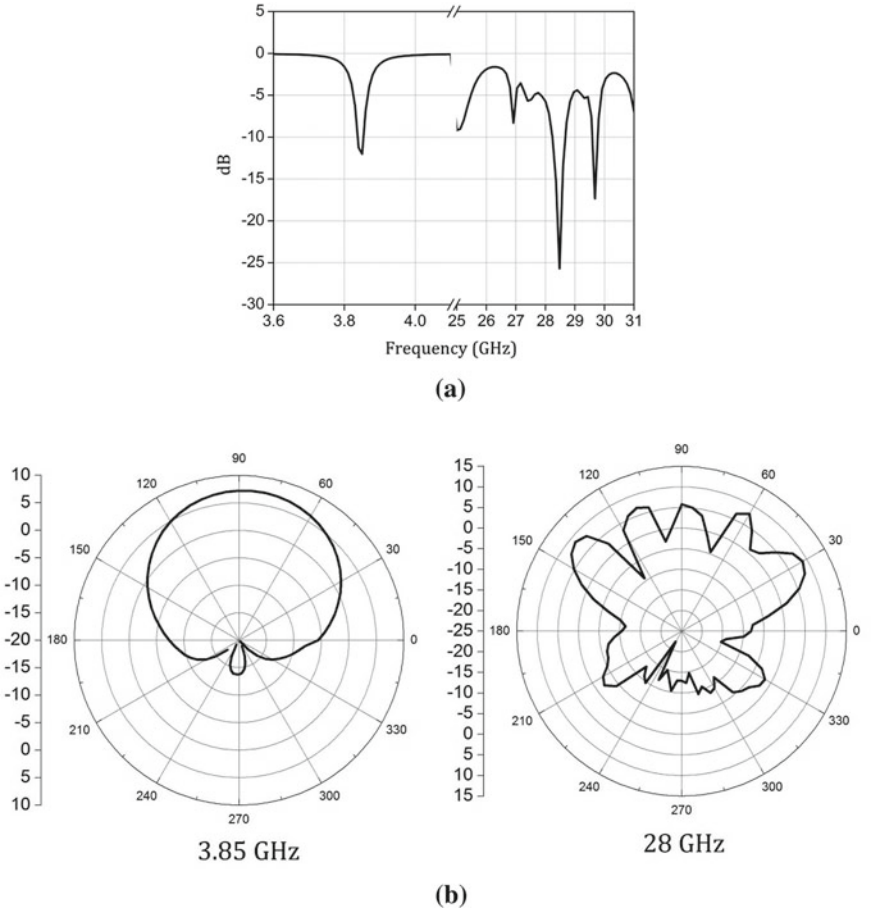

Fig. 4.2 **a** $|S_{11}|$ of the microwave patch antenna, **b** radiation patterns of the microwave patch antenna

Naturally, the primary resonance of the printed dipole is at 28 GHz, as seen in the strong dip of $|S_{11}|$ in Fig. 4.4a. The dipole arms are of half-wavelength in the given substrate, hence resonates at the desired band. The pattern is unidirectional due to the design of the ground plane of the printed dipole. The microwave behavior of this antenna is investigated in the 3–4 GHz band. As observed in Fig. 4.4a, the element is strongly mismatched in the microwave regime. Miniaturized tuning networks could be introduced to achieve the desired impedance tuning, but that would simultaneously deteriorate its impedance behavior in the mmWave zone. The low frequency pattern of Fig. 4.4b also proves that downscaling leads to a gain less than -1dBi.

To sum up, the idea of simultaneous dual bands for microwave and millimeter wave bands would be difficult to design. Hence multi-port antenna systems would be designed and characterized in this Chapter.

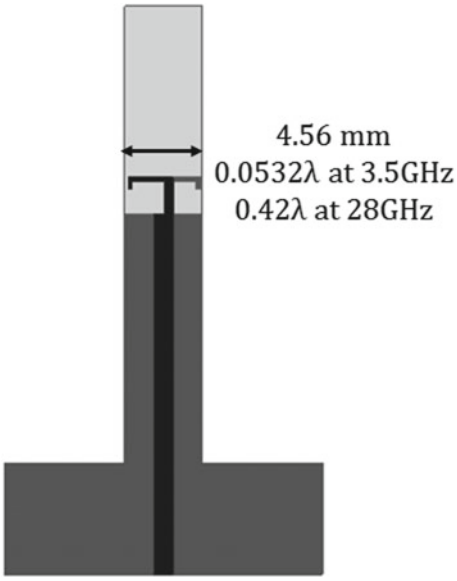

Fig. 4.3 Schematics of a mmWave printed dipole antenna

4.4 Co-design of CPS-Fed Sub-6 GHz Antenna with a MmWave Conformal Array

In this Section, the first design example of co-design strategy of sub-6 GHz and mmWave antennas would be illustrated. Even though it appears that multiband antennas with the necessary performance metrics for the respective bands for lower and higher frequencies might be difficult to attain, the problem is that the antenna must operate as a standing wave element at the lower frequency (sub-6 GHz) and traveling wave at higher frequency (mmWave). This line of design thinking might be harder, hence a simpler strategy for co-design or collocated antennas is explored in the current and subsequent Sections.

The desired characteristics mentioned in Sect. 4.2 would stand as a basis for realizing co-design antenna systems for smartphone applications. It is important to note that sub-6 GHz antennas must just fit within the form factor without necessarily exhibiting good radiation characteristics. The mmWave 5G antenna on the other hand, must have high gain for a sustainable link. In the designs to be illustrated in this Chapter, 3.5 GHz is the chosen carrier frequency for the sub-6 GHz band. The design methodology discussed here could be extrapolated to design the sub-6 GHz antenna with a different resonant frequency. Also, 28 GHz is chosen as the center frequency for the mmWave 5G band, the designs could be scaled up or down depending on the actual carrier frequency. The design strategy needs to be focused on to achieve desired results for both the bands. All the five co-designed antenna systems presented in this Chapter illustrate various ways of designing the elements and their placement to satisfy the form factor without any compromise in the performance

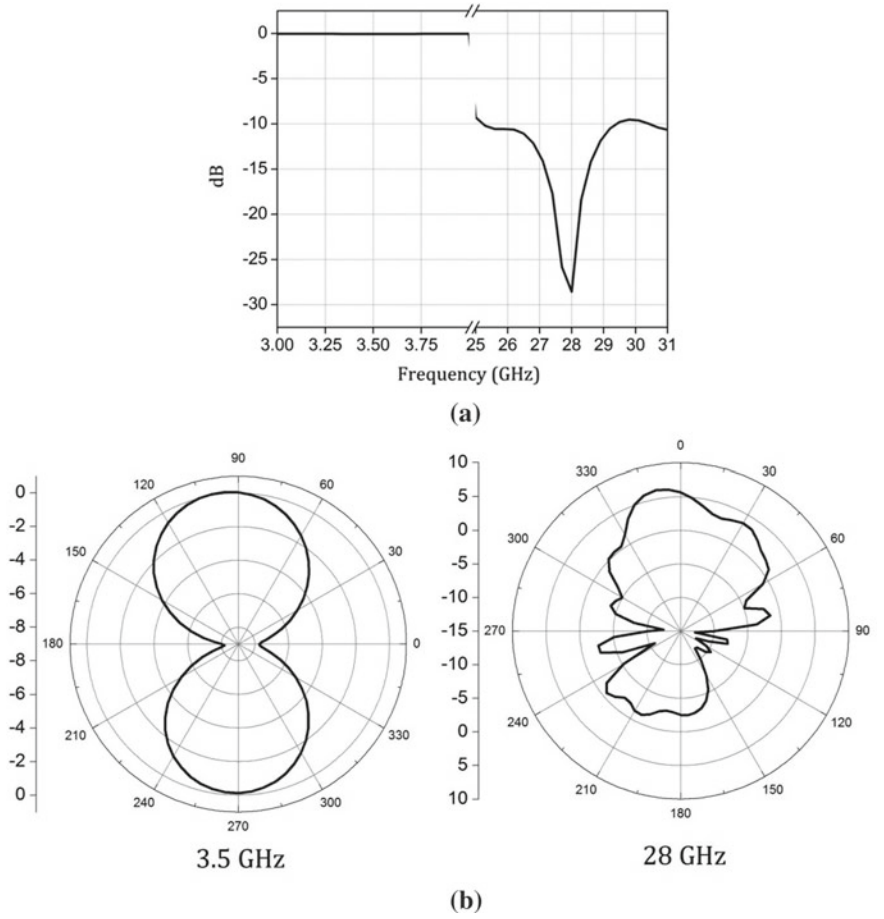

Fig. 4.4 **a** $|S_{11}|$ of the mmWave printed dipole antenna, **b** Radiation patterns of the mmWave printed dipole antenna

metrics. Initially, individual stand-alone antennas are described in detail followed by the co-designed or co-located antenna system.

4.4.1 CPS-Fed Sub-6 GHz Antenna

The sub-6 GHz band chosen for this illustration is 3.5 GHz. Numerous articles and reports have advertised 3.5 GHz for sub-6 GHz 5G applications. In this design example, a CPS (Coplanar Stripline) fed electrically small corner bent antenna is presented. The schematic of the proposed element is illustrated in Fig. 4.5a. The feeding connector is not explicitly shown but implied with the structure. The design

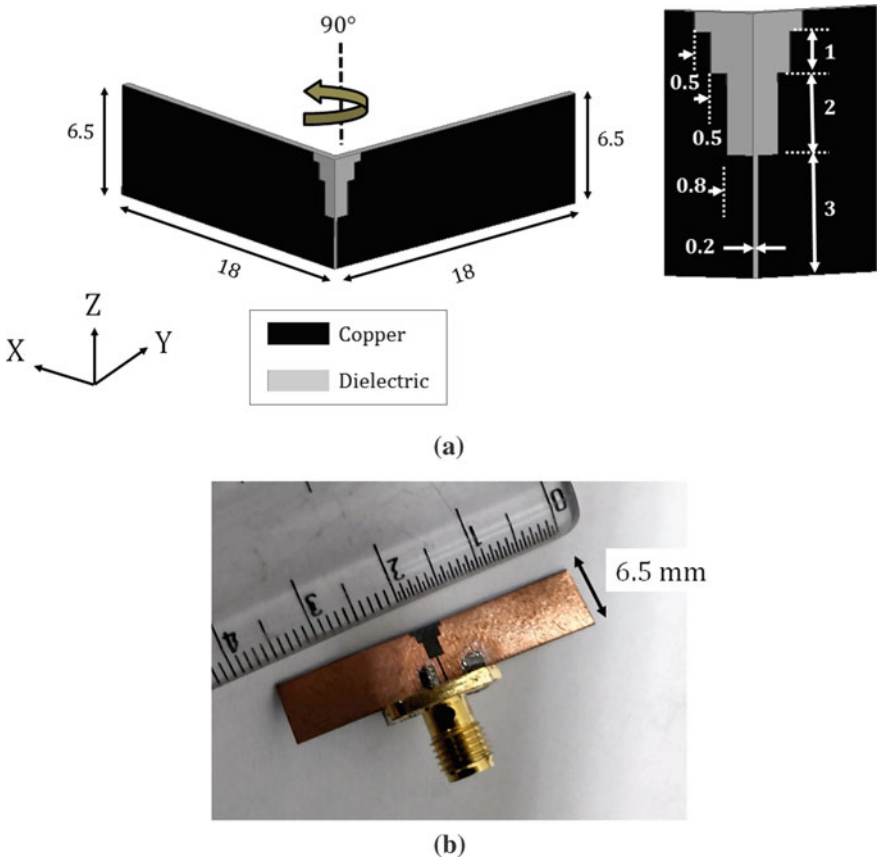

Fig. 4.5 **a** Corner bent CPS fed antenna, **b** photograph of the fabricated prototype (All dimensions are in mm)

is a straight-forward printed dipole with an adequate bandwidth and corner bending. Each dipole arm is 18 mm (or 0.21 λ, computed at 3.5 GHz). The overall length of the dipole is 36 mm (or 0.42 λ, computed at 3.5 GHz). The CPS feeding is at the bottom of the proposed antenna, wherein the gap between the two dipole arms is 0.2 mm, evident from the inset of Fig. 4.5a. The stepped structure is incorporated to achieve proper impedance matching with the 50 Ω feed.

The proposed antenna is designed on Rogers 5880 substrate with a low dielectric constant of 2.2 and a dielectric loss tangent of 0.0009. The choice of the substrate is not a very stringent requirement as the design could also be realized with two all-metallic dipole arms without any loss of generality. But most of the back-end circuitry is built upon PCBs (Printed Circuit Boards), the antenna also must be compatible with the same, to maintain feasibility of manufacturing process. CPS feeding is chosen for the ease of feeding the antenna arms. A microstrip feeding would have been on both the sides of the substrate and hence might not offer the compactness,

which could be delivered by this technique. An example of microstrip feed for the sub-6 GHz antenna would be discussed in Sect. 4.5, the advantage with CPS-feeding would be evident when the microstrip fed antenna and the current proposed antennas are compared.

The thickness of the chosen substrate is 0.508 mm or 20 mil, much thicker substrate would have resulted in higher impedance bandwidth at the cost of poor bendability. It must be noted that Roger's substrate is not very brittle, at this thickness, but would serve the current application without heavy deviation from the theoretically expected results. The height of the printed dipole also decides the impedance bandwidth in the current example, a height of 6.5 mm is chosen for a reasonable bandwidth and compliance with the form factor. The antenna is corner bent at the center to be edge mountable with the smartphone. The logic behind bending would be clear when the assembled antenna system would be presented. The proposed antenna is chemically etched as the minimum dimension is greater than 50 μm in the current design. The planar version of the fabricated sample is shown in Fig. 4.5b.

A standard SMA (sub-miniature A) connector is soldered on to the Copper portions of the antenna. The flat mouthed SMA connector is preferred over the cylindrical mouthed one to avoid additional mismatches from the connector to the antenna. Also, minimal solder is used at the transition points to avoid lead inductances, which detunes the antenna.

It must be noted that end-launch connectors used in the previous Chapter would be unsuitable for measurement of this form factor for the simple reason that the clearance required for the trace pin and the grounding clamps must be at least 6 mm and the radiator should be 10 mm away from the trace pin to avoid specular patterns by the connector mould itself. To get some perspective, the current SMA has wider dimension of 12 mm, but the end-launch connector is at least 20 mm wide with 15 mm height. In other words, the ground metallic footprint of the connector would swamp the antenna and would lead to erroneous measurements in both the S-parameter and patterns. However, end launch connectors could be used for microstrip feeding without much degradation in the measurement quality.

The input reflection coefficient of the proposed printed dipole is illustrated in Fig. 4.6. There's no sharp resonance at 3.75 GHz and the antenna seems to be wide band even beyond 4 GHz. These characteristics of the stand-alone element would alter when it is integrated with the mmWave 5G antenna. The discrepancy between simulated and measured curves is due to the bending stress of the corner bent substrate. The soldering is non-ideal with the corner bent substrate.

The radiation patterns at 3.3 GHz and 3.5 GHz are illustrated in Fig. 4.7, these are like the conventional standard dipole patterns but inclined at 45°, as the antenna is corner bent, making it an effective radiator at this angle. The slight discrepancy between the simulated and measured curves is due to the metallic footprint of the connector and poor absorption of the RF absorbers used within the anechoic chamber, especially with oblique incidence from the standard gain horn antenna. Nevertheless, these patterns are useful as they are almost omnidirectional as expected from the sub-6 GHz panel mountable antennas for consumer electronics. The peak gain is around 2dBi, as expected from printed dipoles.

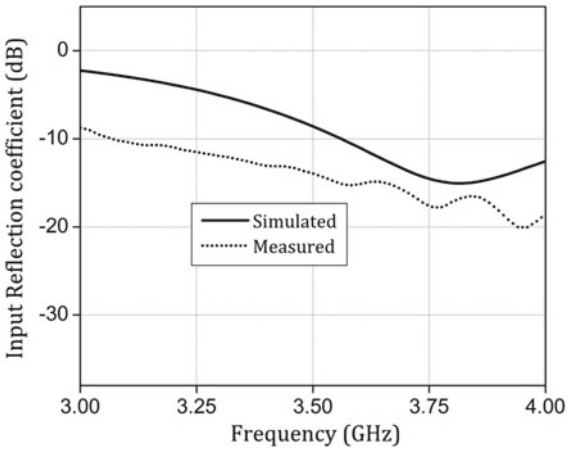

Fig. 4.6 $|S_{11}|$ of the corner bent CPS fed antenna

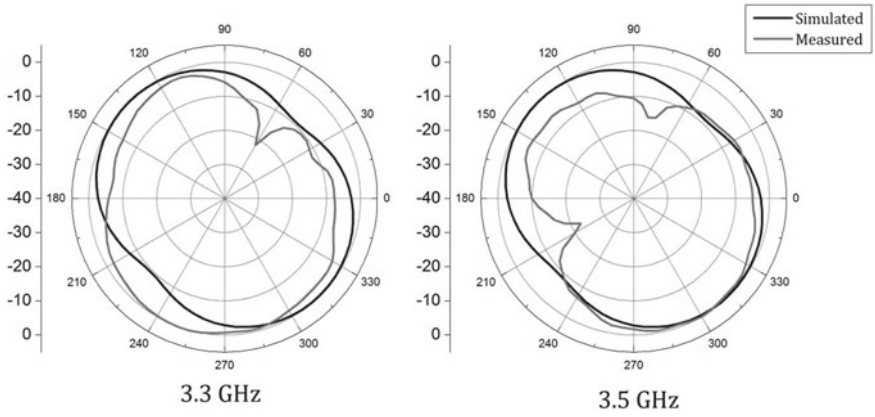

Fig. 4.7 Radiation patterns of the CPS fed antenna

4.4.2 mmWave Conformal Array

The colocated antenna system would have two entities, one is the sub-6 GHz and the other is a mmWave antenna. Sub-6 GHz antenna was discussed in the preceding Section, compact mmWave antenna would be explained here. The proposed antenna is shown in Fig. 4.8a and its corner bent version in Fig. 4.8b. It is designed on Rogers 5880 substrate, which is identical to that of the 3.5 GHz antenna.

The observant reader would notice that the corner bent antenna illustrated here is almost identical to the antenna presented in Sect. 3.4.1. The only difference is that the corner bent antenna here is wider compared to the earlier design. The wider design choice would become apparent in the subsequent assembled design. The

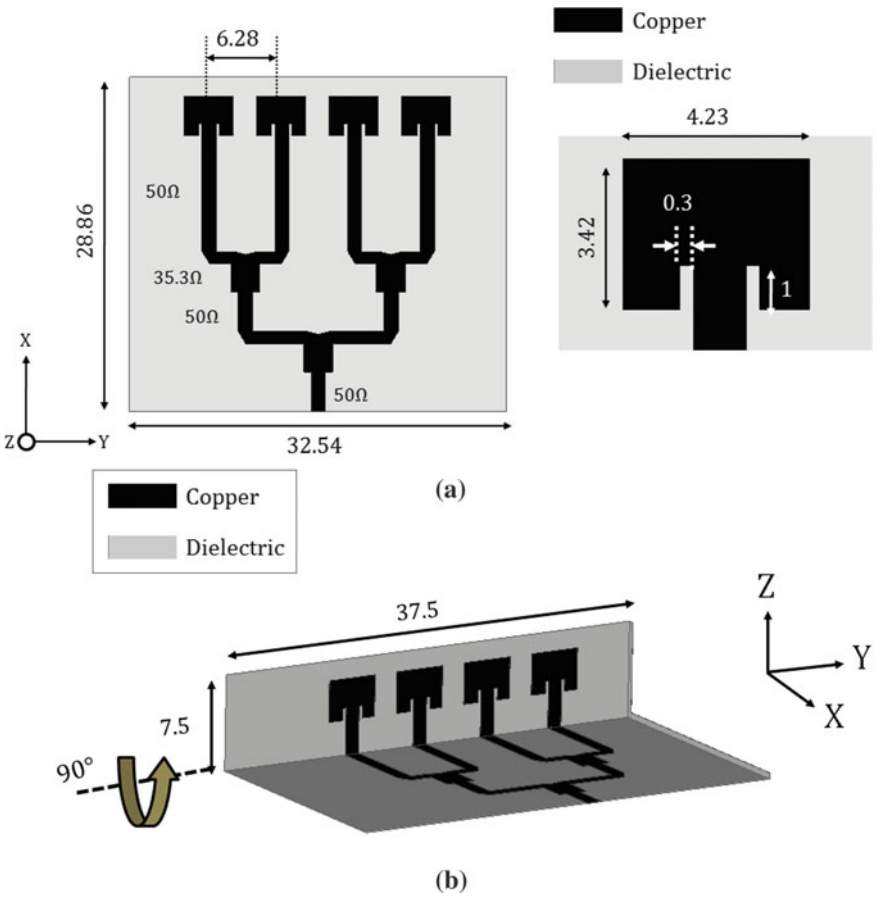

Fig. 4.8 Schematics of the mmWave antenna: **a** planar version, **b** corner bent version (All dimensions are in mm)

characteristics of the mmWave antenna is available in Sect. 3.4.1 and it remains invariant with the additional 5 mm widening of the width of the antenna. The rationale behind choosing a corner bent array topology is high gain with low physical footprint. The other advantage with this design is the electrically large ground plane which doubles up as a system ground. The corner bent array could be replaced by any corner bent radiator with forward radiation and electrically wide complete ground plane.

4.4.3 *Electrically Close Integrated Design*

The sub-6 GHz antenna of Sect. 4.4.1 and the mmWave antenna of Sect. 4.4.2 would be co-designed for a two port compact antenna system. The proposed electricaly close antenna system is illustrated in Fig. 4.9. The corner bent sub-6 GHz printed dipole is edge mounted with the mmWave antenna as shown in the schematic. A gap of 1.5 mm is maintained between the ground plane of the mmWave antenna and the dipole arm of the microwave antenna. If the dipole arm is shorted with the electrically large ground plane, then the resonant action of the antenna would be mitigated. The corner bent dipole is placed at a height of 1 mm above the system ground plane to prevent additional coupling, as the height of the microwave antenna is 6.5 mm, the overall form factor is not compromised. It must also be observed that 5 mm additional dielectric spacer is introduced in the system ground plane to maintain the resonance of the microwave antenna at 3.5 GHz.

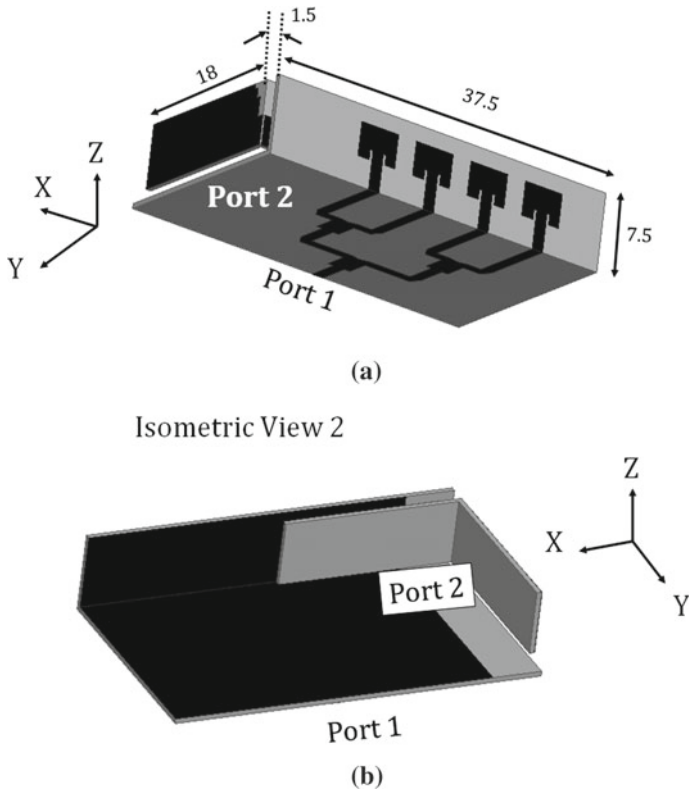

Fig. 4.9 Schematic of the electrically close integrated design: **a** isometric view 1, **b** isometric view 2 (All dimensions are in mm)

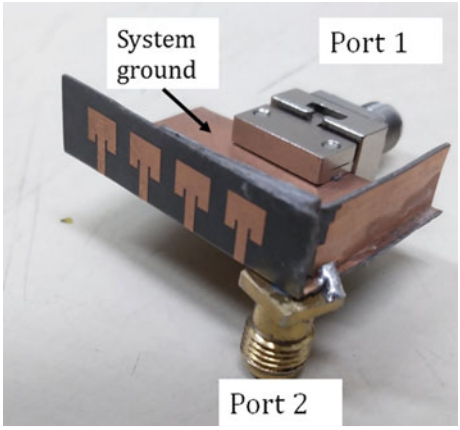

Fig. 4.10 Photograph of the integrated prototype

Further sliding of the microwave antenna within the contour of the mmWave antenna would strongly detune the sub-6 GHz antenna to much lower frequency as the stronger coupling would virtually increase the electrical length of the printed dipole. The fabricated antenna assembly is shown in Fig. 4.10. A dielctric spacer of thickness 1.5 mm was introduced between the elements and sufficient clearance was introduced in the substrate of mmWave antenna to accommodate the SMA connector, soldered onto port 2. Port 1 of the mmWave antenna is fed through the wideband industry standard end-launch connector. The same connector would not be viable for mounting with the sub-6 GHz antenna due to lack of clearance, as mentioned earlier. The compactness of the proposed antenna system is evident in the photograph, wherein the entire system could be integrated at one of the corners of a mobile device.

The 10-dB impedance bandwidth of the millimeter wave antenna is from 25.7 to 28.4 GHz or 10% wide as observed in the simulated and measured $|S_{11}|$ shown in Fig. 4.11. Both the millimeter and microwave S-parameter measurements were done using Keysight E8364C analyser. The discrepancy between simulated and measured curves is due to the non-ideal assembly of the end-launch connector with the corner bent antenna array. Also, bending stress of the substrate might have altered the measured S-parameter at higher end of the spectrum. It is evident that the microwave compact dipole has minimal influence on the impedance characteristics of the millimeter wave antenna. This could be attributed to the placement of the microwave antenna behind the ground plane of the mmWave element. Mutual coupling between the two antennas is less than 30 dB across the 25–31 GHz band as illustrated in Fig. 4.12. Measured mutual coupling seems to be higher than the simulated values because of non-ideal placement of the microwave antenna with respect to the mmWave antenna. This measurement could have been improved with 3D-printed aligners for this specific application. The non-uniform spacing between one of the dipole arms of the microwave antenna and the system ground plane also enhances the measured value of mutual coupling.

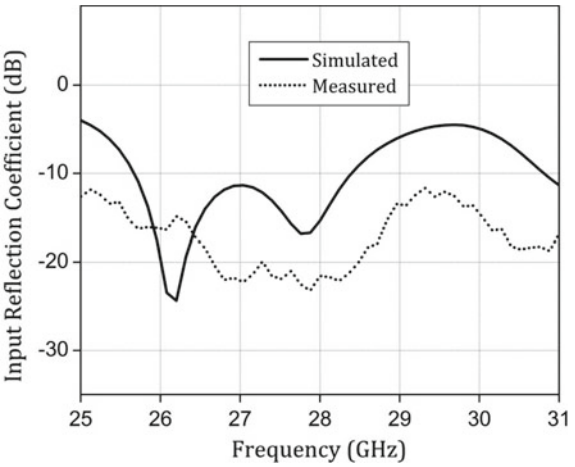

Fig. 4.11 Input reflection coefficient at Port 1

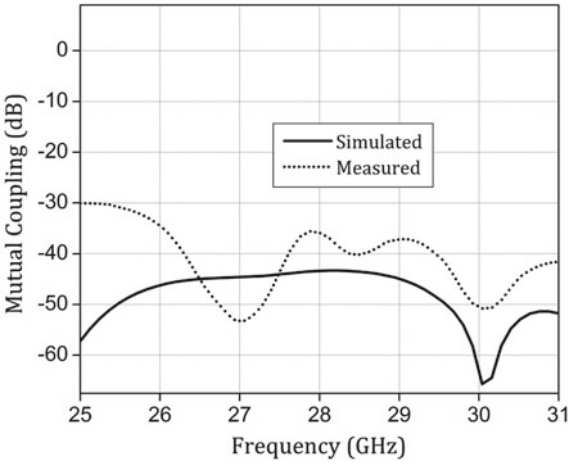

Fig. 4.12 Mutual Coupling at the higher band

The forward radiation patterns are illustrated in Fig. 4.13. These patterns are almost identical to that of the stand-alone element, which illustrates the minimal influence of microwave antenna on the radiating aperture of the mmWave antenna. The forward gain of port 1 within the antenna system is also similar to that of the stand-alone corner bent array as evident from Fig. 4.14.

The simulated value of 10-dB impedance bandwidth for port 2 is from 3.4–3.84 GHz or 20% as observed in Fig. 4.15. The measured value shows a strong resonance at 3.56 GHz, probably due to the alignment error of the microwave antenna, and unnecessary shorting of the dipole arm with the electrically large system ground plane. Mutual coupling is less than 20 dB in spite of the electrically close 1.5 mm (or 0.0175 λ at 3.5 GHz) as seen in Fig. 4.16.

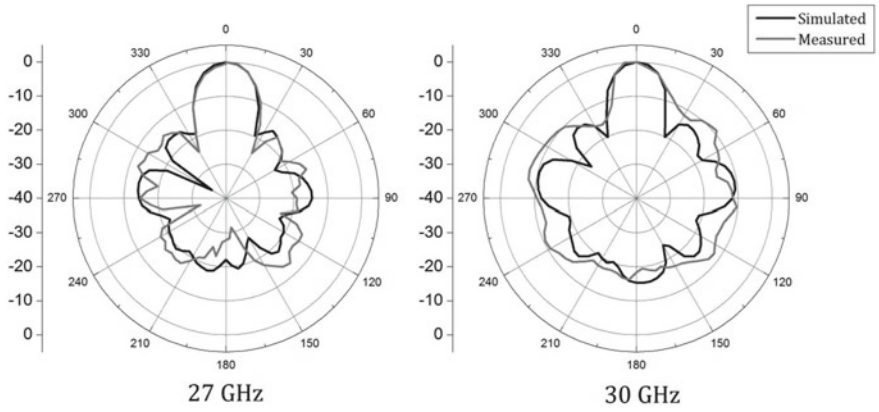

Fig. 4.13 Radiation patterns in the higher band

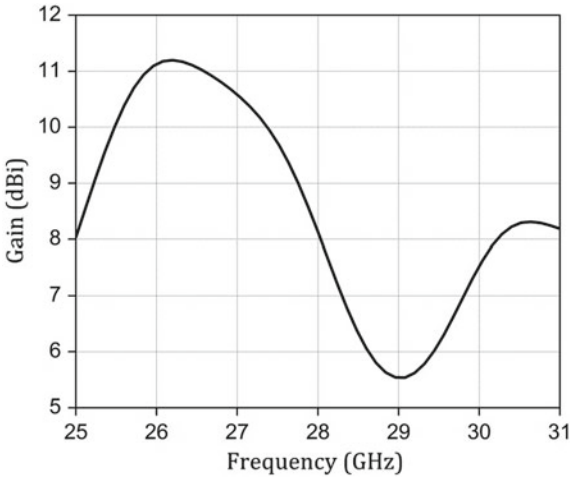

Fig. 4.14 Forward gain when port 1 is activated

Low mutual coupling means that low energy coupling between the ports in both the microwave and millimeter wave bands. The radiation patterns are altered when compared to the stand-alone element's patterns mainly because of the electrically large ground plane of the mmWave antenna. The patterns at 3.3 GHz and 3.5 GHz of the corner bent dipole within the antenna system are illustrated in Fig. 4.17.

As the radiating aperture of the microwave antenna is significantly altered, the pattern also seem to be directed towards the user. But if the overall contour of the radiated power profile is considered, then it is quasi-omnidirectional as expected from a compact antenna. Peak gain is similar to resonant printed dipole antennas as observed in Fig. 4.18.

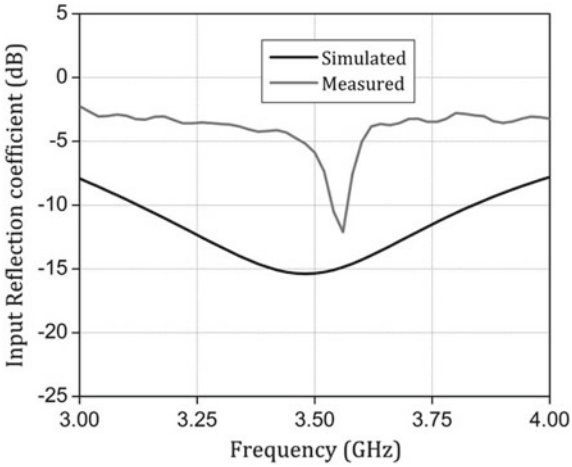

Fig. 4.15 Reflection coefficient of Port 2

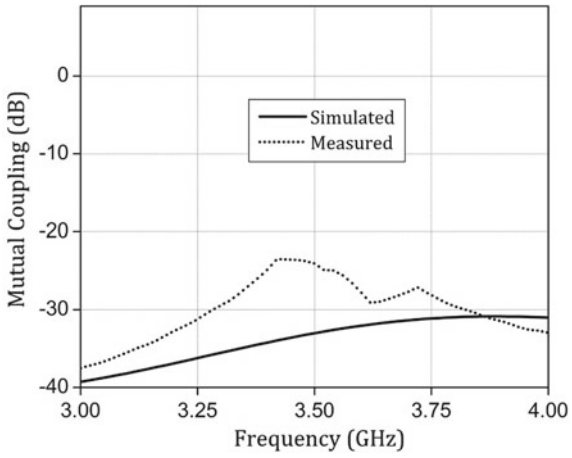

Fig. 4.16 Mutual coupling in the sub-6 GHz band

3D radiation patterns with respect to the proposed antenna system are illustrated in Fig. 4.19a. It is evident that the desired or expected characteristics of the sub-6 GHz and mmWave co-design has been achieved. The mmWave pattern has minimal radiation towards the user with high gain and the microwave antenna has quasi-omnidirectional pattern. A typical placement of the proposed antenna system with a commercial smartphone is shown in Fig. 4.19b. The antenna system fits at the edge of the mobile terminal. The proposed system could be either mounted as shown or along the perpendicular direction depending on the data mode required.

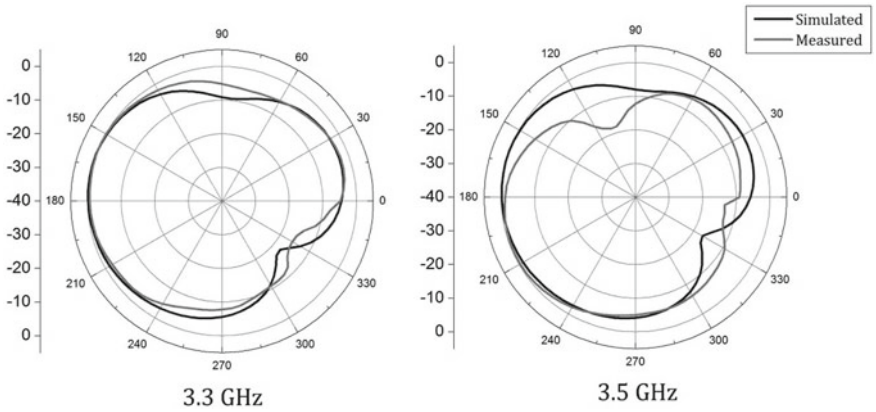

Fig. 4.17 Radiation patterns in the lower band

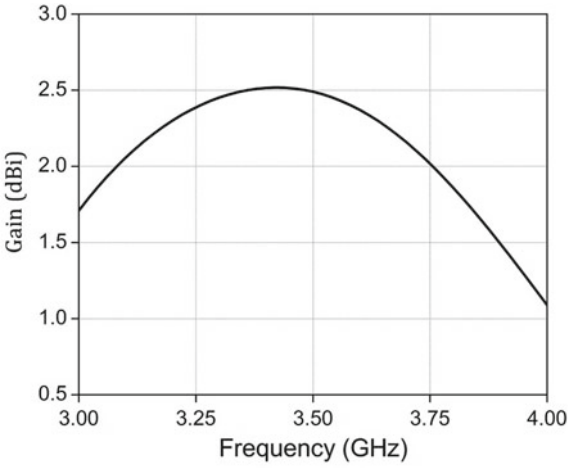

Fig. 4.18 Peak gain when port 2 is activated

4.5 Co-design with a Compact Monopole

4.5.1 Corner Bent mmWave Array with Truncated Aperture

As with the earlier example, the microwave-millimeter wave antenna assembly has two separate elements operating at their respective frequencies. The millimeter wave design is like that of the design presented in Sect. 3.5.1, the only difference here is the truncated aperture of the antenna. The schematic is illustrated in Fig. 4.20a. As observed in the figure, width of the antenna is 27.8 mm which is achieved by truncating one of the non-radiating edges of the corner most radiator of the corner bent array. For each radiating element, only about 0.5 mm clearance is required

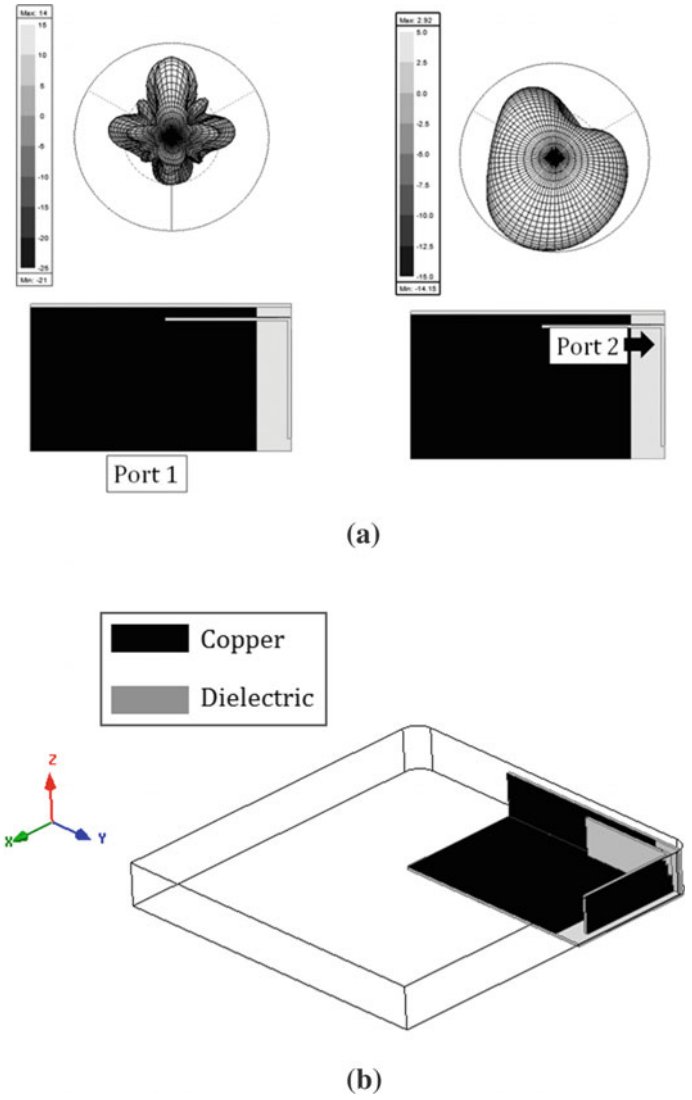

Fig. 4.19 **a** 3D patterns when different ports are activated, **b** typical integration within a Smartphone

along the radiating edge for a reasonable beamforming so that the truncation along the non-radiating edge would not hamper the aperture performance much. It must be observed that only the corner element's edge is truncated which also keeps the deterioration to the minimum. The same logic is not implemented on the opposite end of the truncated element to have minimal influence on the electrically small microwave antenna. The corner bent array demonstrated here is only for illustrative

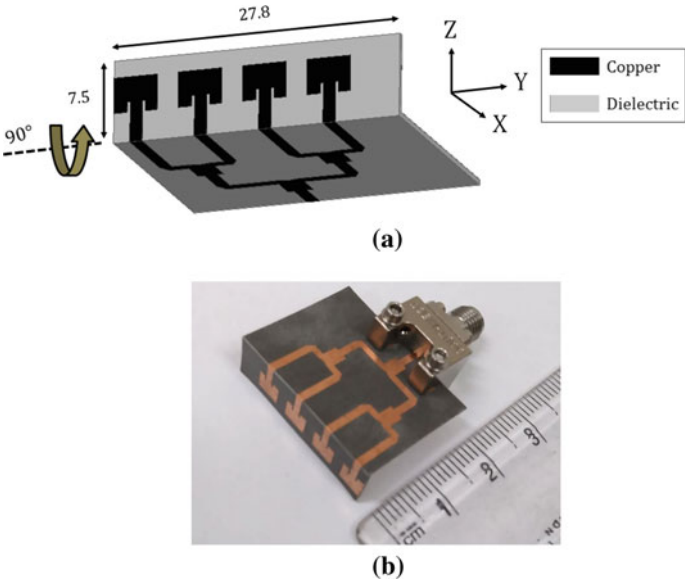

Fig. 4.20 **a** Schematics of corporate fed array: Corner bent version (All dimensions are in mm), **b** photograph of the fabricated prototype

purpose, the same could be replaced by any flexible corner bent radiator, which could be panel mounted but has a unidirectional hemispherical beam.

The substrate choice and feed network design is identical to that of the array presented in Sect. 3.4.1. The corner bent fabricated prototype with end-launch connector mount is shown in Fig. 4.20b. Additional solder is necessary to reinforce the strained ground plane at the edge. A thinner substrate, such as 5 mil or 10 mil would have performed better, as far as the bending is concerned with a consequent increase in cost of production and a decrease in the impedance bandwidth. The truncated edge of the presented antenna could be aligned with one of the corner-most edges of the smartphone which offers minimal interaction with the user's hands. The electrically large ground plane of the antenna itself doubles up as a system ground plane, wherein back-end RF electronics could be built upon.

4.5.2 Panel Mountable Microstrip Fed Microwave Antenna

The second antenna of the microwave-millimeter wave antenna system is the microwave antenna. The chosen carrier frequency for this illustrative example is 3.5 GHz, whose half-wavelength in free space is close to 43 mm. Imagine a half-wavelength dipole of length 43 mm, this dimension is feasible in one of the edges

of the mobile device. The length does not hint the dimension of the width, which in turn decides the impedance bandwidth as observed in the previous Section.

In this example, microstrip feeding technique is explored. The proposed antenna's schematic and its corresponding fabricated prototype are shown in Fig. 4.21a, b respectively. The antenna is a microstrip fed modified monopole antenna design with a partial or truncated ground plane. The microwave antenna is also designed on Rogers 5880 substrate with 20mil thickness, like its millimeter wave counterpart. The choice of substrate is not very critical in the microwave regime as the radiator is electrically small, hence poor radiation efficiency by nature. The element has a tapered feeding line which is integrated with an impedance transformer to the primary monopole radiator. The truncated ground plane is incorporated to enhance impedance bandwidth of the presented antenna. The width of the antenna is 3.5 mm (or 0.035 λ at 3.5 GHz), which is lesser than the panel height hence this element could be

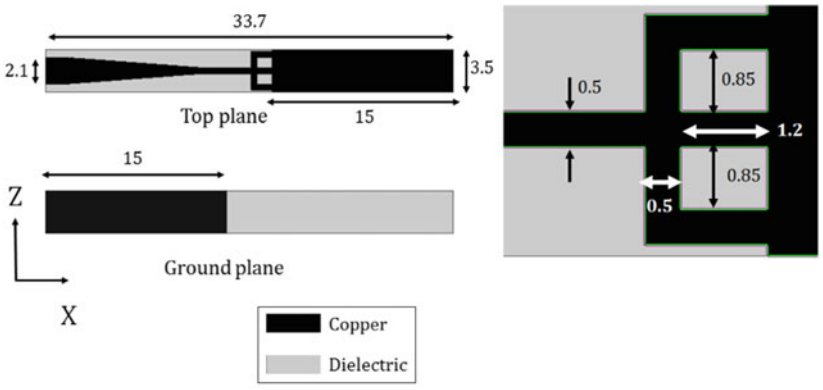

(a)

(b)

Fig. 4.21 **a** Schematics of microwave monopole (All dimensions are in mm), **b** photograph of the fabricated prototype

vertically mounted beneath the smartphone casing. The antenna is X-polarized, with reference to Fig. 4.21a. The presented antenna is very sensitive to the dimension of the radiator and that of the truncated ground plane, this indicates that large metal rim or the system ground plane must be maintained at a strategic location to prevent detuning of this antenna. Bending or conforming of this antenna is not essential as the width is half of the panel height. Furthermore, bending of the ground plane might detune the element.

4.5.3 Panel Mountable Antenna Assembly

The co-design solution for this example is simple and straight-forward. The schematics of the co-designed antenna assembly is demonstrated in Fig. 4.22a. Here the mmWave antenna array of Sect. 4.5.1 is orthogonally placed with the electrically compact microwave antenna of Sect. 4.5.2. The edge of the microwave antenna could be attached to the extended dielectric portion of the millimeter wave antenna array,

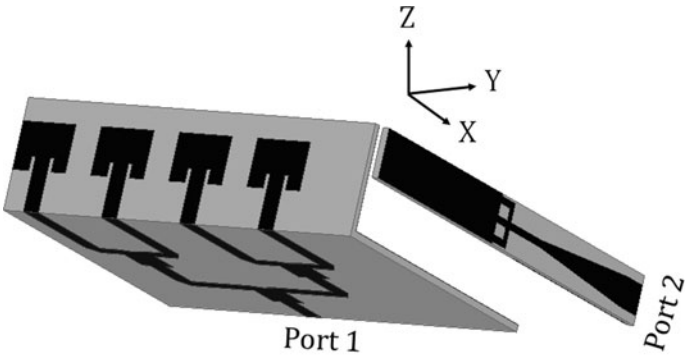

(a)

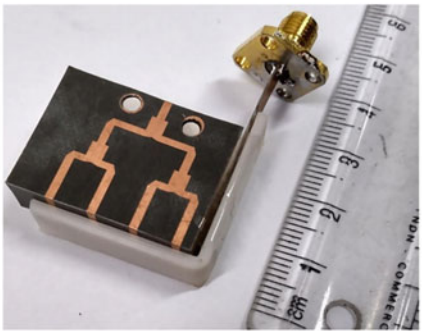

(b)

Fig. 4.22 **a** Schematics of the assembled antenna, **b** photograph of the fabricated assembly

without any deterioration in the respective domains. The fabricated antenna system is shown in Fig. 4.22b, the microwave antenna is connected to a SMA connector with flat pin and the mmWave antenna would be mounted with an end-launch connector. mmWave antenna also could be integrated with a SMA connector with a thin tin solder, this results in mild increase in the impedance mismatch at port 1. Both the antennas are fastened to a 3D-printed smartphone mock-up. The performance metrics characterized in this sub-section would be of this antenna assembly.

The 10-dB input impedance bandwidth of microwave antenna is from 3.22 to 3.6 GHz or 11.1% as per the simulated result as observed in Fig. 4.23a. The measured curve looks almost flat, less than 15 dB across the band. This could be attributed to the soldering error with the standard SMA connector. The width of the antenna is

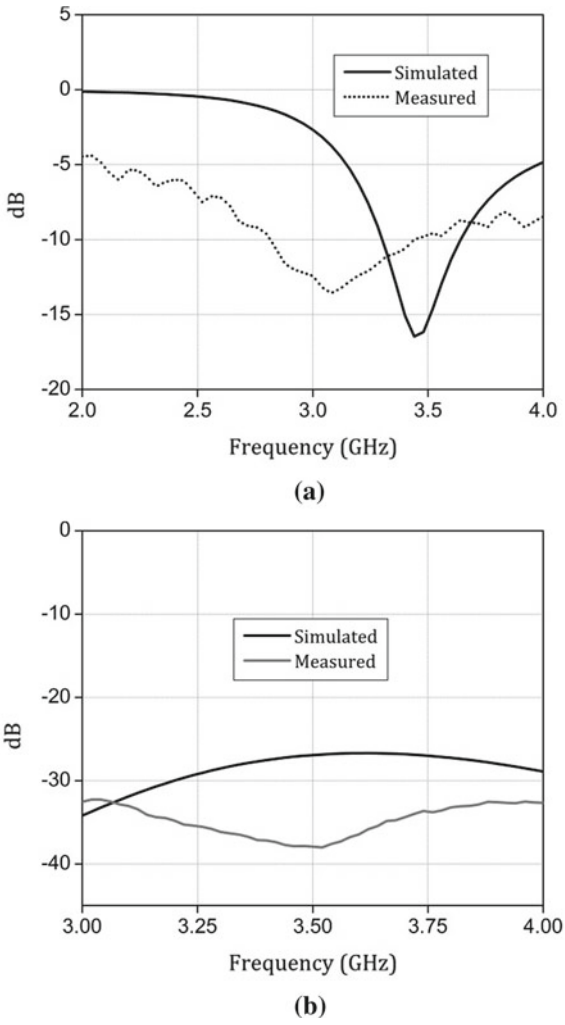

Fig. 4.23 S-parameters in the microwave domain, **a** input reflection coefficient, **b** mutual coupling

3.5 mm, which is lesser than the diameter of the dielectric portion within the SMA connector, hence additional solder was used to create contact between the rim of the SMA connector and the partial ground plane of the microwave antenna. This problem could be solved using either mini-SMA connector or a compact end-launch connector. The conventional end-launch connector used for port 1 cannot be used with port 2 as the microwave antenna's ground plane needs to be laterally extended leading to downshifting of the resonant frequency. The impedance characteristics of the microwave antenna is like that of the stand-alone element, which means that the presence of the mmWave antenna has minimal influence on the S-parameters of port 2 in the low frequency. Mutual coupling between the ports is less than 25 dB in the 3–4 GHz band, as observed in Fig. 4.23b. The measured values are lesser than the simulated values due to the placement errors of the assembled antenna system.

The co-polarized radiation patterns when port 2 is activated is illustrated in Fig. 4.24, it is quasi-omnidirectional, like any electrically small, printed monopole. The patterns are almost unaltered by the presence of the mmWave antenna. The reason is that the mmWave antenna does not have any sub-harmonic modes at least in the 3 to 4 GHz band. The placement of the mmWave antenna is orthogonal with respect to the radiating axis of the microwave antenna. The other reason due to poor interaction between the two ports in the low frequency is the orthogonal polarization.

On the other end of the spectrum, $|S_{11}|$ is almost identical to that of the stand-alone element as observed in Fig. 4.25. Mutual coupling is also below 40 dB. The measured mutual coupling magnitude seems to be higher than the simulated values in the higher spectrum, this could be attributed to the alignment error. The simulated and measured patterns of port 1 is illustrated in Fig. 4.26, which is identical to its stand-alone counterpart. As the radiating aperture is orthogonal to that of the microwave radiator, the mmWave patterns are unharmed by the presence of the low frequency antenna.

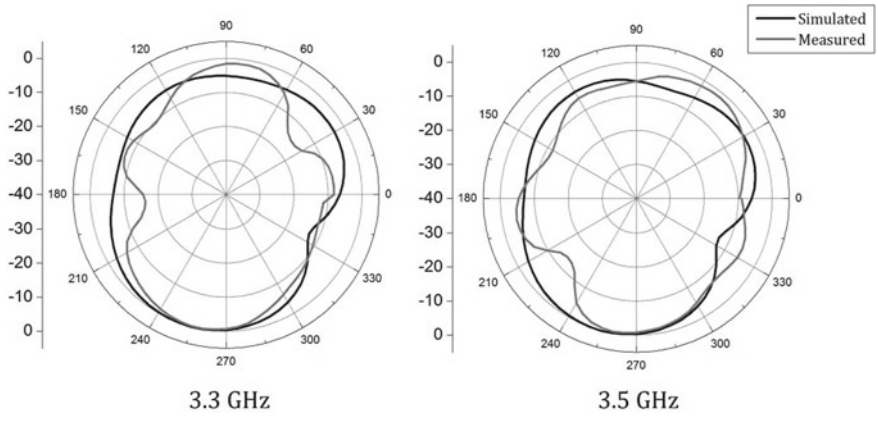

Fig. 4.24 Radiation patterns of the microwave antenna

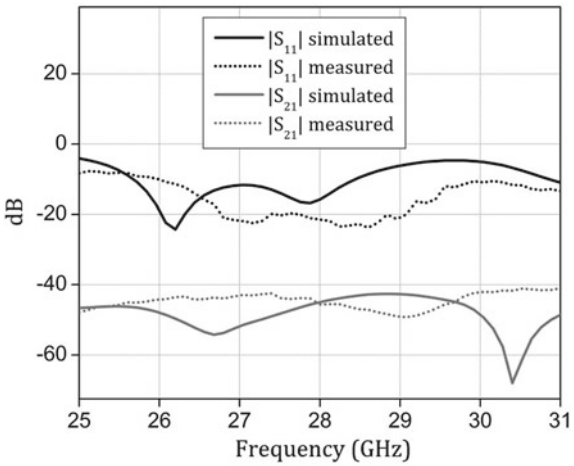

Fig. 4.25 S-parameters in the mmWave domain

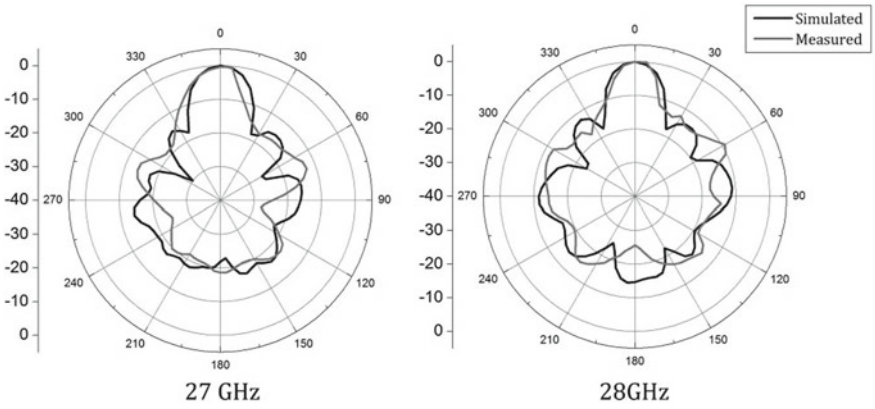

Fig. 4.26 Radiation patterns of mmWave antenna

The slightly higher side-lobe level at 28 GHz might be due to the discontinuity of the truncated aperture. Figure 4.27 illustrates the peak gains for both the ports. The correlation between beamwidth and gain is apparent from this graph.

3D patterns with respect to the antenna assembly are illustrated in Fig. 4.28a, the narrow beam-wide beam for mmWave-microwave is evident. A typical placement of the presented antenna system with a commercial smartphone is shown in Fig. 4.28b. As with the previous design, the antenna assembly fits well, and this could be placed on either corner of the smartphone.

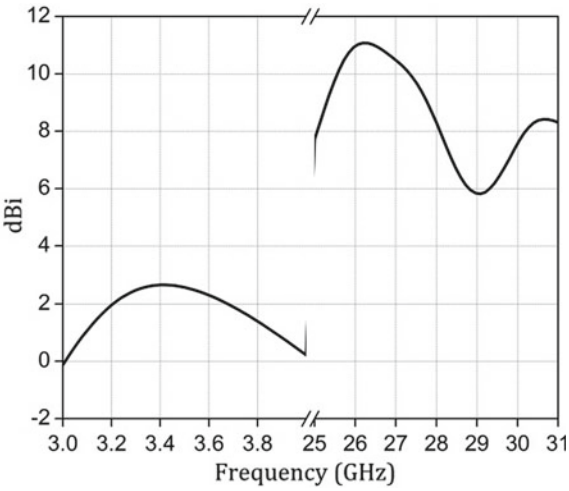

Fig. 4.27 Peak gain of both microwave and mmWave antennas

4.6 Overlapped Co-design of Microwave and mmWave Antennas

4.6.1 Constituent Antennas of the Antenna Assembly

Like the previous Sections, the design presented in this Section also needs two distinct antennas operating independently in the microwave and millimeter wave domains. In this design, the concept of overlapped ground is investigated and characterized. The schematics of the mmWave antenna is illustrated in Fig. 4.29, this design is like the one presented in Sect. 3.6. It is designed on F4B substrate which has a dielectric constant of 2.6 with a corresponding loss tangent of 0.001. These parameters are like the previously designed mmWave antennas in this book. The thickness of the chosen substrate is 20 mil or 0.508 mm, which ensures minimal dimensions when plugged into the panel of a commercial smartphone. The feed is a standard 50 Ω line which is connected to the radiating aperture through an impedance transformer. The width of the primary antenna is 5 mm, hence this design could be vertically mounted for the intended application. It must be noted that any broadside antenna with electrically compact width would serve the purpose. The current choice of design is for illustrative purpose only. For instance, a wideband aperture coupled antenna would also work in this context. A simple patch antenna with truncated width would also work at the cost of reduced impedance bandwidth.

The schematic of the microwave antenna is illustrated in Fig. 4.30, the design is like the microwave antenna of Sect. 4.5. The radiator length is reduced to achieve impedance matching in the overlapped ground context. The width of the antenna is only 3.5 mm, which also supports vertical mounting of the microwave antenna.

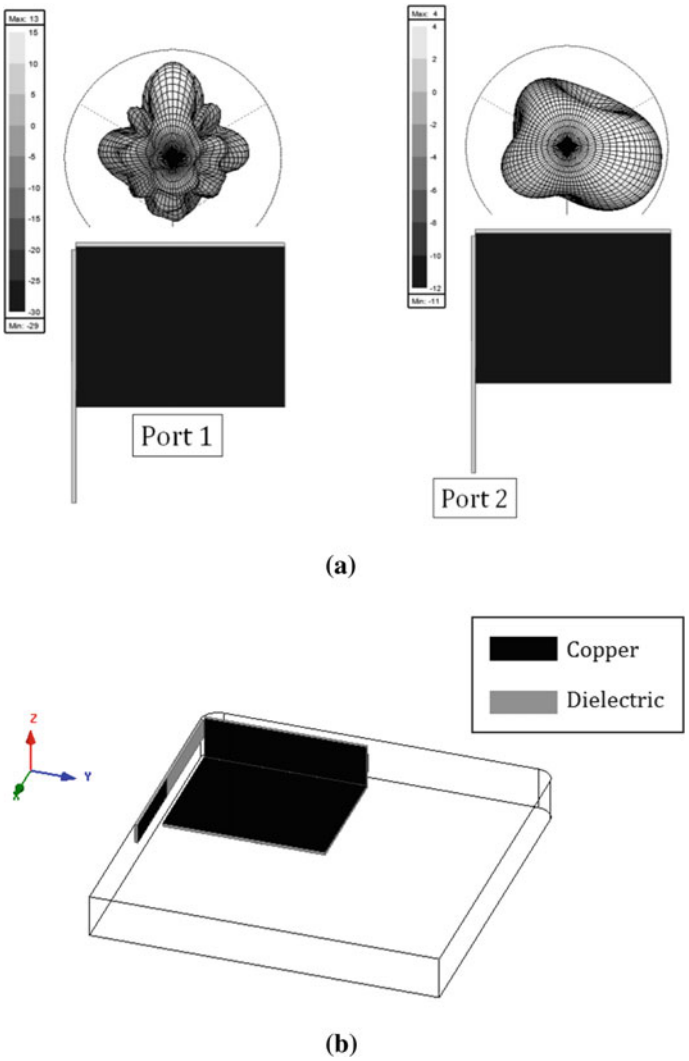

Fig. 4.28 **a** 3D patterns at different frequencies of the assembled antenna system, **b** typical placement of the antenna system within the smartphone

4.6.2 Overlapped Co-design of Microwave and mmWave Antennas

The constituent antennas of Figs. 4.29 and 4.30 must be closely packed without any compromise in the respective constituent antenna's characteristics. The proposed overlapped co-design antenna assembly is demonstrated in Fig. 4.31a. The mmWave antenna is mounted over the flipped version of the microwave antenna. In other

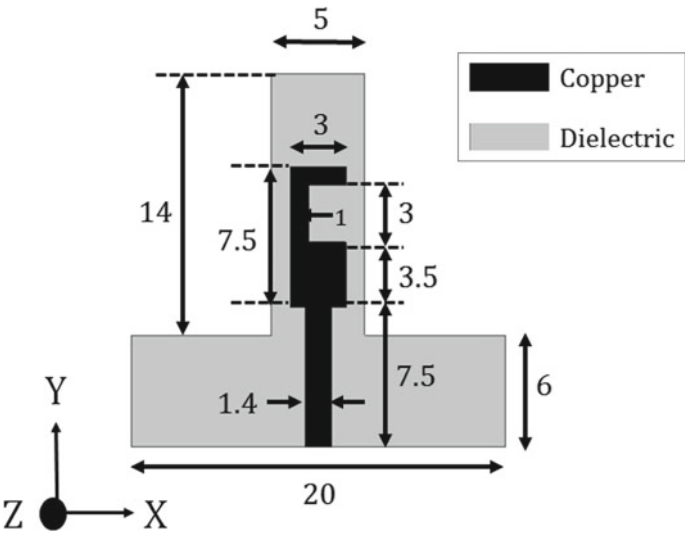

Fig. 4.29 Schematic of mmWave antenna (All dimensions are in mm)

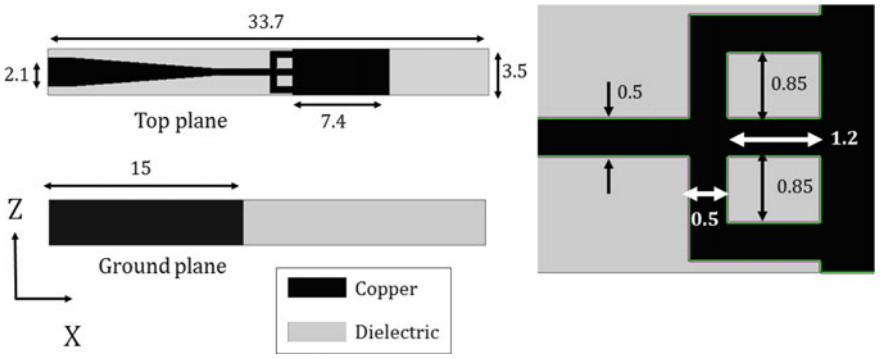

Fig. 4.30 Schematics of the microwave antenna (All dimensions are in mm)

words, the ground plane of the mmWave antenna is attached to the ground plane of the microwave antenna. The concept is clearer in the illustration of Fig. 4.31b. The mmWave antenna would be on top of the microwave antenna with a shared ground. The entire antenna assembly could be manufactured in a single process, with a few tweaks in the manufacturing process flow.

Port 1 feeds the broadside radiator operating in the 28 GHz band and Port 2 feeds the omnidirectional radiator operating in the 3.5 GHz band. An offset of close to 5 mm is introduced at port 2 to achieve impedance matching and clearance for introducing the connector for measurement purposes. The overall length of the antenna assembly

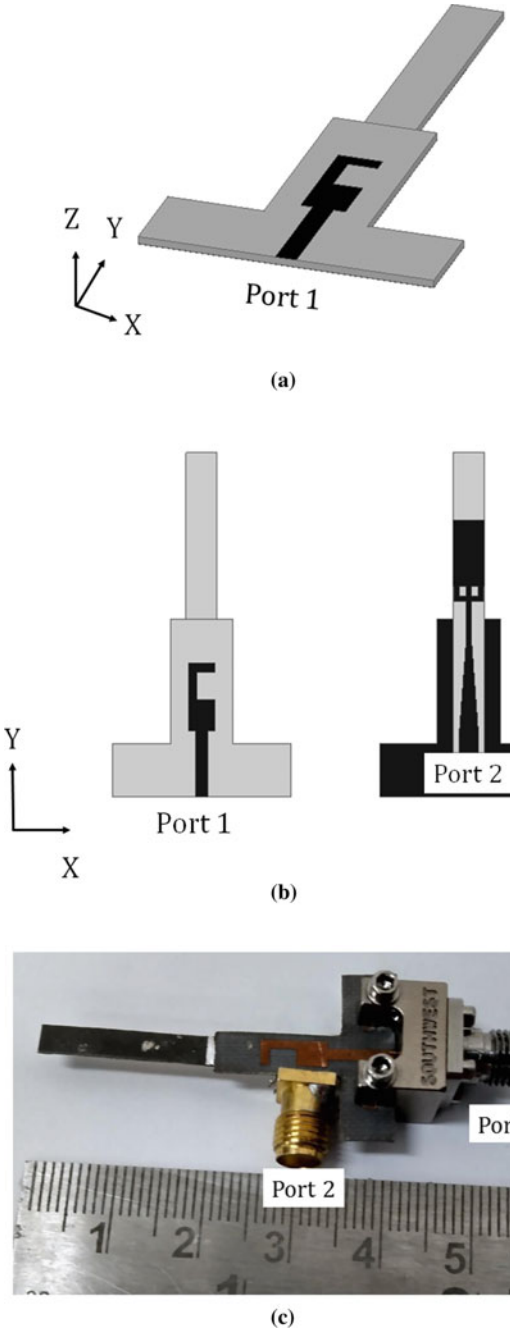

Fig. 4.31 Schematics of the overlapped antenna system: **a** isometric view, **b** top and bottom view, **c** photograph of the fabricated prototype

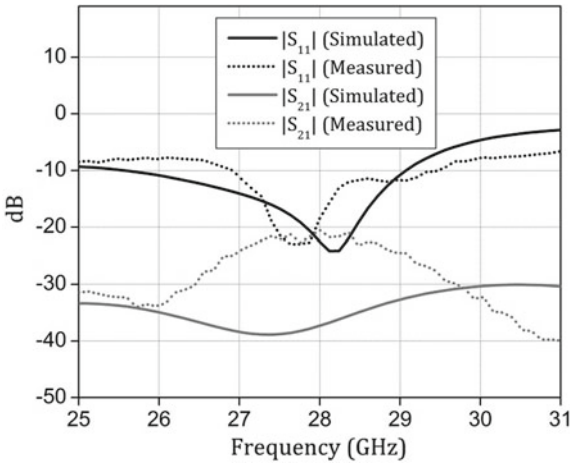

Fig. 4.32 S-parameters of the assembled mmWave antenna system

is 32.7 mm with a corresponding width of 5 mm. The fabricated and assembled prototype is shown in Fig. 4.31c. Both the antennas were individually fabricated by chemical etching and attached using silver epoxy. The end-launch connector is mounted for mmWave port 1 measurement and SMA connector is soldered orthogonally to the microwave antenna (Port 2). It is clear from the photograph that the presented antenna assembly is electrically and physically compact to operate at 3.5 GHz and 28 GHz. An extender cable could have been used for port 2 measurement for better accuracy.

The S-parameters of the mmWave antenna within the presented antenna assembly is illustrated in Fig. 4.32. The input impedance bandwidth is from 25.5 GHz to 29 GHz, translating to a fractional impedance bandwidth of 12.8%, the impedance characteristics is like that of the stand-alone mmWave antenna. These values prove that the shared ground with microwave antenna has minimal influence on the impedance characteristics of the mmWave antenna. As the microwave antenna is mounted beneath the mmWave antenna's ground plane, the radiating aperture has negligible interference from the microwave element.

As observed, mutual coupling is less than 20 dB across the operating band. The measured mutual coupling is higher than the simulated values due to fabrication and assembly errors, especially the proximity of the two connectors, as evident in Fig. 4.31c. The input reflection coefficient in the mmWave domain would be maintained for any complete ground broadside radiator. In other words, the overlapped ground design could be generalized for any broadside mmWave radiator with complete ground plane and an electrically compact microwave antenna with an adequately large ground plane.

The broadside radiation patterns in the mmWave frequencies when port 1 is activated is illustrated in Fig. 4.33. Beamwidth is 60° at 28 GHz, with a front to back ratio of greater than 10 dB across the operational bandwidth. the broadside patterns are unidirectional, and these are almost identical to that of its stand-alone counterpart.

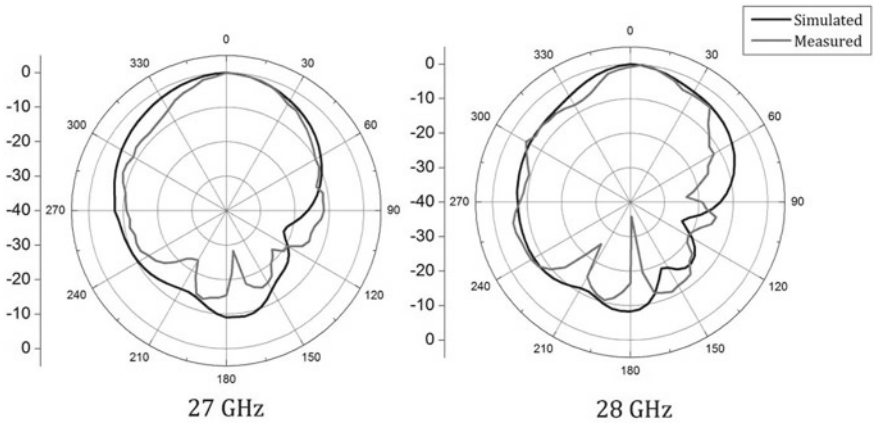

Fig. 4.33 XY plane patterns when port 1 is activated

As the microwave antenna is attached to ground plane of mmWave radiator, the radiating beams are unidirectional and broadside. The patterns are X-polarized (with reference to Fig. 4.31b), which means that vertically polarized radiation could be achieved when the antenna assembly is mounted for commercial application. The forward gain for port 1 is 6.7 dBi at 28 GHz, which is a reasonable value given the electrically compact size of the element as shown in Fig. 4.34. The input reflection coefficient of the microstrip fed monopole antenna is illustrated in Fig. 4.35. This is the stand-alone version of the antenna which operates at 4.2 GHz. as the element has a reduced radiator with a truncated ground plane, it operates at 4.2 GHz. Once this monopole is integrated with the mmWave antenna, the resonance shifts downward

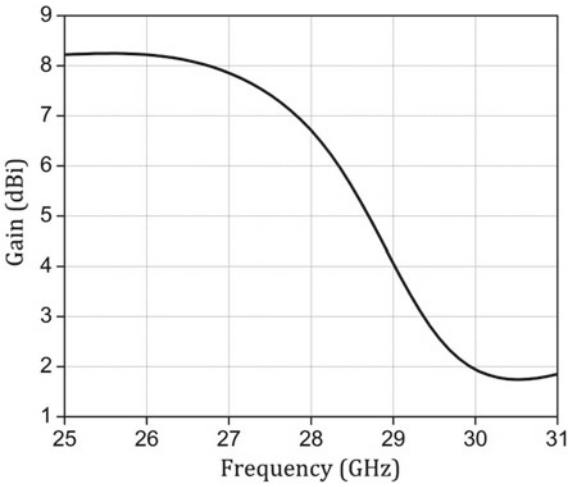

Fig. 4.34 Forward gain when port 1 is activated

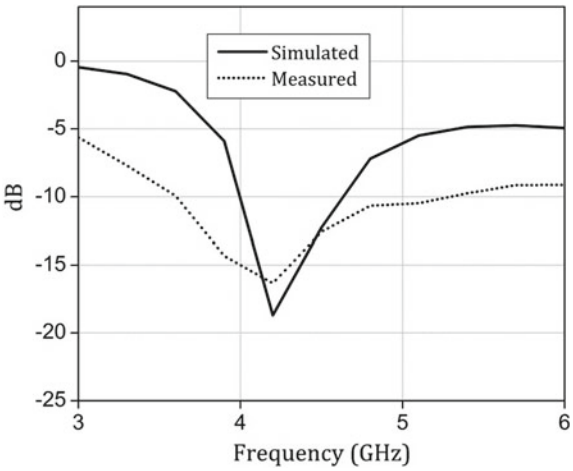

Fig. 4.35 Input reflection coefficient of the stand-alone microwave antenna

to 3.5 GHz, as the ground plane of the monopole is extended, effectively increasing the operating wavelength of the microwave monopole.

The S-parameters of port 2 of the antenna assembly is illustrated in Fig. 4.36. The input impedance bandwidth is from 3.3 GHz to 3.6 GHz or 8.7%, with a mutual coupling less than 20 dB across the band. Measured mutual coupling is lower than the simulated values as the bulky feeding connectors from the VNA (Vector Network Analyzer) hamper the measurement integrity. The simulated and measured radiation patterns in the microwave domain is illustrated in Fig. 4.37, these patterns are expected, given the electrically small (0.38 $\lambda \times 0.06\ \lambda$, computed at 3.5 GHz) nature of the antenna element.

The 3D radiation patterns for port 1 (28 GHz) and Port 2 (3.5 GHz) are shown in Fig. 4.38a. These patterns meet the design requirements mentioned in Sect. 4.2. A

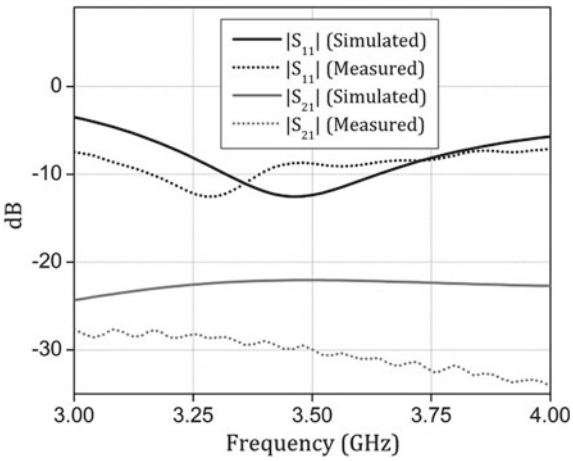

Fig. 4.36 S-parameters of the assembled microwave antenna system

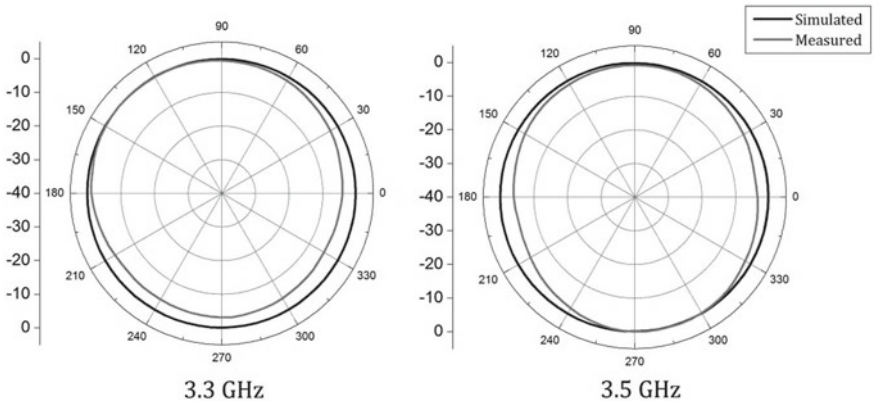

Fig. 4.37 XY plane patterns when port 2 is activated

typical placement example of the proposed antenna module in a commercial smartphone environment is demonstrated in Fig. 4.38b. The broadside mmWave antenna must coincide with the panel of the smartphone to radiate away from the user at 28 GHz and beyond. The proposed antenna module could be placed along the shorter edge or the longer edge of the smartphone depending on the data mode requirement.

4.7 Uniplanar Design of Broadside mmWave Antenna and a Microwave Monopole

Previously presented topologies of co-designs had multiple substrates and would complicate fabrication and assembly. In this Section, a uniplanar design would be presented. Both the antennas would share a single substrate with two distinct feeds for the low frequency and high frequency operations. The proposed antenna is illustrated in Fig. 4.39. The two-port antenna system is realized on F4B substrate with a thickness of 20 mil. Port 1 feeds the broadside-unidirectional mmWave radiator and Port 2 feeds the omnidirectional microwave radiator. The top plane of the design is illustrated in Fig. 4.39a. Port 1 feeds a 50 Ω line connected to an impedance transformer, which in turn feeds the X-polarized radiator; this design is like the mmWave antenna of Sect. 4.6.1. This element also could be replaced by any mmWave planar antenna which meets the dimensional and radiation requirements illustrated in Sect. 4.2. The width of the antenna is 5.5 mm or 0.51 λ computed at 28 GHz. The dielectric elongation X axis near the feeding port is for the end-launch connector mount and could be truncated for real-world deployment without any deterioration in the performance metrics. The compact width of the mmWave antenna restricts the achievable gain of the broadside element. The width also restricts the impedance bandwidth since the effective radiating volume is directly correlated with the impedance bandwidth.

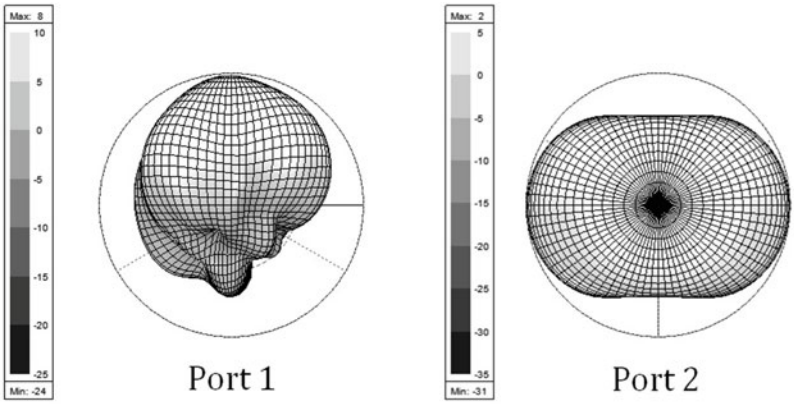

(a)

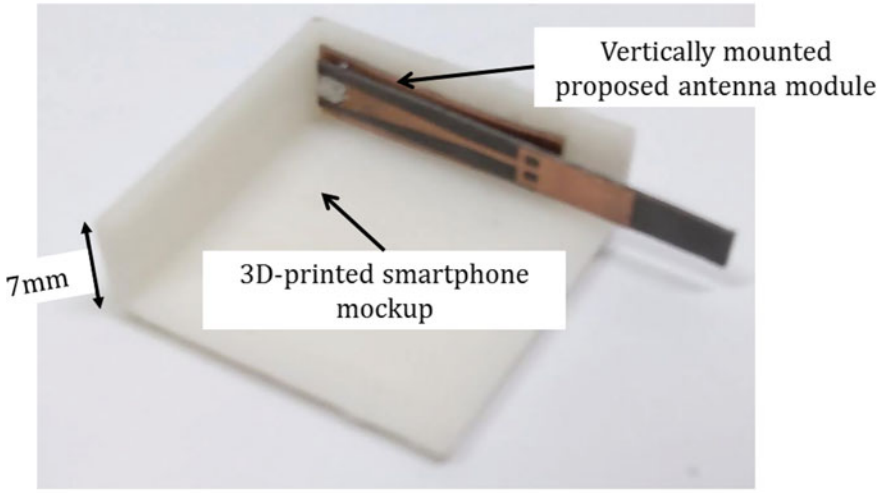

(b)

Fig. 4.38 **a** 3D patterns when different ports are activated, **b** placement of the antenna in a typical smartphone mockup

Ground plane under the entire geometry of the mmWave antenna is completely metallic to aid a hemispherical unidirectional beam.

Port 2 is connected to the microwave monopole antenna as illustrated in Fig. 4.39a. The orthogonal extension of the feed line is purely for measurement purposes. The microstrip feed of port 2 could also be replaced by a coaxial feed with modified integrated transformers. The close to 50 Ω feed line connects to a tapered line feeding the primary monopole antenna.

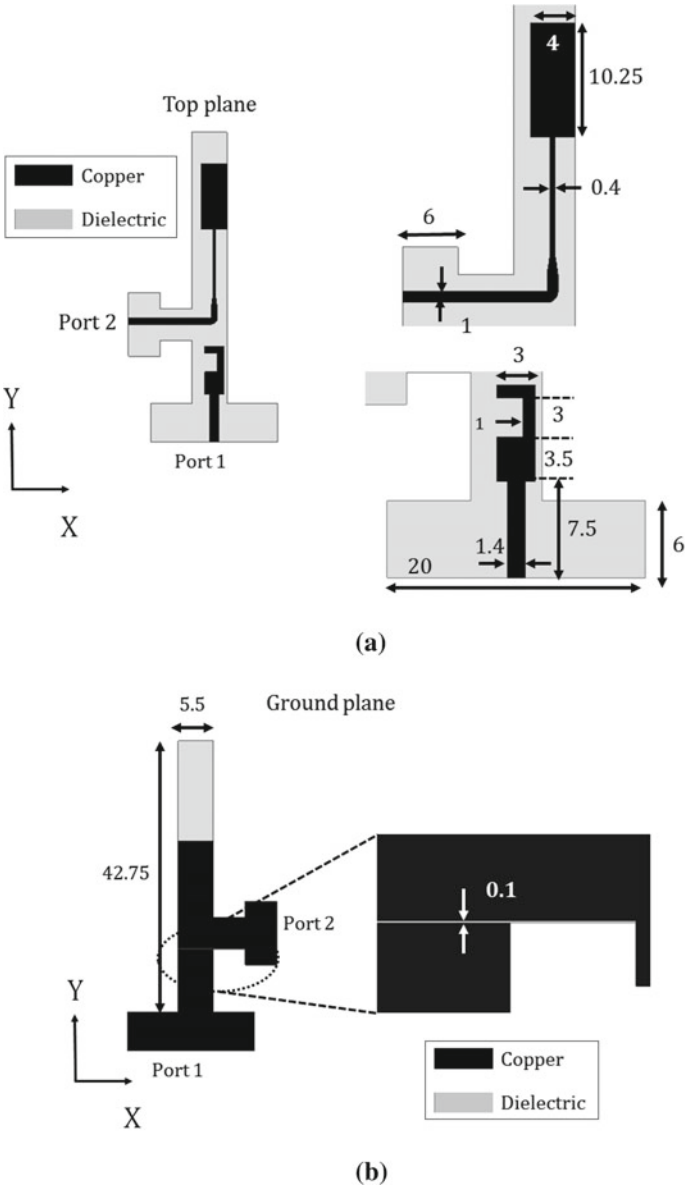

Fig. 4.39 Schematics of the uniplanar antenna: **a** top view, **b** ground plane view (All dimensions are in mm)

The dimensions of the microwave monopole are optimized for the sub-6 GHz band; to be operational in the proximity of the mmWave radiator. The minimum distance between the two antennas is 3.5 mm (or 0.04λ at 3.5 GHz and 0.32 λ at 28 GHz) which indicates the electrical proximity of the microwave and mmWave antennas. The feeding line of port 2 could be further brought closer to the mmWave antenna, this would compromise the mutual coupling between the two ports. The microwave antenna of the uniplanar design is sensitive to the ground plane; hence an electrically small slot is introduced in the ground plane as illustrated in Fig. 4.39b, the 0.1 mm wide slot prevents detuning of the microwave antenna without any compromise in the metrics of the mmWave element.

The overall length of the two-port uniplanar antenna system is 42.75 mm, which could be mounted on either edge of the smartphone. The width of the proposed antenna system is compliant with the smartphone panel height, hence supporting vertical mounting with the same plane microstrip feeding. The fabricated prototype along with the assembled connectors is illustrated in Fig. 4.40. The feed lines' extension for connector mounting is clear from the figure. A cylindrical coaxial trace pin SMA connector was used to solder the antenna at port 2, to minimize additional impedance mismatch at this port. No specialized laser cutting tools were used to realize the contour of the uniplanar antenna.

The S-parameters in the mmWave spectrum is shown in Fig. 4.41, the input impedance bandwidth is from 27 GHz to 29.3 GHz, translating to 8.2%. The discrepancy between simulated and measured curves could be due to the deviation of the dielectric constant assumed in simulation and the actual value of the dielectric constant. Nevertheless, the measured impedance bandwidth agrees with simulated value within the limits of experimental and measurement errors. The $|S_{11}|$ of port 1 is like that of a stand-alone wideband broadside antenna. The impedance characteristics is agnostic to the presence of the electrically compact microwave antenna.

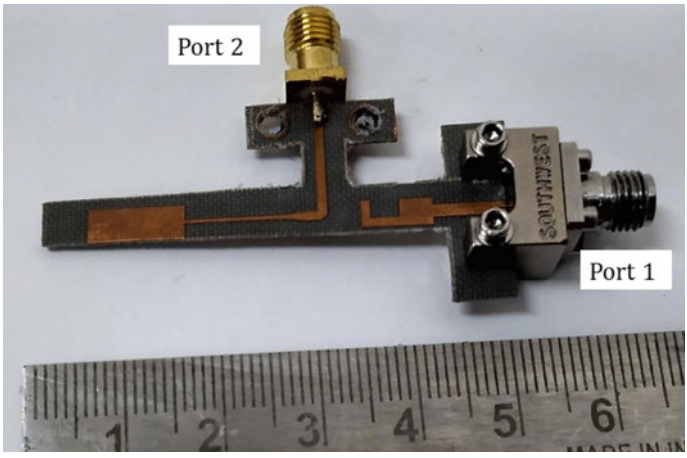

Fig. 4.40 Photograph of the uniplanar antenna

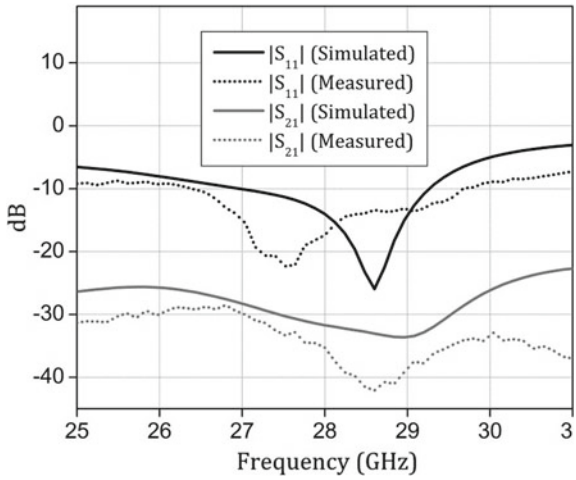

Fig. 4.41 S-parameters of the uniplanar mmWave antenna

Mutual coupling between the two ports is less than 20 dB in the operational bandwidth. The primary reason for low mutual coupling value despite the electrical proximity is that the microwave radiator is not a resonator at 28 GHz. Also, the orthogonal feeding line emanating from port 2 is a poor coupler of energy in the mmWave domain. The broadside patterns when port 1 is activated is illustrated in Fig. 4.42, as the microstrip fed monopole does not influence the radiating aperture of the mmWave element, pattern integrity of the mmWave antenna is maintained throughout the band. Front to back ratio is close to 10 dB even with an electrically small ground plane.

Forward gain is 6.3 dBi at 28 GHz as shown in Fig. 4.43, forward gain is almost independent of the microwave antenna. Gain could be enhanced by widening the

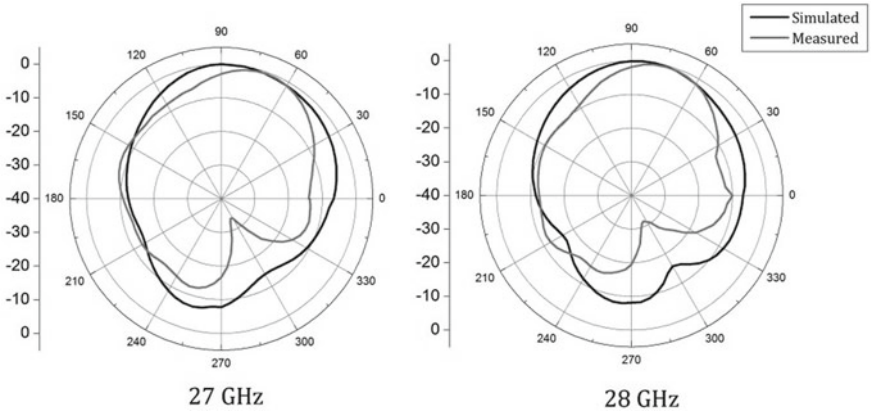

Fig. 4.42 Broadside patterns when port 1 is activated

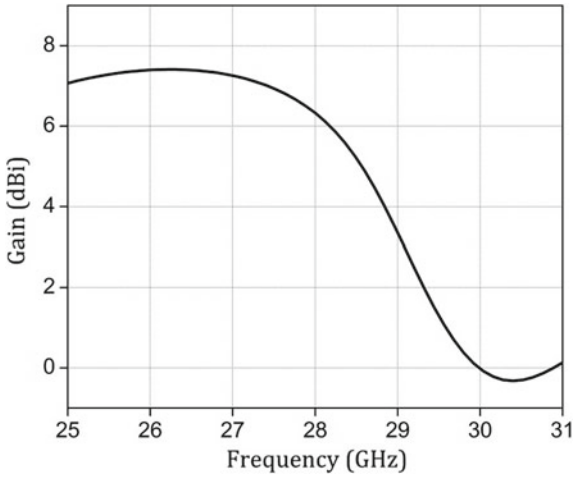

Fig. 4.43 Forward gain of the uniplanar antenna when port 1 is activated

mmWave element, which compromises the dimensional advantage of the proposed antenna. S-parameters in the sub-6 GHz is illustrated in Fig. 4.44.

The impedance bandwidth for port 2 is from 3 to 4 GHz or 26.6% fractional bandwidth. The discrepancy between simulated and measured curves might be due to poor transition from the SMA connector to the orthogonal feed line at port 2. Mutual coupling is less than 30 dB across the band; this could be attributed to the geometry of the mmWave radiator. The mmWave radiator does not have a sub-harmonic resonance at 3.5 GHz, thus leading to low mutual coupling. The patterns are almost omni-directional as observed in Fig. 4.45. Peak gain of the microwave antenna is around 2 dBi at 3.5 GHz as observed in Fig. 4.46. 3D-patterns for different ports activation are illustrated in Fig. 4.47a. The unidirectional-hemispherical pattern of port 1 at

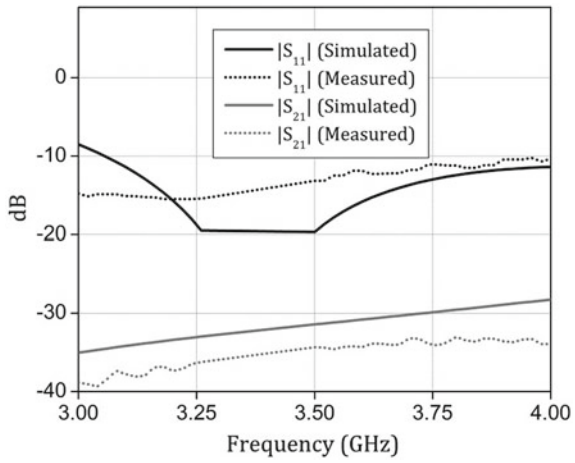

Fig. 4.44 S-parameters of the uniplanar microwave antenna

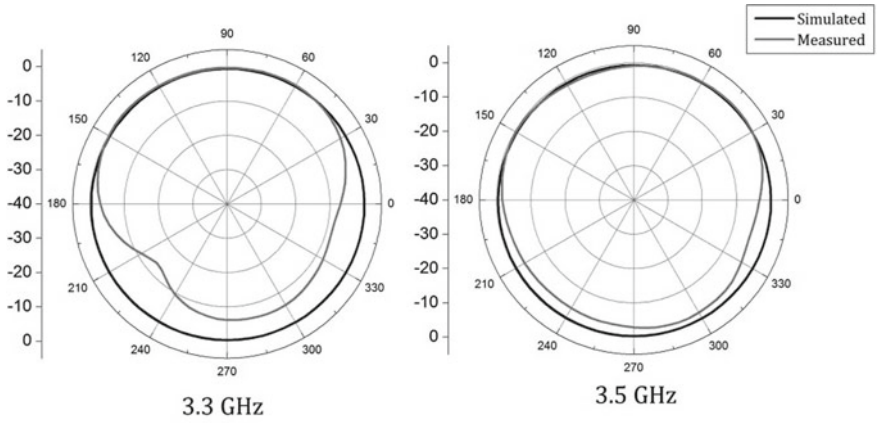

Fig. 4.45 Radiation patterns when port 2 is activated

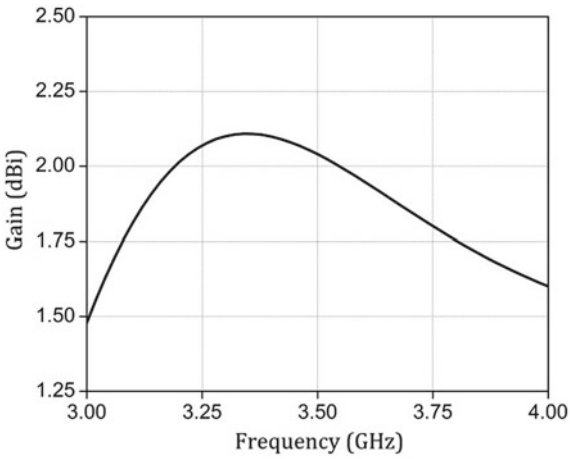

Fig. 4.46 Peak gain when port 2 is activated

28 GHz and omnidirectional pattern of port 2 at 3.5 GHz is evident. Typical placement scenario of the proposed uniplanar antenna system with 3D-printed mock-up is shown in Fig. 4.47b.

4.8 Uniplanar Design of End-Fire mmWave Antenna and a Microstrip Fed Microwave Radiator

In the previous Section, a broadside uniplanar mmWave antenna co-designed with a microstrip fed monopole was investigated. In this Section, an end-fire radiator co-designed with a microwave antenna would be explored. The proposed design is

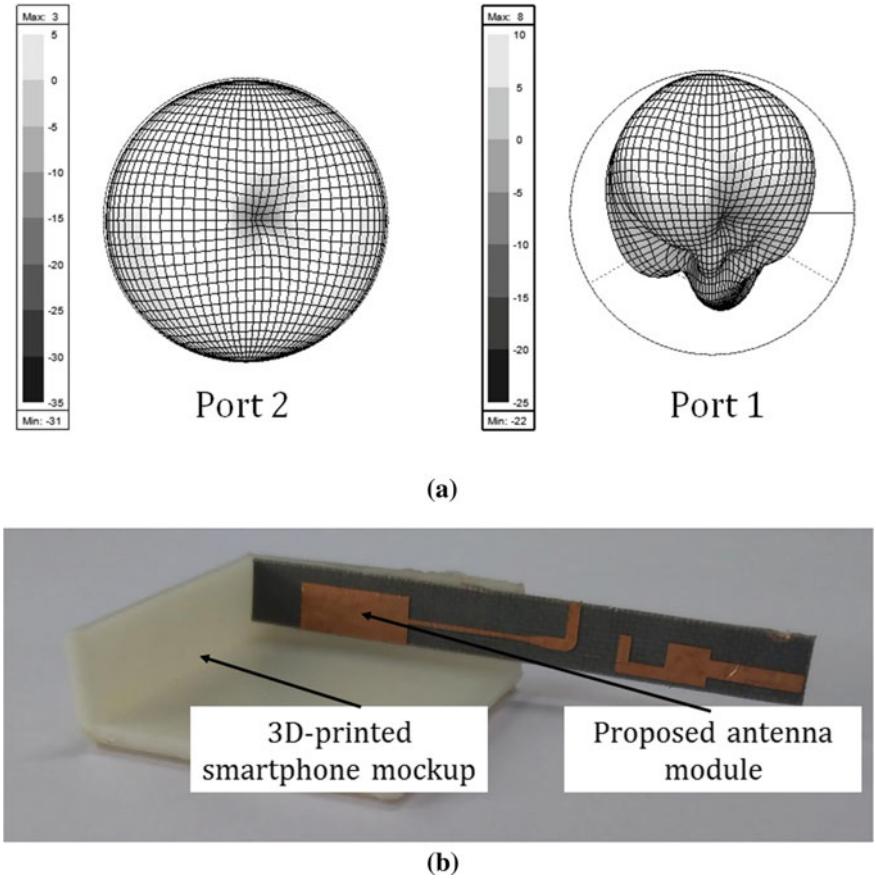

Fig. 4.47 **a** 3D patterns for different port activation, **b** typical placement of the uniplanar antenna in a smartphone mockup

illustrated in Fig. 4.48. Like the previous designs reported in this Chapter, the antenna module consists of two ports: one feeding the mmWave radiator and the other port feeding microwave radiator. The design is realized on F4B substrate with a dielectric constant of 2.6 and a corresponding loss tangent of 0.001, the chosen substrate has a thickness of 20 mil. The lower dielectric constant is preferred for lower surface wave modes leading to higher radiation efficiency in the mmWave band. The dielectric constant choice is not very critical in the microwave domain. Lower dielectric loss tangent is preferable in both the bands.

Port 1 feeds the mmWave antenna which radiates in the end-fire orientation or in the positive X-axis, with reference to Fig. 4.48a, the feeding line is a 50 Ω for the chosen substrate connected to a couple of impedance transformers, clearly visible in the inset of Fig. 4.48a, which is in turn connected to a printed dipole. The dipole is orthogonal with respect to the feed line to facilitate vertical mounting of the

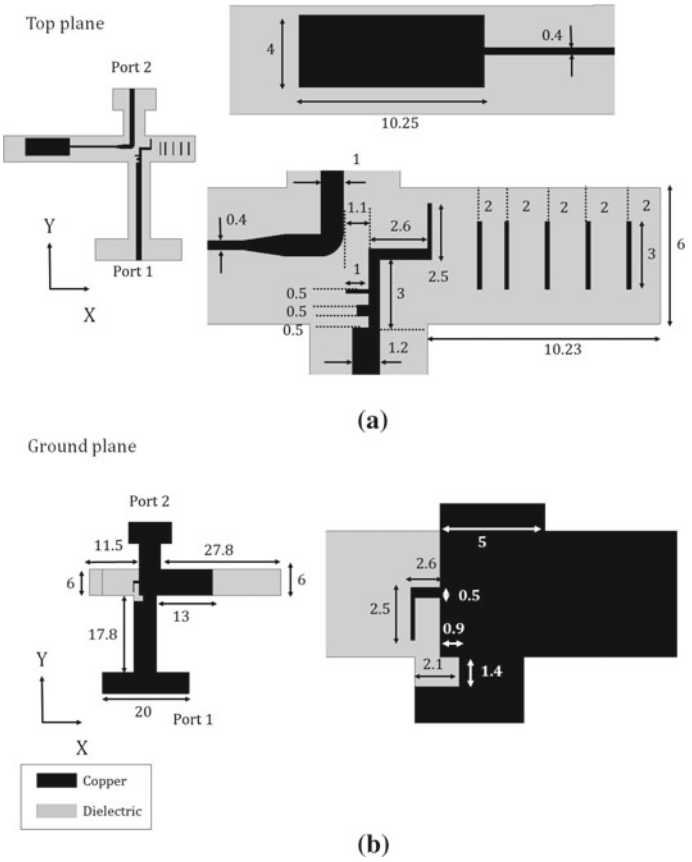

Fig. 4.48 Schematics of the uniplanar co-designed antenna: **a** top view, **b** ground plane view (All dimensions are in mm)

uniplanar antenna. The impedance transformers serve dual purpose of impedance matching and channelizing energy towards the orthogonal direction, with respect to the feedline. The ground plane is illustrated in Fig. 4.48b. The ground plane of the mmWave is shared with that of the microwave antenna. Also, the design of the ground plane is electrically large enough for a high front to back ratio when port 1 is activated. The width of the mmWave antenna is 6 mm, which is less than the standard smartphone panel height. The parasitic directors aid in gain enhancement of the mmWave radiation. The directors could be neglected if a wide-angle beam is necessary at the mobile terminal.

Port 2 feeds the microstrip fed electrically compact monopole antenna operating in the sub-6 GHz domain. The monopole element requires a truncated ground plane, which is realized as a shared ground plane with the mmWave antenna. The additional ground plane beneath the mmWave dipole does not hamper the impedance characteristics of the microwave monopole element. Ground plane of the microwave

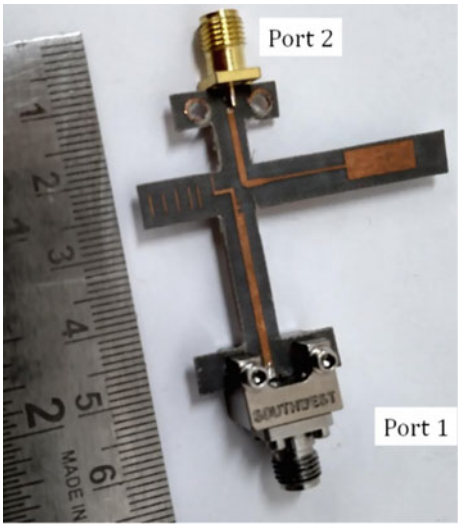

Fig. 4.49 Photograph of the uniplanar co-designed antenna

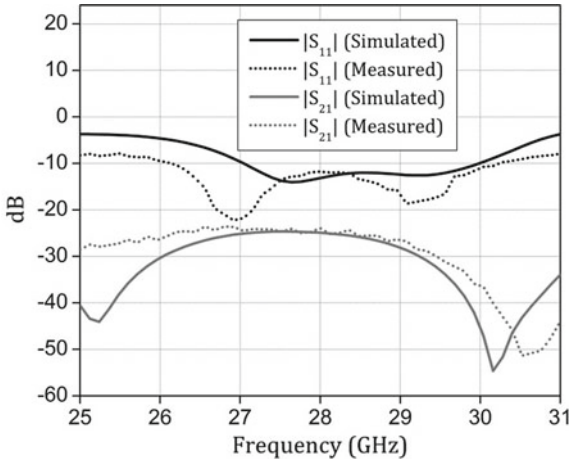

Fig. 4.50 S-parameters of the uniplanar co-designed mmWave antenna

antenna is 13 mm long as observed in Fig. 4.48b. The feeding lines for both the ports are on the opposite sides of the substrate to accommodate the respective connectors for measurement purposes. The minimum distance between the antennas is 1.1 mm, which translates to 0.012 λ at 3.5 GHz and 0.1 λ at 28 GHz, the impedance and radiation characteristics of the elements of both the higher and lower bands are not significantly deteriorated the presence of the other element in proximity. The fabricated prototype with assembled connectors is depicted in Fig. 4.49. As the thickness of the substrate was 20mil, no precision tooling was required to cut the antenna system along the contour.

The input impedance bandwidth of port 1 is from 27 to 30 GHz, translating to a fractional bandwidth of 10.5%, as observed in Fig. 4.50. Wideband is achieved due to the series of impedance transformers and the elongated aperture along the radiating axis of the mmWave antenna. Mutual coupling is less than 30 dB across the entire high frequency band as seen in Fig. 4.50. Low mutual coupling could be attributed to poor coupling between the feeding portion of the printed dipole and the orthogonal feeding line of the microwave antenna.

If the microwave antenna is brought closer to the mmWave antenna, the mmWave element would be detuned in addition to getting specular beam in the end-fire orientation. The end-fire co-polarized patterns when port 1 is activated is illustrated in Fig. 4.51. The discrepancy between simulated and measured values is due to the

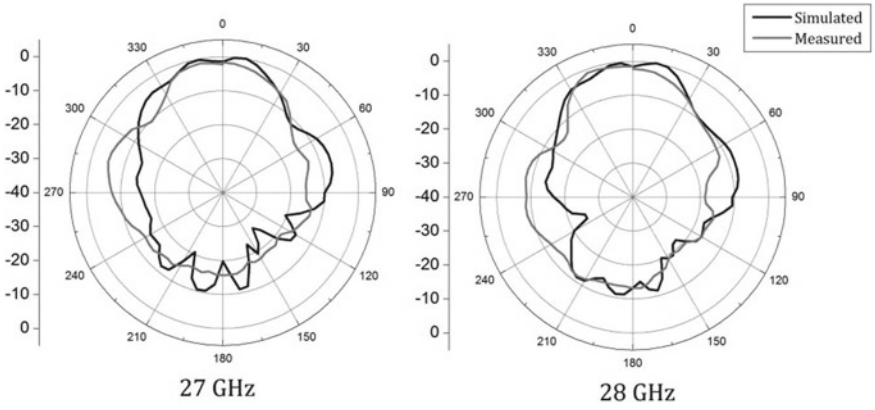

Fig. 4.51 Radiation patterns when port 1 is activated

Fig. 4.52 Peak forward gain of uniplanar antenna when port 1 is activated

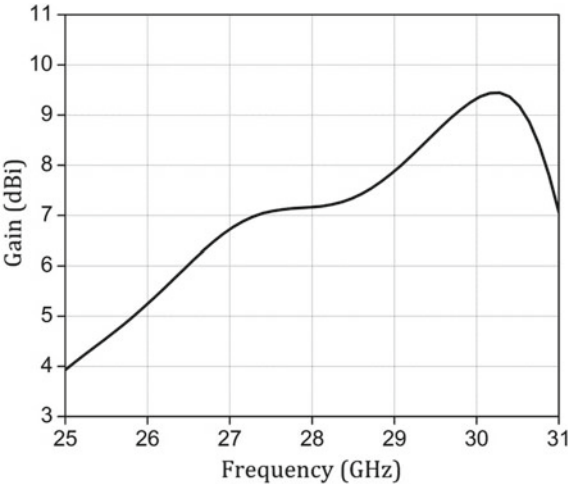

alignment error in the anechoic chamber. It must also be noted that the electrically long feed line makes it difficult to mount and align within the Ka-band anechoic chamber. The pattern integrity of the uniplanar antenna system is like that of the orthogonally fed printed Yagi-Uda antenna as the microwave antenna has minimal influence on the parasitics of the mmWave radiator.

The patterns also suggest that the uniplanar antenna system could be mounted at the edge of the smartphone terminal. The forward end-fire gain is 7 dBi at 28 GHz, which is a reasonably high value given the electrical size of the radiating aperture. Gain could be further increased by adding more directors, at the cost of increased length of the overall antenna system. Forward gain is depicted in Fig. 4.52.

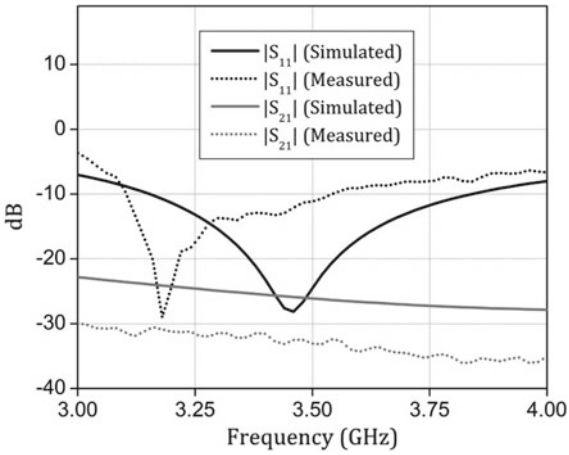

Fig. 4.53 S-parameters of the uniplanar co-designed microwave antenna

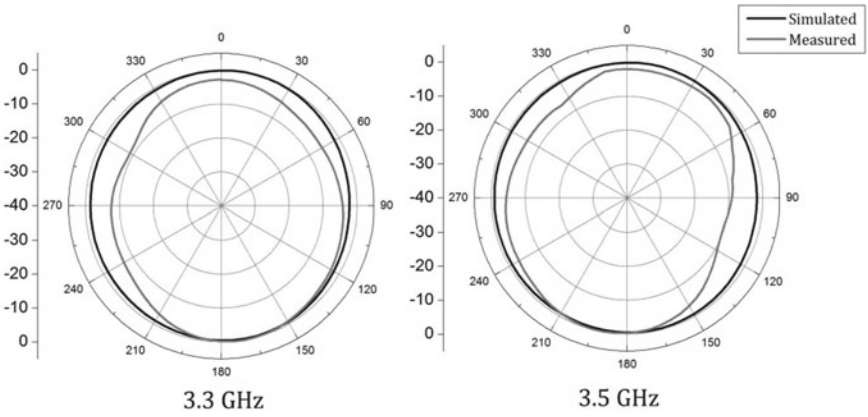

Fig. 4.54 Radiation patterns when port 2 is activated

The S-parameters in the microwave domain is illustrated in Fig. 4.53. 10-dB input impedance bandwidth for port 2 is 3.1 GHz to 3.8 GHz, translating to 19.4%, like the operational characteristics of a conventional truncated ground microstrip fed monopole antenna. mutual coupling is less than 20 dB across the band as the printed dipole would be electrically too small to resonate at 3.5 GHz. Patterns are omnidirectional, as expected from printed monopoles, results are shown in Fig. 4.54.

The discrepancy between simulated and measured results is due to the poor absorptivity of the RF absorbers in the anechoic chamber, especially at oblique incidence. 3D-patterns for port 1 (at 3.5 GHz) and port 2 (at 28 GHz) are illustrated in Fig. 4.55a, the omnidirectional sub-6GHz pattern and unidirectional behaviour at 28GHz is clear. A typical smartphone mounting is illustrated in Fig. 4.55b, note that the feeding lines have been eliminated, this could be the case in a real-world deployment scenario. The

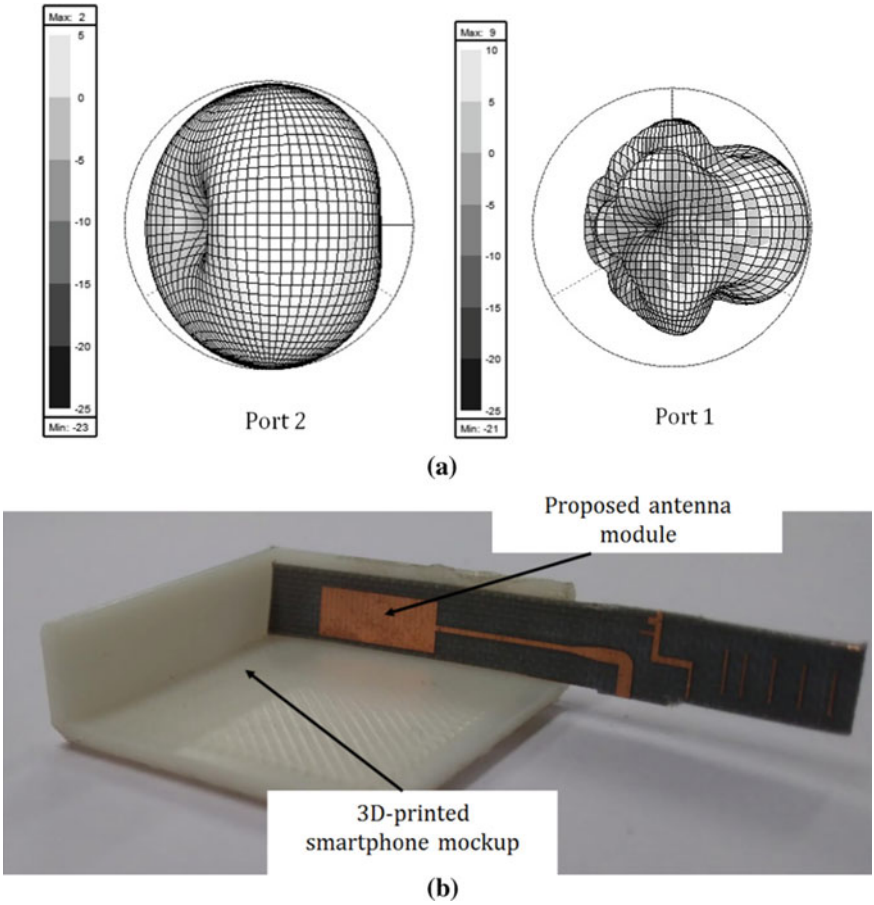

Fig. 4.55 **a** 3D-patterns for different port activation, **b** typical placement of the uniplanar antenna with a smartphone mock-up

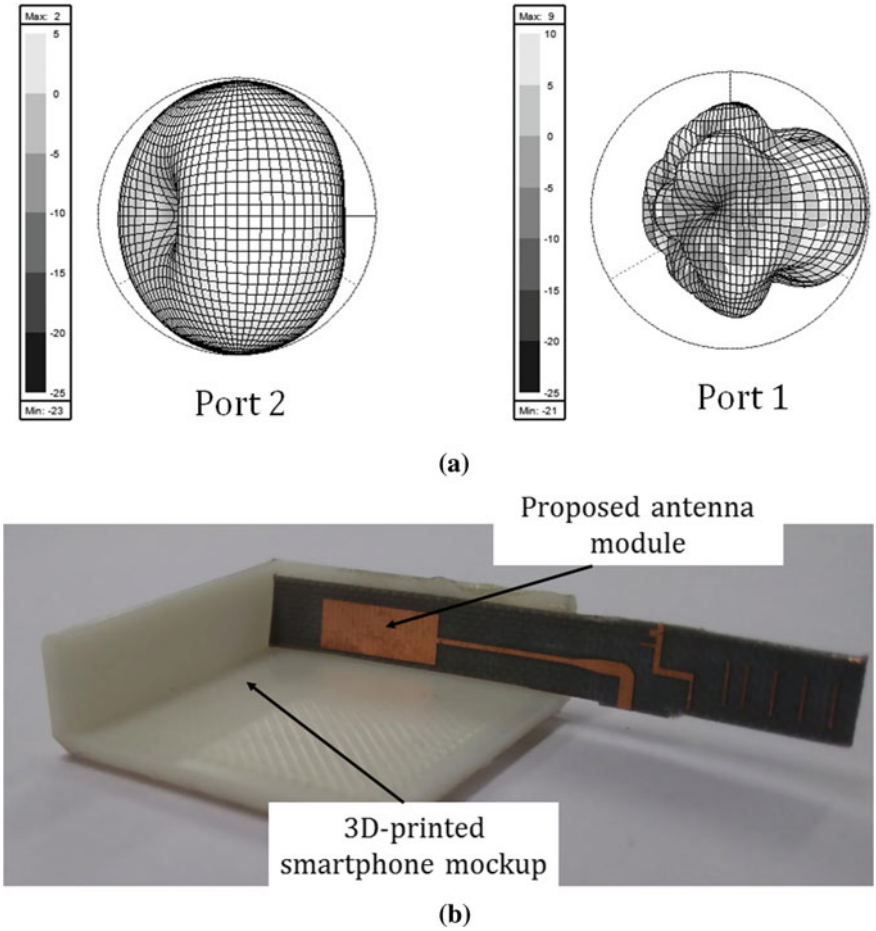

Fig. 4.56 **a** 3D-patterns for different port activation, **b** typical placement of the uniplanar antenna with a smartphone mock-up

end-fire mmWave dipole must coincide with the corner of the smartphone's panel for the mmWave data link to work. The 3D-printed smartphone mock-up has a panel height of 7mm like commercial models (Fig. 4.56).

4.9 Design Guidelines

- The low frequency element must meet the smartphone panel dimensions. Designing sub-6 GHz antennas for smartphones is straightforward, as antenna

engineers in the industry have been doing it since couple of decades. The underlying principle would be to design a modified version of a monopole element and add parasitics to achieve multibands, as dictated by the specific handset. The impedance bandwidth could be compromised depending on the available electrical space within the smartphone panel. It would be preferable to use the same substrate for sub-6 GHz and mmWave antenna designs. This would mean that the microwave element also must be realized on an electrically thin, low dielectric constant substrate. The pattern integrity or the profile of the radiation patterns are irrelevant, as the electrically small antennas would radiate omni-directionally.

- The high frequency antenna also must fit within the smartphone panel. In this case, the antenna must have high gain with a unidirectional beam across the mmWave bands. The placement of the mmWave antennas should be in such a way as to radiate away from the user, when integrated with the smartphone.
- Mutual coupling between the sub-6 GHz antenna and the mmWave antenna should be as low as possible in both the frequency domains. The mmWave antenna's influence on the microwave antenna would detune the element without degradation in the radiation patterns. On the other hand, if the microwave antenna is placed electrically (for wavelengths calculated in the mmWave regime) close to the mmWave antenna, the performance metrics of the high frequency antenna would be severely degraded. Hence, the mmWave antenna placement and design should be a higher priority compared to its sub-6 GHz counterpart. Hence, the co-design flow would be to first design the mmWave antenna as per the 5G requirements and extend the same dielectric substrate to accommodate the microwave element.

4.10 Scope for Research

- Multiband design: if a single antenna could be designed, within the dimensional constraints of a handheld mobile device, that works at both microwave and mmWave bands, this design would be highly appreciated by the mobile industry. The catch is that the antenna should radiate omni-directionally in the microwave band and uni-directionally in the mmWave band. One solution could be to design an electrically small antenna in the microwave domain, which would simultaneously work as a traveling wave element in the mmWave domain. Another alternative could be to design an end-fire antenna in the mmWave domain and add parasitics which are electrically favourable to create resonance in sub-6 GHz bands, without hampering the beam integrity of the mmWave end-fire element.
- A dual port shared radiator could be imagined, wherein the electrically large (computed at mmWave frequencies) radiator would create a unidirectional beam and the same radiator behaves as an electrically small (computed at microwave frequencies) omnidirectional element.

4.11 Conclusion

In this Chapter, need for co-designed antenna systems for future smartphones is discussed in detail. The concept of multiband antennas and their inability for frequency upscaling is also discussed. Design examples for co-design of microwave and mmWave antennas are investigated thoroughly with adequate technical justification.

References

1. Lee, J.Y., Choi, J., Park, J., Kwon, W., Hong, W.: Compact MIMO antenna concept realizing entire 4G LTE and 5G spectrum for full-display metallic handsets. In *Proceedings of IEEE International Working Antenna Technology (iWAT)* (2019, March)
2. Alreshaid, A.T., Hussain, R., Podilchak, S.K., Sharawi, M.S.: A dual-element MIMO antenna system with a mm-wave antenna array. In: 2016 10th European Conference on Antennas and Propagation (EuCAP), pp. 1–4. IEEE (2016, April)
3. Kurvinen, J., Kähkönen, H., Lehtovuori, A., Ala-Laurinaho, J., Viikari, V.: Co-designed mm-wave and LTE handset antennas. IEEE Trans. Antennas Propag. **67**(3), 1545–1553 (2018)
4. Yamagajo, T., Koga, Y., Kai, M., Tonooka, T., Sumi, H., Hoshino, M.: A Nobel 4G and 5G antenna solution for future smartphones. In: 2018 IEEE International Symposium on Antennas and Propagation & USNC/URSI National Radio Science Meeting, pp. 1785–1786. IEEE (2018, July)
5. Taheri, M.M.S., Abdipour, A., Zhang, S., Pedersen, G.F.: Integrated millimeter-wave wideband end-fire 5G beam steerable array and low-frequency 4G LTE antenna in mobile terminals. IEEE Trans. Veh. Technol. **68**(4), 4042–4046 (2019)
6. Naqvi, S.I., Naqvi, A.H., Arshad, F., Riaz, M.A., Azam, M.A., Khan, M.S., Amin, Y., Loo, J., Tenhunen, H.: An integrated antenna system for 4G and millimeter-wave 5G future handheld devices. IEEE Access**7**, 116555–116566 (2019)
7. Al Abbas, E., Ikram, M., Mobashsher, A.T., Abbosh, A.: MIMO antenna system for multi-band millimeter-wave 5G and wideband 4G mobile communications. IEEE Access **7**, 181916–181923 (2019)
8. Liu, Y., Li, Y., Ge, L., Wang, J., Ai, B.: A compact hepta-band mode-composite antenna for sub (6, 28, and 38) GHz applications. IEEE Trans. Antennas Propag. **68**(4), 2593–2602 (2020)
9. Khalid, M., Naqvi, S.I., Amin, Y., Tenhunen, H.: An integrated 4G Array with mm-wave 5G MIMO antenna for future mobile applications. In: 2020 3rd International Conference on Computing, Mathematics and Engineering Technologies (iCoMET) (pp. 1–6). IEEE (2020, January)
10. Ikram, M., Nguyen-Trong, N., Abbosh, A.M.: Common-Aperture sub-6 GHz and millimeter-wave 5G antenna system. IEEE Access **8**, 199415–199423 (2020)
11. Li, H., Cheng, Y., Mei, L., Guo, L.: Frame integrated wideband dual-polarized arrays for Mm-wave/sub 6-GHz mobile handsets and its user effects. IEEE Trans. Veh. Technol. **69**(12), 14330–14340 (2020)
12. Hussain, R.: Shared Aperture Slot-Based Sub-6 GHz and mm-Wave IoT Antenna for 5G Applications. IEEE Internet of Things J. (2021)
13. Islam, S., Zada, M., Yoo, H.: Low-pass filter based integrated 5G smartphone antenna for sub-6-GHz and mm-wave bands. IEEE Trans. Antennas Propag. (2021)
14. Bae, J.H., Yoon, Y.J.: 5G dual (S-/Ka-) band antenna using thick patch containing slotted cavity array. IEEE Antennas Wirel. Propag. Lett. **20**(6), 1008–1012 (2021)
15. Ko, M., Lee, H., Choi, J.: Planar LTE/sub-6 GHz 5G MIMO antenna integrated with mmWave 5G beamforming phased array antennas for V2X applications. IET Microwaves Antennas Propag. **14**(11), 1283–1295 (2020)

Chapter 5
Gain Switchable Antenna Modules

5.1 Introduction

Future mobile devices have integrated mmWave radios, the coverage is still in the nascent stage, as the base stations and the layouts need huge investment and approvals from policy makers, which means that pattern requirements on the mobile device and that of the base station must be carefully designed.

It is well known that higher frequencies suffer from higher free space power loss [1]. To combat the additional loss, the transmitted power at the base station and/or the mobile device could be increased, but this is not a sustainable solution since the additional power requirement would be at least over 20–30 dB. It must also be noted that Ka-band power amplifiers are not very efficient thus losing out on the economic front. Hence, beam management would be an important feature of the future 5G networks for sustainable operation. In other words, antenna systems of the transceivers must quickly adapt to the required beam, depending on the requirement at hand.

To realize a feasible layout for 5G network, gains of the antennas on the mobile towers and the portable handheld devices must be increased respectively as proved earlier. The gain criteria have been emphasized in the preceding Chapters of this book as well. The catch with this line of thinking is that the angular coverage would be compromised when high gain antenna systems are activated. This means that beam-locking and tracking algorithms and controllers must be in place to monitor the received signal strength at the mobile device and the base station. This method contrasts with the commercially deployed 4G systems, wherein the mobile device constantly monitors available signals from various base stations and would latch on to the tower with highest power. A simple RSSI (Received Signal Strength Indicator) would perform the task of monitoring. 5G antenna systems would be much more complex, as it requires beam scanning.

This is a complicated process as the computational resources on the smartphone would be pushed to the limit thus draining out the battery quickly during data

S. K. Koul and K. G. S., *Antenna Architectures for Future Wireless Devices*,
Signals and Communication Technology,
https://doi.org/10.1007/978-981-16-7783-0_5

consumption mode. These network related computations must be performed in addition to the routine tasks of the smartphone. In this Chapter, the need for gain switchability for 5G mobile terminals is explained with adequate design examples. The most common solution to realize a high gain antenna system on the mobile phone is to design a phased array. This topology increases the complexity of the antenna system with respective compromise in the physical footprint. Even though half wavelength at 28 GHz is 5.35 mm, higher number of elements within a phased array would constrain space availability for other wireless modules' integration. Numerous articles and patents have been published in the recent years which investigates solution to the antenna problem in a smartphone targeting the 28 GHz and beyond [2–6].

For instance, a periodic structure which aids in gain enhancement is presented in [7], even though the gain yield for the physical size is high, the antenna might not be compatible with modern commercial smartphones. Periodic structures in the broadside direction might enhance gain of the antenna but achieving dynamic beam switching would be challenging in the Ka-band. The sub-wavelength unit cells must be integrated with active circuitry to achieve beam switching. In other words, an active aperture must be designed to achieve low gain-high gain beams for a given antenna. Realization of this design would have a myriad of diodes and it's associated bias lines. This solution might not be commercially feasible solution for beam switching problem.

A power divider-based array operating in the 60 GHz band is illustrated in [8], the principle could be scaled down to 28 GHz, but the broadside radiator would radiate towards the user, if the antenna's plane matches with that of the mobile device. It must be noted that vertical integration of this class of antennas would be impossible at 28 GHz for the required gain and the panel height of 7 mm or lesser. Design of power divider integrated with end-fire antenna, such as a printed dipole, would also lead to higher physical footprint. Also, end-fire antennas must be redesigned to radiate away from the user within a smartphone. Mobile device compatible phased array is proposed in [9], high gain could be achieved with this architecture, but the complexity is very high specially to realize the back-end electronics and its associated data converters. An integrated chip based phased array would be compact but would be complex to design and integrate. Wideband dipole array of [10] has a compatibility issue with the panel height. Dual-polarized antenna system further doubles up the complexity of phased array [11]. The space available for antenna integration in addition to the antennas of various wireless services is shown in [12]. Compact antennas of [13–15] have low gain and lack gain switchability. High gain antennas have lower coverage due to a consequent decrease in the beamwidth [16, 17].

Hence compact antenna systems which are compliant with commercial smartphone panels are presented in this Chapter. Need for gain switchability and design requirements is discussed in Sect. 5.2, followed by design examples in subsequent sections.

5.2 Need for Gain Switchability

In modern mmWave based 5G smartphones, the antenna system must be able to broadcast signals and deliver a pencil beam depending on the use case under consideration. For instance, when the mobile device is activated for a 5G link, then the device must radiate an omni-directional broadcast beam to sense any response from a base station. The issue with omni-directional beam on a mobile device is that the power radiated towards the user would be attenuated heavily, hence a unidirectional beam would be preferred for broadcast or control signal transmission application. Once the link is established, higher gain pencil beam could be activated to maintain a high data rate link within a feasible distance from the closest base station or access point. This ordeal could be achieved by an 8-element or 16-element phased array wherein only a few elements would be activated for low gain or high beamwidth pattern and higher number of elements could be activated in-phase for a lower beamwidth pattern [10, 11]. This architecture increases the complexity of the antenna design as the number of wideband phase shifters and its associated controllers also increase.

It must be noted that phased array deployment need not necessarily mean that the system could be plugged into a mobile device's panel. The ones that are commercially available are multi-layered chip-based designs, which are expensive and might lack compatibility with the existing industry standard PCB (Printed Circuit Board) based antennas. Hence the design requirements for a smartphone compliant gain switchable antenna system are as follows:

1. The system must offer beam switchability between wide beamwidth and narrow beamwidth. Both the patterns must be unidirectional, wherein the front to back ratio must be greater than 10 dB across the intended band of operation.
2. The number of ports in the system to be restricted to two. A shared ground design would be desirable as this could be integrated with the system ground of the mobile device.
3. The physical footprint of the entire antenna system including the feeding circuitry and the anticipated switches must fit within the panel height of modern commercial smartphones i.e., a height of 7 mm or lesser.

A generic layout of the gain switchable antenna system is demonstrated in Fig. 5.1. The shared ground module would be fed by two individual ports. The expected beam when the respective port is activated is also illustrated in the same figure. Both the beams must be unidirectional and must radiate away from the user.

5.3 A Three Port Antenna Module Design

In this Section, a three-port shared ground with gain switchability is presented. Microstrip-fed corporate feed array is shown in Fig. 5.2, which would be eventually

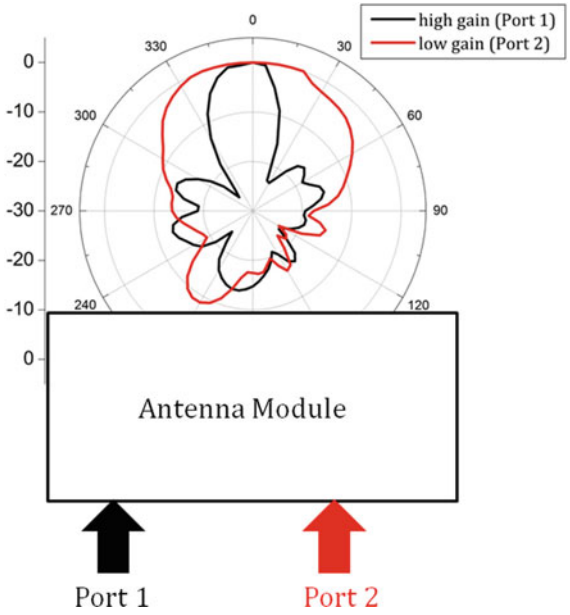

Fig. 5.1 Generic layout of a gain switchable antenna system

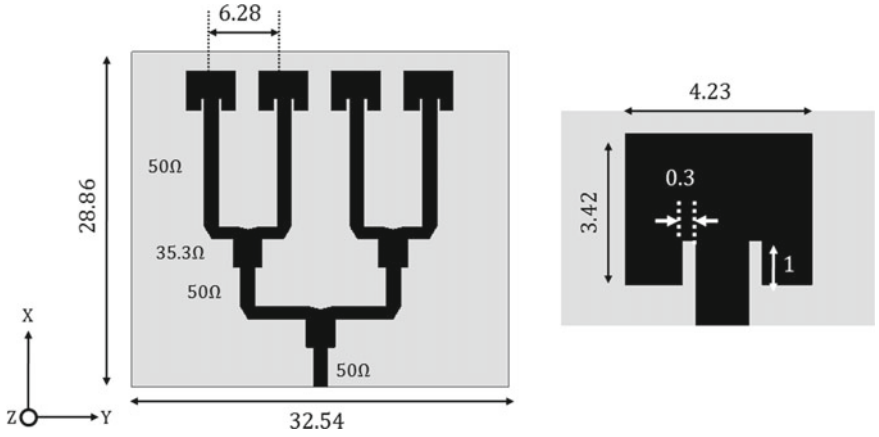

Fig. 5.2 Schematic of Corporate fed array (units: mm)

conformed for portable device compatibility. It is constructed on Nelco NY9220 substrate with 20 mil thickness. The thickness decides flexibility and strength of the conformed element. The inset-fed patch is also shown in the Fig. 5.2. A four-element corporate fed array is designed as a compromise between gain and the available physical aperture in a smartphone. Increasing the number of elements would increase gain but the angular coverage would be compromised. The feed line is a standard 50 Ω

line which is impedance matched to the four inset-fed patch antennas. Power dividers are realized with quarter-wave transformers. This antenna when conformed onto a mobile device would radiate away from the user.

The afore-mentioned array would be operational for single hand mode but would fail to operate in the dual hand mode as the beam must be radiated in the orthogonal orientation as well. The requirement for this design is that radiation and feed must be orthogonal to each other. A simple Vivaldi antenna would have served the purpose but the achievable gain for the panel height constraint would be limited. Hence, a compact corner bent Yagi antenna is proposed as shown in Fig. 5.3. The antenna is designed on the same substrate as that of the array. The 50 Ω transmission line is impedance matched to the dipole arms, which are orthogonally oriented, through the stubs as observed in the inset of Fig. 5.3. The physical radiating aperture is 7.46 mm which is compliant with most commercial smartphones. The placement and the number of the parasitic radiators decides the gain. The proposed element is chosen to maintain compactness and a reasonable gain.

The proposed conformal antenna module for gain switchability and orthogonal beams is depicted in Fig. 5.4a. The module integrated with customized 3D-printed radome is shown in Fig. 5.4b. The corporate fed array is bent in such a way that the radiators and hence the overall radiating aperture of the array would be on the panel of a smartphone. The clearance needed for the inset-fed patch antennas is only 0.5 mm on either side of the radiating edges. Bending does not affect the impedance

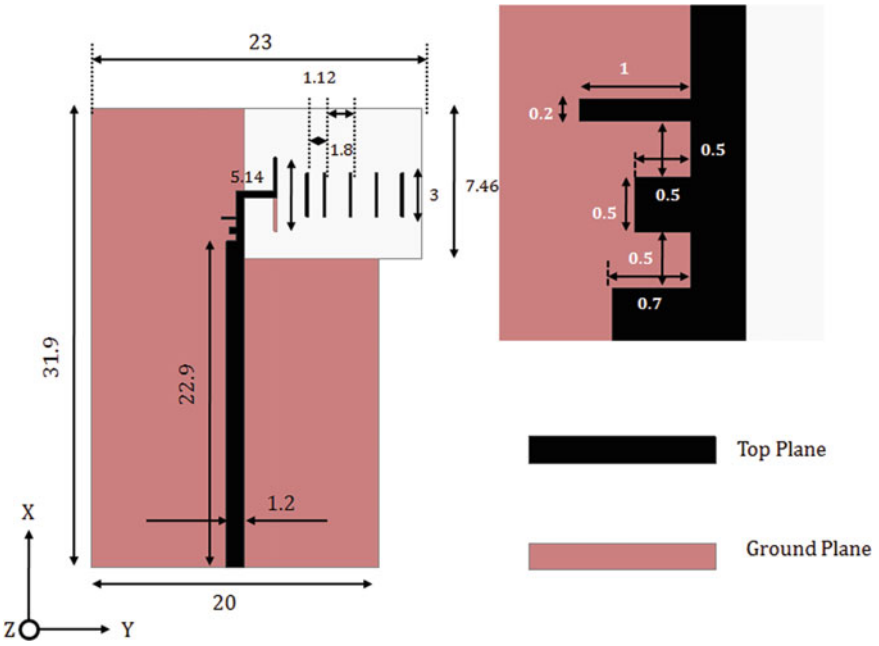

Fig. 5.3 Schematics of corner bent array (units: mm)

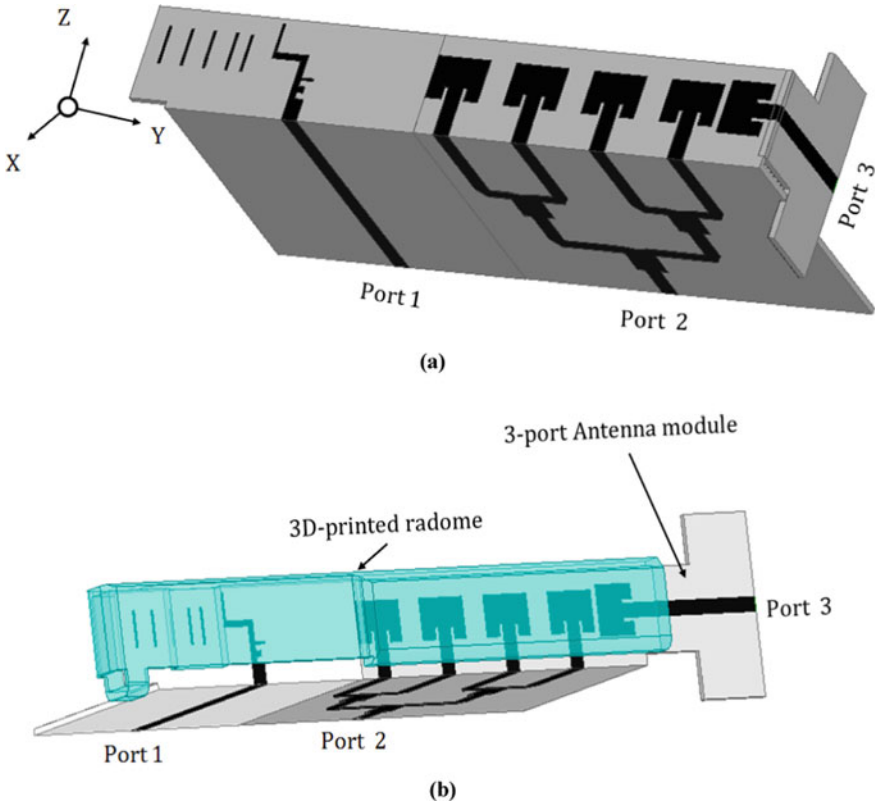

Fig. 5.4 Schematics of the proposed module: **a** without radome, **b** with radome

characteristics of the array. Even though the schematics present a perfect 90° bend of the antenna, the design still works when the array is wrapped around the panel of a typical smartphone as the alignment of the radiating edges of the component antennas are not altered much with wrapping. Also, wrapping would effectively reduce the antenna height from 7.46 mm to 6 mm or lesser depending on the curvature of the panel. The microstrip ground of the array doubles up as the system ground wherein RF back-end electronics could be integrated with. As the radiators are backed by a ground plane, the vertically polarized radiation is directed away from the user post integration with a smartphone or a mobile device.

To achieve an orthogonal beam, the conformed Yagi antenna is integrated as shown in Fig. 5.4. The distance between the array and Yagi antenna could be as low as 1.2 mm translating to 0.11 λ at 28 GHz. The characteristics of the compact shared ground design is like that of the individual antenna elements. The separation has been increased to accommodate the end-launch connector, solely for measurement purposes.

A third port is added with an inset-fed patch antenna within the constraints of the smartphone's panel height. The substrate is elongated near the feeding port for connector mounting and could be avoided in an actual deployment scenario. A shared radiator design could have been realized between ports 2 and 3 but the extent of variation in gain switching seems to be unusable. The inset fed patch antenna has a clearance of 1 mm with the conformal array. The patch antenna would be switched for broadcast applications or for the beam-locking sequence when sensing radio signal strength. A customized 3D-printed radome is also investigated, this is built using PLA (PolyLactic Acid) substrate which has a dielectric constant of 2.75 with a loss tangent of 0.01. The gap between the antenna module and the radome is 0.5 mm, if the gap is lesser than this value then the antennas would detune due to the dielectric parasitic loading.

The input reflection coefficient of the conformal array is shown in Fig. 5.5. The 10 dB impedance bandwidth is from 26 to 29 GHz translating to 11%. Wider bandwidth compared to a conventional strongly resonant patch antenna is due to the design of the power divider network. The conformal or wrapping around action does not influence the $|S_{11}|$ as insertion loss specifically due to bending is negligible. The bandwidth could be further enhanced by incorporating a Wilkinson power divider but implementing this would be a challenging task due to the additional parasitics which may occur due to resistors' integration.

The measured mutual coupling is depicted in Fig. 5.6 and the value is lesser than 35 dB across the ports and throughout the operating band of interest. Even though the antennas have a shared ground, mutual coupling is relatively low due to maximum radiation from the antennas and the geometry of the topology has been designed for low coupling between the respective elements.

The gain switchability is shown in Fig. 5.7a; the effect of beam-width widening is pretty evident and hence would be suitable for data link application with narrow beam and broadcast applications with wider beam. The front to back ratio is greater

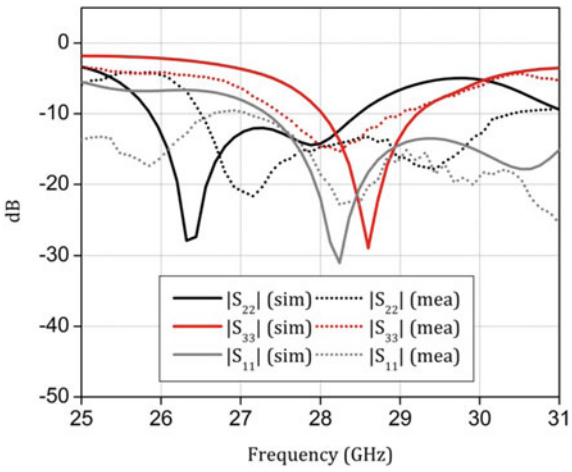

Fig. 5.5 Input reflection coefficients of various ports

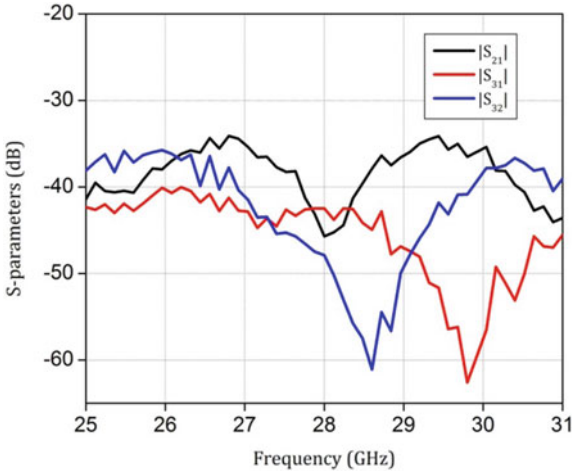

Fig. 5.6 Measured S-parameters of the proposed module

than 10 dB across the ports indicating minimal radiation towards the user irrespective of the antenna which is activated. The orthogonal beam is illustrated in Fig. 5.7b the radiation in this case is also away from the user.

The fabricated prototypes are shown in Fig. 5.8. The connector holes to accommodate the electrically large end-launch connector is also visible. The antenna module in the actual deployment scenario could be much more compact as the additional transmission lines and clearance for connector would be eliminated altogether.

5.4 A Two Port Shared Radiator Design

5.4.1 Planar Shared Radiator

The proposed two-port planar version of the gain switchable shared radiator is depicted in Fig. 5.9. Dual conformity would be introduced to this design to save space and effectively reduce the height of the antenna system. The proposed antenna is designed on Rogers 5880 substrate with a dielectric constant of 2.2 $\pm$ 0.02 and a corresponding dielectric loss tangent of 0.0009. The thickness of the substrate is 20 mil or 0.508 mm, which decides the bendability of the substrate. Elasticity of the substrate is also a matter of concern for a conformable realization of a chemically etched antenna. The chosen substrate is reasonably well-suited for the present application. Flexible substrates such as polycarbonate or PET (Polyethylene terephthalate) might offer higher flexibility with little or no strain on the substrate post bending, but the dielectric loss tangent is relatively higher which would effectively deteriorate the forward gain by up to 1–2 dB. A low dielectric constant such as 2.2 ensures low surface wave modes and allows for a feed line width lesser than quarter-wavelength

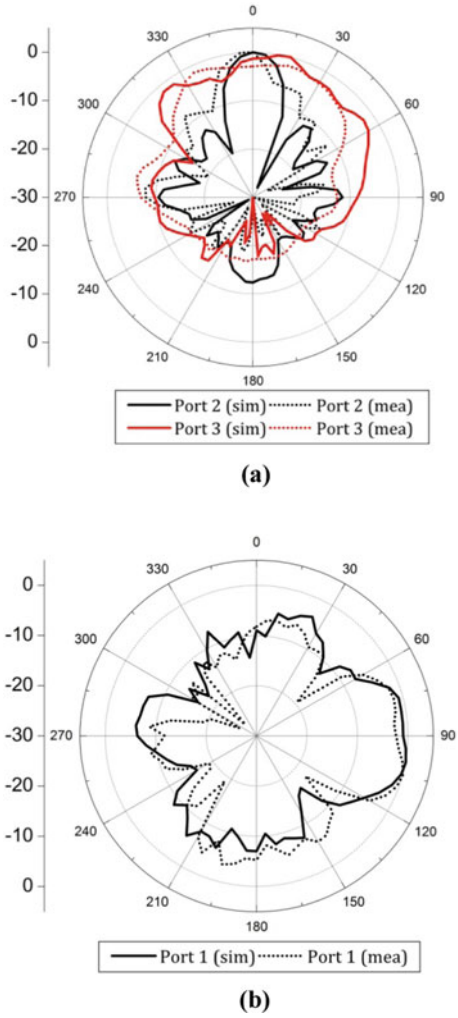

Fig. 5.7 Radiation patterns at 28 GHz when **a** Ports 2 and Port 3 are excited, **b** Port 1 is excited

hence minimizing spurious radiation from the feeding line itself. Wider feed lines would deteriorate the pattern integrity resulting in gain degradation.

The chosen feed line for port 1 is a standard 50 Ω line on this substrate to avoid mismatch with the port impedance of the same value. It is fed to two arms of the power divider through a quarter wave transformer, which has a characteristic impedance of 35.3 Ω on the given substrate. The V-shaped notch introduced at the power divider is to improve impedance matching. The first and second power dividers lack 100 Ω resistor design (or the Wilkinson power divider) due to additional cost and difficulty in fabrication without introducing parasitics into the feeding network. Due to this choice of the power divider network design, the isolation between the ports is quite

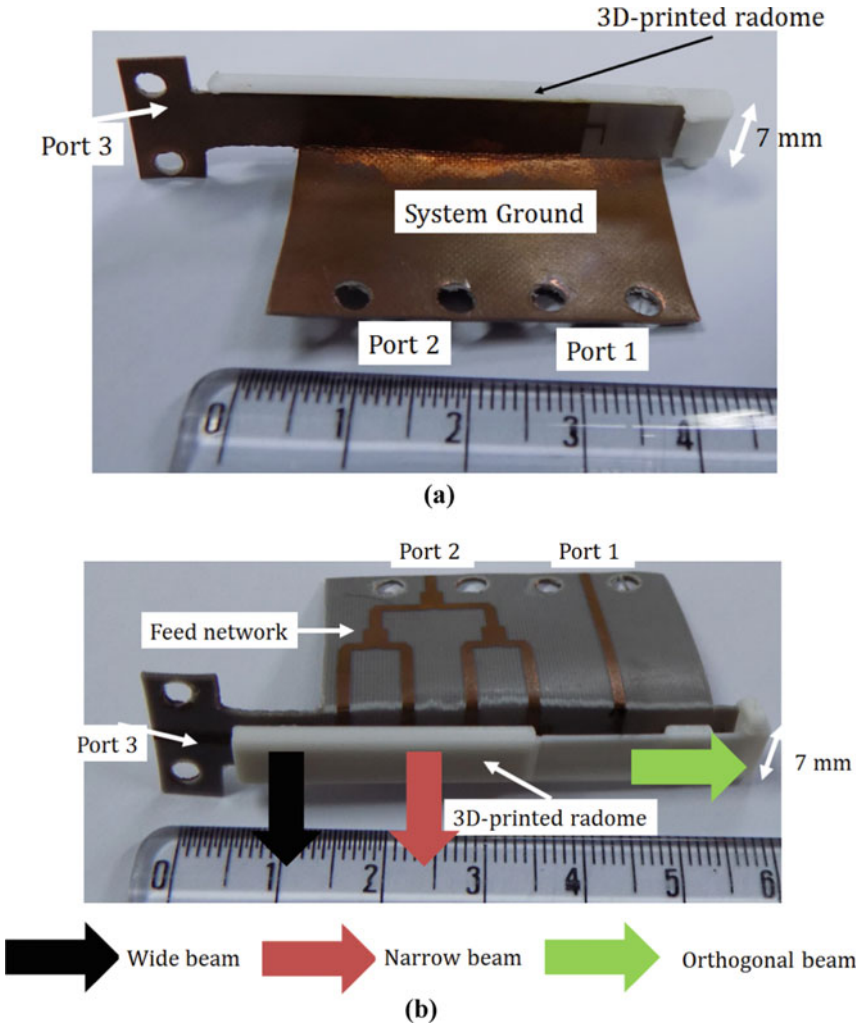

Fig. 5.8 Photographs of the fabricated module: **a** back view, **b** front view

low thus leading to poor effective forward gain when all the terminals are fed with in-phase signals. The choice for a four ports' power divider network is based on the gain requirement and the available real estate on a mobile device. The transmission lines of the power divider are loaded with identical inset fed patch antennas as observed in Fig. 5.9.

The radiator is a standard inset fed patch antenna matched to a 50 Ω line. The power dividers' impedances are optimized to match that of the radiator as far as port 1 is concerned. Typically, inset fed patch antenna designed on an electrically thin substrate would have an impedance bandwidth of 3–4% but in the proposed design,

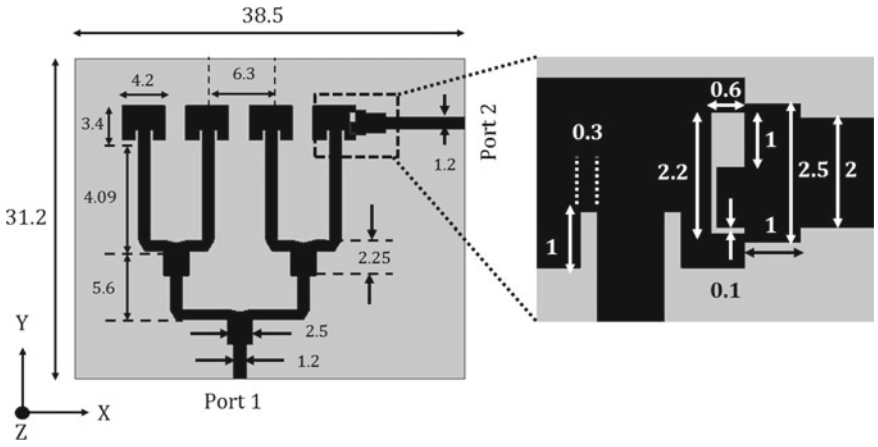

Fig. 5.9 Schematics of the proposed shared radiator (All dimensions are in mm)

the 10-dB impedance bandwidth is from 26.2 to 29 GHz, translating to 10.1%. The wider band has been achieved due to the wide impedance matching of the feeding circuitry.

If all the four elements are fed in-phase, the co-polarized radiating E-fields combine and leads to higher gain if the separation between the radiators is close to half-wavelength on the chosen substrate. The in-phase action of beamforming is evident from E-fields plot of Fig. 5.10 when port 1 is activated at 28 GHz. Here the first power divider almost equally splits power in half to each port and a similar action is subsequently repeated by the other two power dividers which feed the radiators in-phase causing a high gain or low beamwidth pattern. As the radiators are backed by an electrically large ground plane, the pattern is unidirectional with a front to back ratio greater than 10 dB across the band.

To achieve gain switchability several approaches could be followed. One of them is to integrate an in-line pin diode or any other switchable series device for respective

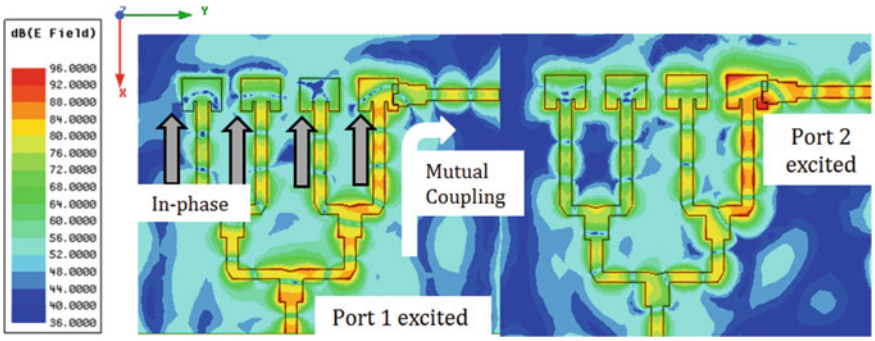

Fig. 5.10 E-fields for different port excitations at 28 GHz

elements of the phased array. The problem with this topology is that the width of the transmission line feeding the antennas is 1.2 mm, pin diodes commercially available that operates in the 28 GHz band, are larger than this dimension and the control circuitry with DC (Direct Current) biases would occupy a large footprint preventing its application in the present context. Another approach is to integrate a reconfigurable or switchable aperture over the phased array, wherein: when the aperture is activated, the beamwidth of the pattern must change. This approach might be complicated to realize especially with the constraints of the panel height. Hence a shared radiator is explored in this Section.

In this topology, the corner most element of the corporate feed array is fed with another port as observed in Fig. 5.9. The corner most element is integrated with two stepped impedance transformers each of widths 2.5 and 2 mm as illustrated in the inset of Fig. 5.9. The transformers alone would not achieve a lower gain pattern, but the introduction of the slot does. The slot matches the impedance for both the ports with a minimal mutual coupling between them. It must be noted that the slot size is 0.2 $\lambda \times 0.056\ \lambda$ at 28 GHz proving to be electrically small hence no additional radiation or grating lobes appear due to this slot. As the primary structure is contiguous, the magnitude of E-fields coupling to the second port is relatively high as observed in Fig. 5.10. The S-parameters of the planar version of the shared radiator is shown in Fig. 5.11.

As port 2 is activated, the corner most element acts as the primary radiator. As there are no additional isolating networks between the inset fed patch radiators, energy flows to other elements as well with decreasing intensity hence losing out on the beamforming capability of a typical corporate fed array. Due to this phenomenon, the pattern is wider compared to its counterpart on port1. The low gain concept is evident from the E-fields' propagation depicted in Fig. 5.10. Both the patterns are Y-polarized as the radiation from port 2 excitation is also Y-polarized, with reference to Fig. 5.9. The radiating edges of all the inset fed patches remain the same, but the

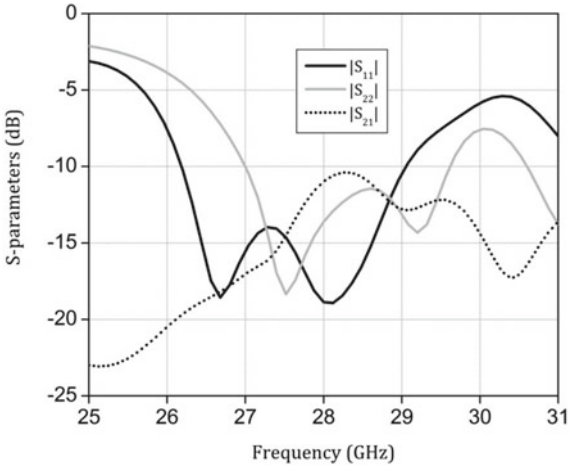

Fig. 5.11 S-parameters of the shared radiator

activation of different ports leads to beam or gain switchability. The pattern could be switched from wide beam to narrow beam.

The electrically long feeding network leads to gain deterioration without a significant deterioration in pattern integrity throughout the band. The impedance bandwidth for port 1 is from 26.2 to 29 GHz or 10.1%, similarly port 2 has an impedance bandwidth from 27 to 29.6 GHz or 9.2%. Both the ports operate in the 28 GHz band with a mutual coupling less than 10 dB across the band. It appears that the mutual coupling is high compared to its counterpart designs with shared ground. The high mutual coupling is due to the electrically compact design of the shared radiator. All the full-wave simulations were done using Ansys HFSS version 18.2. All the components of the design were modelled as lossy materials.

5.4.2 Dual Conformal Shared Radiator

The proposed gain switchable 2-port antenna system of Fig. 5.9 would radiate towards the user when engaged with a smartphone, as the proposed antenna is a broadside radiator. Broadside radiation, when radiated towards human head or torso, would experience an attenuation of at least 20 dB in the 28 GHz band, hence an alternate topology to remedy this issue is explored in this Section. The placement of the antenna system within the constraints of the smartphone's dimension is also investigated in this Section.

The schematic of the dual conformal shared radiator is illustrated in Fig. 5.12. The design logic is that the planar antenna of Fig. 5.9 is dual bent along the anticipated smartphone panel's dimensions. The primary space required for the radiation

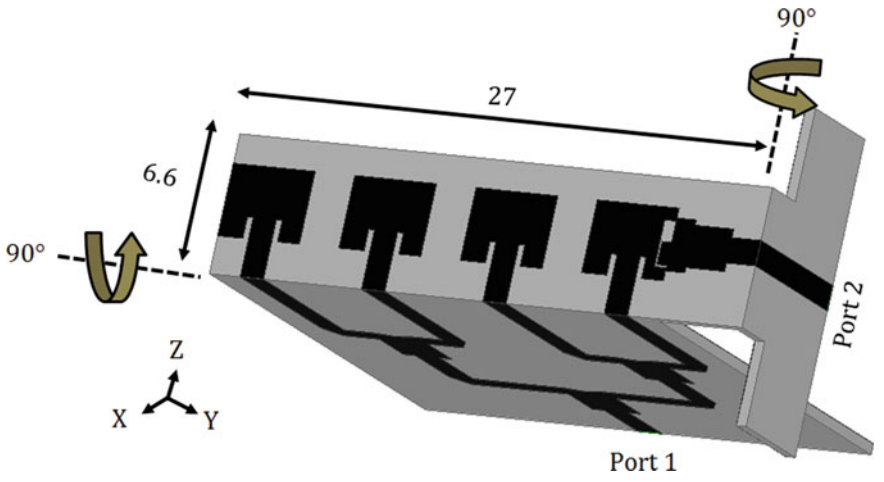

Fig. 5.12 Schematic of the dual conformal shared radiator (all dimensions are in mm)

mechanism of the corporate fed array-based gain switchable system is primarily the four inset fed patch antennas with a clearance on either side of the patches to support radiation. In other words, an electrically small clearance near the radiating edges of the patches would suffice for the application in hand. Simulations have verified that a clearance of only 0.5 mm (or 0.046 λ at 28 GHz) would be sufficient for the radiation. In the present context of 3.4 mm $\times$ 4.2 mm patch radiator, the actual height required for adequate radiation is only 4.4 mm (3.4 mm + (0.5 mm $\times$ 2 radiating edges)).

In principle, a height of 4.4 mm would work, but it might be difficult to fabricate and conform twice. Hence a clearance of 3.2 mm is chosen which results in an overall height of 6.6 mm as depicted in Fig. 5.12. The corner most element is chopped off at the non-radiating edge of the antenna without any deterioration in the performance metric of the corporate fed array. This concept of shortening the width at the non-radiating edge aids in further compactness of the antenna system. As observed in Fig. 5.12, there are two 90° or corner bends: one in the horizontal (or XY) plane and the other in the vertical (or XZ) plane. Both these bends aid in placement of the antenna within a modern smartphone. The term conformal is used to imply that the antenna could be wrapped around the curved panel of the smartphone without losing pattern/gain/impedance integrity of the antenna system [18, 19]. The protrusion along Z axis near port 2 is specifically to accommodate the industry standard end-launch connector and could be shortened in a commercial phone integration. The overall dimensions of the effective radiating space of the proposed antenna are 27 mm $\times$ 6.6 mm $\times$ 0.508 mm.

The electrically large ground plane of the proposed design acts as a natural shield to the RF (Radio frequency) electronics and the patterns of the antenna would be invariant even if a multi-layered board is integrated beneath it. The fabricated prototype mounted with the end-launch connectors is illustrated in Fig. 5.13. As the least

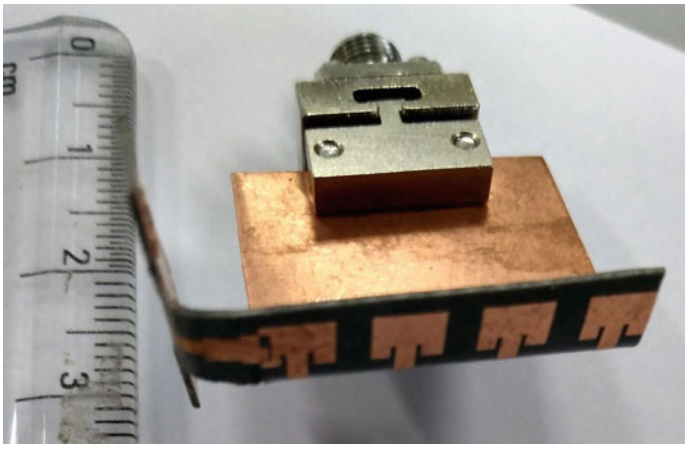

Fig. 5.13 Photographs of the proposed antenna

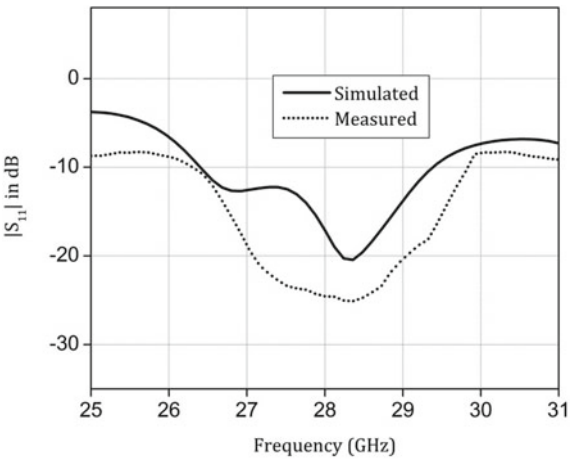

Fig. 5.14 $|S_{11}|$ of the dual conformal antenna

dimension of the proposed antenna system is 0.1 mm, industry standard chemical etching was used to realize the same. A customized 3D-printed smartphone panel mock-up was used as a scaffolding to bend the antenna. It must be noted that Rogers 5880 is not very elastic hence not conformal friendly at 20 mil. There were a few aberrations and metal fracture in the ground plane which did not result in significant deviations in the experimental results. The input reflection coefficient for port 1 of the proposed antenna system is illustrated in Fig. 5.14. The simulated 10-dB impedance bandwidth is 10.1%. The discrepancy between simulated and measured curves is due to the improper bending and the lack of solder with the trace pin of the end-launch connector. All the S-parameter measurements were done using Keysight E8364C. The bandwidth of port 1 is decided by the choice of the radiating elements, design of the power divider network and the thickness of the substrate. If wider band Wilkinson based power dividers could be incorporated, wider bandwidth could be achieved, with a consequent compromise in the pattern integrity at the band edges. A thicker (30 mil for instance) substrate behind the radiators also would enhance the bandwidth at the cost of decreased flexibility or conformability. The impedance variance with and without dual conformity is negligible. The proposed dual conformal shared radiator works well in the 28 GHz band.

The forward H-plane (XY plane) radiation patterns at 27 GHz and 28 GHz are shown in Fig. 5.15, the beamwidth is 20° at 28 GHz. The high pattern integrity could be attributed to the aperture behavior of the corporate fed array. The front to back ratio is greater than 15 dB across the band, indicating minimal radiation towards the user engaged with the mobile device when activated. The narrow beamwidth could be further shrunk by increasing the number of radiators, but the coverage would be questionable even for an indoor link. As the feeding network is placed in the orthogonal plane (XY plane) with respect to the radiating aperture (YZ plane), spurious radiation from the discontinuous power dividers is kept to a minimum. The placement of this antenna system would be at the corner edge of the mobile device

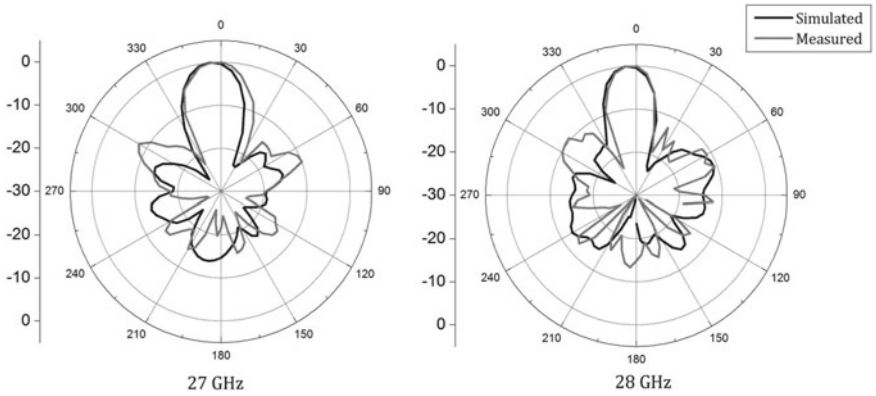

Fig. 5.15 Radiation patterns when port 1 is activated

without any loss of generality. The second port feeding line would lie along the perpendicular edge of the mobile device.

The input reflection coefficient for port 2 is depicted in Fig. 5.16 the variation between the planar version and its dual conformal counterpart is due to the additional inductance due to bending of the feeding lines or the network. The 10-dB impedance bandwidth is 9.2%. The variation with simulated and measured curves is little high at the higher end of the spectrum primarily due to the experimental challenges involved in the measurement setup especially with a large footprint connector as observed in Fig. 5.13. Nevertheless, the antenna system still operates in the 28 GHz band when port 2 is activated. Even this port offers a wide impedance bandwidth despite the compact size of the antenna.

The forward simulated and measured patterns at 27 GHz and 28 GHz when port 2 is switched on are illustrated in Fig. 5.17. The beamwidth is 49° at 28 GHz. The front

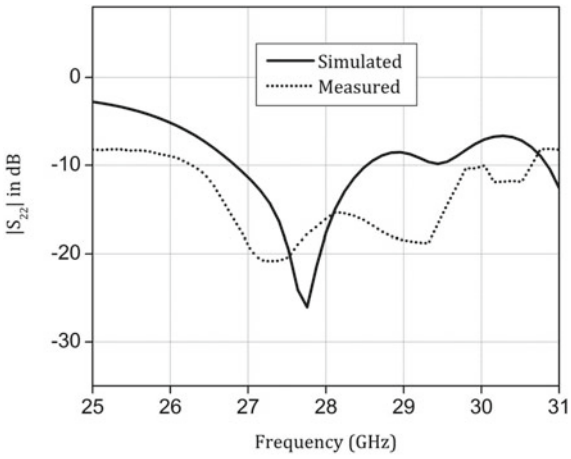

Fig. 5.16 $|S_{22}|$ of the dual conformal antenna

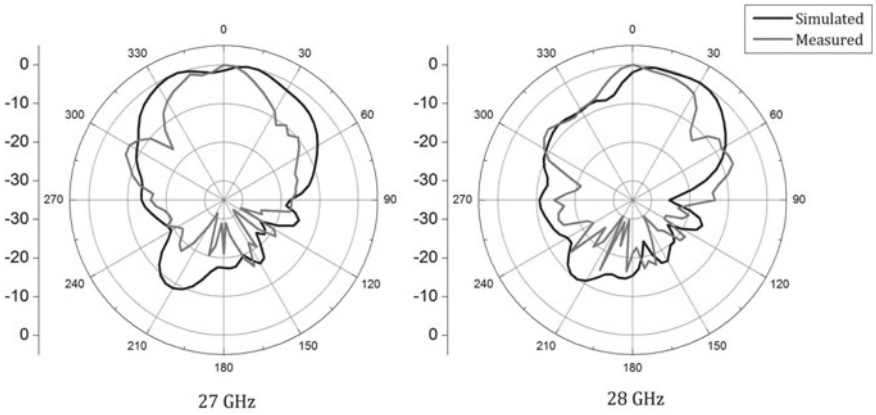

Fig. 5.17 Radiation patterns when port 1 is activated

to back ratio is also greater than 10 dB throughout the band. The larger beamwidth indicates that this port could be fired up when low gain or broadcast applications is needed.

Mutual coupling between the ports is depicted in Fig. 5.18. As the design is an electrically compact shared radiator, mutual coupling is less than 10 dB across the band. A noticeable difference between simulated and measured values of $|S_{21}|$ is due to improper contact between the trace pin of the end-launch connectors and that of the complicated non-planar prototype. This experimental error could be further reduced in principle by using SMP (Sub-miniature push on) connectors with proper calibration.

The gain switchable action is evident in Fig. 5.19 which illustrates the forward gains for both the ports. It must be noted that both the port excitations lead to a

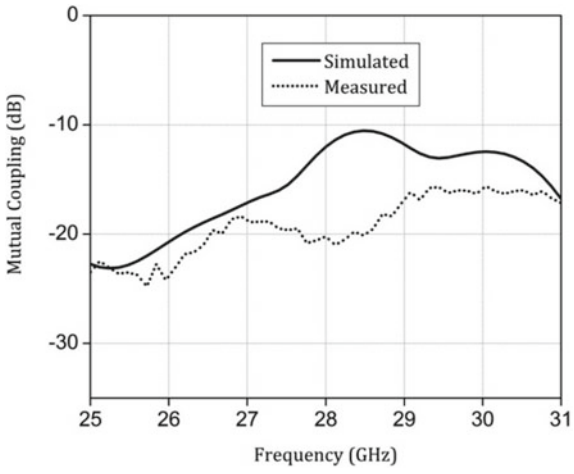

Fig. 5.18 Mutual coupling of the proposed antenna system

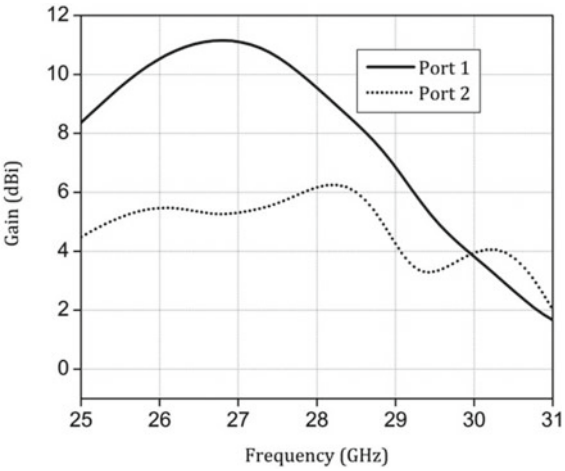

Fig. 5.19 Forward gains for both ports

vertical or Z-polarization (with reference to Fig. 5.12). The forward high gain for port 1 is 9.5 dBi at 28 GHz and low gain of port 2 is 6.2 dBi at 28 GHz. Gain corresponding to port 1 could be increased by increasing the number of radiators with a fixed separation of half-wavelength. The same principle is not valid for port 2 as the low gain remains the same even if the number of elements is increased. Thus, proving the design to be scalable.

The composite forward radiation patterns for both the ports are shown in Fig. 5.20a, b which clearly demonstrates the gain switchable action. Table 5.1 illustrates various figures of merit of the proposed dual conformal antenna system in comparison to previously published designs. The proposed system has gain switchability with panel height less than 7 mm.

5.5 Three Port Shared Radiator Design

The dual conformal shared radiator could be expanded to a three-port design to realize wide beam angular coverage on a smartphone. As observed in Sect. 5.4, two port design based on corporate fed array leads to a narrow beam and wide beam with vertical polarization. If another port is added symmetrically to the four-element corporate fed array, wide angle beam scanning at 28 GHz could be achieved. The planar version of the proposed three port design is illustrated in Fig. 5.21a. The design is realized on Rogers 5880 substrate with a dielectric constant of 2.2 and a dielectric loss tangent of 0.0009. As the antenna would be wrapped around or bent around the inner contour of the mobile terminal, the substrate must be a little flexible, polycarbonate or polyimide substrate would have been much flexible, with a compromise in the dielectric loss tangent.

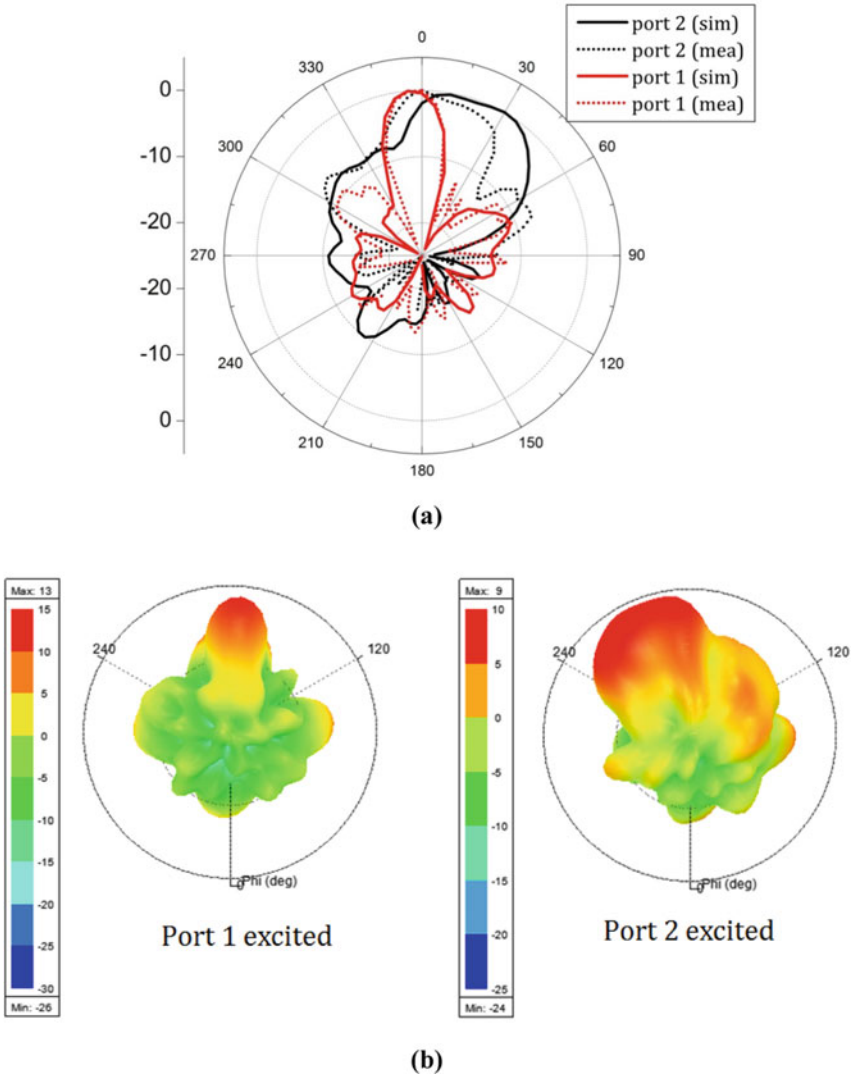

Fig. 5.20 **a** Composite radiation patterns at 28 GHz, **b** 3D patterns for different port excitations

The proposed antenna is a shared radiator, shared ground design with three ports. The feed lines for all the three ports are standard 50 Ω lines to minimize impedance mismatch between the antenna and the port. Port 1 is connected to a two-way power divider through an appropriate quarter wave transformer with characteristic impedance of 35.3 Ω. The V-shaped notch at the power divider aids in impedance matching. The two-way transmission lines emanating from the first power divider are further connected to a four-way power divider with similar transformers. These

Table 5.1 Comparison of the proposed module with reported articles

References	Freq	ERV	GS	MI	Con	SG
[17]	28	0.138	Yes	No	No	Yes
[10]	28	0.207	Yes	No	No	Yes
[20]	28	0.05	No	No	No	Yes
[21]	28	0.006	No	No	No	Yes
[22]	28	0.027	No	Yes	No	Yes
[23]	28	0.005	Yes	No	No	Yes
[24]	28	0.026	No	No	No	-NA-
[25]	26	0.192	No	No	No	Yes
Proposed	28	0.07	Yes	Yes	Yes	Yes

* Ref = Reference, Frq = Frequency (GHz), ERV = Effective Radiating Volume (λ_0^3), G = Gain (dBi), GS = Gain Switchability, MI = Mobile Integration, Con = Conformal, SG = Shared Ground

four arms of the power dividers are connected to the inset fed patch antennas spaced at 6.3 mm from each other. The edge elements of the corporate fed array are in turn connected to two other ports: Port 2 and Port 3 as observed in Fig. 5.21a. Ports 2 and 3 are connected to the non-radiating edges of the patch elements through a couple of stepped impedance transformers and an electrically small slot. The shared radiator action is identical to the design illustrated in Sect. 5.4. The proposed design is realized on a complete ground plane, which means that radiating beams with high front to back ratio could be easily achieved. The proposed design, when mounted on the mobile device would radiate towards the user, hence a conformal version is explored.

The proposed design is bent along the effective radiating aperture of the shared radiator as shown in Fig. 5.21b. The height is 6.2 mm, which meets the dimensional criterion of most modern smartphones. As the radiators are backed by electrically large ground plane, radiation would be unidirectional when mounted onto an appropriate mobile device. The choice of four elements is to achieve narrow beam when Port 1 is activated. Feeding lines corresponding to Ports 2 and 3 could also be bent backwards around Z axis (with reference to Fig. 5.21b) to further miniaturize the design. The photograph of the fabricated prototype is shown in Fig. 5.22, additional solder was applied at the edges, as the feeding lines experienced metal snapping. Ports 2 and 3 are also fed orthogonally, which indicates that only the active radiating aperture would coincide with the curved panel of the smartphone.

Simulated and measured input reflection coefficients for Port 1 are illustrated in Fig. 5.23. The 10-dB input impedance bandwidth is from 26.5 GHz to 29.7 GHz, translating to 11.4%. Wideband is achieved due to the design of the impedance transformers.

The input reflection coefficients for ports 2 and 3 are shown in Fig. 5.24. The 10-dB input impedance bandwidth is from 27 to 30 GHz, translating to 10.5% for port 2 and 27.5 GHz to 28.1 GHz, translating to 2.1% for port 3. The discrepancy

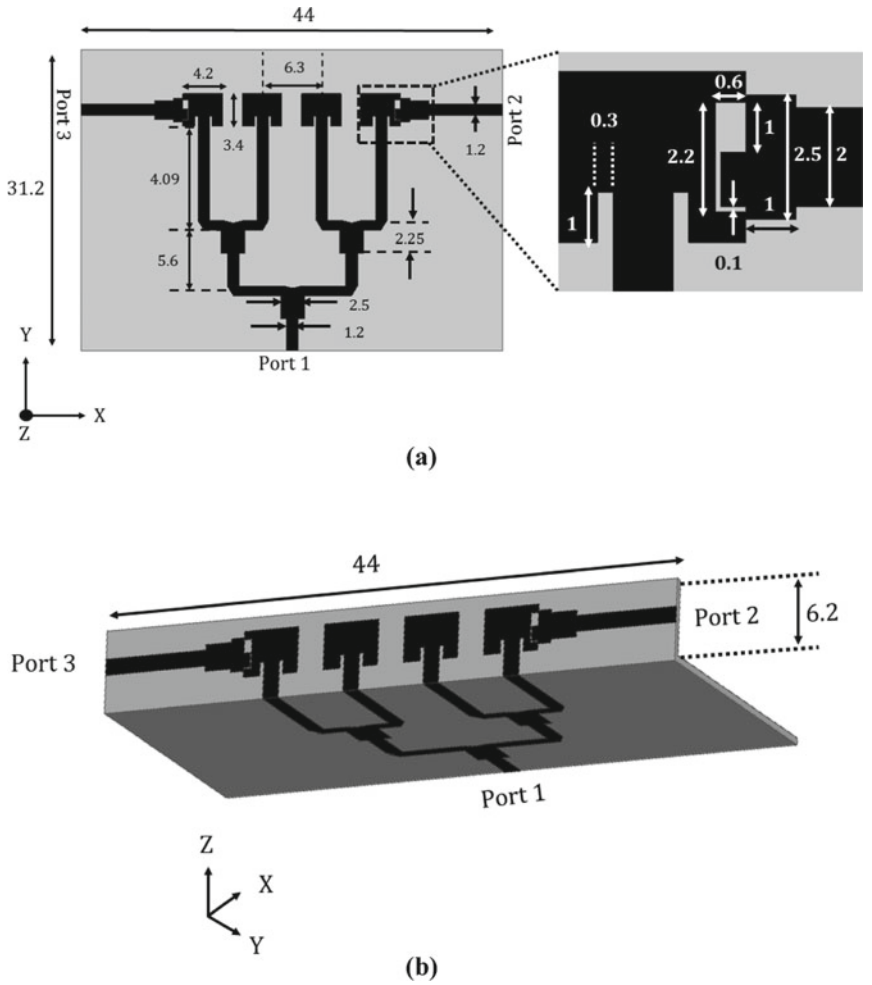

Fig. 5.21 Schematic of the three-port shared radiator: **a** planar version, **b** conformal version (All dimensions are in mm)

between simulated and measured values could be attributed to improper mounting of the electrically large end-launch connector with the antenna assembly. As the design is three-dimensional, the room for measurement errors is high. All the S-parameter measurements were done using Agilent PNA E8364C.

The patterns when three ports are activated are shown in Fig. 5.25. When port 1 is activated, the corporate fed array mode is activated, which means that the beam-forming happens amongst the four elements. The beamwidth corresponding to Port 1 activation is 20°. When port 2 is activated, the right most element is energized, as the power divider feeding this element lacks isolating network, the element adjacent to the corner most element is also activated. The combined effect of the two elements

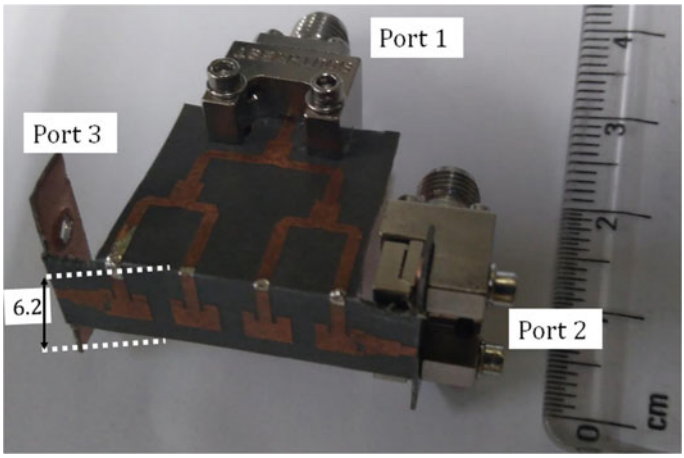

Fig. 5.22 Photograph of the fabricated prototype

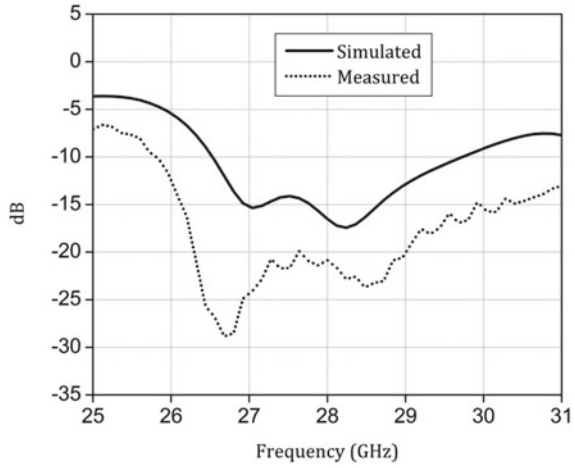

Fig. 5.23 Input reflection coefficient of Port 1

leads to radiation with an offset with respect to the phase center of the antenna. Pattern corresponding to Port 2 activation has an angular coverage from 0° to 50°.

A beam-tilt at 28 GHz could be attributed to the activation of right most elements which are offset from the phase center. Port 3 has a similar effect on the opposite side of the angular space. Mutual coupling between the ports is illustrated in Fig. 5.26, all the values are below 10 dB across the entire spectrum of operation. Mutual coupling is less than 10 dB due to the topology of the impedance transformers. Gains for the respective ports is illustrated in Fig. 5.27.

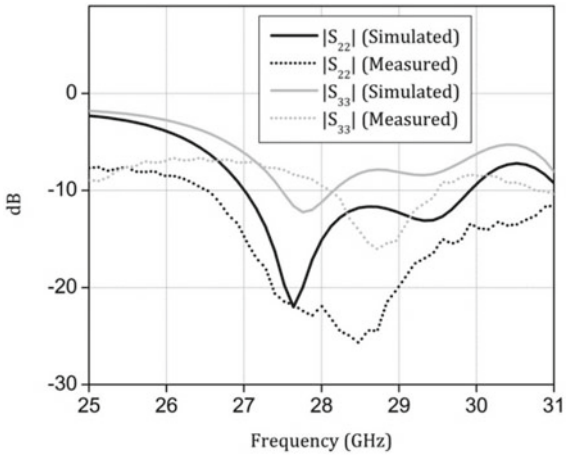

Fig. 5.24 Input reflection coefficients of Port 2 and 3

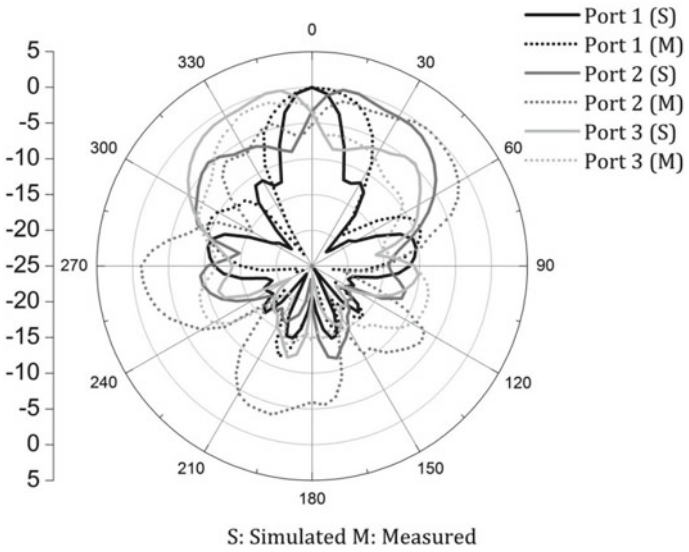

Fig. 5.25 Radiation patterns of the proposed shared radiator

The reduced gains for ports 2 and 3 are due to the wider angular spread of the beams when these ports are activated. A typical placement of the proposed antenna within a 3D-printed smartphone mock-up is illustrated in Fig. 5.28, only the radiating portion of the antenna system would coincide with the smartphone panel.

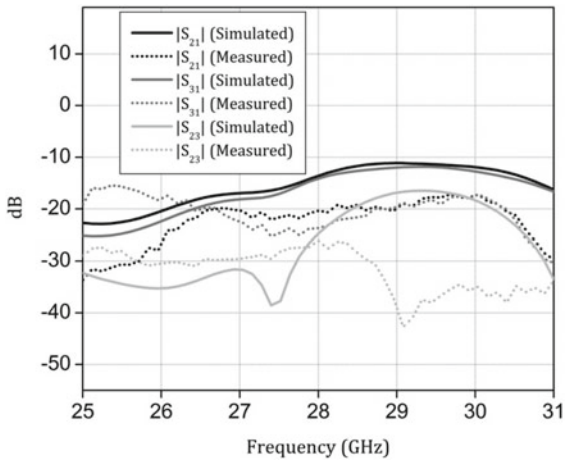

Fig. 5.26 Mutual coupling between the ports

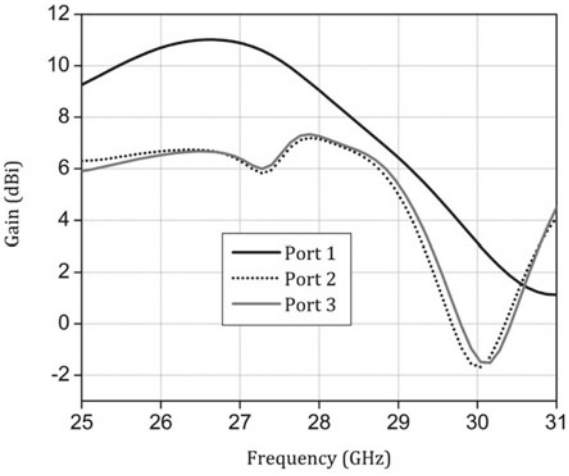

Fig. 5.27 Gains of various ports of the shared radiator

5.6 Conclusion

In this Chapter, various antenna architectures for gain switchability are discussed. Need for gain switchability is illustrated, wherein the beam radiated from the antenna must be narrow for high data rate applications and wide for broadcast applications. Conventional phased arrays could be used to achieve gain or beam switchability by selectively activating the desired number of ports within the phased array. This method would be complicated to realize, hence various multi-port antenna systems were introduced in this Chapter. A three-port beam switchable corner bent antenna system with shared ground is presented. Here, two electrically close antennas with different forward gains are used to achieve gain switchability. The concept of shared

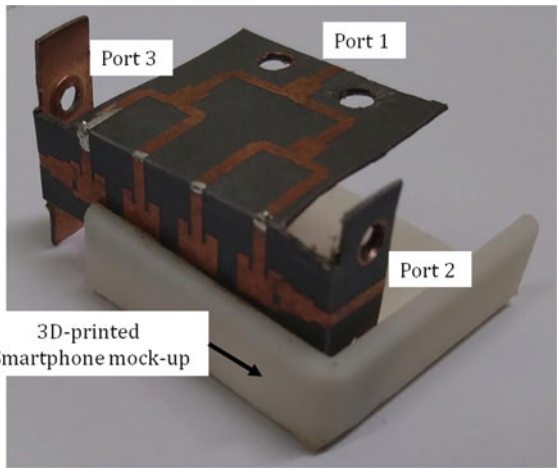

Fig. 5.28 Typical placement of the fabricated prototype with the 3D-printed smartphone mock-up

radiator is also explored in this Chapter. Here, a single radiator is fed with two distinct ports to achieve gain switchability.

References

1. Friis, H.T.: A note on a simple transmission formula. Proc. IRE **34**(5), 254–256 (1946)
2. Ullah, R., Ullah, S., Ullah, R., Faisal, F., Mabrouk, I.B., Al Hasan, M.J.: A 10-ports MIMO antenna system for 5G smart-phone applications. IEEE Access **8**, 218477–218488 (2020)
3. Li, H., Cheng, Y., Mei, L., Guo, L.: Frame integrated wideband dual-polarized arrays for mm-wave/sub 6-GHz mobile handsets and its user effects. IEEE Trans. Veh. Technol. **69**(12), 14330–14340 (2020)
4. Lu, R., Yu, C., Zhu, Y., Hong, W.: Compact millimeter-wave endfire dual-polarized antenna array for low-cost multibeam applications. IEEE Antennas Wirel. Propag. Lett. **19**(12), 2526–2530 (2020)
5. Yu, B, Yang, K.: "Antenna array integrated on the metal back cover of the 5G mobile terminal. U.S. Patent 10,333,221 issued 25 June 2019
6. Shehan, J.W.: High gain, multi-beam antenna for 5G wireless communications. U.S. Patent 10,256,551, issued 9 Apr 2019
7. Haraz, O.M., Elboushi, A., Alshebeili, S.A., Sebak, A.R.: Dense dielectric patch array antenna with improved radiation characteristics using EBG ground structure and dielectric superstrate for future 5G cellular networks. IEEE Access **2**, 909–913 (2014)
8. Bondarik, A., Sjöberg, D.: Gridded parasitic patch stacked microstrip array antenna for 60 GHz band. IET Microw. Antennas Propag. **14**(8), 712–717 (2020)
9. Zhang, S., Chen, X., Syrytsin, I., Pedersen, G.F.: A planar switchable 3-D-coverage phased array antenna and its user effects for 28-GHz mobile terminal applications. IEEE Trans. Antennas Propag. **65**(12), 6413–6421 (2017)
10. Ta, S.X., Choo, H., Park, I.: Broadband printed-dipole antenna and its arrays for 5G applications. IEEE Antennas Wirel. Propag. Lett. **16**, 2183–2186 (2017)
11. Moreno, R.M., Kurvinen, J., Ala-Laurinaho, J., Khripkov, A., Ilvonen, J., van Wonterghem, J., Viikari, V.: Dual-polarized mm-wave endfire chain-slot antenna for mobile devices. IEEE Trans. Antennas Propag. **69**(1), 25–34 (2020)

12. Huo, Y., Dong, X., Xu, W.: 5G cellular user equipment: from theory to practical hardware design. IEEE Access **5**, 13992–14010 (2017)
13. Masoodi, I.S., Ishteyaq, I., Muzaffar, K., Magray, M.I.: Low-cost substrate based compact antennas for 4g/5g side-edge panel smartphone applications. Prog. Electromagn. Res. Lett. **91**, 145–152 (2020)
14. Magray, M.I., Karthikeya, G.S., Muzaffar, K., Koul, S.K.: Compact co-design of conformal 4G LTE and mmWave 5G antennas for mobile terminals. IETE J. Res. 1–12 (2019)
15. Kurvinen, J., Kähkönen, H., Lehtovuori, A., Ala-Laurinaho, J., Viikari, V.: Co-designed mm-wave and LTE handset antennas. IEEE Trans. Antennas Propag. **67**(3), 1545–1553 (2018)
16. Stutzman, W.L., Thiele, G.A.: Antenna theory and design. Wiley, New York (2012)
17. Yang, B., Yu, Z., Dong, Y., Zhou, J., Hong, W.: Compact tapered slot antenna array for 5G millimeter-wave massive MIMO systems. IEEE Trans. Antennas Propag. **65**(12), 6721–6727 (2017)
18. US Patent Application: Conformal antenna module with 3D-printed radome. No. 63033884
19. Karthikeya, G.S., Abegaonkar, M.P., Koul, S.K.: Gain compensated conformal antennas with pattern diversity for mmWave 5G smartphones. In: 2019 IEEE Indian Conference on Antennas and Propagation (InCAP), pp. 1–4. IEEE (2019, December)
20. Wani, Z., Abegaonkar, M.P., Koul, S.K.: Millimetre-wave antenna with wide-scan angle radiation characteristics for MIMO applications. Int. J. RF Microw. Comput.-Aided Eng. **29**(5), e21564 (2019)
21. Shim, J.Y., Go, J.G., Chung, J.Y.: A 1-D tightly coupled dipole array for broadband mmWave communication. IEEE Access **7**, 8258–8265 (2019)
22. Ikram, M., Al Abbas, E., Nguyen-Trong, N., Sayidmarie, K.H., Abbosh, A.: Integrated frequency-reconfigurable slot antenna and connected slot antenna array for 4G and 5G mobile handsets. IEEE Trans. Antennas Propag. **67**(12), 7225–7233 (2019)
23. Hwang, I.J., Ahn, B., Chae, S.C., Yu, J.W., Lee, W.W.: Quasi-Yagi antenna array with modified folded dipole driver for mmWave 5G cellular devices. IEEE Antennas Wirel. Propag. Lett. **18**(5), 971–975 (2019)
24. Hasan, M.N., Bashir, S., Chu, S.: Dual band omnidirectional millimetre wave antenna for 5G communications. J. Electromagn. Waves Appl. **33**(12), 1581–1590 (2019)
25. Pan, Y.M., Qin, X., Sun, Y.X., Zheng, S.Y.: A simple decoupling method for 5G millimetre-wave MIMO dielectric resonator antennas. IEEE Trans. Antennas Propag. **67**(4), 2224–2234 (2019)

Chapter 6
Highly Efficient Antennas for the Base Stations

6.1 Introduction

As we have seen in the preceding Chapters that higher data throughput could be achieved by migrating to millimeter wave frequencies and beyond [1, 2]. To envision this system with increased carrier frequency, the entire hardware infrastructure must be redesigned [3]. The hardware to be designed and deployed must happen on both the mobile terminal or device and the base station or access point. An important component to realize wireless links for future 5G networks is the antenna [4]. One of the solutions to realize a commercially feasible mmWave 5G network is to increase the transmitted power by at least 20–30 dB to mitigate the additional path loss [5]. This line of thinking is not sustainable due to poor power transmission of commercial amplifiers operating in the Ka band [6]. Traveling wave tube amplifiers might be a solution but would be commercially unfeasible due to high installation and maintenance costs [7]. The most popular approach to realize a feasible data link for mmWave 5G network is to increase the gains of the Tx/Rx (Transmitter/Receiver) antennas of the transceivers involved in the 5G cellular communication [3].

Increasing the electrical aperture would increase the forward gain of the antenna [8]. But the available real estate on a portable mobile device is limited [9]. Hence the effective radiated power transmitted by the antenna is an equally important criterion for the mmWave band antennas. To maximize the radiated power from an integrated antenna, several efficiency enhancement techniques have been reported in the literature [10]. It is anticipated that millimeter wave base station towers would be deployed in higher numbers compared to its 4G counterpart. This deployment would mean that high efficiency antennas would be necessary for all the constituents of the cellular communication system. The problem of radiation efficiency is critical for mmWave antennas as higher efficiency would mean higher transmitted or radiated power, which maximizes the reliability of the data link. Radiation efficiency was not at all a problem of concern for low frequency previous generation antennas since the antennas would be electrically small leading to poor radiation efficiencies. The same

S. K. Koul and K. G. S., *Antenna Architectures for Future Wireless Devices*,
Signals and Communication Technology,
https://doi.org/10.1007/978-981-16-7783-0_6

logic need not be extended for implementing mmWave antennas as the wavelength is 10.7 mm at 28 GHz, which implies that antennas with a respectable gain could be integrated on to mobile terminals with a panel height of 7 mm or lesser [8].

One of the most common and ubiquitous antennae designs for mmWave 5G applications is the PCB (Printed Circuit Based) based antennas [11, 12]. The popularity for this technique is that the standard manufacturing processes of 4G antennas could be extrapolated for mmWave 5G antennas. PCB based or dielectric based antennas tend to yield lesser gain with a corresponding decrease in the radiation efficiency [13]. A simple technique is to design antennas on a substrate with a nearly zero dielectric loss tangent but would increase the manufacturing cost hence losing out on the commercial viability.

Another alternative for increasing radiation efficiency is to realize the concept of micromachining with substrate like the CMOS (Complementary metal oxide semiconductor) process. Here the lossy dielectric is selectively removed beneath the radiating portion of the antenna. This concept is apparent in the silicon micromachined antennas [14]. The same technique could be scaled to regular panel mountable dielectrics with 3D-printing as demonstrated in [15]. The micromachined 3D-printed antenna would increase the overall size of the antenna thus might not be a potential candidate for future mmWave 5G applications. As the radiation efficiency is poor in CMOS based antennas, it is an unsuitable class of antennas for base stations or access points.

Another popular idea is substrate integrated waveguide (SIW) feeding technique, which would increase the efficiency of the antenna at the cost of increased complexity in fabrication and manufacturing cost [16, 17]. Air-filled SIW is another alternative without any relaxation in the fabrication process [18]. SIW based antennas do not forego the usage of dielectric hence leading to the component of dielectric loss with a subsequent reduction in radiation efficiency and the effective radiated power [18].

Minimal dielectric-based antennas such as the printed ridge gap (PRG) waveguide fed antennas also have a high radiation efficiency compared to their microstrip fed counterparts [19, 20]. PRG based antennas require precision manufacturing. It is also important to note that the higher end of the mmWave spectrum would require smaller unit cells of PRG. The computational resource requirement to realize a PRG based antenna is also high compared to an all-metallic antenna, for instance.

Recently, recessed ground technique has been reported in [21, 22]. The authors have micromachined an electrically large ground plane for efficiency enhancement. Even this technique has a dielectric component in the antenna. The only way to achieve maximum radiation efficiency is to design dielectric free antennas with highly conductive metals for mmWave 5G applications. The only component of loss in an all-metallic antenna is that of the finite conductivity of the metal used for fabrication. The impedance mismatch is not necessarily a feature specific to all-metallic antennas, hence neglected. In the exhaustively researched topic of mmWave 5G antennas, there are few articles based on all-metallic designs.

All-metallic antennas have been designed and deployed since the onset of commercial radio. But all-metallic antennas designed specifically for 5G applications is a recent research interest. All-metallic antennas designed for satellite and defence

applications [23] might not be directly applicable to 5G applications due to a different set of design requirements. This Chapter gives a comprehensive overview of highly efficient antennas for integration with the base station towers of mmWave 5G cellular systems. Initially, classification of all metallic antennas is presented followed by detailed analysis of each type of antenna.

6.2 Classification of All-Metallic Antennas

All-metallic antennas for 5G applications could be broadly categorized as aperture antennas and wire antennas. The broad classification is depicted in Fig. 6.1. The aperture and wire antennas are a generic classification which also works for dielectric based antennas. Aperture antennas have an active recognizable radiating aperture which aid in radiation. On the other hand, wire radiators have a simple dipole or monopole configuration which aid in the radiation. Aperture antennas could be further classified into four categories as additively manufactured, subtractively manufactured, cavity based and planar antennas. Sections 6.3–6.7 give a detailed explanation of these antennas and their operation.

Any all-metallic antenna has three components, as illustrated in Fig. 6.2, namely feed, impedance transformer and the radiating aperture. The feed could be probe-fed from a coaxial line [24], waveguide [25] or a piece of transmission line [11, 12]. The impedance transformer is typically a balun [26] which aids in impedance matching between the standard feed and the radiating aperture. The radiating aperture helps to

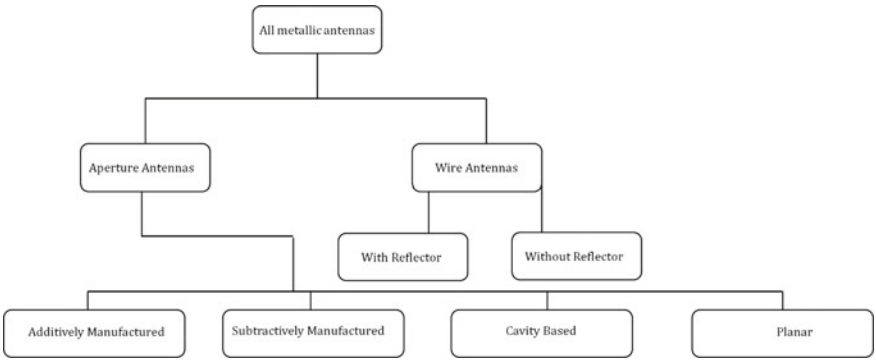

Fig. 6.1. Classification of all-metallic antennas

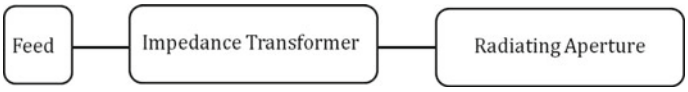

Fig. 6.2 Components of a generic all-metallic antenna

transmit waves from the antenna to free space. The following Sections gives details on these components of the antenna as well.

6.3 Additively Manufactured Antennas

A recent process of manufacturing or fabricating antennas is additive manufacturing (AM). Typically, 3D-printing is employed for building dielectric based antennas, wherein the dielectric scaffolding is initially printed and metallized by electroplating or a variation of it as illustrated in [27, 28]. Although these kinds of antennas could be realized with low investment and low turnaround time, the scaffolding would lead to higher dielectric loss hence cannot be classified as all-metallic antennas even though it appears to be so. It must also be noted that the joints, especially at the mouth of the feeding plane needs intricate metallization and might lead to additional losses [29].

The concept of additive manufacturing of all-metallic or dielectric-free antennas is illustrated in Fig. 6.3. This is a bottom-up approach of constructing antennas. Various techniques or processes could be used to realize the same. Techniques such as Selective Laser Sintering (SLS) or Direct Metal Laser Sintering (DMLS) are common methods. The primary idea is that metal powder is selectively burnt by a powerful controlled laser to build the geometry layer by layer [30]. This process is expensive and typically suffers from low turnaround time as the thickness of each layer built would be in the order of 10–50 μm [30]. The metal wastage is minimal compared to subtractive manufacturing technique. One of the disadvantages of additive manufacturing to realize all-metallic aperture antennas is the high surface roughness which attracts post-processing such as milling to improve the surface finish. The schematics of Fig. 6.3a illustrates the process of 3D-printing and a typical horn antenna built by this bottom-up approach is demonstrated in Fig. 6.3b. The dimensions feasible by this method of manufacturing are decided primarily by the laser sintering machine under use. Most of the commercially available laser sintering machine could be used for fabricating mmWave antenna if the upper frequency is less than 60 GHz, beyond which the performance metrics of the antenna might be compromised.

One of the advantages of additive manufacturing is that the prototype could be realized as single work piece [30] which avoids alignment errors due to fastening screws, typical in the commercial subtractive manufacturing. A double ridge square horn fabricated using an Aluminum alloy is shown in Fig. 6.4a, b. This antenna was reported in [31] manufactured using Selective Laser Melting (SLM) process. The surface roughness is less than 6 μm translating to 0.00056 λ computed at 28 GHz. This value of surface roughness does not typically reflect upon the gain or the input reflection coefficient as the surface roughness is minimal. The antenna's radiation characteristics is also like that of a simulated all-metallic smooth antenna model. The input reflection coefficient of the fabricated antenna is shown in Fig. 6.5a, the $|S_{11}|$ is less than 10 dB in the entire Ku-band, which is expected of a horn antenna which is well matched to the input waveguide feeding port and does not necessarily

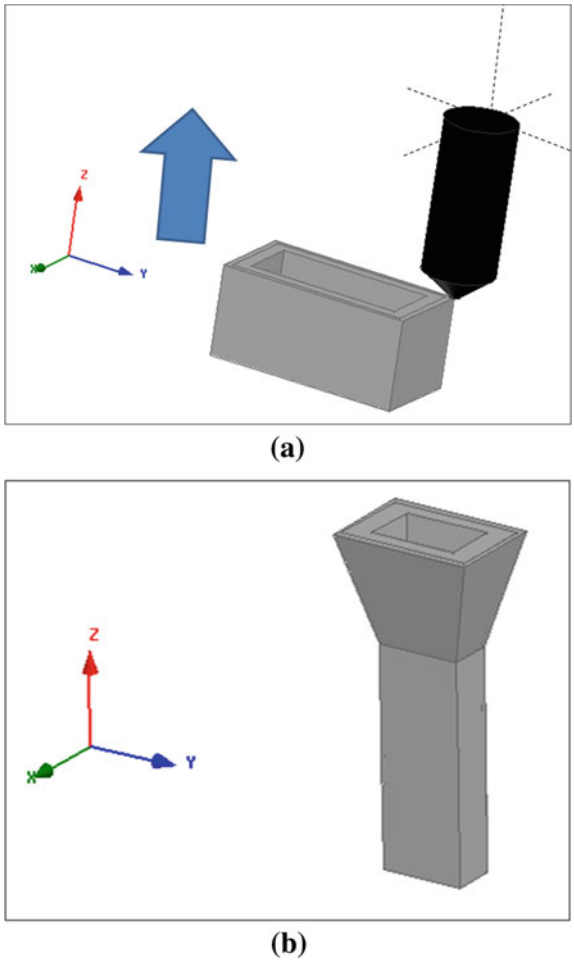

Fig. 6.3 **a** Schematics for additive manufacturing. **b** Layout of a typical horn antenna

distinguish between the fabrication method to realize the antenna. The deviation between simulated and measured curves is probably due to the alignment error at the feeding plane.

It must also be observed that the surface roughness at the intersection of the waveguide port and that of the antenna also contributes to the mismatch in $|S_{11}|$. Figure 6.5b illustrates radiation patterns at 18 GHz. It is evident that the mismatch between simulated and measured curves is minimal proving the feasibility of metallic printing. Forward gain also is comparable to the simulated values as observed in Fig. 6.6. The material used for metallic printing also has minimal influence on the gain if the bulk conductivity is comparable to that of the metals used for designing commercial Ka-band antennas. This manufacturing method could be easily extended up to 40 GHz without severe deterioration in the $|S_{11}|$, patterns and gain characteristics.

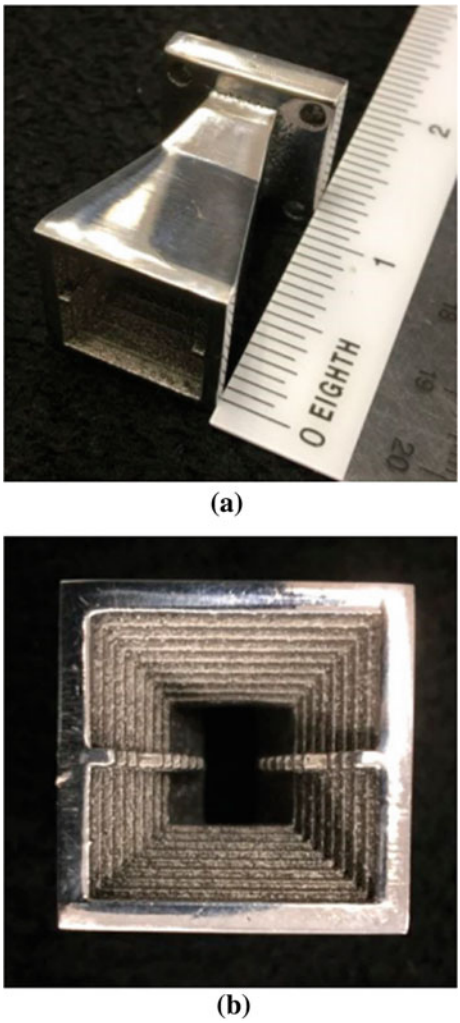

Fig. 6.4 **a** Isometric view of the additively manufactured antenna, **b** front view of the additively manufactured antenna [31]

Another all-metallic 3D-printed antenna operating in the Ku-band is reported in [32]. The authors have measured the surface roughness using a profilometer to benchmark the commercial Ku-band antenna and the 3D-printed element. The RMS (Root Mean Square) surface error was found to be 39.7 μm. This value of surface error is across the whole geometry of the feeding port and that of the aperture.

A gain difference of 1–2 dB is expected in the Ku-band. If the same design philosophy is extrapolated to the Ka-band, the gain difference might deteriorate to 2–3 dB, which means that 3D-printed all-metallic antennas might offer performance like that of the machined antennas. [33] also illustrates the difference in characteristics of antennas with 3D-printing and conventional machining technique. The fabrication method of metallic 3D-printing has been demonstrated up to 170 GHz in [30] and

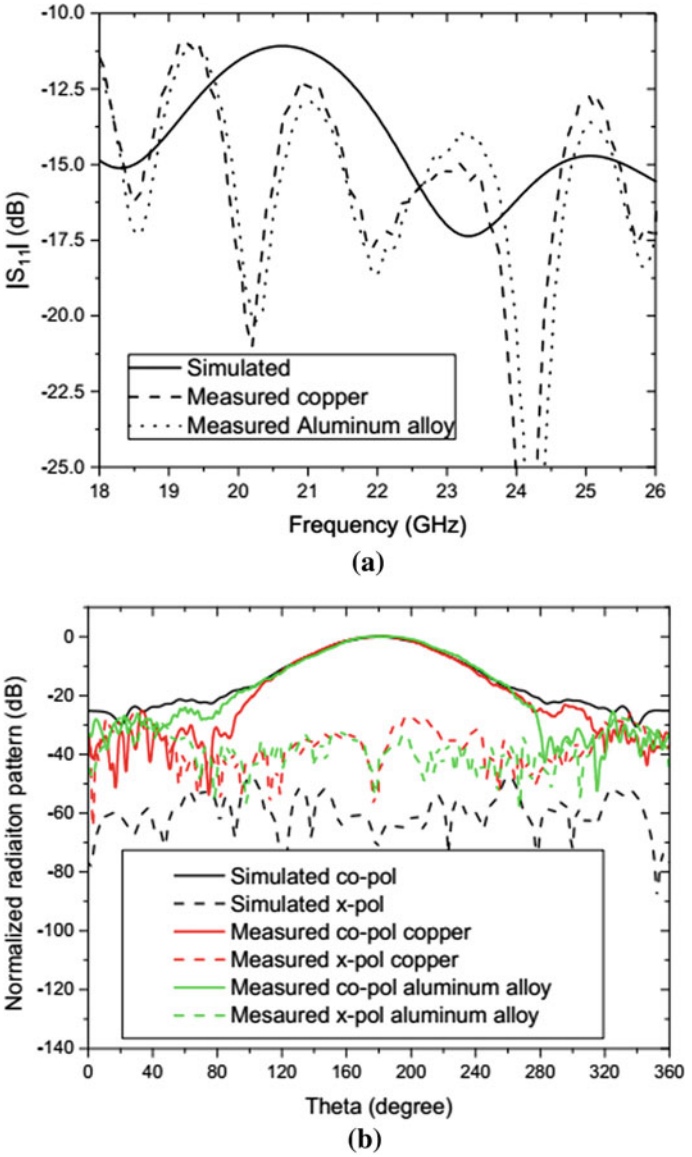

Fig. 6.5 **a** $|S_{11}|$ of the additively manufactured antenna, **b** Radiation patterns of the additively manufactured antenna [31]

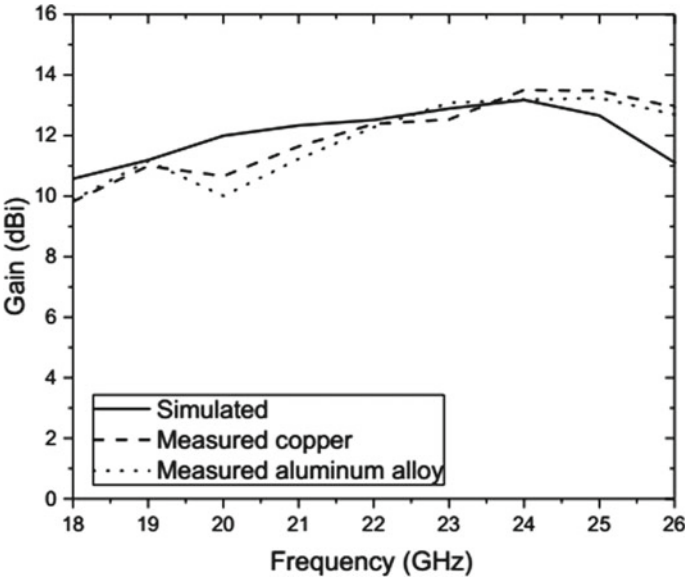

Fig. 6.6. Forward gain of the antenna [31]

the forward gain deterioration is close to 1 dB between the theoretical and measured values, proving the utility of additive manufacturing (AM) for sub-millimeter wave applications as well.

6.4 Subtractively Manufactured Antennas

Subtractive or reductive manufacturing is a commercially viable solution to realize all-metallic antennas. As the method has been around in the industry over decades, it is a relatively cheaper solution compared to AM. Subtractive manufacturing is a top-down approach wherein a solid block of metal would be machined away to realize a desired geometry.

A typical subtractive manufacturing is illustrated in Fig. 6.7a. Typically, a high precision tooling machine such as a CNC (Computer numerically controlled) is used to machine the solid block of metal. The metal wastage is higher than AM as it is a reductive process. The scrap metal could be fused together for recycling but is rarely practiced in the industry. The cutting tool as depicted in Fig. 6.7a has dimensions typically larger than the Ka-band antenna to be manufactured for 5G applications. For instance, the lateral dimension of the drill bit is 2–5 cm which translates to 1.8–4.6 λ at 28 GHz. In other words, the tooling part would have a hard time to manufacture intricate parts of an all-metallic antenna as the bulky tool head prohibits accessibility. Hence the designer must carefully engineer the actual fabrication by

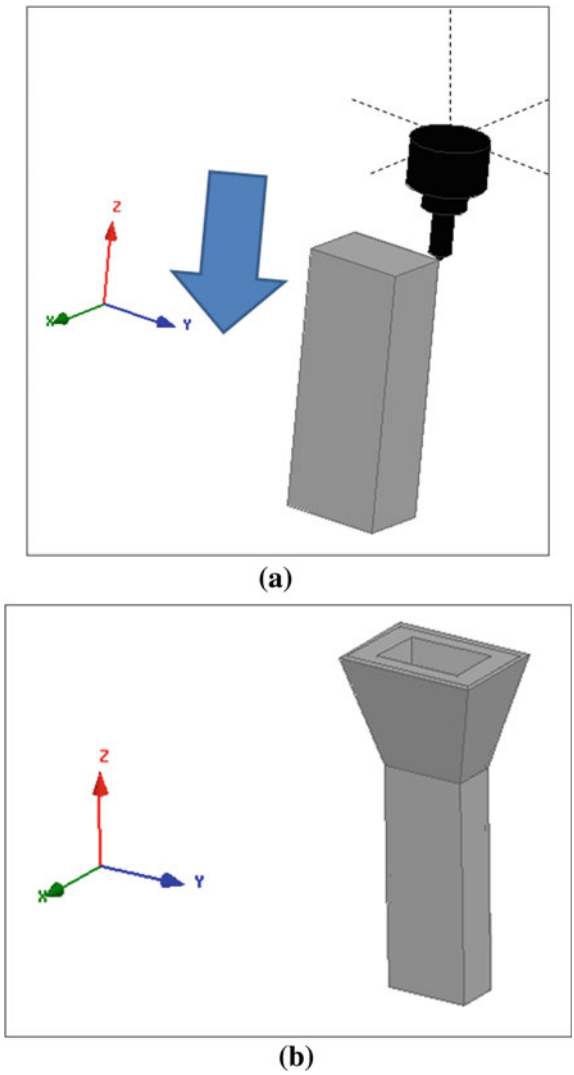

Fig. 6.7 **a** Typical setup for subtractive manufacturing. **b** A typical horn antenna

considering the feasibility of the tool head's movement in the coordinate axes. Hence, most of the aperture antenna designs would be based on split architecture, wherein the horn antenna would be first split along a reference axis in the CAD (Computer Aided Design) tool and both the tool parts would be machined separately.

Both these parts would be fastened together by screws or other mechanical locking mechanisms. The screws need additional clearance around the periphery of the antenna's radiating aperture. The placement of these fasteners is also frequency dependent, as they must be far away from the aperture to avoid unnecessary interference from the additional metallic footprint.

Another problem with the subtractive manufacturing is that the split blocks of the prototype would lead to alignment errors between the blocks when fastened together. This phenomenon is due to the finite tolerance of the machined prototype and that of the metallic screws. These alignment errors would manifest as poor impedance match of the antenna and might result in a shift in the phase center of the antenna leading to undesired beam tilt of the main beam. The alignment error could be mitigated by using laser assisted aligners which would increase the production cost. The schematics of a typical machined horn antenna is illustrated in Fig. 6.7b. The fastening mechanisms are not shown in the illustration.

A typical subtractively manufactured antenna is reported in [34] which operates in the W-band. The prototype is a CNC machined aluminum horn antenna. The split blocks and the space for mounting screws are apparent from the photograph. The radiating aperture is 7 mm × 7 mm (2.2 λ × 2.2 λ calculated at 94 GHz) but the overall size of the antenna with the additional clearance is 25 mm × 25 mm (7.8 λ × 7.8 λ calculated at 94 GHz). In other words, the additional metal loading required to realize a high frequency antenna is 357% which means that the metal footprint of at least 3 times is necessary to implement this genre of machined antennas. The metal loading would be much lesser when realizing Ka-band antenna. It must be noted that any subtractively manufactured aperture antenna has two sets of fastening screws. One set for mounting the antenna with the waveguide feed, the other set for fastening the split blocks of the machining.

$|S_{11}|$ is less than 10 dB across the operating bandwidth. The variation between simulated and measured curves is minimal. This performance metric is like that of an additively manufactured antenna. The surface roughness and the alignment error of the horn antenna has affected minimally. The reduction in radiation efficiency could be attributed to the finite conductivity of the metal used for fabrication.

Another subtractively manufactured Ka band antenna is illustrated in Fig. 6.8 as reported in [35]. Here the metallic loading for fastening the split blocks is lesser due to the lower frequency of operation compared to the previously presented W-band antenna. Figure 6.9 depicts the variation between subtractively manufactured (CNC)

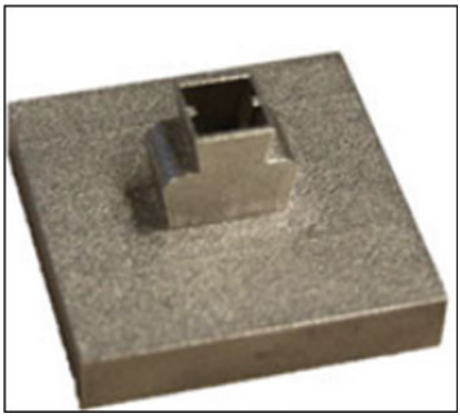

Fig. 6.8 Ka band antenna (Ignatenko et al. [35], reprinted with permission from IEEE)

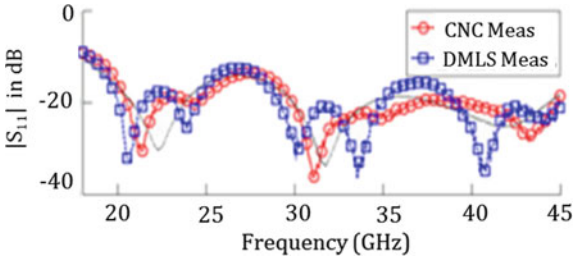

Fig. 6.9 $|S_{11}|$ of additively and subtractively manufactured Ka band antenna (Ignatenko et al. [35], reprinted with permission from IEEE)

and additively manufactured (DMLS) antennas. The error between the two curves is minimal proving that both the processes are readily feasible to fabricate Ka band antennas for 5G applications.

The ultra-wideband quad-ridge horn antennas of [36, 37] are fabricated by subtractive manufacturing. The same design process could be extrapolated to Ka-band antennas without any loss of generality. The coaxial-fed all-metallic antenna of [38] would be difficult to scale up to 28 GHz band as probe-feeding is unreasonable for all-metallic design at those high frequencies. A variant of horn antenna for compactness is reported in [39]. This is manufactured as a single piece horn antenna.

6.5 Cavity Based Antennas

Another category of aperture antenna which are designed with only metal is cavity based or cavity backed antennas, typically high gain antennas with high radiation efficiency and lower physical footprint is realized by cavity-based antennas instead of the horn or its variants. A generic layout of a cavity-based antenna is illustrated in Fig. 6.10, the feed is not explicitly shown in the schematics. It is implied that the feed could be probe-feed or waveguide feed or a variant of these feeding techniques.

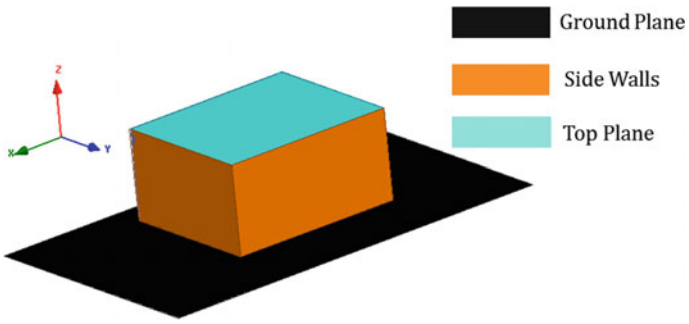

Fig. 6.10 Generic layout of a cavity-based antenna

The electrically large ground plane is primarily designed to prevent back radiation and to realize unidirectional beam.

The radiation aperture could be on the side walls or the top plane. For the side walls to act as a radiator, half-wavelength slots must be etched on the side walls by shorting the top plane. Similarly, to realize radiation from the top plane, radiating slot or an array of slots should be etched out on the top plane with shorted walls on the sides. The design constraint is decided by the application at hand and the gain-bandwidth requirements. Even though Fabry–Perot antennas such as the ones reported in [40, 41] are considered as cavity based antennas, the antenna construction involves a substrate leading to dielectric loss thus cannot be classified under the all-metallic antennas' banner.

One of the simple approaches to realize an all-metallic antenna is to design an electrically large ground plane which is shorted strategically to aid radiation from the fringing fields as demonstrated in [42]. This design is readily feasible for sub-6 GHz antennas, but this design approach needs to be realized in the mmWave spectrum. The problem with scaling this idea to 28 GHz is the implementational challenge to realize this design. The solder and other binding materials might lead to spurious radiation at 28 GHz. It could be an interesting topic for research.

Another variant of the cavity-based design is illustrated in [43]. Here the side walls act as radiator due to the 45° inclined slots. It is a quasi-omnidirectional antenna operating at 38 GHz as evident from the simulated and measured patterns presented in [43]. The fabricated prototype is realized using high precision defense grade CNC machining with tight tolerance and assembled with mounting screws.

A waveguide fed high gain cavity backed antenna is shown in Fig. 6.11, adapted from [44]. This is a multi-layer all-metallic design, wherein the electrically large metallic ground plane is fitted with a metallic structure which has a modified bow-tie slot, which doubles up as a coupler and impedance transformer to the radiating aperture. The radiating aperture has four slots as shown in Fig. 6.11a the same is extended to 64 slots for higher gain as shown in Fig. 6.11b. The overall dimension of the antenna array is $100 \times 100 \times 20$ mm^3 translating to $9.3\ \lambda \times 9.3\ \lambda \times 1.86\ \lambda$ at 28 GHz.

The input reflection coefficient is depicted in Fig. 6.12. The 10-dB impedance bandwidth is 24–31 GHz or 25.2%. The bandwidth is limited compared to the horn or all-metallic Vivaldi antenna. This is due to design of the impedance transformer and the electrically compact volume of the realized design. The curves also illustrate the tight tolerance of the impedance transformer layer to be attached with the feeding plate. The E-plane pattern at 28 GHz is shown in Fig. 6.13. The pattern and polarization integrity is high due to a dielectric-free design.

6.6 Planar or Quasi Planar Antennas

Planar antennas form another class of all-metallic antennas which are often neglected in the research community. A typical planar antenna is illustrated in Fig. 6.14a. It is an

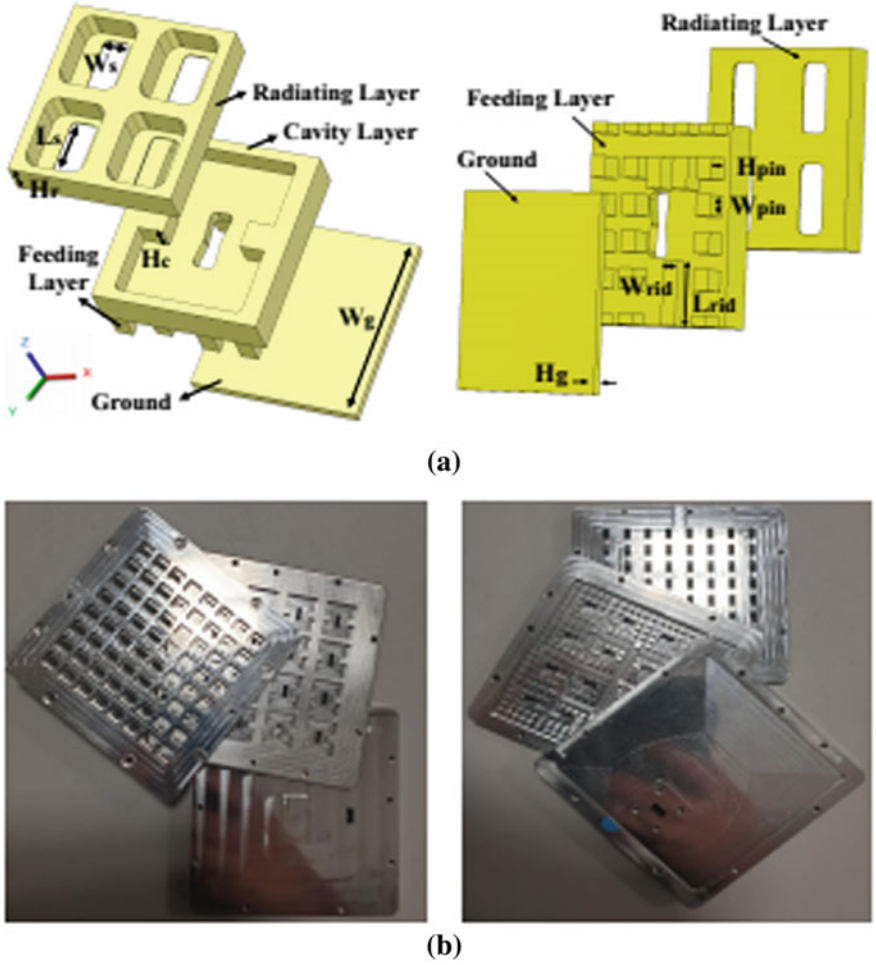

Fig. 6.11 Wideband Cavity backed Ka-band antenna: **a** Schematics. **b** Photographs (Yong et al. [44], reprinted with permission from IEEE)

inset fed microstrip patch antenna designed on a low dielectric constant substrate. The design principles of a microstrip fed patch antenna are well-known and several articles on the dielectric based passive antennas for 5G applications have been reported [11, 12].

Typical design of a planar all-metallic antenna is shown in Fig. 6.14b. Here, the antenna consists of a feed, an impedance transformer, and the radiating aperture. In the low frequency or the sub-6GHz spectrum, designing such antennas would be feasible with a probe-feed and a small ground but the same technique cannot be extrapolated to 28 GHz band due to the limitation in the ground plane design. The other option could be to design a micromachined substrate wherein the feed

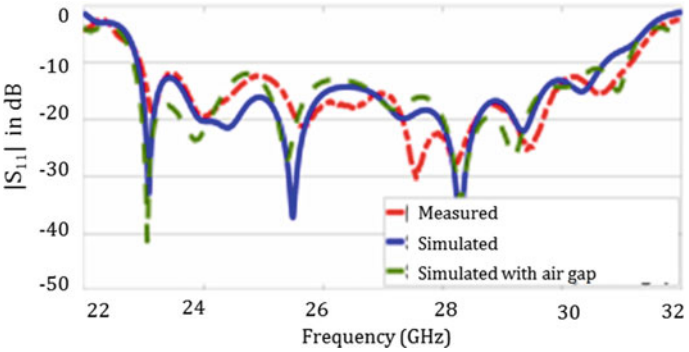

Fig. 6.12 $|S_{11}|$ of the wideband Ka-band antenna (Yong et al. [44], reprinted with permission from IEEE)

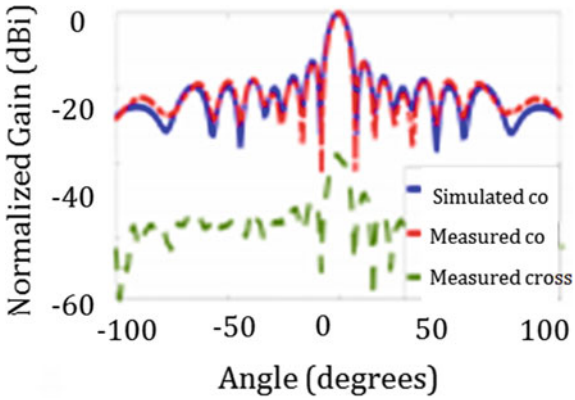

Fig. 6.13 E-plane pattern at 28 GHz (Yong et al. [44], reprinted with permission from IEEE)

line with the antenna is separated by the electrically large ground plane and both the metal geometries are probably held by an electrically small non-metallic scaffolding. Different feeding techniques such as ACS (Asymmetric Coplanar Stripline) or SIW might hold the key to realize all-metallic planar antennas for mmWave 5G band.

Radiation efficiency is of utmost importance for space and defense applications. The design of all metallic antenna shown in Fig. 6.15. as reported in [45] would be essentially for radar applications. It is designed on a 5 mm thick Aluminum slab, hence could be categorized as a quasi-planar element. It is a Vivaldi antenna wherein a coaxial feeding technique is used. The antenna element was fabricated using a subtractive manufacturing process called the wire-EDM (Electrical discharge machining) with a low surface roughness over the entire geometry. It is a wideband antenna operating in the 4–18 GHz band with reasonable pattern integrity as expected from a typical traveling wave antenna. The photograph of Fig. 6.15 shows an array which can scan $\pm$ 40º with low scanning loss. This design could be up-scaled to Ka-band by optimizing the aperture and balun feeding the aperture.

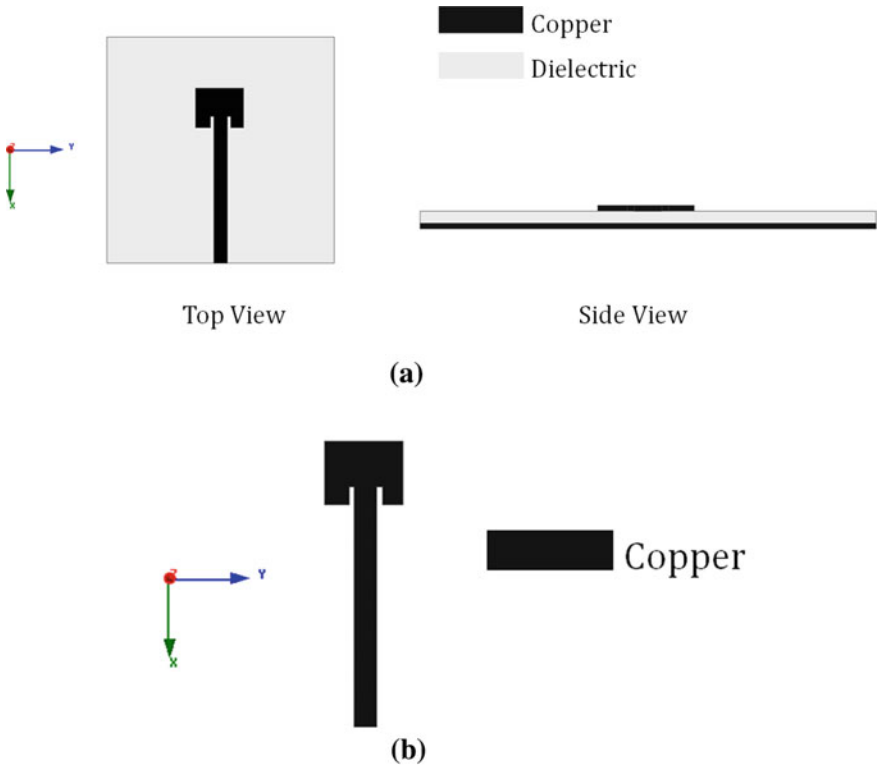

Fig. 6.14 Schematic of **a** A typical planar antenna. **b** A typical all-metallic planar antenna

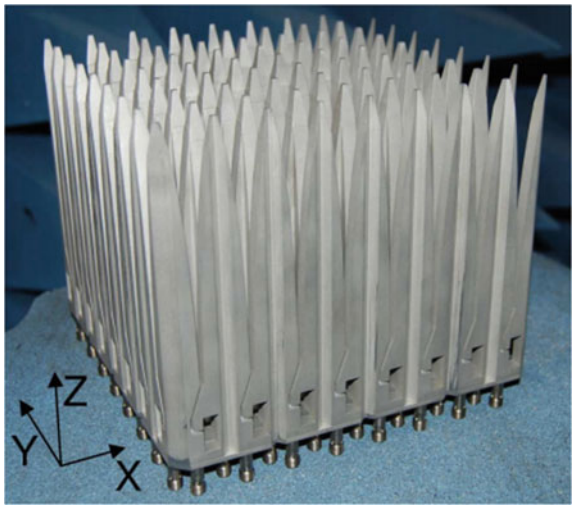

Fig. 6.15 An all-metallic Vivaldi array (Kindt and Pickles [45], reprinted with permission from IEEE)

Recent design reported by the authors in [46] is also a planar antenna designed on a 500 μm thick Copper sheet with high radiation efficiency and pattern integrity across the spectrum of operation centered around the 28 GHz band. It is also manufactured by a subtractive manufacturing process, which is chemical etching in this case. Planar all-metallic antennas with high pattern integrity and unidirectional beam operating at 28 GHz is an open-ended research topic now.

6.7 Wire or Wire-Based Antennas

Probably the simplest all-metallic antenna to implement is wire antennas. These are readily feasible in the lower frequency including the sub-6 GHz bands. The dipole length and the wire width would be easy to fabricate with conventional machining techniques. A typical mmWave dipole antenna is illustrated in Fig. 6.16. As evident from the figure, the half-wavelength dipole is of length 5.5 mm with a wire diameter of 0.5 mm. Even though this antenna could be fabricated, the feed must be designed specifically to realize this dipole. Also, the electrically large connector such as the end-launch connector would strongly influence the impedance and radiation characteristics of the dipole antenna.

The input reflection coefficient of the dipole is depicted in Fig. 6.17a. The dipole is strongly resonant at 28 GHz with a gain close to 2.5 dBi at 28 GHz, which is as per the theory of dipole antenna. The 3D radiation pattern at 28 GHz is shown in Fig. 6.17b. The electrically small connector such as the mini-SMP [47] could be used for minimal interference from the compact connector. But this technique might involve a small piece of non-metallic scaffolding which could be neglected.

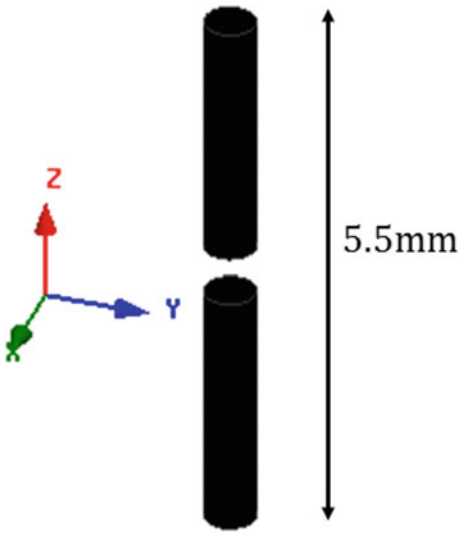

Fig. 6.16 A 28 GHz dipole antenna

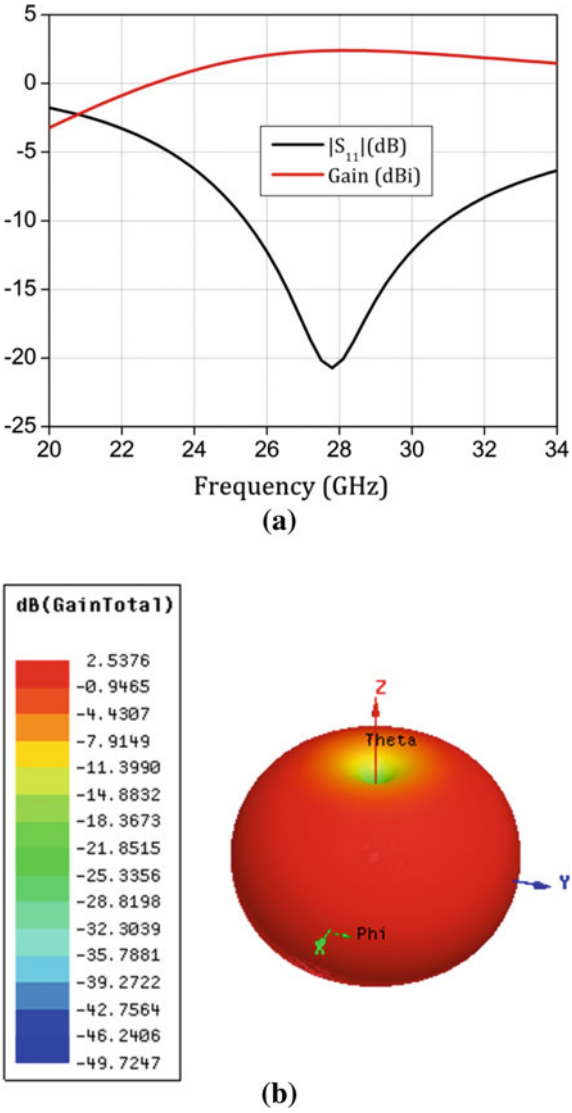

Fig. 6.17 **a** Input reflection coefficient and gain of dipole **b** 3D patterns of the dipole at 28 GHz

The origami inspired reflector integrated with a circularly-polarized helical antenna is reported in [48]. The antenna is designed at 3 GHz and could be scaled to 30 GHz with precision manufacturing. The prototype antenna is shown in Fig. 6.18. Another approach to realize all-metallic wire antenna is to use liquid metal alloy as demonstrated in [49] and shown in Fig. 6.19. The antenna is designed at 5 GHz and could be up-scaled to 28 GHz, assuming the resolution of the liquid metal fabrication permits the same. The scaffolding could be strategically removed for minimal dielectric loss.

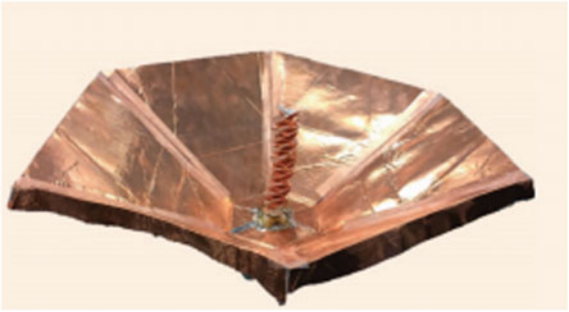

Fig. 6.18 Origami inspired antenna (Liu et al. [48], reprinted with permission from IEEE)

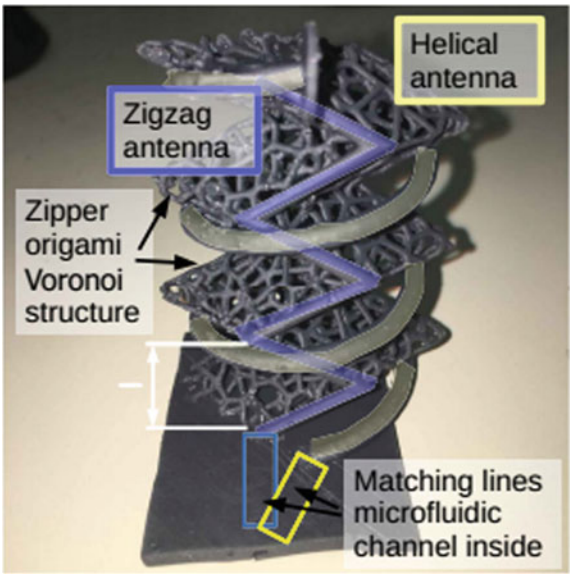

Fig. 6.19 Liquid metal antenna (Su et al. [49], reprinted with permission from IEEE)

6.8 Design Example of a Planar All-Metallic Antenna

Microstrip feeding would incorporate a dielectric and hence leads to losses. Same problem is observed with aperture coupling or proximity feed. To design a planar all-metallic antenna, CPW feeding technique is the preferred choice. But, designing a CPW feed is challenging at millimetre wave frequencies due to the inherent issues in realizing the dimensions necessary for matching the antenna with the 50 Ω of the port. For instance, to realize a 50 Ω CPW feeding line the trace width must be 2 mm with a gap of 20 μm. These dimensions would be impossible to achieve with standard chemical etching whose minimum resolution is only 50 μm. Hence, a feeding line of 78 Ω is designed which has a trace width of 2 mm and a gap of 0.2 mm. The arms of the planar traveling wave antenna would be based on CPS (Coplanar Stripline) which has a high impedance of 168 Ω. To match the characteristic impedance of 78 Ω of

the CPW feed with the 168 Ω of CPS lines of the radiator, a balun is introduced in between both these structures which doubles up as an impedance transformer.

The proposed coplanar waveguide fed planar all-metallic antenna is depicted in Fig. 6.20a. The inset of Fig. 6.20a clearly indicates the feeding structure of the antenna. The fabricated prototype is shown in Fig. 6.20b. The CPW feed is optimized for the 50 Ω port impedance of the end-launch connector. The connector type is 2.92 mm southwest end-launch connector which works up to 40 GHz. The width of the primary trace of the CPW feeding line is chosen to accommodate the grounding screws of the connector and to maintain feasible transition to the radiating aperture. The width of the overall antenna at the feeding plane is designed to incorporate the connector, the feeding width otherwise could be smaller. A balun is designed for impedance matching between the CPW feed line and the radiating aperture. Tapering of the antenna is optimized for a gain of 8 dBi in the end-fire. A copper sheet of 80 μm thickness was used for fabrication using industry standard chemical etching. Thinner copper sheets would be fragile to handle during chemical etching and thicker copper sheets would consume more time and chemicals for fabrication. In addition to this, thicker sheets beyond 500 μm would be difficult to clamp with the end-launch connector. A 3D-printed dielectric spacer of thickness 500 μm was used at the feed to prevent shorting of the trace pin and the clamping plate of the end-launch connector. This concept is unique to the class of planar all-metallic antennas.

Figure 6.21a illustrates the E-fields in the XY-plane for the proposed all-metallic antenna at 28 and 30 GHz. The transmission line mode and travelling wave modes are distinctly visible in the illustration. The balun acts as an impedance transformer from CPW to CPS (coplanar stripline). The variation of the input reflection coefficient with respect to the radius of the balun is shown in Fig. 6.21b, the parametric analysis clearly indicates that the radius of the balun is a key parameter to control the impedance matching. When the circular slot is 0.5 mm, the CPW feed is poorly matched with the CPS antenna. On the other hand, the antenna is detuned to 29 GHz when the slot radius is 1.5 mm. Hence, the optimal radius is 1 mm.

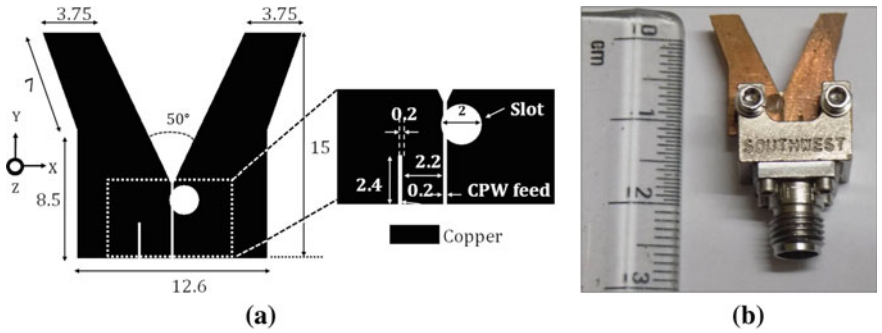

Fig. 6.20 Proposed all-metallic planar antenna. **a** Schematic of the all-metallic antenna (Units: mm). **b** Photograph of the fabricated prototype [46]

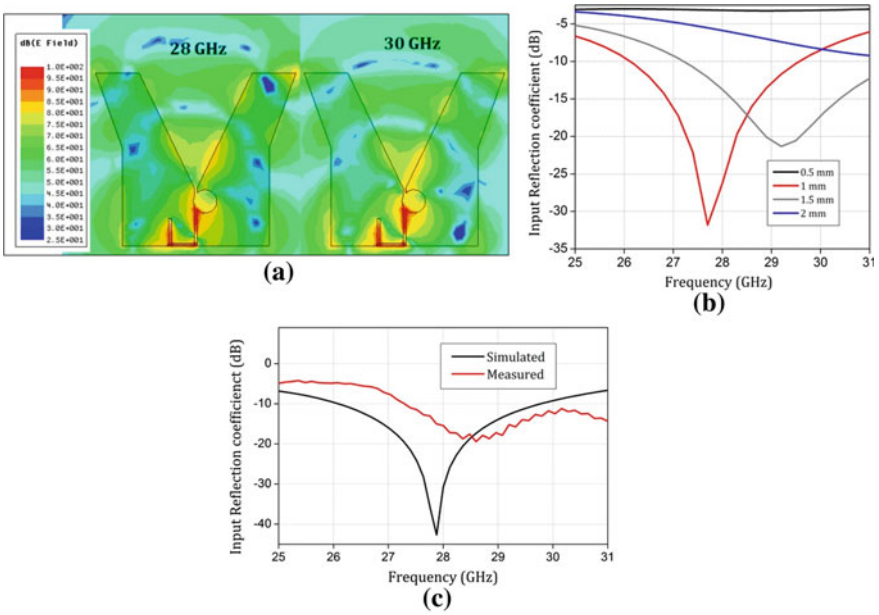

Fig. 6.21 **a** E-fields at 28 and 30 GHz. **b** Parametric analysis of the antenna. **c** Input reflection coefficients of the proposed all-metallic antenna [46]

The input reflection coefficient of the proposed element is depicted in Fig. 6.21c. The simulated 10 dB impedance bandwidth is from 26 to 30 GHz translating to 14.3%, but the measured impedance bandwidth is from 27.2 to 31 GHz translating to 13%. The effects of electrically large connector were not accounted for in full-wave simulations in Ansys HFSS. The discrepancy between simulation and measured results is due to lack of soldering at the transition of the antenna with the connector It must also be noted that the spacer included in the measurements to avoid shorting of the trace pin and the grounding plate of the end-launch connector has created deviation from the simulated curve. it is well known that the characteristic impedance of the end-launch connector is close to 50 Ω up to and including 40 GHz. The deviation might also be due to the bending stress encountered at the transition between the trace pin of the connector and the antenna, due to multiple mating cycles of the connector.

The E-plane (XY plane) radiation patterns are shown in Fig. 6.22a for 28 and 30 GHz, the beamwidth is 36° ± 0.5°, indicating high pattern integrity across the band. The H-plane (YZ plane) patterns are illustrated in Fig. 6.22b. The front to back ratio is more than 10 dB despite the electrically small ground.

The cross-polarization level is less than 30 dB across the band, in the E-plane as the radiator is coplanar with minimal radiation in the orthogonal polarization. The forward gain is close to 8 dBi at 28 GHz indicating high gain yield for minimal physical footprint. The gain variation is within 1 dB across the band as observed in

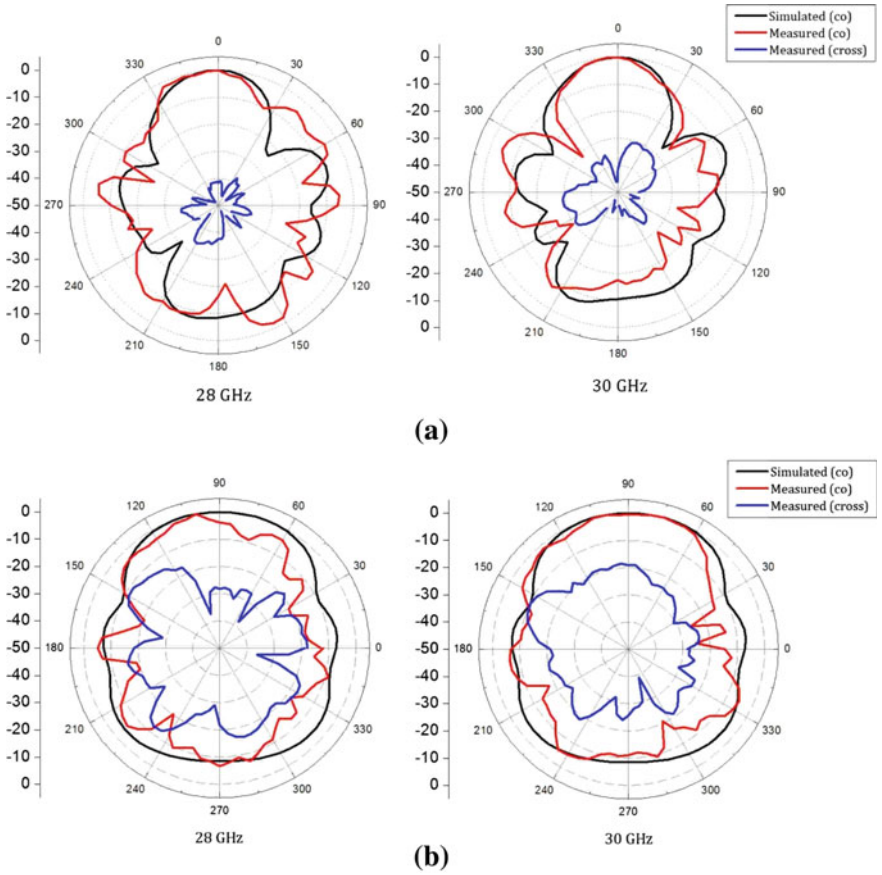

Fig. 6.22 Radiation patterns of the all-metallic antenna: **a** E-plane. **b** H-plane [46]

Fig. 6.23. The measurement was done using the gain transfer method. The discrepancy between the simulated and measured results is primarily due to the alignment error during measurement. Customized stands with laser aligners would have improved the measurement results. The dielectric based antenna for the same physical dimensions would yield a gain of close to 7.5 dBi.

It must also be noted that the dielectric based antenna has a limitation on the power handling capability due to the inherent dielectric breakdown. On the other hand, all-metallic design has a relatively higher power handling capability proving to be a useful design feature for access points. The typical power handling requirement for indoor access points would be in the range of +30 to +50 dBm. A comparison of simulated radiation efficiency of the proposed all-metallic antenna and conventional PCB antenna based on Nelco NY9220 substrate of 500 μm thickness and dielectric loss tangent of 0.0009 is depicted in Fig. 6.24. The proposed antenna has a radiation efficiency of 99.5%, the only loss encountered in the proposed antenna is that of

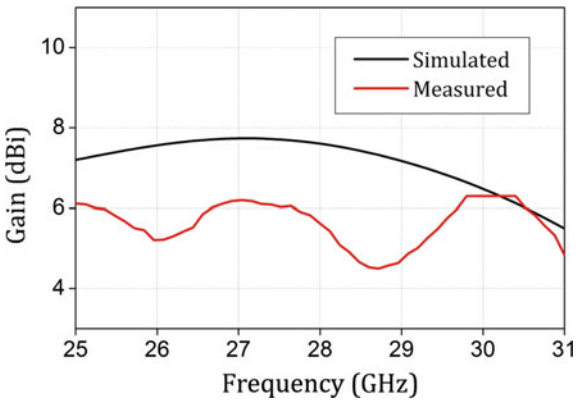

Fig. 6.23 Forward gain of the proposed antenna [46]

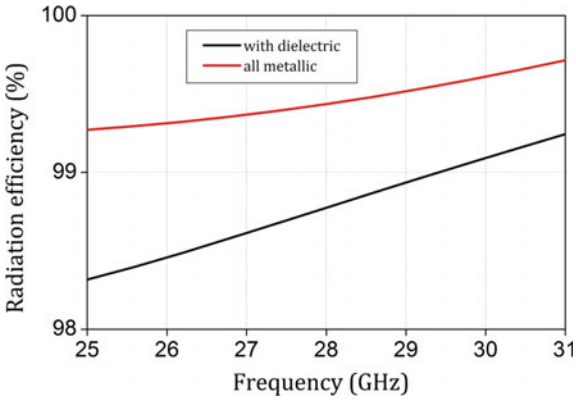

Fig. 6.24 Radiation efficiency of the proposed antenna [46]

the finite conductivity of copper. The other alternate strategy for radiation efficiency enhancement is to use electrically thinner substrate, which increases the cost of manufacturing.

To achieve beam switching for wide angular coverage a compact co-polarized stacked multi-beam module is proposed. Conventional phased arrays designed for beam scanning suffers from scanning loss, hence degrading the beam integrity during scanning. A co-polarized stacking beam switching module is proposed as observed in Fig. 6.25a and the fabricated prototype is shown in Fig. 6.25b. The distance between the antenna elements is maintained at 10 mm to accommodate the end-launch connector. In addition to this, if the antenna elements are mounted closer, then the central element's pattern would be distorted due to waveguiding effect of the top and bottom metallic antennas. A customized 3D-printed scaffolding was designed using polylactic acid (PLA) material, with a dielectric constant of 2.75 and a loss tangent of 0.015. The scaffolding does not influence the radiation characteristics of the mounted antennas. Additional scaffoldings were designed for holding the bulky connector and the radiating beams were measured one port at a time.

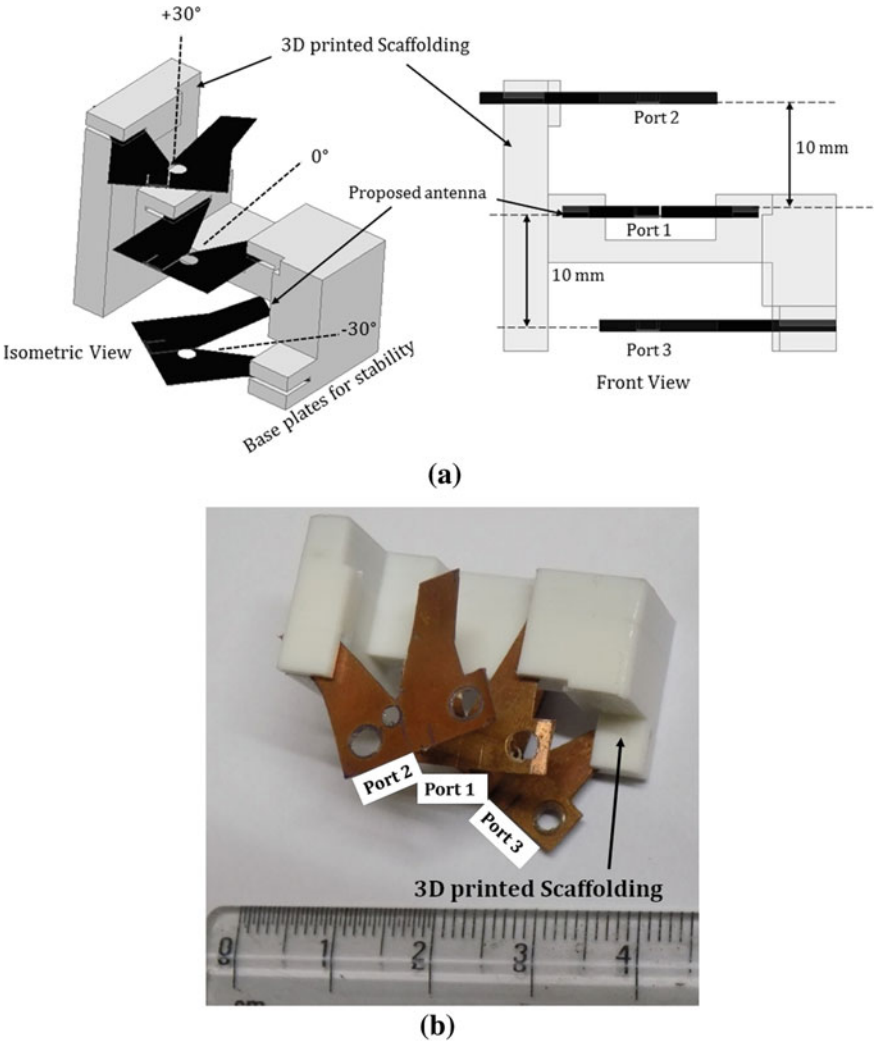

Fig. 6.25 Beam switching module: **a** Schematic of the module (units: mm). **b** Photograph of the fabricated module (isometric view) [46]

The orientation of the individual antennas is to maintain a reasonable angular coverage. The angular coverage of the beam switching module is ± 50° as seen in Fig. 6.26a. The simulated mutual coupling is less than 25 dB across the band and ports as seen in Fig. 6.26b, primarily due to low cross-polarization levels of individual radiators and its associated angular orientation. It is assumed that a high isolation SP3T (Single Pole Triple throw) switch would switch the antennas depending on the users required in that specific angular zone.

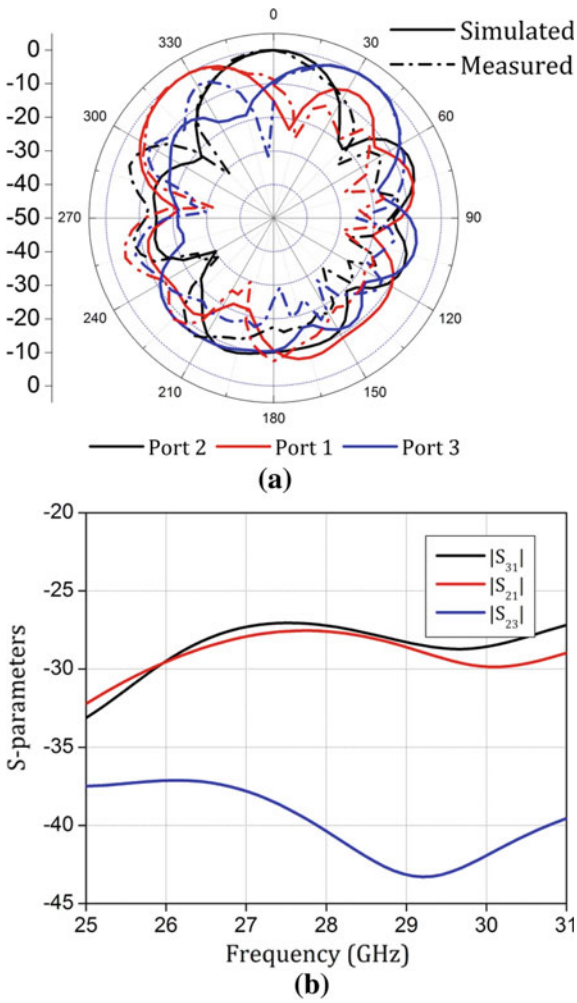

Fig. 6.26 **a** Radiation pattern of the module at 28 GHz. **b** Mutual Coupling of the stacked module [46]

6.9 Conclusion

All-metallic antennas are an important class of antennas for high radiation efficiency applications especially for base stations and access points. This Chapter presented a classification of all-metallic antennas with adequate design examples for each category. Every section of the antenna category is explained by a generic explanation of the type of the antenna followed by design examples. An all-metallic antenna design example is also explained.

References

1. Rappaport, T.S., Sun, S., Mayzus, R., Zhao, H., Azar, Y., Wang, K., et al.: Millimetre wave mobile communications for 5G cellular: it will work! IEEE Access **1**, 335–349 (2013)
2. Hong, X., Wang, J., Wang, C.X., Shi, J.: Cognitive radio in 5G: a perspective on energy-spectral efficiency trade-off. IEEE Commun. Mag. **52**(7), 46–53 (2014)
3. Roh, W., Seol, J.Y., Park, J., Lee, B., Lee, J., Kim, Y., et al.: Millimeter-wave beamforming as an enabling technology for 5G cellular communications: theoretical feasibility and prototype results. IEEE Commun. Mag. **52**(2), 106–113 (2014)
4. Hong, W., Baek, K., Lee, Y., Kim, Y.G.: Design and analysis of a low-profile 28 GHz beam steering antenna solution for future 5G cellular applications. In: 2014 IEEE MTT-S International Microwave Symposium (IMS2014), pp 1–4. IEEE (2014)
5. Friis, H.T.: A note on a simple transmission formula. Proc. IRE **34**(5), 254–256 (1946)
6. Campbell, C.F., Liu, Y., Kao, M.Y., Nayak, S.: High efficiency Ka-band gallium nitride power amplifier MMICs. In: 2013 IEEE International Conference on Microwaves, Communications, Antennas and Electronic Systems (COMCAS 2013), pp. 1–5. IEEE (2013, October)
7. Jiang, X., Ortiz, S.C., Mortazawi, A.: A Ka-band power amplifier based on the traveling-wave power-dividing/combining slotted-waveguide circuit. IEEE Trans. Microw. Theory Tech. **52**(2), 633–639 (2004)
8. Garg, R., Bhartia, P., Bahl, I.J., Ittipiboon, A.: Microstrip Antenna Design Handbook. Artech House (2001)
9. Huo, Y., Dong, X., Xu, W.: 5G cellular user equipment: from theory to practical hardware design. IEEE Access **5**, 13992–14010 (2017)
10. Yusuf, Y., Cheng, H., Gong, X.: A seamless integration of 3-D vertical filters with highly efficient slot antennas. IEEE Trans. Antennas Propag. **59**(11), 4016–4022 (2011)
11. Ta, S.X., Choo, H., Park, I.: Broadband printed-dipole antenna and its arrays for 5G applications. IEEE Antennas Wirel. Propag. Lett. **16**, 2183–2186 (2017)
12. Jilani, S.F., Alomainy, A.: A multiband millimeter-wave 2-D array based on enhanced Franklin antenna for 5G wireless systems. IEEE Antennas Wirel. Propag. Lett. **16**, 2983–2986 (2017)
13. Karthikeya, G.S., Koul, S.: Insights into fabrication and measurements of PCB-based passive Millimetre wave antennas. In: IETE Technical Review, pp. 1–8 (2020)
14. Singh, V.K.: Ka-band micromachined microstrip patch antenna. IET Microwaves Antennas Propag. **4**(3), 316–323 (2010)
15. McKerricher, G., Titterington, D., Shamim, A.: A fully inkjet-printed 3-D honeycomb-inspired patch antenna. IEEE Antennas Wirel. Propag. Lett. **15**, 544–547 (2015)
16. Ashraf, N., Haraz, O., Ashraf, M.A., Alshebeili, S.: 28/38-GHz dual-band millimeter wave SIW array antenna with EBG structures for 5G applications. In: 2015 International Conference on Information and Communication Technology Research (ICTRC), pp. 5–8. IEEE (2015, May)
17. Wei, D.J., Li, J., Yang, G., Liu, J., Yang, J.J.: Design of compact dual-band SIW slotted array antenna. IEEE Antennas Wirel. Propag. Lett. **17**(6), 1085–1089 (2018)
18. Ghiotto, A., Parment, F., Vuong, T.P., Wu, K.: Millimetre-wave air-filled SIW antipodal linearly tapered slot antenna. IEEE Antennas Wirel. Propag. Lett. **16**, 768–771 (2016)
19. Benavides-Vazquez, J., Vazquez-Roy, J.L., Rajo-Iglesias, E.: High-gain resonant continuous transverse stub array using ridge gap-waveguide technology. In: 2020 14th European Conference on Antennas and Propagation (EuCAP), pp. 1–4. IEEE (2020, March)
20. Hsieh, C.K., Kehn, M.N.M., Rajo-Iglesias, E.: Design of a transverse slot array in groove gap waveguide using horns at 28 GHz band. In: 2019 IEEE International Symposium on Antennas and Propagation and USNC-URSI Radio Science Meeting, pp. 2045–2046. IEEE (2019, July)
21. Jaiswal, A., Abegaonkar, M.P., Koul, S.K.: Highly efficient, wideband microstrip patch antenna with recessed ground at 60 GHz. IEEE Trans. Antennas Propag. **67**(4), 2280–2288 (2019)
22. Jaiswal, A., Abegaonkar, M.P., Koul, S.K.: Impedance transformer for recessed ground patch antenna at 60 GHz. IEEE Antennas Wirel. Propag. Lett. **18**(10), 2036–2040 (2019)

23. Kumar, P., Kedar, A., Singh, A.K.: Design and development of low-cost low sidelobe level slotted waveguide antenna array in X-band. IEEE Trans. Antennas Propag. **63**(11), 4723–4731 (2015)
24. Sharma, Y., Sarkar, D., Saurav, K., Srivastava, K.V.: Three-element MIMO antenna system with pattern and polarization diversity for WLAN applications. IEEE Antennas Wirel. Propag. Lett. **16**, 1163–1166 (2016)
25. Anderson, J.M., Hatch, T.: U.S. Patent No. 8,248,321. U.S. Patent and Trademark Office, Washington, DC (2012)
26. Schaubert, D.H., Kasturi, S., Boryssenko, A.O., Elsallal, W.M.: Vivaldi antenna arrays for wide bandwidth and electronic scanning. In: The Second European Conference on Antennas and Propagation, EuCAP 2007, pp. 1–6. IET (2007, November)
27. Ghazali, M.I.M., Park, K.Y., Byford, J.A., Papapolymerou, J., Chahal, P.: 3D printed metalized-polymer UWB high-gain Vivaldi antennas. In: 2016 IEEE MTT-S International Microwave Symposium (IMS), pp. 1–4. IEEE (2016, May)
28. Tak, J., Kang, D.G., Choi, J.: A lightweight waveguide horn antenna made via 3 D printing and conductive spray coating. Microw. Opt. Technol. Lett. **59**(3), 727–729 (2017)
29. Yao, H., Sharma, S., Henderson, R., Ashrafi, S., MacFarlane, D.: Ka band 3D printed horn antennas. In: 2017 Texas Symposium on Wireless and Microwave Circuits and Systems (WMCS), pp. 1–4. IEEE (2017, March)
30. Zhang, B., Zhan, Z., Cao, Y., Gulan, H., Linner, P., Sun, J., et al.: Metallic 3-D printed antennas for millimeter-and submillimeter wave applications. IEEE Trans. Terahertz Sci. Technol. **6**(4), 592–600 (2016)
31. Zhang, B., Guo, Y.X., Sun, H., Wu, Y.: Metallic, 3D-printed, K-band-stepped, double-ridged square horn antennas. Appl. Sci. **8**(1), 33 (2018)
32. Garcia, C.R., Rumpf, R.C., Tsang, H.H., Barton, J.H.: Effects of extreme surface roughness on 3D printed horn antenna. Electron. Lett. **49**(12), 734–736 (2013)
33. Lomakin, K., Pavlenko, T., Sippel, M., Gold, G., Helmreich, K., Ankenbrand, M., et al.: Impact of Surface Roughness on 3D Printed SLS Horn Antennas (2018)
34. Al-Tarifi, M.A., Filipovic, D.S.: On the design and fabrication of W-band stabilised-pattern dual-polarised horn antennas with DMLS and CNC. IET Microwaves Antennas Propag. **11**(14), 1930–1935 (2017)
35. Ignatenko, M., Simakauskas, B., Notaros, M., Filipovic, D.S.: A phase center-stabilized K/Ka/V-band linearly polarized horn for Luneburg lenses. IEEE Antennas Wirel. Propag. Lett. **16**, 2726–2729 (2017)
36. Dehdasht-Heydari, R., Hassani, H.R., Mallahzadeh, A.R.: A new 2–18 GHz quad-ridged horn antenna. Progr. Electromagn. Res. **81**, 183–195 (2008)
37. Jacobs, O.B., Odendaal, J.W., Joubert, J.: Quad-ridge horn antenna with elliptically shaped sidewalls. IEEE Trans. Antennas Propag. **61**(6), 2948–2955 (2013)
38. Kolosowski, W., Gajewski, P., Jeziorski, A., Sedek, E.: The dielectric-free tapered slot antennas array. In: 2006 European Conference on Wireless Technology, pp. 257–260. IEEE (2006, September)
39. Sun, J., Li, T., Dou, W., Meng, H.: A low-profile horn antenna at Ka-band. In: 2020 IEEE MTT-S International Microwave Workshop Series on Advanced Materials and Processes for RF and THz Applications (IMWS-AMP), pp. 1–3. IEEE (2020, July)
40. Qin, F., Gao, S., Wei, G., Luo, Q., Mao, C., Gu, C., et al.: Wideband circularly polarized Fabry-Perot antenna [antenna applications corner]. IEEE Antennas Propag. Mag. **57**(5), 127–135 (2015)
41. Qin, P.Y., Ji, L.Y., Chen, S.L., Guo, Y.J.: Dual-polarized wideband Fabry-Perot antenna with quad-layer partially reflective surface. IEEE Antennas Wirel. Propag. Lett. **17**(4), 551–554 (2018)
42. Chang, L., Li, Y., Zhang, Z., Feng, Z.: Compact all-metallic cavity-cascaded antenna. Electron. Lett. **52**(6), 413–414 (2016)
43. Verma, P.K., Kumar, R., Singh, M.: Ka-band circularly polarised omnidirectional antenna for wide elevation coverage. Electron. Lett. **50**(22), 1563–1564 (2014)

44. Yong, W.Y., Haddadi, A., Emanuelsson, T., Glazunov, A.A.: A bandwidth-enhanced cavity-backed slot array antenna for mmWave fixed-beam applications. IEEE Antennas Wirel. Propag. Lett. **19**(11), 1924–1928 (2020)
45. Kindt, R.W., Pickles, W.R.: Ultrawideband all-metal flared-notch array radiator. IEEE Trans. Antennas Propag. **58**(11), 3568–3575 (2010)
46. Karthikeya, G.S., Abegaonkar, M.P., Koul, S.K.: CPW-Fed All-metallic vivaldi antennas with pattern diversity for millimeter wave 5G access points. Progr. Electromagn. Res. **94**, 41–49 (2020)
47. https://www.radiall.com/media/files/SMPM.pdf
48. Liu, X., Georgakopoulos, S.V., Rao, S.: A design of an origami reconfigurable QHA with a foldable reflector [antenna applications corner]. IEEE Antennas Propag. Mag. **59**(4), 78–105 (2017)
49. Su, W., Nauroze, S.A., Ryan, B., Tentzeris, M.M.: Novel 3D printed liquid-metal-alloy microfluidics-based zigzag and helical antennas for origami reconfigurable antenna "trees". In: 2017 IEEE MTT-S International Microwave Symposium (IMS), pp. 1579–1582. IEEE (2017, June)

Chapter 7
Pattern Diversity Architectures for Base Stations

7.1 Introduction

Base station design and deployment is equally important as that of the portable hand-held wireless terminals. This necessity is apparent in the mmWave 5G deployment, due to the layout of the 5G base stations in each geography. Base stations would be operational for a longer duration of time compared to the portable wireless devices engaged in communication; a typical base station would be serving myriad of devices simultaneously throughout a given timeframe. One of the critical components of a base station is the antenna system.

The 4G base stations were straightforward to design: three high gain antennas to cover the entire azimuthal plane. Extrapolating the same logic to high frequency 5G systems might not yield the desired angular coverage with adequate gains of the radiators. Also, placement of 5G antennas within a tower is also important, as increasing the height to 30 ft or 10 m (as seen in the current 4G systems) would severely degrade the signal received on the smartphone in the 5G domain. Design of 5G base stations needs careful examination in terms of the performance metrics and placement within the tower for optimal coverage.

The most popular solution to design mmWave 5G base station antennas is phased arrays, as reported in [1–5]. The phased array operates very well within a narrow angular range with decent pattern integrity. In any phased array, scanning loss would increase as the beam is scanned away from the intended boresight axis. As we have seen in earlier Chapters, high gain is required even in the base stations, which means that the number of elements required in a phased array would be high, further complicating the beam control algorithm and implementation. Also, the complexity increases multi-fold when multiple users access a particular base station. The problem with phased arrays is its inability to deliver multiple beams simultaneously [6]. Design of phase shifters for a wide bandwidth centred around 28 GHz also would be challenging. Due to the design constraint of the phase shifters, the performance of the phased array would be limited.

S. K. Koul and K. G. S., *Antenna Architectures for Future Wireless Devices*,
Signals and Communication Technology,
https://doi.org/10.1007/978-981-16-7783-0_7

The other class of antennas for wide angular coverage on base stations is leaky wave antennas [7, 8]. Here, beam scanning is achieved by varying the center frequency, for instance, a 15° change in the primary beam could be achieved by a 20% change in the operating frequency. If we look at commercially deployed cellular systems, the bandwidth available would be around 5–10% of the allotted carrier frequency. If this logic is applied to the leaky wave antenna, then a simple 15° beam-tilt itself would detune the antenna beyond the bandwidth acquired by the commercial carrier. It must also be noted that the pattern integrity deteriorates as the beam is scanned away from the primary axis, like the behavior of phased arrays.

Another alternate approach for base stations is pattern reconfigurable designs, like the ones reported in [9, 10]. Here, active elements such as diodes or transistors would be selectively switched to achieve a desired pattern. Even though this concept works well in the RF and microwave frequencies, extrapolating to the 28 GHz band would be challenging. The bias circuitry for the active components would contribute to radiation, thus compromising pattern integrity of the antenna. Also, high-speed switching within the radiator might not be reliable after a certain number of switching cycles.

Hence multiport beam switchable antenna systems seem to be an attractive candidate for 5G base stations and the same shall be explored in this Chapter.

7.2 Beam Switching in 5G Base Stations

This Section explains the technical requirements for beam switchable antenna systems for 5G base stations. High gain antennas should be activated when a particular port is triggered. The actual value of gain depends on the pumped power, distance, and frequency of operation. Typically, gain of 8–12 dBi would be good enough for base stations. Any value lower would lead to decreased distance between the base station and the mobile device. Any value higher would lead to narrower beam, indicating a need to incorporate more than 3 or 4 elements in the antenna system, further complicating the design. The designer must first consider the angular coverage required, and then work backwards on the antenna architecture.

Typically, a coverage range of the entire 360° would be required for most of the applications, the same could be implemented by replicating antenna modules of lower coverage for better spatial efficiency. For instance, if a single antenna setup or module covers 120°, then three such modules would cover the entire azimuth. The angle at which the antenna would be tilted with respect to the vertical axis is discussed in Sect. 2.6.

The antenna module must be physically and electrically compact. A typical antenna module might be accommodated within 50 mm × 50 mm × 50 mm. Multiport compact antenna systems could be realized with shared radiator and/or shared ground concept, which aids in compactness. Increasing aperture efficiency of the constituent antennas would lead to compaction of the entire module. Miniaturization

techniques of the microwave domain [11, 12] would lead to poor pattern integrity in the mmWave domain.

The antenna module should be easily compatible with dielectric radome. Most of the base station towers would be deployed outdoors, which in turn would be exposed to the environmental elements. Thus, radome integration is necessary. The antenna module's performance metrics should be invariant of the radome integration. A gain deterioration of 0.5–1 dB across the band post integration with radome will result in a decent design.

Power handling capacity of antennas is not a critical parameter, as most of the mmWave 5G base stations would work on low power, typically +30 to +50 dBm per antenna. The designer must ensure that the constituent antennas do not get detuned due to thermal expansion of the metallic geometry due to prolonged usage. A wideband design would overcome this effect.

The impedance integrity of the constituent antenna elements within a module must be identical to that of the stand-alone elements. The input impedance characteristics would be altered when antenna elements are placed in close electrical proximity. If the constituent elements share the substrate or ground plane, then the antennas might be detuned within the module. Therefore, designing backwards from the antenna module to the constituent elements would lead to better input reflection coefficients. Also, the amount of reflected power at the individual ports might increase when the constituent antenna elements are placed in a module, this could be attributed to the mutual coupling between the constituent elements.

Reduction in mutual coupling would automatically ensure that the constituent elements have minimal detuning. But mutual coupling could be reduced by increasing the electrical distance between the antennas. Hence, it's a trade-off between input impedance, mutual coupling, pattern integrity and overall size of the antenna module.

Pattern engineering for 5G base stations would be different from that of the 4G base stations, the reason being high gain requirement. Pattern integrity of the constituent antennas within the module must be like its stand-alone elements. Often, this feature cannot be realized in practice. As the elements are placed close to each other, the radiating aperture would be influenced by the presence of other elements leading to poor patterns. Hence, patterns of the multiport integrated design must be thoroughly understood prior to deployment. The correlation between the patterns must be minimal to achieve a wide angular coverage for a given electrical size.

Planar antennas, such as most of the designs explained in this book, need additional transition circuitry to be compatible with the industry standard elliptical waveguides of the antenna towers. Two design examples would be introduced in this Chapter.

7.3 High Aperture Efficiency Wideband Antenna

In the first design, high aperture efficiency end-fire antenna would be presented [13]. High aperture efficiency indicates higher forward gain for smaller physical footprint. Lot of techniques could be explored in the broadside radiator designs, for instance,

Fabry-Perot cavity (FPC) based antennas [13, 14]. Even though very high aperture efficiencies could be achieved with narrow beam, achieving wide bandwidth for a given gain or aperture efficiency would be challenging. The concept of stacking antenna elements for wider angular coverage, like the design presented in Sect. 6.8, would be difficult to achieve with Fabry-Perot based technique. FPC based design would be favourable for dual or even multi-polarization design with shared radiator.

The other common technique of gain enhancement in the mmWave domain is to integrate a dielectric lens [15, 16]. Very high gains up to 20 dBi could be easily achieved by using electrically large dielectric lens. This technique increases the physical footprint of the antenna, thus compromising the element's suitability for an integrated antenna module within a base station. Techniques such as series-fed array [17] or corporate fed array [18] would increase gain of the single element. However, both the techniques maintain the same aperture efficiency as that of the single element, hence failing to aid in size reduction of the overall antenna.

It must be noted that aperture efficiency enhancement has been reported mostly for broadside radiator. Very few articles are available on aperture efficiency studies on end-fire antennas. In this Section, a metamaterial integrated traveling wave antenna with high aperture efficiency will be presented.

7.3.1 Metamaterial Loaded Design

Proposed antenna is designed on 10 mil thick RT5870 substrate with $\varepsilon_r = 2.33 \pm 0.02$ and dielectric loss tangent of 0.0012. As the power handling requirement for a 5G base station is low, microstrip based planar antenna would work for the application. To keep surface wave modes to minimum, substrate of low relative permittivity is chosen [19]. Electrically thin substrate is chosen to decrease cross polarization in the end-fire. Polarization purity is often an important criterion for base station antennas. The reason being higher cross-polarization levels might deteriorate the quality of multipath signals leading to poor signal reception. The choice of 10 mil substrate is arbitrary, a 20 mil substrate also would have served the purpose with a minimal loss in the forward gain. Proposed antenna is electrically compact having dimensions of $14 \times 33 \times 0.254$ mm^3, which translates to $1.44\ \lambda \times 2.98\ \lambda \times 0.023\ \lambda$ computed at 28 GHz. On the outset, it appears to be electrically large, but given the traveling wave nature of the radiating element, the dimensions seem reasonable. The elongation at the ground plane could have been reduced, it is maintained exclusively for measurement purposes.

The radiating aperture is fed by a microstrip to slotline transition. The wide impedance bandwidth is due to the impedance characteristics of the microstrip to slotline transition. Once this transition is integrated with a tapering aperture, wide bandwidth is achieved for the antenna. The impedance matching was realized with respect to the 50 Ω port impedance. Schematics of the proposed antenna are shown in Fig. 7.1 with ground and top planes respectively. Photograph of the proposed antenna is shown in Fig. 7.2. The corrugations on one of the ground plane sections

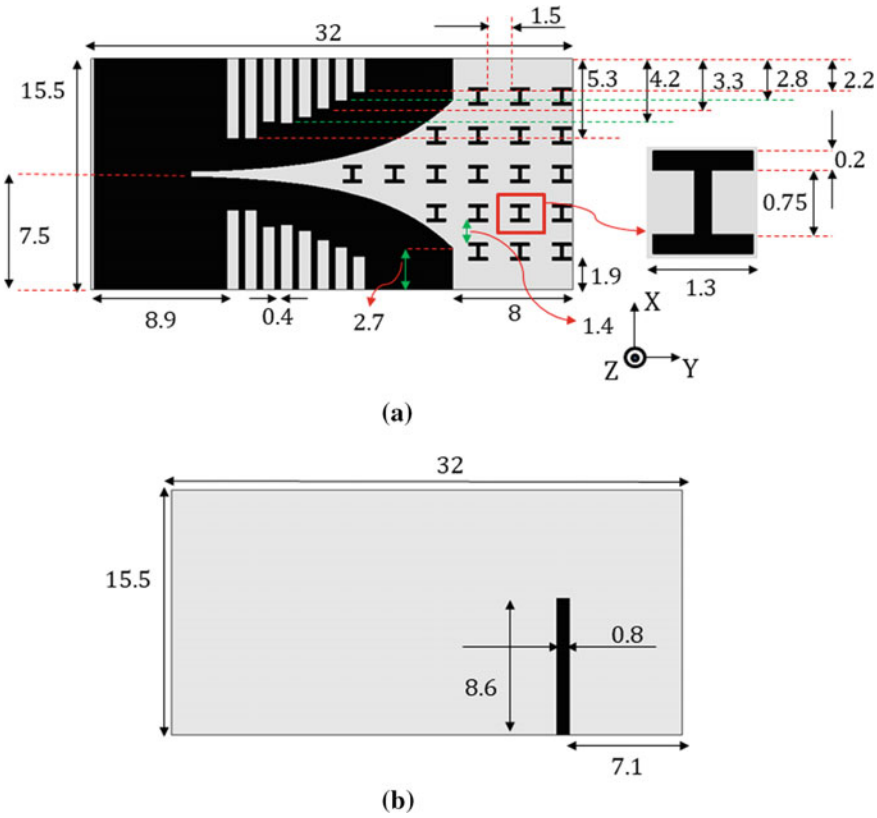

Fig. 7.1 Schematic of the proposed metamaterial inspired Vivaldi antenna with **a** ground plane and **b** top plane (All dimensions are in mm) ([13], Reprinted with permission from John Wiley and Sons)

was removed to mount the ground plane of the end-launch connector. The prototype was fabricated using the industry standard chemical etching process. Etching using laser bits or other milling procedures might fail to deliver a decent prototype, as the thickness of the substrate is only 254 μm, which is fragile for milling operations.

Corrugations were inserted strategically to reduce the cross polarization and back lobe radiation, henceforth aiding in pattern integrity and polarization integrity, as demanded by base station antennas [20]. Varying length corrugations cater to pattern integrity across the whole bandwidth.

Gain must be enhanced for this element without any significant increase in the physical dimensions of the element. Planar gain enhancement is preferred, hence planar metamaterial unit cells are investigated to enhance gain and aperture efficiency. An epsilon near zero (ENZ) sub-wavelength unit cell has been designed for optimal phase correction for the entire operating band. Gain enhancement would mean that E-fields emanating out of the antenna should be ideally planar. This indicates that as

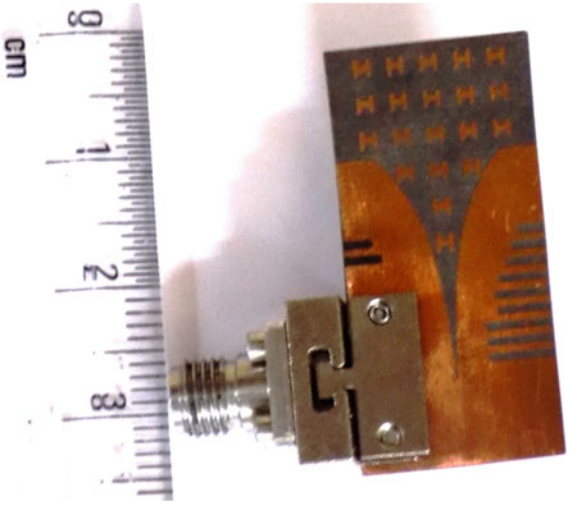

Fig. 7.2 Photograph of the proposed metamaterial inspired Vivaldi antenna ([13], Reprinted with permission from John Wiley and Sons)

the wave emanating out of the antenna's physical edge should be highly planarized compared to the element without the metamaterial unit cells. This aspect could be characterized by measuring the phase error along the edge of the antenna with and without the sub-wavelength metamaterial unit cells. It must be carefully noted that the phase characterization should be for the dominant radiating co-polarized E-fields. These fields and their respective phase behavior could be analysed using commercial full-wave software.

Proposed H-shaped unit cell is depicted in Fig. 7.3. Standard periodic boundary conditions were applied in simulation model. The current metamaterial is finite in

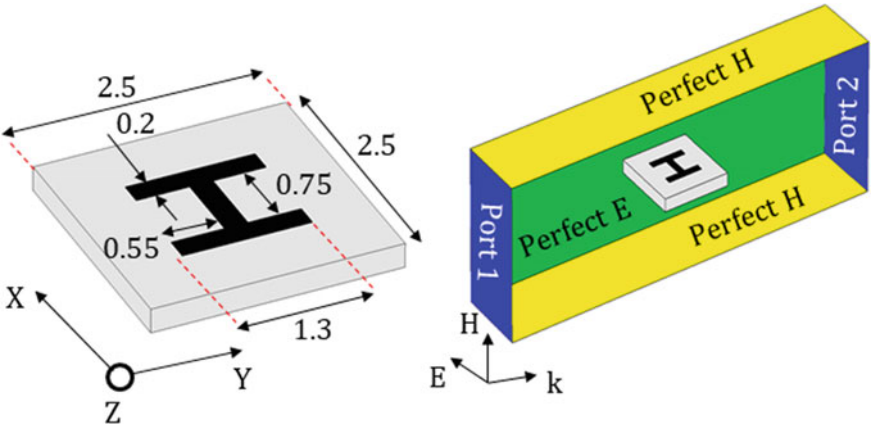

Fig. 7.3 Simulation model of the proposed H-shaped ENZ metamaterial unit cell ([13], Reprinted with permission from John Wiley and Sons)

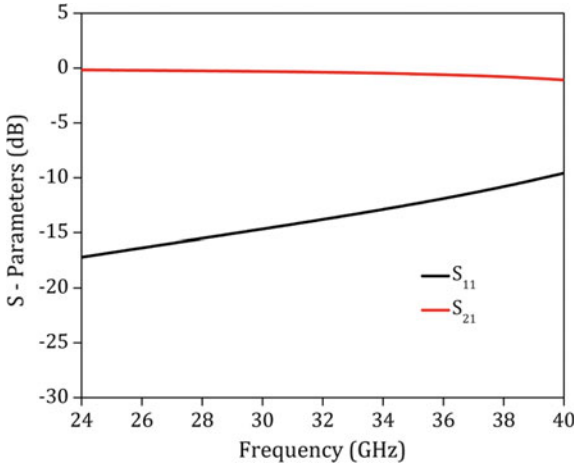

Fig. 7.4 Simulated S-parameters of the H-shaped unit cell ([13], Reprinted with permission from John Wiley and Sons)

nature due to the boundaries of the antenna. The infinite boundary simulations give an idea about the behavior of the metamaterial unit cells, which could be useful for integration with the radiating aperture. Polarization of the ports was matched with the polarization of the proposed Vivaldi antenna as metamaterial unit cells will be finally loaded with the same polarization as of proposed antenna. Unit cell simulation is done by using full wave computer simulation technology (CST) microwave studio (MWS). The co-polarized radiating E-field is along X-axis, with reference to Fig. 7.1a, hence the E-field which mimics this source of radiation is also along X-axis in the periodic boundary simulations, with reference to Fig. 7.3. The width of the periodic boundary box is identical to the periodicity of the unit cells, post integration, in X axis. The height of the box is around 2 λ at the center frequency. The length of the box (along the direction of propagation) must be over 2–3 λ to promote dominant mode of propagation.

Simulated S-parameters of the proposed H-shaped unit cell is depicted in Fig. 7.4. Standard retrieving procedure is followed for unit cell parameter extraction which is attained from reflection and transmission parameters [21, 22].

For proposed ENZ unit cell:

$$\varepsilon_{eff} = \frac{N_{eff}}{Z_{eff}} \tag{7.1}$$

where,

$$Z_{eff} = \pm\sqrt{\frac{(1+S_{11})^2 - S_{21}^2}{(1-S_{11})^2 - S_{21}^2}} \tag{7.2}$$

and

$$N_{eff} = \frac{1}{k_0 d_{eff}}\{Im\left[\ln\left(e^{iN_{eff}k_0 d_{eff}}\right)\right] + 2m\pi - iRe\left[\ln\left(e^{iN_{eff}k_0 d_{eff}}\right)\right] \tag{7.3}$$

where

$$e^{iN_{eff}k_0 d_{eff}} = \frac{S_{21}}{1 - S_{11}\frac{Z_{eff}-1}{Z_{eff}+1}} \tag{7.4}$$

From the above relations, ε_{eff} is the equivalent permittivity, N_{eff} is the refractive index, Z_{eff} is the wave impedance, S_{11} and S_{21} are the reflection and transmission co-efficients respectively, k_0 is the free space wavenumber, d_{eff} is the effective length of metamaterial unit cell and m is an integer denoting the branch index. It must be noted that S-parameters must be considered as complex values for all the calculations, unless otherwise specified.

The extracted ε_{eff} of the proposed unit cell is shown in Fig. 7.5. By properly optimizing the dimensions of the unit cell, the ENZ characteristics can be obtained in the specific frequency range. Incorporation of heterogeneous metamaterial unit cells would have increased the pattern bandwidth. Proposed unit cell behaves like an equivalent LC circuit in which the stubs contribute to inductance and space between extreme arms attribute to capacitance. Sharp electrical behavior can be observed at 28 GHz and thus if the assemblage of unit cells strategically placed in the radiating aperture of proposed Vivaldi antenna will aid in phase correction resulting in gain enhancement, provided polarization of the incident E-field matches with that of unit cell. Negative permittivity is obtained almost in the entire operating band.

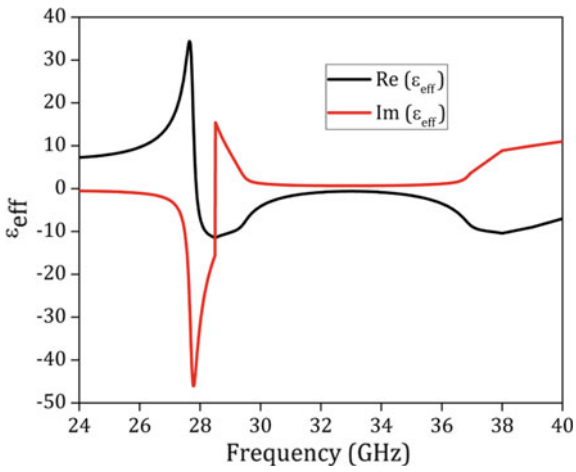

Fig. 7.5 Extracted permittivity of the H-shaped unit cell ([13], Reprinted with permission from John Wiley and Sons)

H-shaped metamaterial unit cells are loaded in the radiating aperture of the proposed Vivaldi antenna with X- and Y-axes periodically. The periodic sub-wavelength distance between MTM (Metamaterial) unit cells is optimized for significant phase correction throughout the bandwidth. Unit cells are inserted in the radiating aperture of Vivaldi antenna for achieving higher aperture efficiency without any significant detuning in input reflection co-efficient. E-field plots for proposed Vivaldi antenna with and without MTM is depicted in Fig. 7.6 in which phase linearization can be observed in MTM loaded Vivaldi antenna. In other words, curvature of the E-fields reduces, as the phase linearization elements are introduced in the radiating aperture.

Simulated and measured input reflection co-efficient of the proposed Vivaldi antenna is depicted in Fig. 7.7. Proposed antenna is wideband covering frequencies from 24 to 40 GHz with fractional impedance bandwidth of 50%, which is a high value thus could be deployed in any geography with different carrier frequencies.

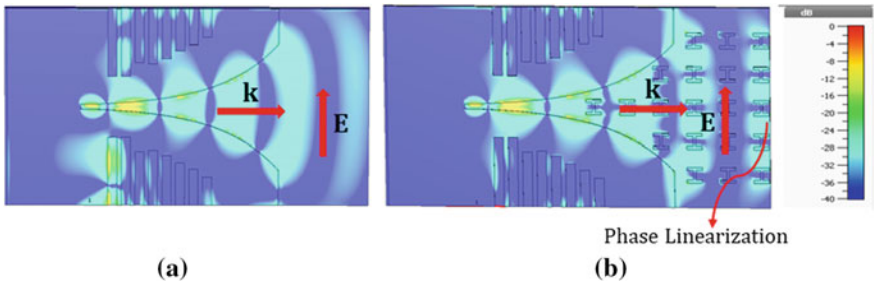

Fig. 7.6 E-field distribution plots for proposed Vivaldi antenna: **a** without MTM and **b** with MTM loading ([13], Reprinted with permission from John Wiley and Sons)

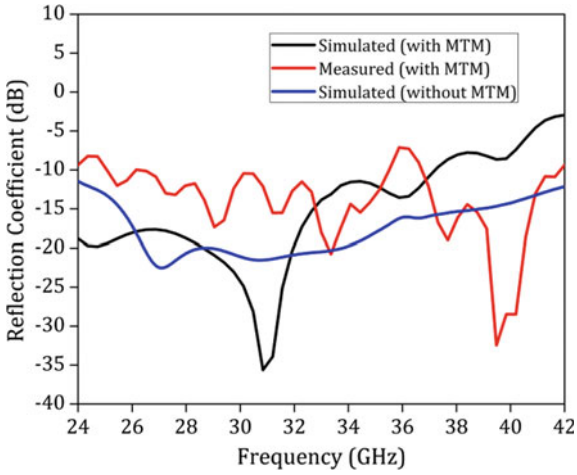

Fig. 7.7 Simulated and measured input reflection co-efficient of the proposed Vivaldi antenna ([13], Reprinted with permission from John Wiley and Sons)

Microstrip to slot line transition is optimized for better impedance matching. Proposed antenna achieves lesser bandwidth when loaded with ensemble of metamaterial units but the periodicity and separation between unit cells is optimized in such a way that both the candidate frequency bands, 28 GHz and 38 GHz are covered. Discrepancies between simulated and measured data are primarily due to following reasons:

1. Solder less transition from end-launch connector to microstrip feedline. Therefore, multiple mating cycles deteriorates the input impedance performance of the antenna with the connector. The measured $|S_{11}|$ could be improved by using a thin-tip solder to mount the trace pin of the connector to the feeding line of the fabricated antenna.
2. Tapering of the feedline was not also considered while fabrication [23]. Tapering of feedline is recommended by the end-launch connector manufacturer. tapering might be difficult to fabricate with the facilities available at the authors' disposal.
3. Simulation of antenna with end-launch connector was not also considered. Simulation with end-launch connector would require higher computational resources, as these connectors are electrically large in all the three dimensions.
4. Fabrication tolerances can also affect the performance of the antenna. Faults in the fabricated element could be visually inspected in a microscope. To enhance the measured performance, multiple copies of the design could be fabricated.

Simulated and measured radiation patterns of proposed metamaterial inspired Vivaldi antenna in both the principal planes, XY-plane (E-plane) and YZ-plane (H-plane) are illustrated in Fig. 7.8. Proposed antenna attains stable radiation patterns over the entire operating band. Measured cross-polarization is minimal in the entire operating band. Front-to-back ratio (FTBR) of more than 20 dB is achieved for 50% impedance bandwidth which is due to proper impedance matching and insertion of variable length corrugations. Higher FTBR is suitable for base stations as minimal power is radiated towards unnecessary angular space. Beamwidth variation for the proposed antenna over the whole operating frequency range is depicted in Fig. 7.9. Variation of 17° can be noticed across the operating band which is very minimal thus achieving the stable radiation or pattern bandwidth. Discrepancies between simulated and measured data may be attributed to alignment errors and adapters used for radiation pattern measurement.

Gain plot of the proposed Vivaldi antenna is depicted in Fig. 7.10. Gain of the proposed MTM loaded antenna lies between 10 and 12.5 dBi. There is around 3-dB gain enhancement after insertion of assemblage of metamaterial unit cells. As seen in Fig. 7.10, gain of the Vivaldi antenna without metamaterial loading remains constant around 9 dBi even after 40 GHz which is due to proper impedance matching at these frequencies.

In addition to this, 1-dB gain bandwidth of the proposed antenna is around 42% with gain varying between 11.5 and 12.5 dBi. Therefore, high pattern integrity is obtained in the entire operating band. Insertion of phase correcting metamaterial unit cells results in the aperture efficiency of around 78% at 28 GHz. Here, the aperture efficiency is computed using the radiating aperture's physical area. The expected gain

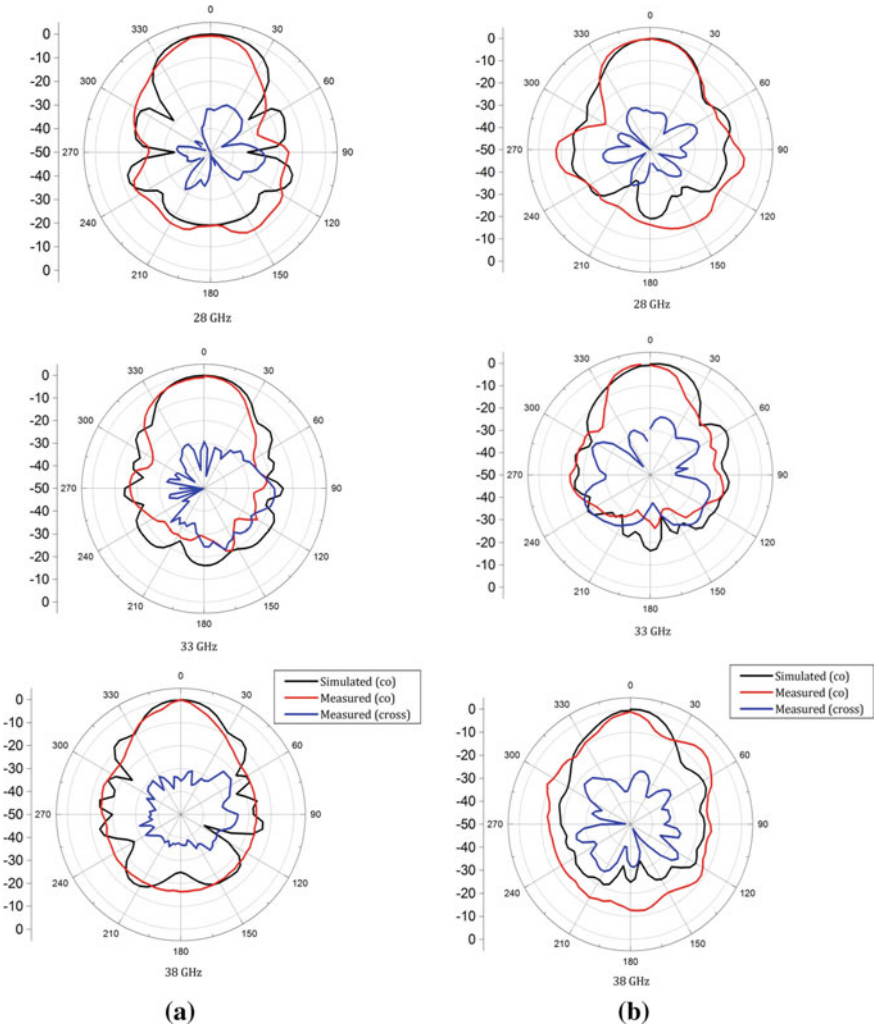

Fig. 7.8 Radiation patterns of proposed MTM loaded Vivaldi antenna in **a** XY-plane and **b** YZ-plane ([13], Reprinted with permission from John Wiley and Sons)

from the physical area is computed by $G_p = (4\ \pi A_p)/\lambda^2$, where A_p is the physical area of the radiating aperture (in square meters) and λ is the free space wavelength (in meters). Gain obtained is the actual value of gain obtained from simulations, G_{act}. With these assumptions, the aperture efficiency is calculated as G_{act}/G_p in linear scale. Any value above 60% is a reasonable value. Simulated and measured aperture efficiency of the MTM inspired Vivaldi antenna is depicted in Fig. 7.11. Proposed antenna attains larger impedance bandwidth with high aperture efficiency and 1-dB gain bandwidth as compared to other reported designs as illustrated in Table 7.1.

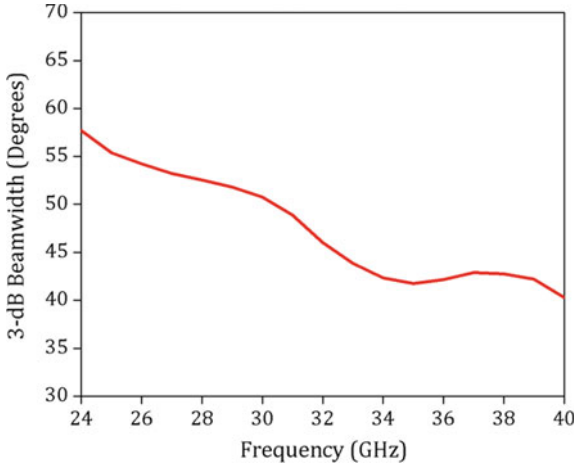

Fig. 7.9 Plot of variation of beamwidth over the entire operating frequencies ([13], Reprinted with permission from John Wiley and Sons)

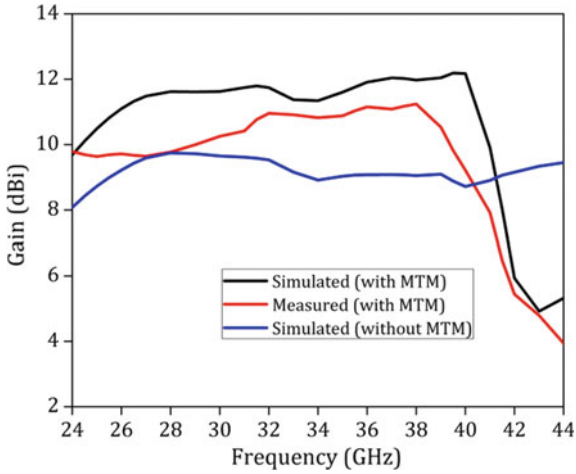

Fig. 7.10 Gain plot of the proposed Vivaldi antenna ([13], Reprinted with permission from John Wiley and Sons)

7.3.2 A Stacked Approach for Base Stations

The design presented in Sect. 7.3.1 is a single port antenna, which gives a very narrow angular coverage. To design an antenna module, this must be extended to a three-port design. A shared radiator design would be impossible to design with this topology, as it is an end-fire traveling wave radiator. The presented element could be placed horizontally with angular offset between each element, this topology would increase the physical footprint of the overall system. Hence compact vertically stacked elements with angular offset is presented. Antenna architecture in which wide angular coverage from $-60°$ to $+60°$ is achieved with beam directing at $0°$, $+45°$ and $-45°$ is illustrated in Fig. 7.12. The fabricated prototype is depicted in Fig. 7.13.

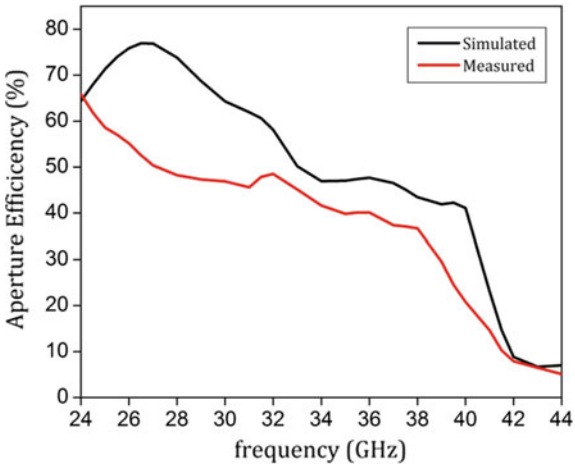

Fig. 7.11 Simulated and measured aperture efficiency of the proposed MTM inspired Vivaldi antenna ([13], Reprinted with permission from John Wiley and Sons)

Table 7.1 Comparison of proposed antenna with other reported designs

REF	Planar	FOP	FBW	P G	1-dB GBW (%)	AE (%)
[24]	Yes	28	10.5	8.5	21.4	77
[25]	Yes	28	53.9	4.5	28.6	20
[26]	Yes	28	18.1	11.3	10.5	30.7
[27]	No	28, 38	>100	15	44	65.4
[28]	Yes	28	39.6	6	37.7	51.8
[29]	Yes	64	14.6	11	6.1	39.6
[30]	Yes	28, 38	53	17.2	22.2	<50
PW	Yes	28, 38	50	12.5	42	78

FOP = Frequency of operation (in GHz), FBW = Fractional bandwidth (in %), PG = Peak gain (in dB), GBW = Gain bandwidth, AE = Aperture efficiency, PW = Proposed work

A custom-made 3D-printed tiny tower was designed with PLA (Polylactic acid). The scaffolding has slots as per the design to hold the individual elements. The end-fire high gain metamaterial inspired Vivaldi antenna elements are mounted at 0° and ±45° to achieve wide coverage. The number of ports is decided based on the required wide angular coverage and ease of implementation. The beamwidth of the stand-alone element decides the number of ports required for the antenna module.

To reduce quasi-waveguide effect caused by electrically large ground planes, separation between individual antenna elements is maintained to be around 10 mm. Uniform coverage of 120° is achieved in the E-plane. Radiation patterns of the proposed pattern diversity antenna architecture in E-plane are illustrated in Fig. 7.14 at 28 GHz and 38 GHz thereby validating pattern integrity in the entire band.

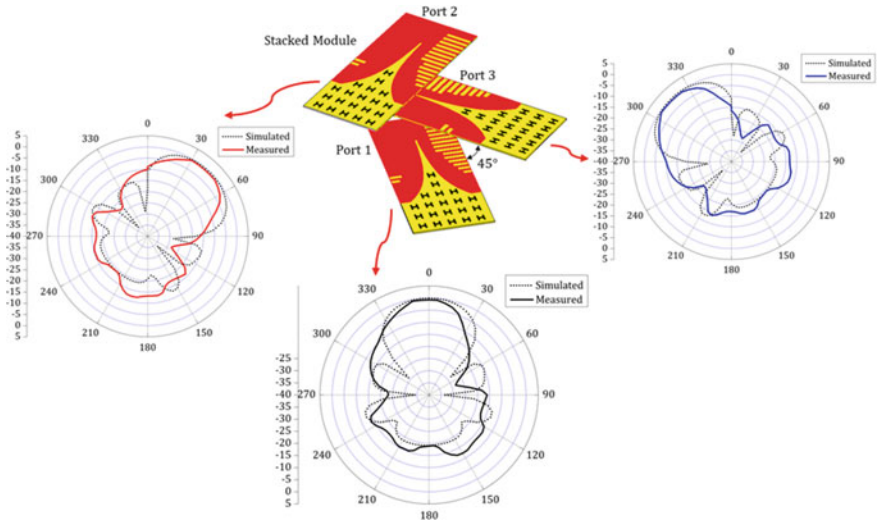

Fig. 7.12 Proposed antenna architecture for pattern diversity ([13], Reprinted with permission from John Wiley and Sons)

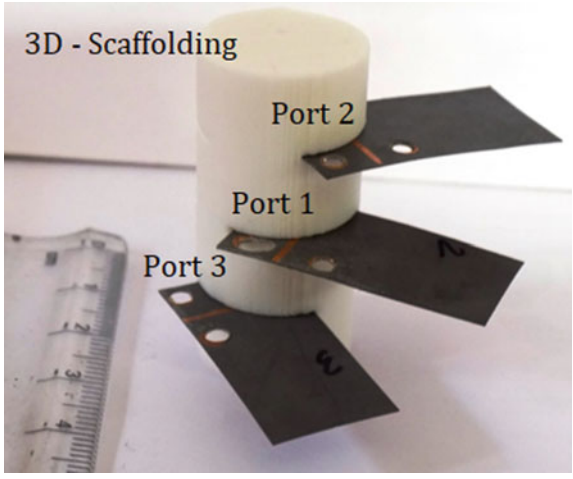

Fig. 7.13 Topology of the fabricated pattern diversity antenna module ([13], Reprinted with permission from John Wiley and Sons)

It is evident from Table 7.2 that proposed pattern diversity antenna module is suitable candidate for mmWave 5G base stations in comparison with other reported designs. Wide uniform angle coverage with high pattern integrity is observed in the entire operating band.

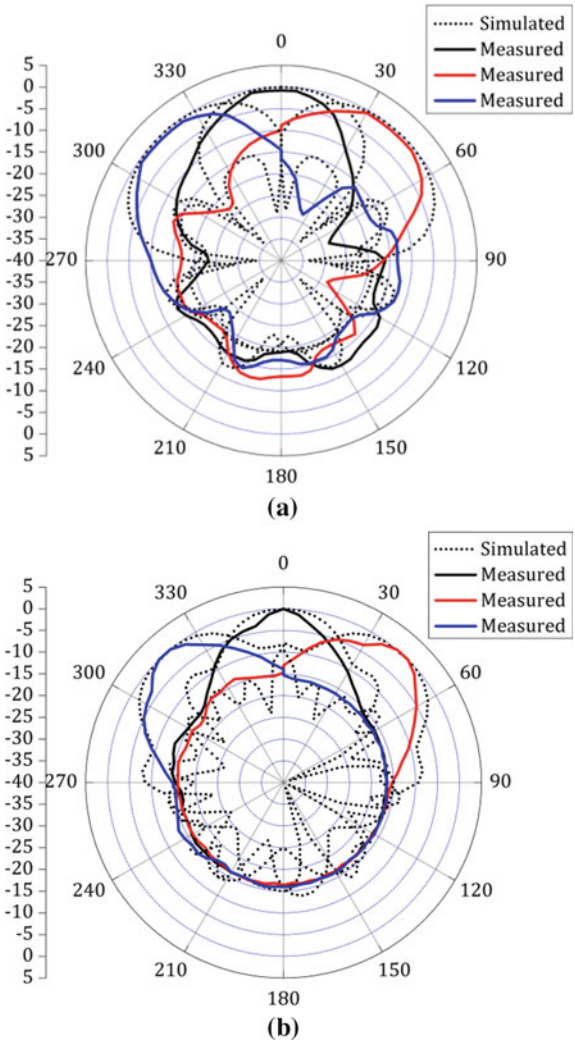

Fig. 7.14 Radiation patterns at **a** 28 GHz and **b** 38 GHz ([13], Reprinted with permission from John Wiley and Sons)

Table 7.2 Comparison of proposed pattern diversity antenna architecture with other reported designs

References	Frequency of operation (GHz)	Peak gain (dBi)	Coverage
[24]	28	5.5, 8.5	±65°
[26]	28	11.3	±30°
[28]	28	6	NA
[31]	28	9	±45°
Proposed work	28, 38	12.5	±60°

7.4 ACS Fed Antennas for Base Stations

In the previous Section, high aperture efficiency element was explained. The objective is to get higher gain for smaller size or lower physical footprint. An alternate technique is explained in this Section. Instead of modifying the radiating aperture of the antenna, the feed itself is modified to yield higher gain with a significant reduction in the width of the antenna. The concept is to cleverly design the feed in such a way that both pattern and impedance integrity is achieved across a pre-designated bandwidth [32].

CPW (Coplanar waveguide) feeding is a uniplanar feeding technique, which has a possibility of miniaturization in lateral direction of the antenna. However, these antennas are limited to radiate only in the end-fire direction for unidirectional beams. On the other hand, asymmetric coplanar strip (ACS)-fed antennas occupy only half of the physical footprint without significant loss in gain, hence achieving the compactness. Like CPW feed, ACS also achieves end-fire radiation. This aspect is not a severe constraint for base station applications. But the arrangement of the radiators must be strategized for wide angular coverage across a broad spectrum. ACS-feeding technique has been implemented at lower frequencies [33]. The design procedure for ACS based antennas is well understood in the microwave domain, but not extensively researched in the mmWave domain. Primary reason for lack of ACS based designs in and around 28 GHz is due to unavailability of design equations for impedance calculations of ACS feeding in the Ka band. The antenna must be designed by optimizing the structure for a given ACS feed. The feed dimensions must match with that of the mmWave connector as well. This section presents a proof-of-concept design at mmWave frequencies with compact antenna architecture and higher impedance bandwidth.

A compact ACS-fed antenna for 5G base stations is initially presented. The proposed antenna operates over a wideband covering mmWave frequencies from 26 to 32 GHz. Forward end-fire gain of 6.5–7.5 dBi is achieved for the available aperture. The proposed antenna exhibits high pattern integrity and stable radiation patterns with front-to-back ratio of more than 13 dB across the operating spectrum. Moreover, a quasi-stacked architecture using the above element and shared ground antennas is presented in the following sub-sections.

7.4.1 Compact ACS-Fed Antenna

The proposed ACS-fed antenna is illustrated in Fig. 7.15 which is designed on 10 mil (0.254 mm) thick Rogers 5870 substrate with dielectric constant (ε_r) of 2.33 $\pm$ 0.02 and dielectric loss tangent of 0.0012. To minimize cross polarization radiation level in the end-fire, electrically thin substrate of 0.025 λ thickness was chosen. The cross-polarization level would be low for uniplanar design, as the radiating aperture is on the same side of the substrate. Higher polarization purity is an added feature for base station antennas. Substrate of low relative permittivity was chosen to keep

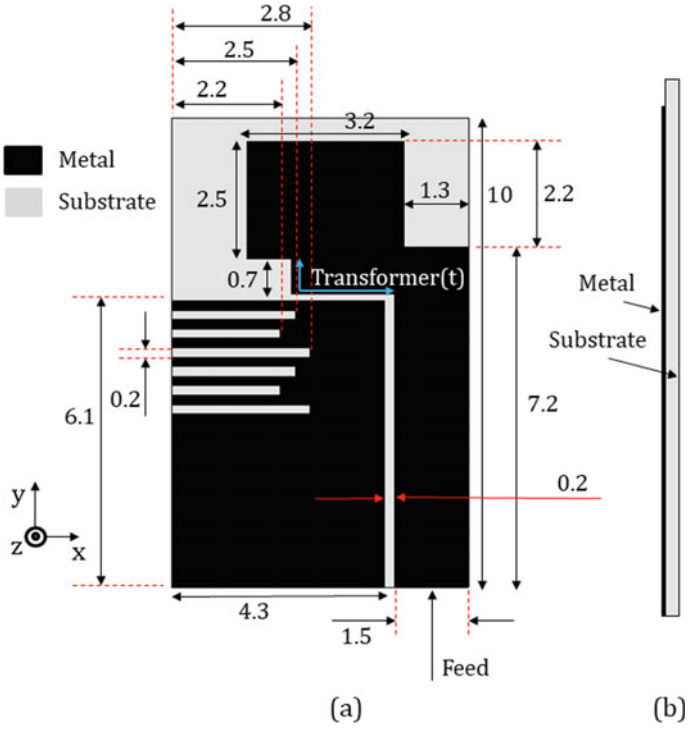

Fig. 7.15 Schematic of the proposed ACS-fed mmWave 5G antenna, **a** top view and **b** side view (All dimensions are in mm) [32]

surface wave modes to minimum, slightly higher dielectric constant up to 4 would not significantly hamper the performance metrics of the antenna. However, variation of dielectric constant would alter the feed dimensions [34]. The proposed antenna is fed by a 50 Ω characteristic impedance ACS-feedline, designed according to standard calculations, whose width is chosen to be 1.5 mm with gap width of 0.2 mm which is feasible with industry standard chemical etching process [33]. The 50 Ω feed is connected to an impedance transformer of 65.4 Ω feeding the rectangular shaped radiator of 85.5 Ω for better impedance matching. The proposed ACS-fed antenna has a small physical footprint with dimensions of 0.6 $\lambda \times 1\ \lambda$ at 28 GHz including the feedline. These dimensions are electrically small, similar design realized with CPW or microstrip feed would have been at least twice the width of the presented element.

Full-wave antenna simulations were carried out using CST Microwave Studio® Software. Topology of the antenna consists of an unbalanced ACS-line, feeding the rectangular shaped radiator whose dimensions are around quarter wavelength at 28 GHz which inherently produces an undesired beam tilt effect. To compensate this beam tilt produced by unbalanced feed, offset of 1.3 mm is introduced in the radiator which produces unidirectional beam in end-fire. Separation of 0.8 λ is

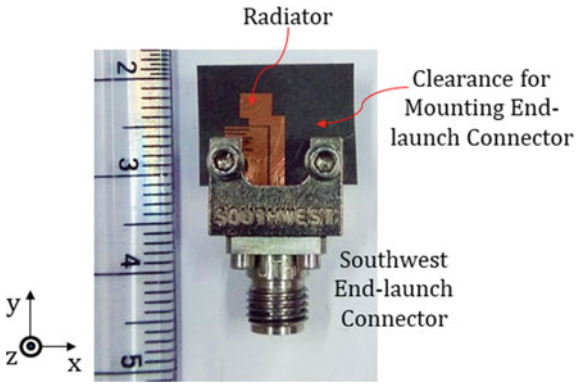

Fig. 7.16 Photograph of the proposed ACS-fed antenna [32]

chosen between feeding plane and the radiator to avoid contamination of the pattern measurements due to the electrically large end-launch connector. Photograph of the proposed fabricated antenna is depicted in Fig. 7.16. Substrate was extended from both the sides of the fabricated prototype to accommodate the industry standard 2.92 mm bulky end-launch connector which operates up to 40 GHz. The dielectric extension along the X axis does not contribute to the deterioration of the antenna's characteristics.

Varying length corrugations were inserted in the ground plane to concentrate the E-field towards the radiator thereby reducing side-lobes. E-field plots at various frequencies for ACS-fed mmWave 5G antenna with and without corrugations are illustrated in Fig. 7.17. The plots illustrate the quasi-traveling wave behavior of antenna which contains the E-plane (XY-plane) parallel to the substrate. It can be also noticed that the radiator is uniformly irradiated irrespective of the frequency of operation, therefore providing wider impedance bandwidth, without a compromise in the pattern integrity. Bulky end-launch connector was modelled in simulations with SMA connector thereby producing less disparity between simulated and measured results.

Variation of the length of impedance transformer (t) on the input reflection coefficient is illustrated in Fig. 7.18a. The optimal length of impedance transformer for higher impedance bandwidth was determined to be 2.7 mm, which is roughly quarter-wavelength at 28 GHz. Measured results of the proposed antenna were carried out using Agilent PNA E8364C. Simulated and measured input reflection coefficient of the proposed ACS-fed mmWave 5G antenna is depicted in Fig. 7.18b. Simulations considered the SMA (Sub Miniature version A) model. The port impedance of SMA connector is like that of an end-launch connector across the frequency of interest. Measured impedance bandwidth of the proposed antenna is from 26 to 32 GHz with fractional bandwidth of 20.7%, which is high value, given the electrical dimensions of the radiator. Also, proposed antenna with corrugated ground achieves higher impedance bandwidth than its non-corrugated counterpart.

Discrepancies between simulated and measured results may be due to fabrication tolerances, inhomogeneity of dielectric constant of the substrate in the Ka-band and

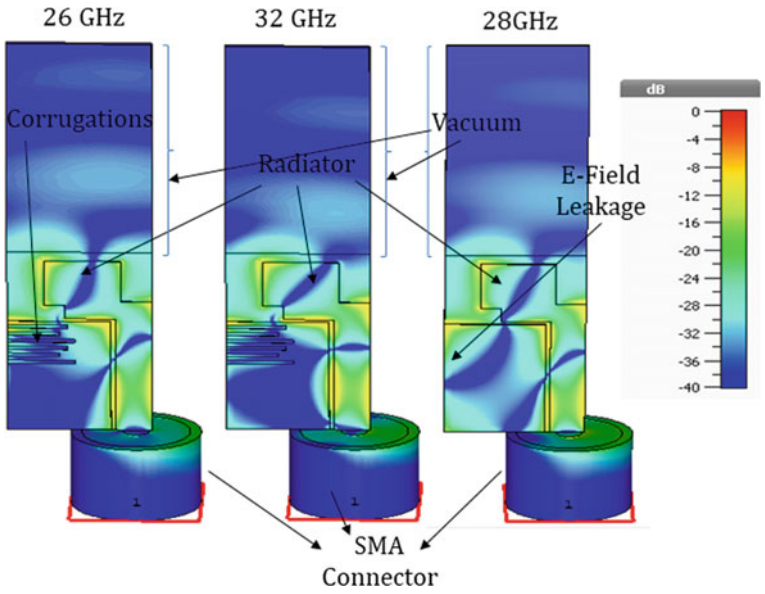

Fig. 7.17 E-field plots at various frequencies [32]

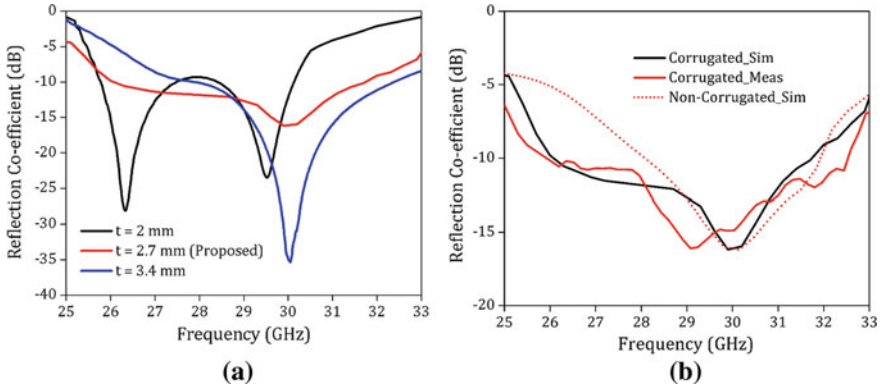

Fig. 7.18 **a** Input reflection co-efficient variation with parameter, 't' and **b** input reflection co-efficient of the proposed antenna [32]

the characteristic impedance deviation from 50 Ω of the end-launch connector used for measurements [35]. Also, the recommended design for mounting the antenna with the end-launch connector is unavailable for ACS feeding. The assembly of the grounding screws might have also created measurement errors. As the fastening of the screws were done manually, alignment errors would have hampered the results.

Measurements were carried out in an anechoic chamber using Keysight standard horn R281B as transmitter. Simulated and measured radiation patterns of the

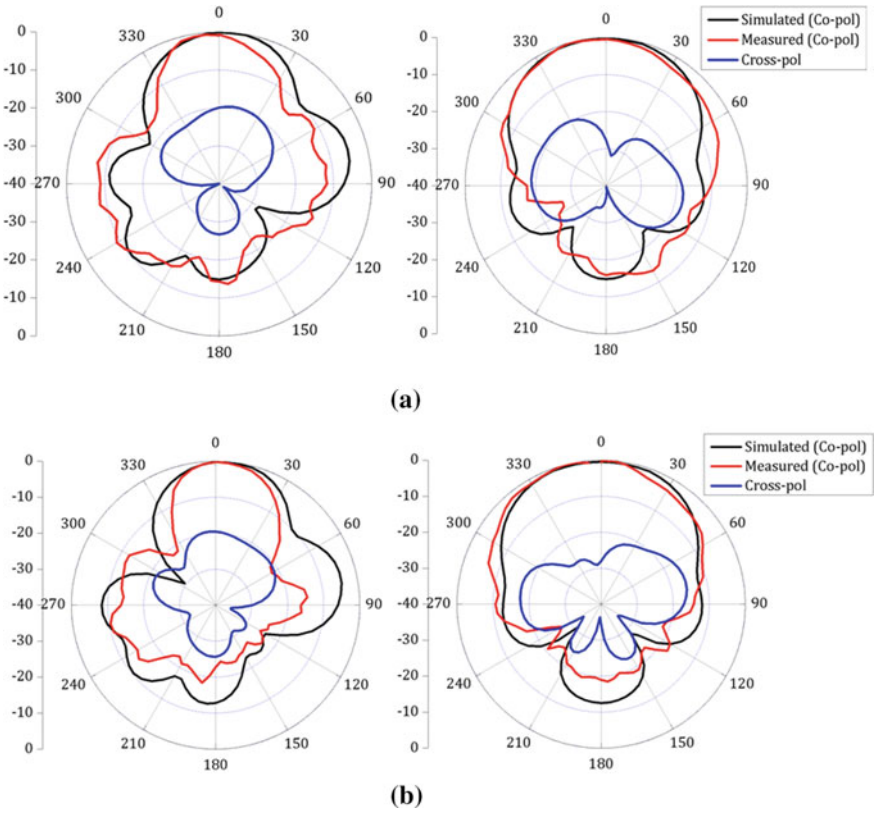

Fig. 7.19 Simulated and measured co-pol and cross-pol radiation patterns in XY and YZ plane at **a** 28 GHz and **b** 30 GHz [32]

proposed antenna in both the principal planes, i.e., E-plane (XY-plane) and H-plane (YZ-plane) are shown in Fig. 7.19 at 28 and 30 GHz.

Radiation patterns with high pattern integrity are achieved in both the planes as evident from Fig. 7.19. Disparity between simulated and measured data might be due to polarization alignment errors and scattering due to electrically large adapters employed for pattern measurements. The scattering effects could not be eliminated even with a clearance of 0.8 λ between the radiator and the feeding plane. Also, electrically massive dielectric board was used as a turntable for pattern measurements. This dielectric board also creates a non-ideal environment within the anechoic chamber. Since the ground plane is electrically close (0.02 λ) to the radiator, radiation patterns are uni-directional in nature. Also, the width of ground plane is large enough to make the antenna radiate in end-fire direction. Front-to-back ratio is more than 13 dB for the whole operating mmWave band. Cross-polarization in both the principal planes is less than −18 dB indicating strong linearly polarized antenna, as

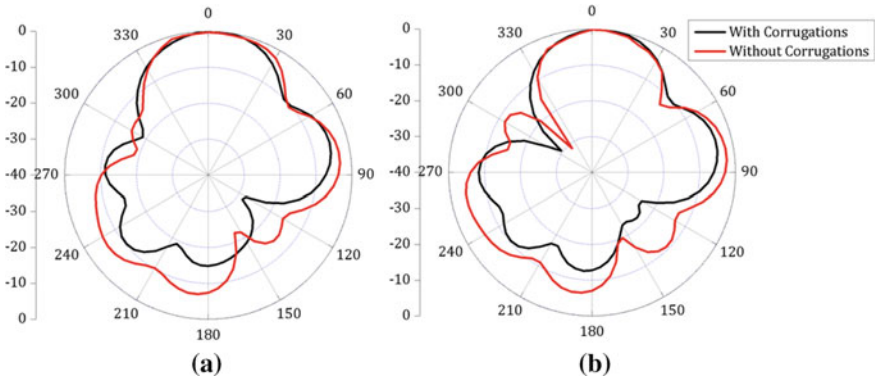

Fig. 7.20 Radiation patterns of proposed antenna with and without corrugations at **a** 28 GHz and **b** 30 GHz [32]

expected from electrically thin uniplanar design. Due to unbalanced ground in ACS-feeding, a small side-lobe of value less than 1.5 dB can be noticed in the E-plane as compared with the main lobe of proposed antenna in end-fire direction. This logic is like the behavior of printed dipole or printed Vivaldi antennas. The measured half-power beamwidth is around $50° \pm 5°$ in the E-plane (XY-plane) and $70° \pm 5°$ in the H-plane (YZ-plane). Figure 7.20 illustrates the reduction of side lobes by insertion of varying length corrugations.

The proposed antenna has an end-fire gain of 6.5–7.5 dBi indicating high gain for the available aperture as compared to reported end-fire antennas. 3D-radiation plots of the proposed antenna are illustrated in Fig. 7.21 at frequencies 28 and 30 GHz thus providing insight about the radiation characteristics of proposed ACS-fed mmWave 5G antenna. Moreover, gain and radiation efficiency of the proposed antenna is depicted in Fig. 7.22. Gain varies between 6.5 and 7.5 dBi over the whole operating band. Since, corrugated ground plane is electrically large enough to create forward radiation, therefore high gain is observed. Also, radiation efficiency is greater than 88% over the entire operating band. The loss in radiation efficiency is mainly due to dielectric loss tangent of the substrate as the antenna possesses end-fire radiation pattern. Electrically small dimension of the antenna also contributes to the reduction in radiation efficiency. The 1-dB gain bandwidth of the proposed antenna is 20% indicating high pattern integrity over the entire operating band.

The proposed antenna occupies small physical footprint with high end-fire gain and pattern integrity compared with other reported planar designs, as illustrated in Table 7.3.

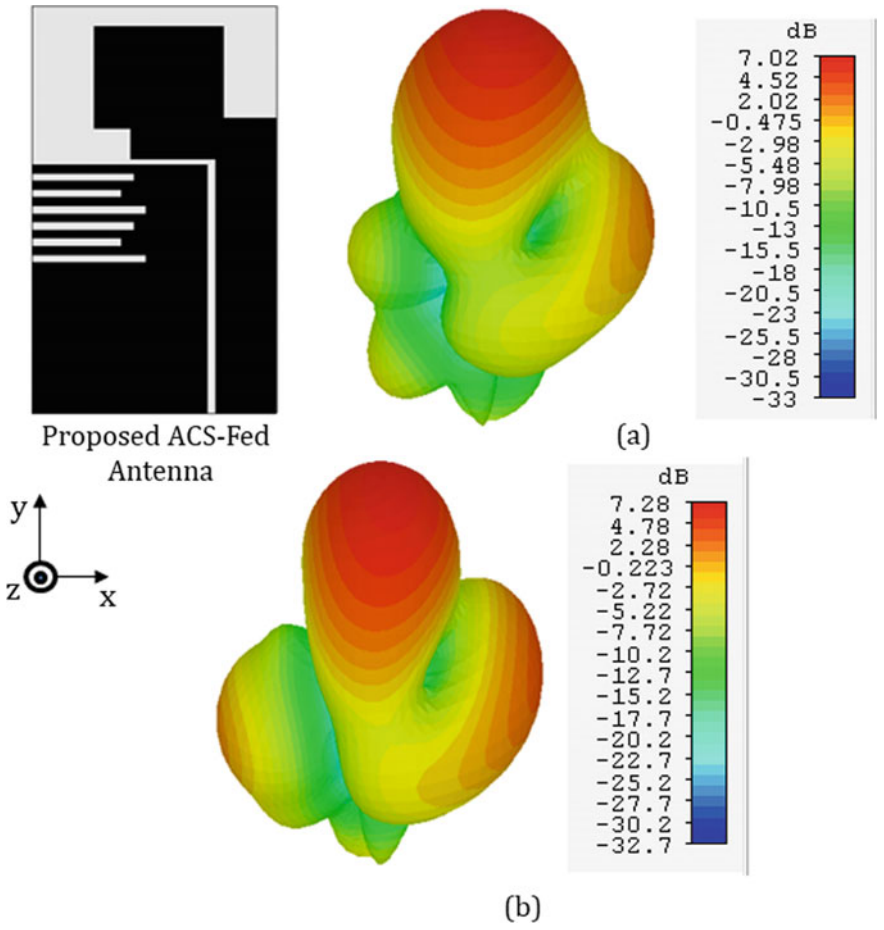

Fig. 7.21 3D-radiation plots at **a** 28 GHz and **b** 30 GHz [32]

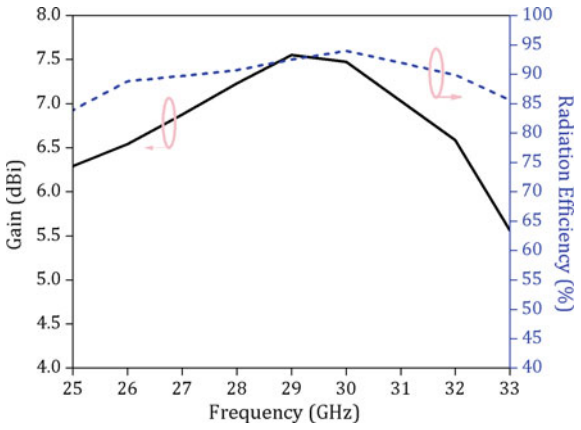

Fig. 7.22 Forward gain and radiation efficiency of the proposed ACS-fed mmWave 5G antenna

Table 7.3 Comparison of the ACS fed antenna with other reported designs

References	SOA	Gain (dBi)	1-dB GB (%)	Feeding type	FTBR
[36]	12 × 12	3–4.5	NA	CPW	NA
[37]	NA	8–10	NA	CPS	NA
[38]	11 × 20	6–7	20	CPW	>12
[39]	10.5 × 10	6–7	20	CPW	>12
PW	6 × 10	6.5–7.5	20.7	ACS	>13

SOA = Size of antenna (in mm^2), GB = Gain bandwidth, FTBR = Front-to-back ratio (in dB), NA = Not available, CPS = Coplanar stripline, PW = Proposed work

7.4.2 Shared Ground Two Port Design

The primary objective of designing the two-port shared ground antenna module is to attain the beam switching at ±30° in the E-plane, which is conventionally achieved by physically orienting antenna elements with separate grounds. To miniaturize this beam switching module, shared ground module is investigated. Two-port antenna module is designed on 10 mil thick Rogers 5870 substrate, like the standalone element. The proposed topology consists of two identical ACS-fed compact antennas sharing the common ground in mirrored configuration. The dimensions of the proposed two port antenna design are 1.0 λ × 1.6 λ at 28 GHz. The antenna topology is symmetrical about the Y-axis. Schematic of the proposed ground shared two port antenna is depicted in Fig. 7.23.

Each antenna element consists of stepped radiator which is fed by 50 Ω ACS feedline, which is exclusively designed for the shared radiator topology. The stepped configuration helps in achieving wide impedance bandwidth in the shared ground context. Here, the unbalanced feedline aids in obtaining beam tilt which mainly depends on length of the ground plane laterally (along X axis) and offset of radiator with respect to phase center of the module. The farther the radiating element from the physical phase center, higher is the beam tilt. Beam tilt would be restricted to 45°, beyond which the phase center offset effect would be minimal. The size of stepped radiator and shared ground is optimized to attain 30° beam tilt as a proof of concept. Varying length corrugations were introduced in the ground, like the standalone element, which helps in reduction of mutual coupling between two closely spaced antenna elements (0.9 λ) across the entire operating frequency band. Proposed antenna geometry is fabricated, and photograph is shown in Fig. 7.24.

Since the space for mounting end launch connectors at both the antenna ports is limited, standard 50 Ω SMA ports are used for measurement purposes which are operational in the Ka-band. Even though SMA connectors are rated up to 26.5 GHz, these are operational up to 30 GHz without significant insertion loss. The solder between the connector and the antenna element must be minimal, to prevent detuning of the antenna due to lead inductance of the solder. Also, the unnecessary legs of the SMA connector were trimmed to prevent interaction with the metallic geometry of the antenna. The trace pin of the SMA connector was shortened to aid better impedance

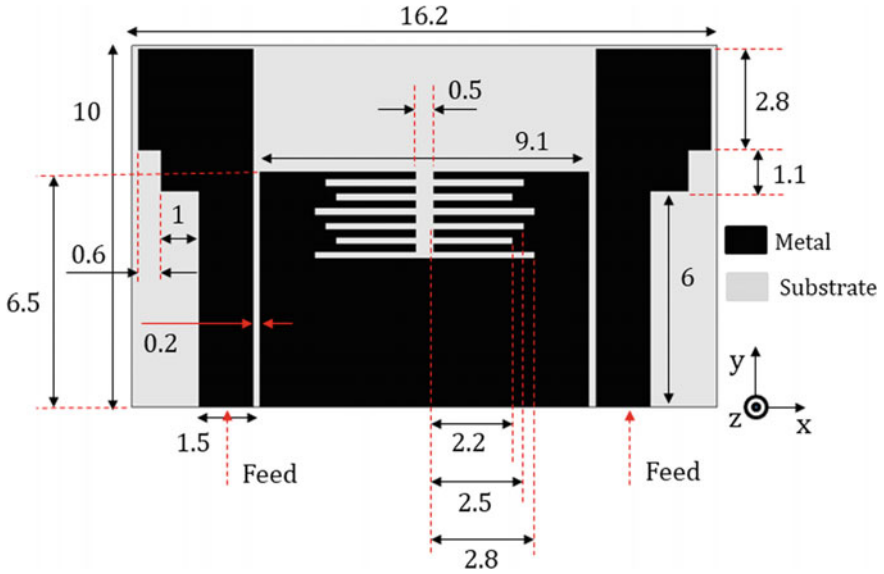

Fig. 7.23 Schematics of the proposed ACS-fed mmWave 5G two port antenna module (All dimensions are in mm) [32]

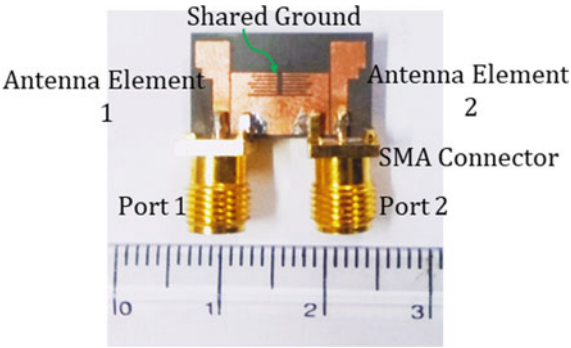

Fig. 7.24 Photograph of the fabricated two port ground shared antenna [32]

matching in the fabricated prototype. Simulated and measured input reflection coefficients of the proposed shared ground antenna are illustrated in Fig. 7.25. Both the antenna elements operate from 23 to 32 GHz with fractional bandwidth of 32.7%. Mutual coupling between the antenna elements is less than 13 dB in the entire operating band, which is a low value given the shared ground nature of the design. Varying length corrugations provides the additional path for the flow of surface currents from one antenna to another thereby enhancing isolation by almost 4 dB over the whole operating frequencies. Figure 7.25a, b depicts the simulated and measured input reflection co-efficient and isolation respectively.

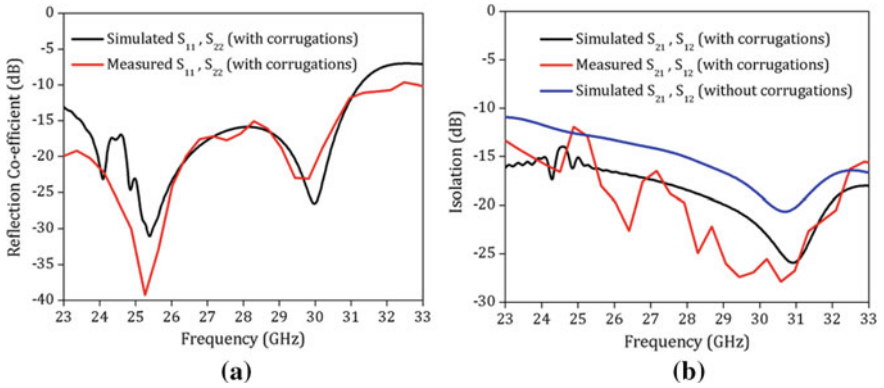

Fig. 7.25 **a** Input reflection co-efficient and **b** isolation plot for both antenna elements [32]

Radiation patterns with high pattern integrity for both the antenna elements in XY-plane (E-plane) are shown in Fig. 7.26 at 28 GHz. Measured beamwidth for each of the antenna elements is $40° \pm 5°$ in the main lobe. Proper beam orientation at $\pm 30°$ can be noticed which is mainly due to reflection caused by asymmetric ground plane and the relative placement of the radiator with respect to the phase center of the shared ground antenna. Front-to-back ratio of more than 18 dB is achieved for both the antenna elements, hence proving its suitability for base stations or access point applications.

End-fire gain of the proposed two port antenna geometry for the main lobe ranges between 5 and 6.8 dBi over the entire operating band as depicted in Fig. 7.27. Due to leakage of radiations occurring between two antenna elements through shared ground plane, gain of either of the antenna element is deteriorated in comparison with single

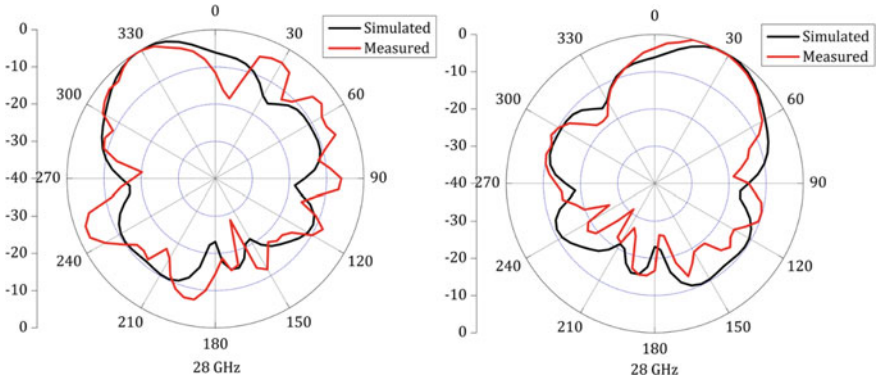

Fig. 7.26 Simulated and measured radiation patterns in XY plane when each antenna port is excited at 28 GHz [32]

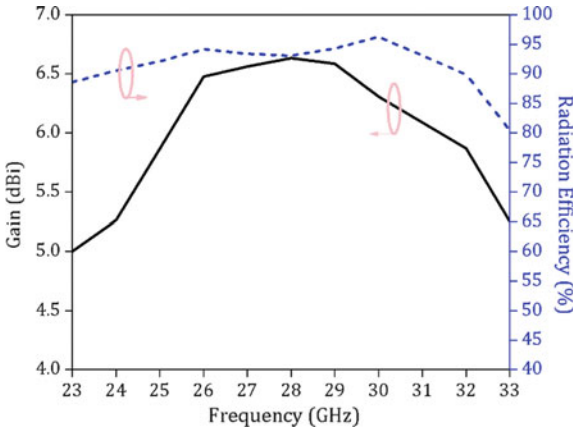

Fig. 7.27 End-fire gain and radiation efficiency of either of the two-port ground shared antenna [32]

element topology discussed in the previous Section. The 1-dB gain bandwidth is around 24.5% in the operating band, indicating high pattern integrity.

7.4.3 A Quasi-Stacking Design for Base Stations

The shared ground design of Sect. 7.4.2 would be useful for firing beams at $+30°$ and $-30°$, which means that there would be a significant blind spot in and around $0°$. Therefore, a three-dimensional compact antenna topology is proposed for mmWave 5G base stations. This topology provides a higher angular coverage compared to the two-port design. Schematics of the proposed antenna architecture is illustrated in Fig. 7.28 with corresponding photograph of the fabricated prototype in Fig. 7.29. The central element is placed above the shared ground module and the separation is around 0.4 λ which is optimized for attaining better isolation.

Compact antenna architecture is placed in a fabricated three-dimensional housing made of Poly Lactic Acid (PLA). PLA has a dielectric constant of around 2.56 with a dielectric loss tangent of 0.018 at 28 GHz. The housing also doubles up as a radome.

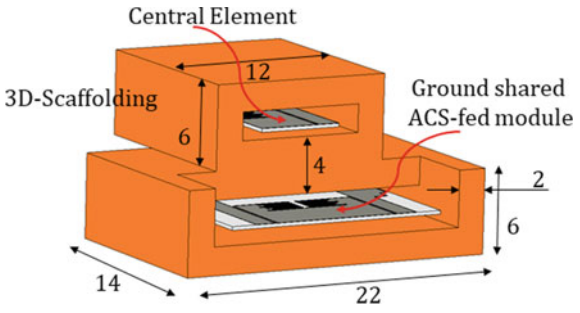

Fig. 7.28 Schematics of the proposed ACS-fed mmWave 5G pattern diversity module (All dimensions are in mm) [32]

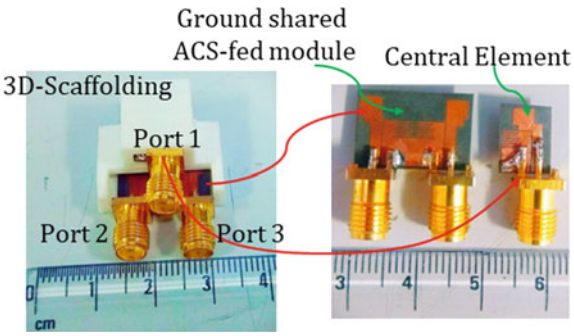

Fig. 7.29 Photograph of the fabricated prototype [32]

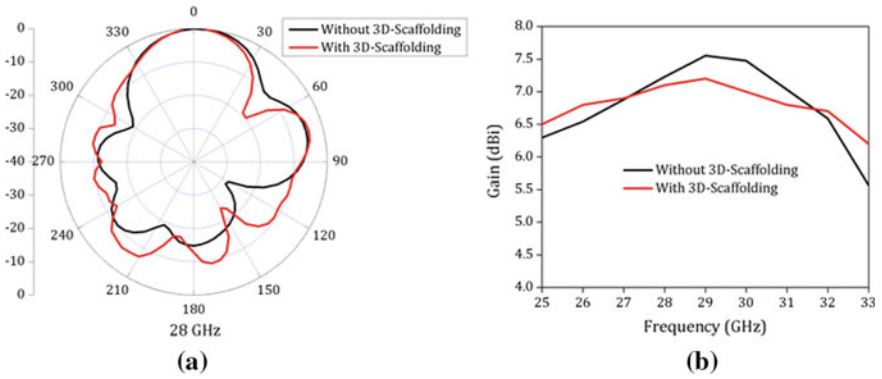

Fig. 7.30 **a** Radiation pattern and **b** gain plot of the central element ACS-fed antenna [32]

The transmission loss of the 3D-printed scaffolding is negligible as demonstrated in the Fig. 7.30, with and without scaffolding, since the transmission loss is only 0.5–0.75 dB across the band of interest. It is also interesting to note that the gain deterioration due to the integration of scaffolding is only 0.5 dB, which is justified in a practical deployment scenario. The gain deterioration is minimal irrespective of the port which is being excited. The measurements were all performed with the integrated scaffolding, hence proving the above features. The patterns and gain are illustrated in Fig. 7.31.

For central element in pattern diversity module, physical offset of 6 mm is introduced in the end-fire direction, in the Y axis with reference to Fig. 7.23, from the feed plane of shared ground antenna architecture in order to reduce the quasi-waveguide effect caused by the shared ground module. Mutual coupling between the antenna elements is less than 14 dB across the entire operating band as illustrated in Fig. 7.32.

Radiation pattern of the three-port pattern diversity module at 28 GHz is depicted in Fig. 7.33. Uniform coverage of $-45°$ to $+45°$ is attained over the entire operating band. Shared ground module directs beam at $\pm 30°$ and the central element shoots

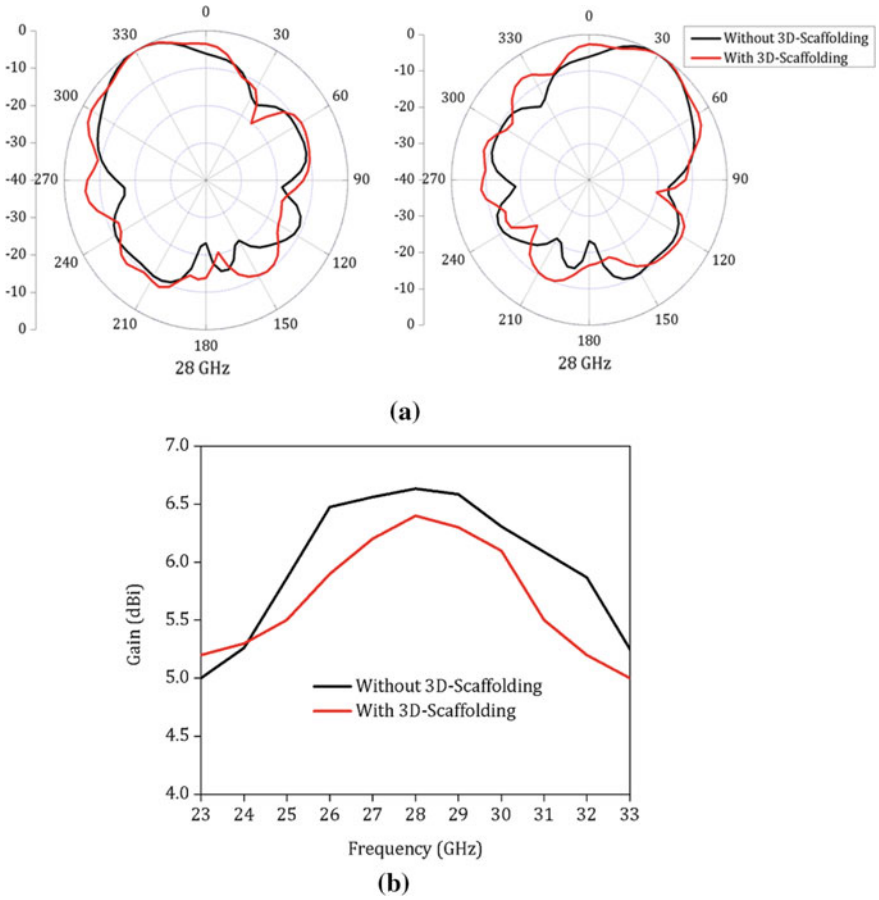

Fig. 7.31 **a** Radiation patterns and **b** Gain plot of the two-port ground shared antennas [32]

the beam at 0° thus obtaining the uniform coverage of 90°. The proposed three port pattern diversity design could be a potential candidate for mmWave 5G base stations.

7.5 Conclusion

In this Chapter, pattern diversity architectures for mmWave 5G base stations are introduced. The design requirements for beam switching are explained in detail. The technical requirements from an antenna implementation perspective also were introduced with typical desired numerical values and feasibility of the same. Couple of techniques for achieving gain with minimal physical footprint was introduced. The first design example was a high aperture efficiency wideband end-fire antenna. here,

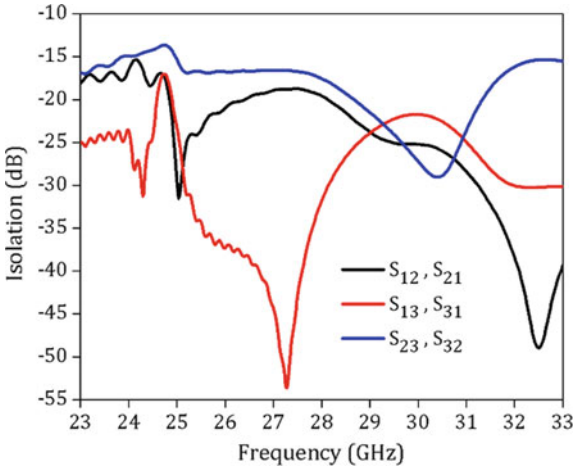

Fig. 7.32 Mutual coupling between antenna elements placed in mmWave 5G pattern diversity module [32]

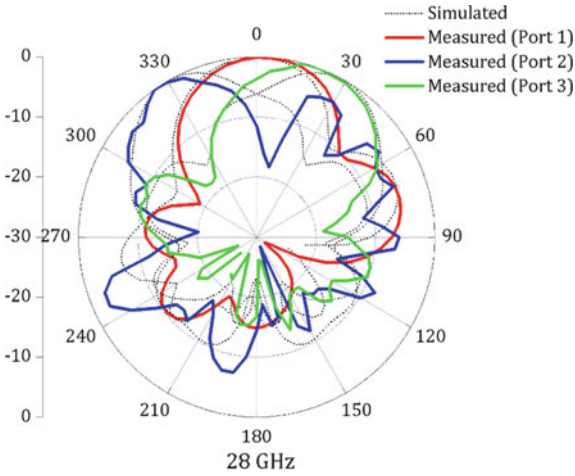

Fig. 7.33 Radiation patterns at 28 GHz [32]

electrically small unit cells were integrated with the radiating aperture of a traveling wave antenna to increase the forward gain. As a result, gain enhancement without compromise in the electrical size, aperture efficiency increased across the operating bandwidth. A stacked pattern diversity module with wide angular coverage also was investigated. This design was followed by a wideband ACS fed end-fire antenna. A shared ground extension of the element to achieve beam switching between $+30°$ and $-30°$ was also explained. A quasi-stacking design using the ACS fed antennas was investigated thoroughly. This Chapter gave a glimpse of design requirements for base station antennas along with practical design examples with theoretical and experimental results.

References

1. Parchin, N.O., Al-Yasir, Y.I., Abd-Alhameed, R.A.: A compact 5G antenna array with ultra-wide bandwidth for MM-wave smartphone applications. In: 2021 15th European Conference on Antennas and Propagation (EuCAP), pp. 1–4. IEEE (2021, March)
2. Bang, J., Choi, J.: A compact hemispherical beam-coverage phased array antenna unit for 5G mm-wave applications. IEEE Access **8**, 139715–139726 (2020)
3. Chang, Y.C., Hsu, C.C., Magray, M.I., Chang, H.Y., Tarng, J.H.: A novel dual-polarized wide-band and miniaturized low profile magneto-electric dipole antenna array for mmWave 5G applications. IEEE Open J. Antennas Propag. **2**, 326–334 (2021)
4. Biswal, S.P., Sharma, S.K., Das, S.: Collocated microstrip slot MIMO antennas for cellular bands along with 5G phased array antenna for user equipments (UEs). IEEE Access **8**, 209138–209152 (2020)
5. Kim, W., Bang, J., Choi, J.: Low-profile vertically polarized endfire phased array antenna for 5G mm-wave applications. In: 2020 International Symposium on Antennas and Propagation (ISAP), pp. 83–84. IEEE (2021, January)
6. Hansen, R.C.: Phased Array Antennas, vol. 213. Wiley, New York (2009)
7. Monavar, F.M., Shamsinejad, S., Mirzavand, R., Melzer, J., Mousavi, P.: Beam-steering SIW leaky-wave subarray with flat-topped footprint for 5G applications. IEEE Trans. Antennas Propag. **65**(3), 1108–1120 (2017)
8. Mak, K.M., So, K.K., Lai, H.W., Luk, K.M.: A magnetoelectric dipole leaky-wave antenna for millimeter-wave application. IEEE Trans. Antennas Propag. **65**(12), 6395–6402 (2017)
9. Su, Z., Vaseem, M., Li, W., Yang, S., Shamim, A.: Additively manufactured frequency/radiation pattern reconfigurable antenna based on monolithically printed VO 2 switch. In: 2019 13th European Conference on Antennas and Propagation (EuCAP), pp. 1–4. IEEE (2019, March)
10. Majid, H.A., Rahim, M.K.A., Hamid, M.R., Ismail, M.F.: Frequency and pattern reconfigurable slot antenna. IEEE Trans. Antennas Propag. **62**(10), 5339–5343 (2014)
11. Saghati, A.P., Saghati, A.P., Entesari, K.: An ultra-miniature SIW cavity-backed slot antenna. IEEE Antennas Wirel. Propag. Lett. **16**, 313–316 (2016)
12. Nesbitt, P.B., Mumcu, G.: A small slot dipole loaded with CRLH TL unit cells. In: 2011 IEEE International Symposium on Antennas and Propagation (APSURSI), pp. 1032–1035. IEEE (2011, July)
13. Muzaffar, K., Magray, M.I., Karthikeya, G.S., Koul, S.K.: Wideband high aperture efficiency antennas with beam switching for mmWave 5G base stations. Int. J. RF Microw. Comput.-Aided Eng. **30**(8), e22254 (2020)
14. Hussain, N., Jeong, M.J., Park, J., Kim, N.: A broadband circularly polarized fabry-perot resonant antenna using a single-layered PRS for 5G MIMO applications. IEEE Access **7**, 42897–42907 (2019)
15. Dias, G., Pinho, P., Gonçalves, R., Carvalho, N.: 3D antenna for wireless power transmission: aperture coupled microstrip antenna with dielectric lens. In: 2017 International Applied Computational Electromagnetics Society Symposium-Italy (ACES), pp. 1–2. IEEE (March 2017)
16. Amiri, M., Tofigh, F., Ghafoorzadeh-Yazdi, A., Abolhasan, M.: Exponential antipodal Vivaldi antenna with exponential dielectric lens. IEEE Antennas Wirel. Propag. Lett. **16**, 1792–1795 (2017)
17. Chauhan, S.S., Abegaonkar, M.P., Basu, A.: Millimeter wave frequency scanning antenna for body centric communication. In: 2017 International Symposium on Antennas and Propagation (ISAP), pp. 1–2. IEEE (2017)
18. Vosoogh, A., Kildal, P.S.: Corporate-fed planar 60-GHz slot array made of three unconnected metal layers using AMC pin surface for the gap waveguide. IEEE Antennas Wirel. Propag. Lett. **15**, 1935–1938 (2015)
19. Zhai, G., Cheng, Y., Yin, Q., Zhu, S., Gao, J.: Uniplanar millimeter-wave log-periodic dipole array antenna fed by coplanar waveguide. Int. J. Antennas Propag. **2013** (2013)

20. Sugawara, S., Maita, Y., Adachi, K., Mori, K., Mizuno, K.: Characteristics of a mm-wave tapered slot antenna with corrugated edges. In: 1998 IEEE MTT-S International Microwave Symposium Digest (Cat. No. 98CH36192), vol. 2, pp. 533–536. IEEE (June 1998)
21. Smith, D.R., Schultz, S., Markoš, P., Soukoulis, C.M.: Determination of effective permittivity and permeability of metamaterials from reflection and transmission coefficients. Phys. Rev. B **65**(19), 195104 (2002)
22. Szabó, Z., Park, G.H., Hedge, R., Li, E.P.: A unique extraction of metamaterial parameters based on Kramers-Kronig relationship. IEEE Trans. Microw. Theory Tech. **58**(10), 2646–2653 (2010)
23. https://mpd.southwestmicrowave.com/end-launch-connectors-installation-procedure/
24. Karthikeya, G.S., Abegaonkar, M.P., Koul, S.K.: Path loss compensated beam switchable antennas with spatially modulated zero-index metamaterial loading for 5G base stations. IET Microwaves Antennas Propag. **13**(14), 2509–2514 (2019)
25. Jilani, S.F., Greinke, B., Hao, Y., Alomainy, A.: Flexible millimetre-wave frequency reconfigurable antenna for wearable applications in 5G networks. In: 2016 URSI International Symposium on Electromagnetic Theory (EMTS), pp. 846–848. IEEE (Aug 2016)
26. Wani, Z., Abegaonkar, M.P., Koul, S.K.: Millimeter-wave antenna with wide-scan angle radiation characteristics for MIMO applications. Int. J. RF Microw. Comput.-Aided Eng. **29**(5), e21564 (2019)
27. Wang, N.N., Fang, M., Chou, H.T., Qi, J.R., Xiao, L.Y.: Balanced antipodal Vivaldi antenna with asymmetric substrate cutout and dual-scale slotted edges for ultrawideband operation at millimetre-wave frequencies. IEEE Trans. Antennas Propag. **66**(7), 3724–3729 (2018)
28. Jilani, S.F., Alomainy, A.: Millimetre-wave T-shaped MIMO antenna with defected ground structures for 5G cellular networks. IET Microwaves Antennas Propag. **12**(5), 672–677 (2018)
29. Sun, M., Chen, Z.N., Qing, X.: Gain enhancement of 60-GHz antipodal tapered slot antenna using zero-index metamaterial. IEEE Trans. Antennas Propag. **61**(4), 1741–1746 (2012)
30. El-Nady, S., Zamel, H.M., Hendy, M., Zekry, A.A., Attiya, A.: Gain enhancement of a millimeter wave antipodal vivaldi antenna by epsilon-near-zero metamaterial. Prog. Electromagn. Res. C **85**, 105–116 (2018)
31. Sadananda, K.G., Abegaonkar, M.P., Koul, S.K.: Gain equalized shared-aperture antenna using dual-polarized ZIM for mmWave 5G base stations. IEEE Antennas Wirel. Propag. Lett. **18**(6), 1100–1104 (2019)
32. Magray, M.I., Karthikeya, G.S., Muzaffar, K., Koul, S.K., Moon, A.H.: Wideband asymmetric coplanar strip fed antennas with pattern diversity for mmWave 5G base stations. IEEE Access **8**, 77482–77489 (2020)
33. Rajkumar, R., Kommuri, U.K.: A compact ACS-fed mirrored L-shaped monopole antenna with SRR loaded for multiband operation. Prog. Electromagn. Res. C **64**, 159–167 (2016)
34. Gauthier, G.P., Courtay, A., Rebeiz, G.M.: Microstrip antennas on synthesized low dielectric-constant substrates. IEEE Trans. Antennas Propag. **45**(8), 1310–1314 (1997)
35. Zhang, C., Gong, J., Li, Y., Wang, Y.: Zeroth-order-mode circular microstrip antenna with patch-like radiation pattern. IEEE Antennas Wirel. Propag. Lett. **17**(3), 446–449 (2018)
36. Jilani, S.F., Abbas, S.M., Esselle, K.P., Alomainy, A.: Millimeter-wave frequency reconfigurable T-shaped antenna for 5G networks. In: 2015 IEEE 11th International Conference on Wireless and Mobile Computing, Networking and Communications (WiMob), pp. 100–102. IEEE (Oct 2015)
37. Alhalabi, R.A., Rebeiz, G.M.: Differentially-fed millimeter-wave Yagi-Uda antennas with folded dipole feed. IEEE Trans. Antennas Propag. **58**(3), 966–969 (2009)
38. Karthikeya, G.S., Abegaonkar, M.P., Koul, S.K.: CPW fed wideband corner bent antenna for 5G mobile terminals. IEEE Access **7**, 10967–10975 (2019)
39. Karthikeya, G.S., Abegaonkar, M.P., Koul, S.K.: A wideband conformal antenna with high pattern integrity for mmWave 5G smartphones. Prog. Electromagn. Res. Lett. **84**, 1–6 (2019)

Chapter 8
Feeding Techniques for mmWave Antennas

8.1 Introduction

Future telecommunication systems would be built upon higher carrier frequencies, as observed in the previous Chapters. This agenda could be realized with an increase in the spectral efficiency of the current modulation schemes [1, 2]. Feeding techniques for antennas in the microwave domain are well understood and commercially viable. The feeding mechanism itself plays a negligible role in the microwave spectrum.

The only feasible option to realize a mmWave link is to increase the gains of the antennas on mobile devices and base stations [3, 4]. The form factor would be a limiting factor for both the applications; hence it is imperative to achieve high gain for the available physical footprint in the 28 GHz band. One of the most common strategies to enhance gain of the antenna is to design a phased array. This method would in fact increase the complexity of the system and leads to a narrower beam, hence compromising coverage.

To design any antenna or antenna system for mmWave 5G cellular communication systems, radiation efficiency must be as high as possible for the chosen substrate parameters. One of the critical aspects for antenna design is the choice of feeding technique used to energize the antenna. The designs reported in [5] are targeted for wearable applications and all the designs are in the sub-6 GHz frequency domain.

An exhaustive variety of feeding techniques are considered in this Chapter. Each section begins with a description of a generic layout of the feeding line connecting to the radiating element followed by the study of feasibility of designing a feed line with a 50 Ω characteristic impedance. The influence of the feeding technique to realize unidirectional broadside and end-fire radiation patterns is also discussed in detail. Feasibility to extend a particular antenna designed by a specific feeding technique, to a phased array is also discussed. Merits and demerits of each feeding method in the context of 28 GHz antennas for 5G applications is explained in detail. Lot of design examples reported in the recent literature are also presented.

S. K. Koul and K. G. S., *Antenna Architectures for Future Wireless Devices*,
Signals and Communication Technology,
https://doi.org/10.1007/978-981-16-7783-0_8

8.2 Microstrip Feeding

One of the most common and popular feeding techniques to realize passive and active PCB (Printed Circuit Board) based antennas is microstrip feeding. Here, a dielectric layer is sandwiched between two metal layers of finite thickness, typically 10–50 μm. The top player is an electrically thin transmission line feeding the radiating element and the bottom layer is typically an all-metallic ground plane, depending on the application. Defected or partial ground plane might be incorporated to achieve wide impedance bandwidth [6, 7] with a consequent compromise in the beam and gain integrity of the element. Most of the mmWave 5G applications require a unidirectional beam, hence most of the reported designs for this application have a complete ground plane. Schematics of the general microstrip feed line are shown in Fig. 8.1.

The choice of substrate would dictate the dimensions of the feeding network to the radiator [8]. Lower dielectric constant would ensure minimal surface wave modes at the cost of increased physical size of the radiator. Dielectric loss tangent also decides the achievable gain and the consequent radiation efficiency of the microstrip fed antenna [9]. The concept of dielectric loss tangent is applicable to any printed antenna and is agnostic to the feeding technique per se. The substrates should be electrically thin, for instance 0.1 λ computed at the highest frequency of operation. Electrically thin substrates would ensure high polarization purity, especially for end-fire antennas [10]. The cross-polarization radiation level increases with the substrate thickness, with a noticeable increase in the impedance bandwidth. Hence, the designer must consider afore-mentioned aspects and deduce the apt candidate for the application at hand. The other reason for relatively higher cross-polarization level is due to the offset of the radiating arms of a dipole [10] or an antipodal element [11]. Often, 20 mil (or 0.508 mm) thick substrate would deliver a reasonable compromise between cross-pol and impedance bandwidth.

Microstrip feeding is readily feasible in the sub-6 GHz frequencies as illustrated by numerous articles [12, 13]. To scale up the frequency to the 28 GHz band, characteristic impedance of the feeding line must be close to the port impedance of 50 Ω and must be electrically thin enough to avoid spurious radiation and over-moding.

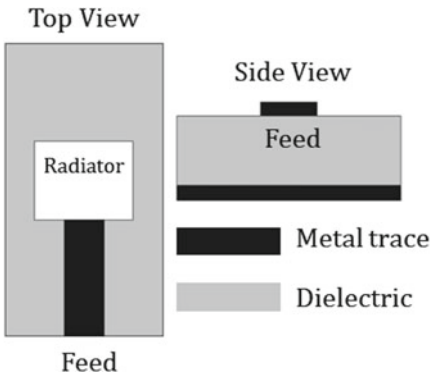

Fig. 8.1 General layout of the microstrip feed line

Table 8.1 50 Ω line widths for microstrip feeding

Substrate	ε_r	Thickness (mm)	Trace width (mm)
Air	1	0.2	0.95
		1	4.9
Rogers 5880	2.2	0.2	0.6
		1	3.5
Silicon	11.9	0.2	0.14
		1	1.33

Table 8.1 illustrates a few common substrates and the trace width of the 50 Ω line on the substrate. If the substrate to be used is constrained due to the PCB to be used for the overall circuitry, then the designer might use a higher impedance line and design an impedance transformer to the radiator to achieve a reasonable beamwidth with high beam integrity.

One of the benefits of microstrip feeding is that the all-metallic ground plane acts as an isolating network or as an EMI (Electromagnetic Interference) shield to the back-end electronics. The problem with microstrip feeding is the lossy, electrically long transmission lines feeding the radiating element. The insertion loss could be mitigated by using low-loss substrate and integrating with a metallic shield over the feeding lines alone. The coaxial feeding has minimal footprint of the feeding lines in the plane of the radiator, leading to reduced influence of the feed on the performance metrics of the radiator. If the microstrip fed feeding network and the radiating apertures are in the orthogonal planes, influence of feed lines on radiation could be reduced to some extent.

Microstrip feeding offers flexibility to achieve broadside and end-fire radiations. If the broadside radiating element is fed through a proper impedance transformer, a unidirectional beam with high gain could be achieved. Gain is decided by the effective radiating aperture. Unidirectional broadside beam could be achieved due to the electrically large ground plane. CPW fed broadside radiator with high front to back ratio would be difficult to achieve. Microstrip feeding also supports easier realization of end-fire antennas. For instance, printed dipole or antipodal antenna could be realized with microstrip feeding with the design of proper feeding network. Microstrip feeding also permits the use of industry standard chemical etching even up to 60 GHz, provided the choice of substrate permits the dimensions feasible with fabrication. Typically, chemical etching permits a minimum dimension of up to and including 100 μm.

Phased arrays seem to be one of the most advertised candidate antennas for 5G systems [14]. Microstrip feeding also supports implementation of phased arrays, but the insertion loss in the feeding lines would be detrimental when the phased array consists of many antenna elements. Even with a single port design, such as in a corporate fed array [8], the discontinuities in the power dividers and other pieces of the feed network would create speckles in the radiation, thus compromising the beam integrity and gain. Wilkinson based power divider might improve the gain, but at the cost of increased complexity to integrate passive resistors in the feed network.

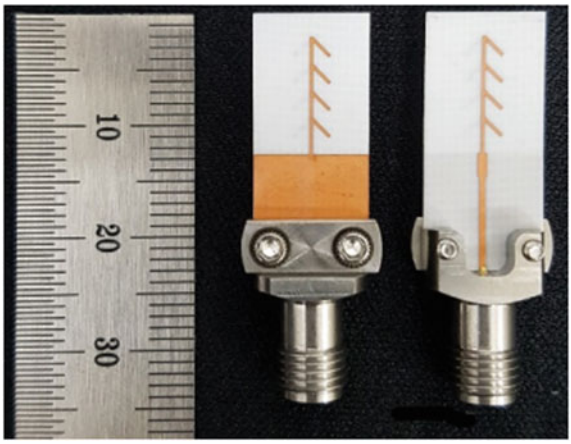

Fig. 8.2 Wideband end-fire antenna [20]

Designing sub-arrays to scale it up to a larger array is also a difficult process with a conventional microstrip feed.

A slot antenna and its corporate fed array, designed at 28 GHz is reported in [15]. The authors have used a reflector to achieve wide impedance bandwidth with a significantly high front to back ratio. A corporate fed array designed on Rogers 5880 is proposed in [16]. Even though the patterns in the H-plane have a smooth profile, the E-plane patterns would be deteriorated due to the complex multi-sectioned power divider network. A wideband, 50% impedance bandwidth broadside radiator is presented in [17]. The presented design is implemented on 0.8 mm thick Rogers 5880 substrate (0.07 λ thick, calculated at 28 GHz). The beam integrity is preserved throughout the band.

Another type of feeding network for broadside narrow beam is reported in [18]. The design process presented in [19] is feasible due to the all-metallic (all-aluminum in this case) ground plane followed by oxidation and selective metallization on top of it. Numerous wideband, end-fire antennas in the 28 GHz band have been reported and thoroughly analyzed [20, 21]. An end-fire antenna with high gain is illustrated in Fig. 8.2.

8.3 CPW Feeding

CPW feeding is another feeding method which is readily feasible in the sub-6 GHz spectrum [22, 23]. It is a truly uniplanar feeding technique wherein the active circuitry or the back-end electronics could be interfaced with the antenna in the same plane as opposed to the microstrip feeding which requires two planes separated by the dielectric height. The construction of a CPW fed antenna has a central trace and the coplanar ground plane on both sides of the signal trace separated by a finite gap as

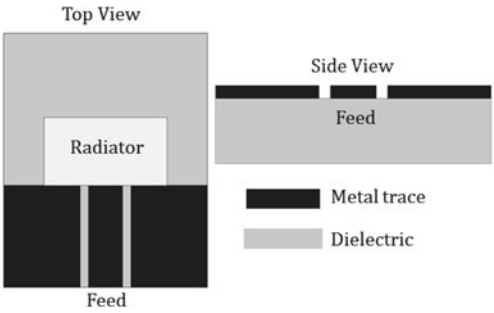

Fig. 8.3 Schematic of the general CPW feed line

illustrated in Fig. 8.3. The dimensions of this feeding line for a desired characteristic impedance are decided by the characteristics of the dielectric substrate [24].

For instance, to realize a 50 Ω feeding line on a substrate with a dielectric constant of 2.2 and a thickness of 0.2 mm, the central trace line must be 3.3 mm wide with a gap of 0.1 mm. The trace width must be preferably less than quarter-wavelength at the operating frequency to avoid spurious radiation emanating from the feed line itself. The critical parameter which decides the characteristic impedance is the gap between the trace and the ground. For electrically thin substrates, the gap width would be less than a fraction of a millimeter. Typical dimensions to realize a 50 Ω line on a few substrates is illustrated in Table 8.2. A wider gap between the trace line and the planar ground plane might lead to spurious radiation from the slot. Hence, it is a compromise between realistic characteristic impedance close to the port impedance and realizability on the given substrate. When it comes to CPW feeding, designers typically ignore the 50 Ω feeding line requirement based on the dimensional constraint laid down by the fabrication process chosen. Another point of concern with the trace width of the feed line is that the dimension must be chosen to lie within the grounding clamps of the end-launch connector which works up to 40 GHz. The trace pin must have adequate clearance to accommodate these dimensions as well.

The substrate to be chosen for a mmWave 5G antenna must be electrically thin, like that of the microstrip fed element. The cross-polarization radiation level might

Table 8.2 50 Ω line widths for CPW feeding

Substrate	ε_r	Th (mm)	TW (mm)	Gap (mm)
Air	1	0.2	6.8	0.1
		1	14.8	0.2
Rogers 5880	2.2	0.2	3.3	0.1
		1	2.17	0.1
Silicon	11.9	0.2	0.14	0.1
		1	0.26	0.2

Th Thickness (mm), *TW* Trace Width (mm)

increase with the thickness of the substrate even with a CPW feeding. To achieve broadside radiation from a CPW feed, the radiating aperture must be backed by a ground plane beneath the aperture or at an electrically close distance to achieve a unidirectional beam. This method of external reflector integration could complicate the assembly and might compromise the form factor of the entire antenna unit. The other alternative is to design a GCPW (Grounded CPW) feeding, wherein the entire substrate could be backed by a metallic ground plane. The 50 Ω characteristic impedance would differ between a conventional CPW line and a GCPW line. For instance, the trace width, on Rogers 5880 substrate with 0.2 mm thickness, for CPW line is 3.3 mm and for a GCPW line is 0.48 mm. The CPW trace line is wider than the GCPW line.

The most common antenna with unidirectional beam and CPW feed is to realize end-fire antennas. The CPW feed line would be connected to the radiating element through an appropriate impedance transformer or a balun. The front to back ratio could be greater than 10 dB with an electrically small form factor with uniplanar design. Wideband end-fire designs are readily feasible with CPW feeding in the 28 GHz band. The only issue with end-fire CPW fed antennas is that the antenna might exhibit a slight beam tilt due to the offset of the radiator with respect to the phase center of the feed. Electrically large traveling wave antennas such as tapered slot antenna or Vivaldi antenna might not have this issue when designed.

CPW feeding is not a preferred method for designing phased arrays as it does not offer flexibility to realize broadside or end-fire elements. It is interesting to note that there a few articles on designing power dividers and other necessary feeding components to realize a complete phased array with CPW feeding. The problem with designing impedance matched power divider for an electrically large array is that the higher impedance values would be difficult to realize with the industry standard chemical etching process. If a compromised impedance network is designed, then the overall realized gain would deteriorate significantly. As the CPW feeding does not offer scalability, it is usually avoided for phased arrays. As the dimensions of the geometry becomes tighter, realizing Wilkinson divider [8] with resistors would become difficult to implement, as the lead inductances of the packaged resistors might influence the impedance integrity of the power divider and would manifest in the performance metrics of the overall phased array system.

As the back-end electronics and the radiating elements would be on the same plane, mutual coupling between the two entities would be higher compared to let's say, coaxial feeding. Also, achieving a vertically polarized antenna element with CPW feeding is difficult.

A dual-polarized antenna system is presented in [25]. One of the antennas is a grounded CPW fed slot antenna operating in the 28 GHz band. The radiation slot is 0.355 λ, which acts as a linearly polarized radiating aperture. The patterns are almost omnidirectional as no metallic reflector is integrated. Another design with CPW feed is reported in [26]. It is a dual beam design with gain control achieved using variable resistances, experimental results have not been presented. A wideband bidirectional radiator is presented by the authors in [27]. To improve the front to back ratio, an external reflector is integrated electrically close to the radiating slot. The

planar version is recreated in Fig. 8.4. Wideband end-fire antennas are proposed in [28, 29]. One of the designs is recreated in Fig. 8.5. CPW feed also facilitates probe-based antenna measurements [30].

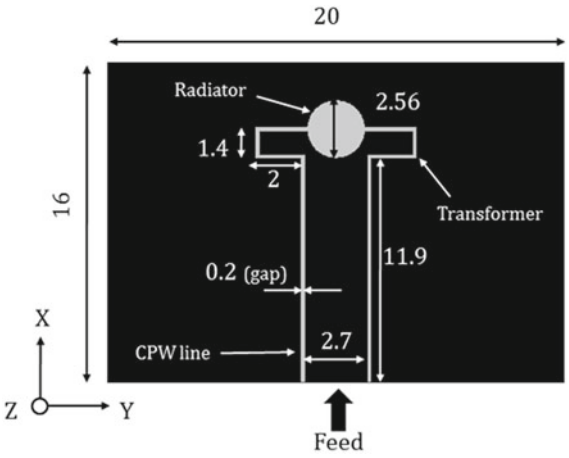

Fig. 8.4 Wideband CPW fed antenna [27]

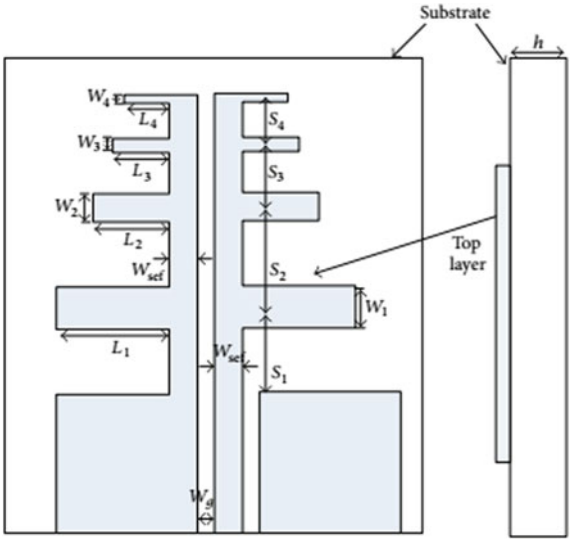

Fig. 8.5 Wideband CPW fed end-fire antenna [28]

8.4 Coaxial Feeding

Another popular technique of feeding antennas is the coaxial or probe feed. This is a well-documented feeding technique in the sub-6 GHz regime. The primary construction is the trace pin of the coaxial connector would be connected to a radiating element, which is placed on top of a suitable substrate. The ground of the connector would be shorted with that of the antenna element. This is a preferred feeding technique for multi-polarization or polarization diversity designs [31, 32]. It is also favorable for pattern diversity applications as demonstrated in the low frequency bands [33, 34]. Schematics of the co-axial feed line are depicted in Fig. 8.6.

This feeding technique is also preferred for scalable array designs, wherein a certain number of antenna elements could be controlled by a single controlling unit. This feature would be harder to implement with a microstrip feed. Most of the designs with a coaxial feed involve an electrically large ground plane which facilitates unidirectional radiation, which would be illustrated in subsequent examples. The thickness of the substrate typically decides the impedance bandwidth like that of microstrip feed. The electrically large ground plane also acts as a natural isolating network or a shield between the radiator and the RF back-end electronics. Probe feeding is also popular in implementing multilayer designs for integrated circuits' applications. Here, the antenna designs are connected by impedance matched probe to the circuitry.

Designers must ensure that the probe or the connector mounted with the antenna for measurements must not create spurious radiation as well. Typically, a sufficiently large ground plane which exceeds the clearance of that of the connector would mitigate this effect. The probe from the connector to the radiator must also be electrically small, typically less than 0.1 λ, to avoid higher cross-polarization radiation and speckles in the broadside patterns. Probe feeding typically results in broadside-unidirectional patterns. This limits the intended applications for the placement of probe-fed antennas. Probe feeding dimensions are adequate for wideband unidirectional antenna designs for mmWave 5G applications. The only point to be considered is that the probe should not exceed the contour of the radiator's surface to prevent detuning of the antenna. Another point for careful implementation is that the solder between the connector and the antenna must be as minimal as possible to avoid

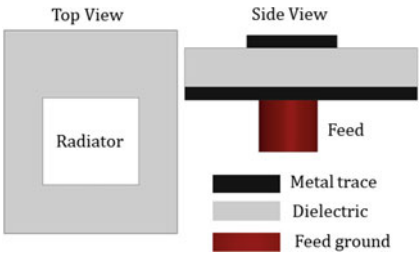

Fig. 8.6 General structure of co-axial feed line

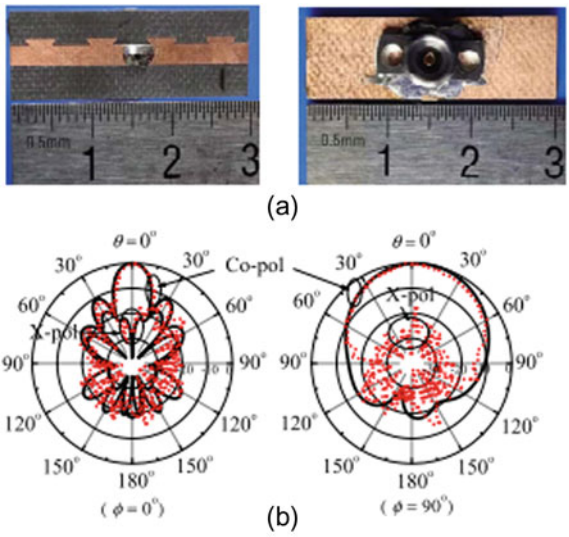

Fig. 8.7 Wideband probe-fed broadside antenna: **a** fabricated prototype and **b** Patterns at 29.1 GHz (Guo et al. [35], Reprinted with permission from IEEE)

additional lead inductance of the feed, which manifests as detuning of the input impedance of the antenna.

A coaxial-fed single layered wideband antenna is reported in [35]. The antenna is designed on Rogers 5880 substrate which has a dielectric constant of 2.2 and a corresponding dielectric loss tangent of 0.0009. Thickness of the substrate is 0.78 mm, translating to 0.07 λ at 28 GHz, implying minimal spurious radiation in the orthogonal plane with respect to the boresight axis. The authors achieved a 10 dB impedance bandwidth from 24.2 to 30 GHz, translating to 21.4% with a simple coaxial feed and no additional impedance tuning elements or baluns. The radiator itself doubles up as an impedance matching entity with the probe. The photograph is displayed in Fig. 8.7a. The reported antenna is electrically compact. The corresponding patterns in the principal planes at 29.1 GHz are illustrated in Fig. 8.7b. The beams are unidirectional, proving the utility of probe feeding. The authors have used conventional SMA (Subminiature A) connectors for measurements.

A low-cost probe fed antenna operating in the 28 GHz is reported in [36]. Even though the antenna is compact and well-matched in the intended band of application, the pattern integrity is compromised at the higher end of the spectrum. A panel mountable coaxial-fed end-fire antenna array is proposed in [37]. The utility of coaxial-feeding is evident in this design, as the feeding network has minimal influence on the radiating aperture of the antenna elements of the phased array. Probe feeding is customized for operation in the 28 GHz band. The overall footprint of the antenna system is less than 7 mm contributed by coaxial feed, wherein the control electronics lie in a different layer as that of the antenna system. The slotted frame acts as a secondary aperture in the presented design.

A wideband differentially fed antenna with an electrically thick substrate is proposed in [38]. The authors realized a wide bandwidth of 55% essentially due

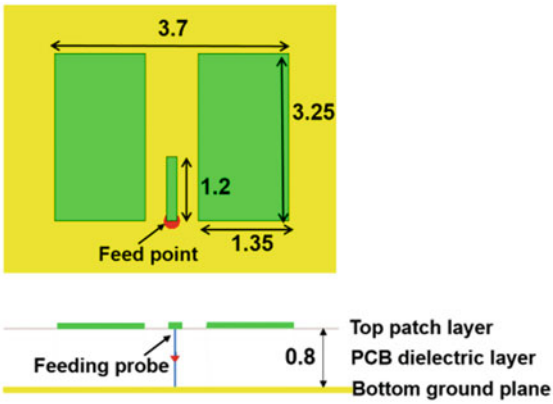

Fig. 8.8 Wideband co-ax fed antenna [42]

to the probe feed. In addition to the bandwidth, the antenna presented has high gain-bandwidth with unidirectional beams across the spectrum. A 21.5 GHz 16 elements' array is proposed in [39]. Here the power divider network and the RF circuitry is integrated beneath the antenna layer, thus minimizing interference on the radiation.

Coaxial-fed antenna design of [40] proves that coaxial feeding technique could be useful to achieve end-fire radiation as well. The authors have used a coaxial-fed SIW arrangement which acts as an impedance transformer from the feed to the planar log-periodic dipole element. The antenna topology illustrated in [41] is an example to achieve broadside and end-fire patterns at 28 GHz with a small form factor.

The scalability of coaxial-feeding is evident from the sub-array reported in [42]. The schematics of the primary element of the phased array are recreated in Fig. 8.8. The coaxial feeding is realized using SMPM connector and the entire phased array could be housed in a modern compact commercial smartphone.

8.5 ACS Feeding

Asymmetric Coplanar Stripline (ACS) feeding is a non-conventional feeding technique that has been primarily utilized at low frequencies [43–47]. Like CPW feeding, this technique is also uniplanar in nature in which the signal trace and ground plane lie in the same plane. However, ACS feeding comprises of single asymmetrical ground plane lying on either side of the signal trace, which is in contrast with CPW feeding where ground planes lie on both sides of signal trace [27]. Thus, ACS feeding aids in the overall miniaturization of antenna. Moreover, in comparison to CPW feeding, implementation of ACS feeding results in suppression of various parasitic modes, like odd mode and parallel plate mode (present in GCPW). Schematics of the general ACS feed line are illustrated in Fig. 8.9.

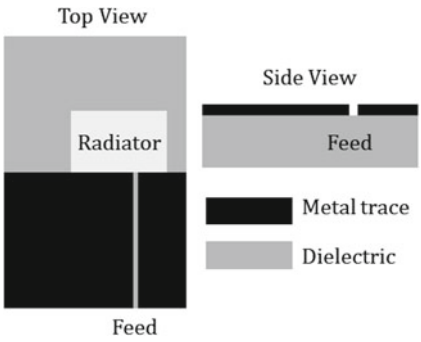

Fig. 8.9 Schematics of the general ACS feed line

This technique utilizes unbalanced feed line that is in contrast with the Co-planar Stripline (CPS) feeding where balanced feed line is used. ACS feeding has the advantage over CPS feeding as the former decreases overall physical footprint of antenna. For measurement purposes, CPS feed line would require a transition design like balun from unbalanced to balanced feed line that will increase the complexity of design and therefore increases overall size of the antenna in comparison to ACS feeding. Moreover, CPS feedline alone wouldn't be adequate for attaining unidirectional radiation pattern since it will require electrically large reflector that CPS feed line is lacking.

The characteristic impedance of ACS feed line is determined by the width of signal trace, gap between signal trace and asymmetric ground plane. Moreover, dielectric constant of substrate lying under the ACS feed line largely determines characteristic impedance of the feed line. The width of signal trace should be kept electrically small to avoid any parasitic radiation emerging out from the feed line. The design parameters of ACS feedline exhibiting some characteristic impedance should be chosen in such a way that physical dimensions of feed line should be able to fabricate. Typically, the physical dimensions of a feed line of the antenna should be greater than 50 μm, to be feasible for chemical etching. For ACS feeding, the antenna characteristics mostly remain unaltered with change in substrate thickness. But the substrate thickness would play a crucial role in contributing to the overall gain and polarization purity. Table 8.3 illustrates the physical dimensions of design parameters for 50 Ω ACS feed line. As evident from the table, lower dielectric constant leads to

Table 8.3 50 Ω line widths for ACS feeding

Substrate	ε_r	Gap (mm)	Trace width (mm)
Air	1	0.1	9.1
		0.2	18.3
Rogers 5880	2.2	0.1	2.5
		0.2	5.1
Silicon	11.9	0.1	0.16
		0.2	0.33

wider lines thus leading to deteriorated radiation performance. But the gap between the trace line and the ground could be engineered to mitigate the parasitic radiation.

At lower frequencies, the asymmetric ground plane is kept electrically small, around quarter-wavelength so that the radiation pattern of the antenna is omni-directional in nature, also the contribution from the ground plane per se at lower frequencies is negligible on the radiation patterns. However, for mmWave 5G antennas, the ground plane should be electrically large enough to make the radiation pattern directional, as the ground plane would act as a reflector. So far there is only one reported design implementing ACS feeding at mmWave 5G frequencies [48]. It is comparatively challenging to design ACS-fed antenna at mmWave frequencies in comparison to lower frequencies. Electrically large asymmetric ground plane plays a vital role in the directionality of radiation pattern of mmWave 5G ACS-fed antenna, thus making it challenging to produce uniform and stable radiation patterns over entire operating bandwidth of antenna. Also, the impedance integrity must be maintained.

The advantage of using ACS feeding is to miniaturize the overall size of an antenna. It is interesting to note that the miniaturization happens due to the nature of the feeding technique itself and not by additional matching circuits. Therefore, it will be quite useful to implement this feeding for mobile phone applications as form factor of cellular devices is getting smaller and smaller every year. The only catch would be to design additional impedance matching transformers from the back-end circuitry to the radiating element. At mmWave 5G frequencies, the end-fire antennas are more preferred over broadside antennas and the implementation of this feeding for end-fire antennas can be comparatively easier, given the uniplanar nature of the feed. However, due to asymmetric ground plane an undesired beam tilt is obtained that should be rectified by proper technique without any deterioration in impedance bandwidth. Like CPW-feeding, it will be hard to design phased antenna arrays by ACS feeding.

A wideband ACS-fed end-fire antenna is presented in [48], which is one of the few reported designs on ACS feeding at 28 GHz. Schematics of the design are depicted in Fig. 8.10. A rectangular radiator of 85.5 Ω is fed by an impedance transformer of 65.4 Ω that connects to 50 Ω ACS feed line. Impedance transformer is used to improve impedance matching. An electrically large ground plane has been used for steering the beam in the end-fire direction with high front-to-back ratio (FTBR). Horizontal and varying length corrugations are used in ground plane for attaining high gain and high FTBR. It can be noticed that a physical offset has been introduced in the radiator for obtaining uniform radiation patterns in the E-plane. End-fire radiation patterns are illustrated in Fig. 8.11. Due to reflected radiations from asymmetric ground plane, an undesired side lobe is produced in the E-plane of antenna. The radiation pattern obtained in the H-plane is uniform and free from any side lobes. The side lobe level should be low enough so that significant radiation is directed towards end-fire direction.

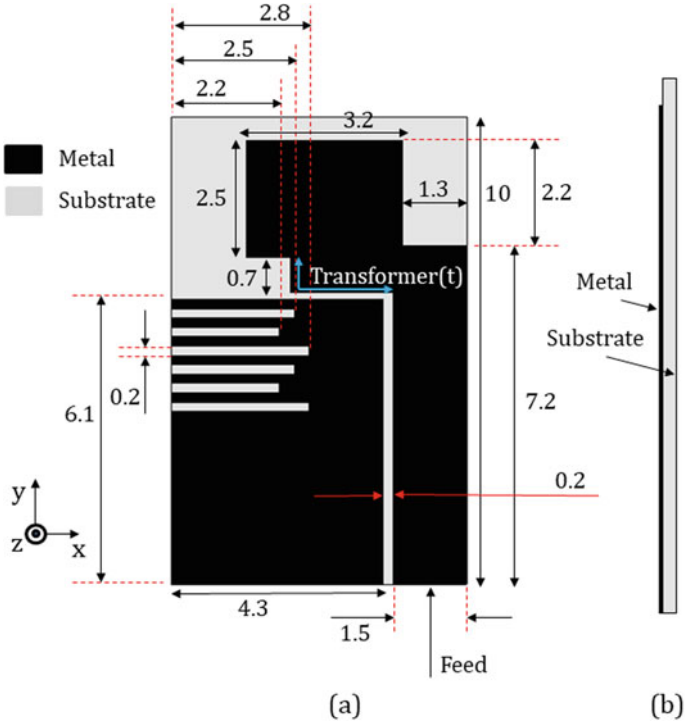

Fig. 8.10 Wideband ACS-fed antenna [48]

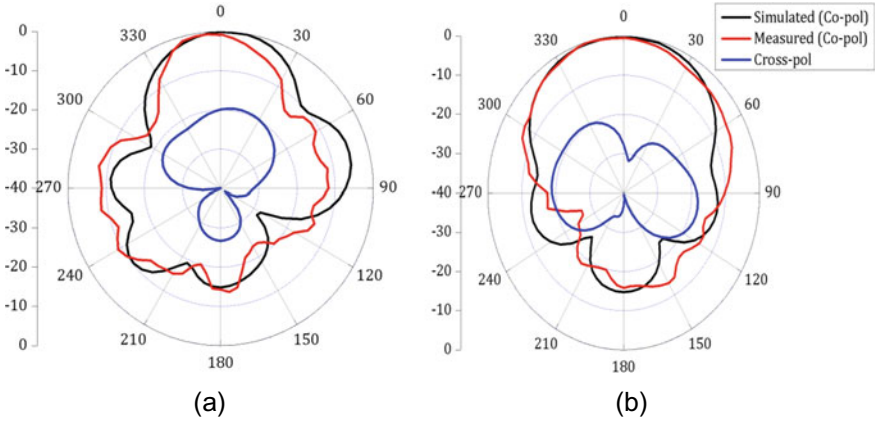

Fig. 8.11 Radiation patterns of the ACS-fed antenna at 28 GHz in **a** E-plane and **b** H-plane [48]

8.6 SIW Feeding

Substrate Integrated Waveguide (SIW) feeding is the technique that has become popular from last one decade due to its planar waveguide structure and low insertion loss at higher frequencies. The insertion loss and spurious radiation from the feed lines would be high in the conventional PCB feeding techniques such as microstrip or CPW. Insertion loss would be a severe problem when the number of elements increase. For instance, an 8-element phased array designed with microstrip feeding would have much higher insertion loss compared to the same design realized using SIW feeding, despite the dielectric loss within the substrate. Also, the increased electrical length of the feed lines in conventional feeding, would contribute to spurious radiation, hence leading to deterioration in the primary beam. SIW feeding is mostly implemented at higher frequencies (mmWave region) due to its low insertion loss in comparison to other planar feeding techniques and ease of integration [49–51]. The only catch is the increased complication in fabrication and an exponential increase in the simulation time. Designers might abstract the closely spaced cylindrical metallic posts as solid metallic rectangular blocks to reduce the simulation time, this would work as a first approximation for the design.

SIW feeding structure is designed by embedding two parallel rows of via walls connecting top and bottom metal planes of dielectric substrate as presented in Fig. 8.12. Unlike other planar feeding techniques, where high spurious radiations and ohmic losses occur at higher frequencies, SIW feeding traps the electromagnetic waves and guides them through the structure without any significant loss. SIW feeding has best of both the worlds: low insertion loss waveguide and planar nature of PCB.

The general rule of thumb for designing SIW feed line is to keep the ratio between spacing (s) and diameter of metallic vias (d) less than 2.5. It has been reported that the losses in the SIW feed line are lesser when spacing between two metallic vias of

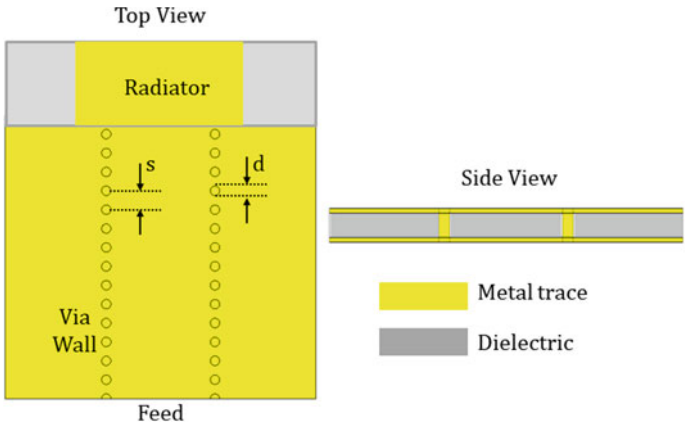

Fig. 8.12 General structure of a SIW feed line

the same via wall is kept smaller and diameter of metallic vias is kept larger [52]. The closely spaced metallic vias will result in the reduction of radiation leakage, through the feeding path itself. This technique is mostly utilized for end-fire mmWave antennas and can be used to obtain various polarizations like horizontal polarization [53], vertical polarization [54] and circular polarization [55].

The metallic vias of SIW feed line act as metallic walls of a classical rectangular waveguide feed. The propagation characteristics of SIW feed line are like that of classical rectangular waveguide feed line. But, the SIW feed line only supports subset of rectangular waveguide modes, TE_{n0} (n = 1, 2, 3 …) modes and the TM modes are not supported due to spacing between metallic vias. SIW structure is planar in nature, hence can be fabricated with existing printed circuit board (PCB) and low temperature co-fired ceramic (LTCC) technologies, which is in contrast with classical rectangular waveguides that are non-planar and metallic in nature. The classical metallic waveguide feed line is therefore bulkier in nature and needs a transition designed for waveguide to PCB based antenna. However, the presence of dielectric inside the SIW structure results in dielectric loss, which is not present in hollow waveguide structures. In addition to this, radiation losses are also greater in SIW structures in comparison to classical waveguide structures, but significantly lesser compared to conventional planar feeding techniques.

The SIW feed line is preferred over classical waveguide feed line because of its ease of fabrication, low cost, low profile, and better integration with other planar circuits. The SIW feeding is also preferred for designing phased antenna arrays by providing low insertion loss. For mmWave 5G frequencies, most of the power dividers are designed with SIW feeding for realization of antenna array [56].

The SIW feeding is also preferred for mmWave 5G antenna-in-package (AiP) applications. Since SIW feed line consists of complete backed ground plane that acts as a shielding plane for radio frequency integrated circuits (RFlCs) lying below the antenna, thus making it suitable for AiP applications. There are some drawbacks also for using SIW feeding like fabrication with respect to other planar feeding techniques is comparatively challenging as it consists of various metallic vias thus making it more costly. Also, this feeding technique needs some design transition like GCPW-to-SIW so that proper excitation and measurement can be performed.

A dual-polarized SIW-fed broadside mmWave 5G antenna array is reported in [57]. Since the SIW-fed structure possesses high quality factor that results in less bandwidth, the presented antenna uses metasurface for obtaining wide impedance bandwidth. The antenna is realized on multilayered substrate topology that consists of three layers of Rogers RT5880 substrate with dielectric constant of 2.2 and a corresponding dielectric loss tangent of 0.0009. The two ports are connected with GCPW-to-SIW feeding transitions followed by orthogonally SIW-fed dual-slots and a pair of 1-to-2-way power dividers that excite the metasurface. The antenna possesses large height and most of the reported SIW-fed antenna designs comprises of large height thereby making it challenging to realize an ultrathin antenna with this feeding structure. The authors attain dual-wideband with impedance bandwidths of 13.85 and 14.81% in the lower (24.2–27.8 GHz) and upper (36.9–42.8 GHz) frequency bands respectively. A 2 × 2 antenna array incorporating two layer based SIW-fed

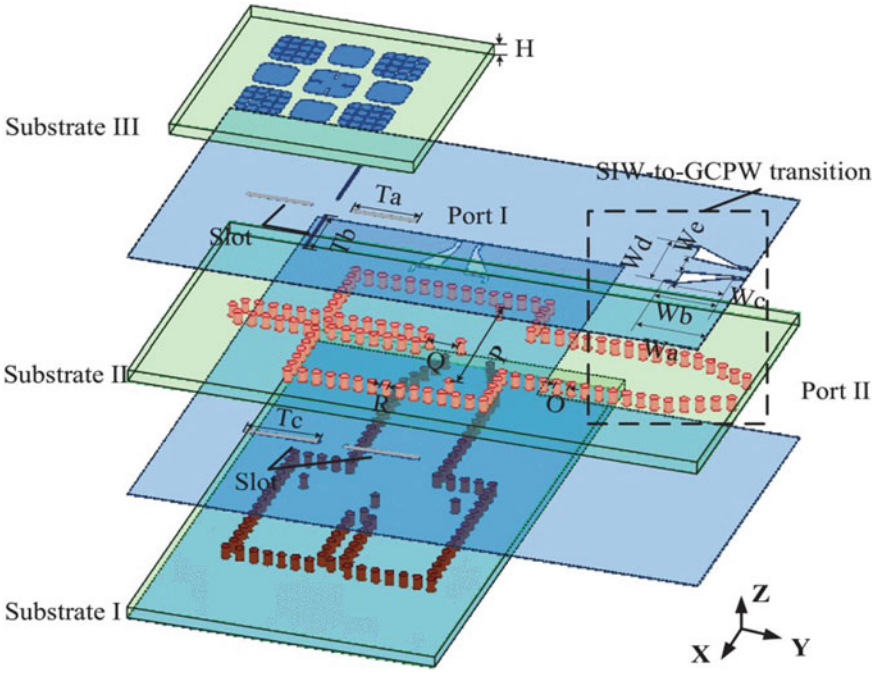

Fig. 8.13 Dual-wideband and dual-polarized SIW-fed antenna [57]

power dividers and E-plane phase shifters is also designed. The reported antenna element is depicted in Fig. 8.13.

A dual linearly polarized end-fire 5G antenna array is presented in [58]. The antenna realizes two different types of magneto-electric (ME) dipoles with horizontal and vertical polarizations (H-pol and V-pol) at 60 GHz. The antenna is fabricated on multilayered substrate topology comprising of four Rogers 5880 dielectric substrates. The prototype possesses overall height of 3.3 mm that is reasonably high for future 5G low profile devices. The antenna possesses wide impedance bandwidth with fractional bandwidths of 26 and 32% for V-pol and H-pol respectively, which is due to multiple resonances of magnetic and electric dipoles. A 1×8 dual-polarized antenna array is also reported with high end-fire gain of 16.1 dBi. To realize presented antenna array at high frequency of 60 GHz, an 8-way SIW based power divider is designed with low insertion loss. Since the excitation of prototype at 60 GHz is achieved by waveguides, a proper SIW-to-waveguide transition is designed for both the polarizations. Cost-effective PCB technology is used for fabrication of the antenna array module. Photograph of the 1×8 dual-polarized antenna array is shown in Fig. 8.14.

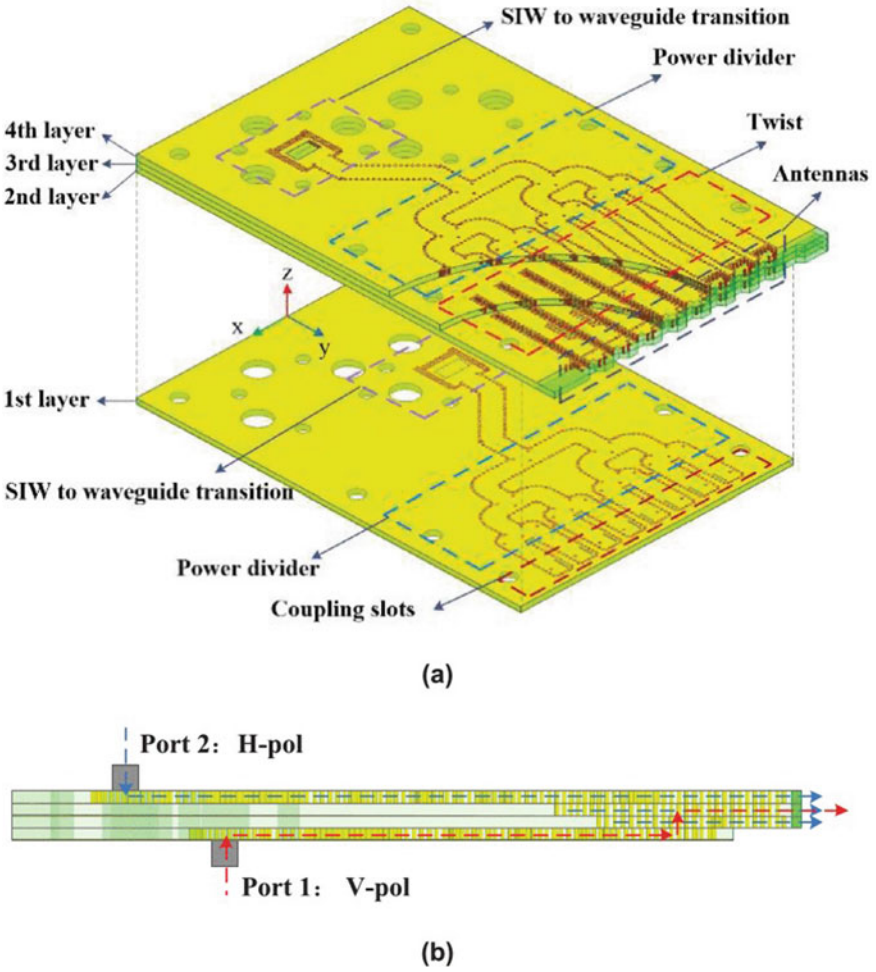

Fig. 8.14 Dual-polarized SIW-fed 1 × 8 antenna array [58]

8.7 Aperture Coupled Feeding

The aperture coupling is a technique usually used for feeding microstrip patch antennas to reduce radiation from the transmission line and enhance the antenna's patch radiation [59, 60]. It was first proposed by Pozar in 1985 [61, 62]. Aperture coupling is an indirect method of feeding between the antenna patch and the feeding source. It is used to couple the antenna patch with a microstrip line through an aperture. The feed line creates an electric field in the aperture, which induces surface currents on the patch [61, 63]. In this way, the patch edges perpendicular to the feed line create fringing fields that radiates into free space. The basic structure of the

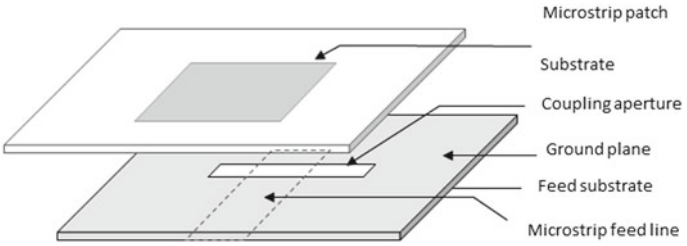

Fig. 8.15 Geometry of the basic aperture coupled microstrip

aperture coupled microstrip antenna is shown in Fig. 8.15. The radiating microstrip patch element is etched on the top of the antenna substrate, and the microstrip feed line is etched on the bottom of the feed substrate.

The useful features of the microstrip antenna coupled to the aperture is that it can provide substantially improved impedance bandwidth. While single layer probe or microstrip line-fed elements are typically limited to bandwidths of 2–5%, aperture coupled elements have been demonstrated with bandwidths up to 10–52% with a single layer [64–68].

Recently, many researchers are focusing on the development of impedance bandwidth enhancement techniques for patch antennas. To satisfy large volume and high-speed data transfer requirements, antennas with high radiation efficiency and gain are desirable [66]. Aperture coupled feeding can provide substantially improved impedance bandwidths [69]. It offers diverse patch shapes, aperture shapes, feed line types, etc. It allows extension to aperture coupled microstrip line couplers, waveguide transitions, dielectric resonators, etc. Very low cross-polarization levels can be achieved by using this technique [65]. Moreover, this technique is commonly used in optimization procedures since it allows good degrees of impedance matching [70], easy integration into arrays [62] and high isolation between ports which is inherently related to the cross-polarization level [71].

The major disadvantages of this feed technique lie in the fact that its construction is more difficult due to its multi-layer topology, which increases the antenna volume as well. The back-lobe radiation level is higher due to the field radiation coming from the slot [69]. Another drawback is that a multilayered substrate structure with the coupling slot on the ground plane can result in coupled surface-wave modes. These modes can lead to distorted radiation patterns and reduced radiation efficiency [66].

The aperture-coupled patch antenna is good candidate for broadside radiation applications. Figure 8.16 presents an HFSS model of aperture coupled patch antenna with two linear polarizations.

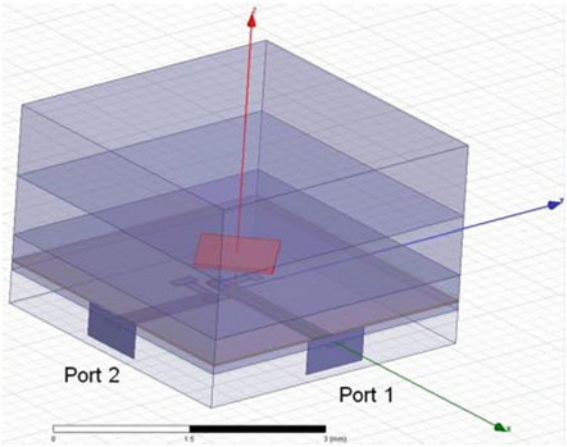

Fig. 8.16 Aperture coupled patch antenna with two linear polarizations (HFSS model)

8.8 Conclusion

Feeding techniques play an important role in overall antenna design especially at higher mmWave 5G frequencies. There are various parameters that should be taken into consideration while designing any mmWave 5G antenna and depending upon the applicability, these parameters decide the feeding technique that should be implemented. For instance, the insertion loss becomes a crucial factor at mmWave 5G frequencies particularly for antenna arrays in which a large power dividing network excites the antenna elements. The power dividing network should possess low insertion loss thereby delivering maximum power to the antenna elements. Also, the form factor plays a vital role for mmWave 5G antennas. Feeding techniques like co-axial and ACS feeding cover less area and therefore becomes suitable candidates for applications having restrictions on total size. There are several other factors that decide the implementation of feeding technique like low cross-polarization, low cost, ease of integration, etc.

Feeding techniques are discussed in detail in this Chapter. Every feeding technique is explained with its implementation, distinct features, merits and demerits and several design examples reported in the literature. Depending upon the application, a user can choose a particular feeding technique for designing an antenna module.

References

1. Rappaport, T.S., Sun, S., Mayzus, R., Zhao, H., Azar, Y., Wang, K., et al.: Millimeter wave mobile communications for 5G cellular: it will work! IEEE Access **1**, 335–349 (2013)
2. Hong, X., Wang, J., Wang, C.X., Shi, J.: Cognitive radio in 5G: a perspective on energy-spectral efficiency trade-off. IEEE Commun. Mag. **52**(7), 46–53 (2014)

3. Pi, Z., Khan, F.: An introduction to millimeter-wave mobile broadband systems. IEEE Commun. Mag. **49**(6), 101–107 (2011)
4. Friis, H.T.: A note on a simple transmission formula. Proc. IRE **34**(5), 254–256 (1946)
5. Pinapati, S.P., Brittain, J., Caldow, A., Fumeaux, C.: Planar feeding techniques for wearable textile antennas. IEEE Trans. Compon. Packag. Manuf. Technol. **10**(7), 1232–1239 (2020)
6. Khandelwal, M.K., Kanaujia, B.K., Kumar, S.: Defected ground structure: fundamentals, analysis, and applications in modern wireless trends. Int. J. Antennas Propag. (2017)
7. Sipal, D., Abegaonkar, M.P., Koul, S.K.: Easily extendable compact planar UWB MIMO antenna array. IEEE Antennas Wirel. Propag. Lett. **16**, 2328–2331 (2017)
8. Garg, R., Bhartia, P., Bahl, I.J., Ittipiboon, A.: Microstrip Antenna Design Handbook. Artech House (2001)
9. Karthikeya, G.S., Koul, S.: Insights into fabrication and measurements of PCB-based passive Millimeter wave antennas. IETE Tech. Rev. 1–8 (2020)
10. Alhalabi, R.A., Rebeiz, G.M.: High-efficiency angled-dipole antennas for millimeter-wave phased array applications. IEEE Trans. Antennas Propag. **56**(10), 3136–3142 (2008)
11. Hsu, H.T., Huang, T.J., Tsao, Y.F.: Ka-band antipodal dual exponentially tapered slot antenna for next generation mobile communication system applications. In: 2017 IEEE Asia Pacific Microwave Conference (APMC), pp. 1051–1054. IEEE (2017, November)
12. Wu, Q., Jin, R., Geng, J., Ding, M.: Printed omni-directional UWB monopole antenna with very compact size. IEEE Trans. Antennas Propag. **56**(3), 896–899 (2008)
13. Affandi, A., Azim, R., Alam, M.M., Islam, M.T.: A low-profile wideband Antenna for WWAN/LTE applications. Electronics **9**(3), 393 (2020)
14. Roh, W., Seol, J.Y., Park, J., Lee, B., Lee, J., Kim, Y., et al.: Millimeter-wave beamforming as an enabling technology for 5G cellular communications: theoretical feasibility and prototype results. IEEE Commun. Mag. **52**(2), 106–113 (2014)
15. Bang, J., Choi, J.: A compact hemispherical beam-coverage phased array antenna unit for 5G mm-wave applications. IEEE Access **8**, 139715–139726 (2020)
16. Hill, T.A., Kelly, J.R., Khalily, M., Brown, T.W.: Cascaded Fresnel lens antenna for scan loss mitigation in millimeter-wave access points. IEEE Trans. Antennas Propag. **68**(10), 6879–6892 (2020)
17. Ramanujam, P., Arumugam, C., Venkatesan, R., Ponnusamy, M.: Design of compact patch antenna with enhanced gain and bandwidth for 5G mm-wave applications. IET Microwaves Antennas Propag. **14**(12), 1455–1461 (2020)
18. Bondarik, A., Sjöberg, D.: Gridded parasitic patch stacked microstrip array antenna for 60 GHz band. IET Microwaves Antennas Propag. **14**(8), 712–717 (2020)
19. Choi, J., Choi, J., Hwang, W.: Miniature millimeter-wave 5G antenna fabricated using anodized aluminum oxide for mobile devices. ACS Omega **5**(40), 26206–26210 (2020)
20. Wang, H., Park, I.: Characteristics of the angled printed dipole array antenna with different numbers of dipole elements. J. Electromag. Eng. Sci. **20**(3), 183–189 (2020)
21. Liu, Y., Zhao, C., Yue, Z., Ren, A., Jia, Y.: A horizontally polarized end-fire antenna with complete ground for 5G mmWave applications. Microw. Opt. Technol. Lett. **62**(12), 3936–3944 (2020)
22. Nguyen, N.A., Le, V.H., Nguyen-Trong, N., Radfar, M., Ebrahimi, A., Phan, K., Desai, A.: Dual-polarized slot antenna for full-duplex systems with high isolation. IEEE Trans. Antennas Propag. (2020)
23. Liu, W.C., Song, C.C., Chung, S.H., Jaw, J.L.: Strip-loaded CPW-fed pentagonal antenna for GPS/WiMAX/WLAN applications. Microw. Opt. Technol. Lett. **51**(1), 48–52 (2009)
24. Simons, R.N.: Coplanar Waveguide Circuits, Components, and Systems, vol. 165. Wiley (2004)
25. Sultan, K.S., Abdullah, H.H., Abdallah, E.A., El-Hennawy, H.S.: Metasurface-based dual polarized MIMO antenna for 5G smartphones using CMA. IEEE Access **8**, 37250–37264 (2020)
26. Jilani, S.F., Abbas, S.M., Esselle, K.P., Alomainy, A.: Millimeter-wave frequency reconfigurable T-shaped antenna for 5G networks. In: 2015 IEEE 11th International Conference on Wireless and Mobile Computing, Networking and Communications (WiMob), pp. 100–102. IEEE (2015, October)

27. Karthikeya, G.S., Abegaonkar, M.P., Koul, S.K.: CPW fed wideband corner bent antenna for 5G mobile terminals. IEEE Access **7**, 10967–10975 (2019)
28. Zhai, G., Cheng, Y., Yin, Q., Zhu, S., Gao, J.: Uniplanar millimeter-wave log-periodic dipole array antenna fed by coplanar waveguide. Int. J. Antennas Propag. (2013)
29. Karthikeya, G.S., Abegaonkar, M.P., Koul, S.K.: CPW fed conformal folded dipole with pattern diversity for 5G mobile terminals. Progr. Electromag. Res. **87**, 199–212 (2018)
30. Jang, T.H., Kim, H.Y., Kang, D.M., Kim, S.H., Park, C.S.: 60 GHz low-profile, wideband dual-polarized U-slot coupled patch antenna with high isolation. IEEE Trans. Antennas Propag. **67**(7), 4453–4462 (2019)
31. Zheng, D.Z., Chu, Q.X.: The design of dual-polarized antenna for base station applications. In: 2016 10th European Conference on Antennas and Propagation (EuCAP), pp. 1–4. IEEE (2016, April)
32. He, Y., Tian, W.: A broadband dual-polarized base station antenna element for European digital dividend, CDMA800 and GSM900 applications. In: 2017 13th International Wireless Communications and Mobile Computing Conference (IWCMC), pp. 659–663. IEEE (2017, June)
33. Roshna, T.K., Deepak, U., Mohanan, P.: Compact UWB MIMO antenna for tridirectional pattern diversity characteristics. IET Microwaves Antennas Propag. **11**(14), 2059–2065 (2017)
34. Sharma, Y., Sarkar, D., Saurav, K., Srivastava, K.V.: Three-element MIMO antenna system with pattern and polarization diversity for WLAN applications. IEEE Antennas Wirel. Propag. Lett. **16**, 1163–1166 (2016)
35. Guo, Y.Q., Pan, Y.M., Zheng, S.Y.: Design of series-fed, single-layer, and wideband millimeter-wave microstrip arrays. IEEE Trans. Antennas Propag. **68**(10), 7017–7026 (2020)
36. Kamal, S., Mohammed, A.S., Ain, M.B., Ullah, U., Hussin, R., Ahmad, Z.A., et al.: A novel negative meander line design of microstrip antenna for 28 GHz mmwave wireless communications. Radioengineering **29**(3), 479 (2020)
37. Rodriguez-Cano, R., Zhang, S., Zhao, K., Pedersen, G.F.: mm-Wave beam-steerable endfire array embedded in a slotted metal-frame LTE antenna. IEEE Trans. Antennas Propag. **68**(5), 3685–3694 (2020)
38. Alzidani, M., Afifi, I., Asaadi, M., Sebak, A.R.: Ultra-wideband differential fed hybrid antenna with high-cross polarization discrimination for millimeter wave applications. IEEE Access **8**, 80673–80683 (2020)
39. Hayashida, Y., Ishikawa, A., Fukagawa, S., Kitaya, R., Eu, G.C., Ide, T., Kanaya, H.: 28GHz $4\times$ 4 one-sided directional slot array antenna for 5G application. In: 2020 IEEE International Symposium on Radio-Frequency Integration Technology (RFIT), pp. 142–144. IEEE (2020, September)
40. Li, X.R., Ye, M., Chu, Q.X.: Novel high gain printed log-periodic dipole antenna. In: 2016 IEEE International Symposium on Antennas and Propagation (APSURSI), pp. 1647–1648. IEEE (2016, June)
41. Khripkov, A., Ilvonen, J., Milosavljevic, Z.: 5G millimeter wave broadside-endfire antenna array. In: 2020 International Workshop on Antenna Technology (iWAT), pp. 1–4. IEEE (2020, February)
42. Stanley, M., Huang, Y., Wang, H., Zhou, H., Alieldin, A., Joseph, S.: A capacitive coupled patch antenna array with high gain and wide coverage for 5G smartphone applications. IEEE Access **6**, 41942–41954 (2018)
43. Li, X., Shi, X.W., Hu, W., Fei, P., Yu, J.F.: Compact triband ACS-fed monopole antenna employing open-ended slots for wireless communication. IEEE Antennas Wirel. Propag. Lett. **12**, 388–391 (2013)
44. Hu, W., Wu, J.J., Zheng, S.F., Ren, J.: Compact ACS-fed printed antenna using dual edge resonators for tri-band operation. IEEE Antennas Wirel. Propag. Lett. **15**, 207–210 (2015)
45. Magray, M.I., Karthikeya, G.S., Muzaffar, K., Koul, S.K.: Electrically small ACS-Fed flipped MIMO antenna for USB portable applications. Progr. Electromag. Res. C **95**, 141–152 (2019)
46. Ibrahim, A.A., Abdalla, M.A., Hu, Z.: Compact ACS-fed CRLH MIMO antenna for wireless applications. IET Microwaves Antennas Propag. **12**(6), 1021–1025 (2018)

47. Masoodi, I.S., Ishteyaq, I., Muzaffar, K., Magray, M.I.: Low cost substrate based compact antennas for 4g/5g side-edge panel smartphone applications. Progr. Electromag. Res. Lett. **91**, 145–152 (2020)
48. Magray, M.I., Karthikeya, G.S., Muzaffar, K., Koul, S.K., Moon, A.H.: Wideband asymmetric coplanar strip fed antennas with pattern diversity for mmWave 5G base stations. IEEE Access **8**, 77482–77489 (2020)
49. Wu, Q., Hirokawa, J., Yin, J., Yu, C., Wang, H., Hong, W.: Millimeter-wave multibeam endfire dual-circularly polarized antenna array for 5G wireless applications. IEEE Trans. Antennas Propag. **66**(9), 4930–4935 (2018)
50. Li, X., Xiao, J., Qi, Z., Zhu, H.: Broadband and high-gain SIW-fed antenna array for 5G applications. IEEE Access **6**, 56282–56289 (2018)
51. Li, A., Luk, K.M.: Single-layer wideband end-fire dual-polarized antenna array for device-to-device communication in 5G wireless systems. IEEE Trans. Veh. Technol. **69**(5), 5142–5150 (2020)
52. Bozzi, M., Pasian, M., Perregrini, L., Wu, K.: On the losses in substrate integrated waveguides. In: 2007 European Microwave Conference, pp. 384–387. IEEE (2007, October)
53. Liu, P., Zhu, X., Jiang, Z.H., Zhang, Y., Tang, H., Hong, W.: A compact single-layer Q-band tapered slot antenna array with phase-shifting inductive windows for endfire patterns. IEEE Trans. Antennas Propag. **67**(1), 169–178 (2018)
54. Khajeim, M.F., Moradi, G., Shirazi, R.S., Zhang, S., Pedersen, G.F.: Wideband vertically polarized antenna with endfire radiation for 5G mobile phone applications. IEEE Antennas Wirel. Propag. Lett. **19**(11), 1948–1952 (2020)
55. Cheng, Y., Dong, Y.: Wideband circularly polarized planar antenna array for 5G millimeter-wave applications. IEEE Trans. Antennas Propag. **69**(5), 2615–2627 (2020)
56. Zhang, L., Wu, K., Wong, S.W., He, Y., Chu, P., Li, W., et al.: Wideband high-efficiency circularly polarized SIW-fed S-dipole array for millimeter-wave applications. IEEE Trans. Antennas Propag. **68**(3), 2422–2427 (2019)
57. Feng, B., He, X., Cheng, J.C.: Dual-wideband dual-polarized metasurface antenna array for the 5G millimeter wave communications based on characteristic mode theory. IEEE Access **8**, 21589–21601 (2020)
58. Li, A., Luk, K.M., Li, Y.: A dual linearly polarized end-fire antenna array for the 5G applications. IEEE Access **6**, 78276–78285 (2018)
59. Civerolo, M., Arakaki, D.: Aperture coupled patch antenna design methods. In: 2011 IEEE International Symposium on Antennas and Propagation (APSURSI), pp. 876–879. IEEE (2011, July)
60. HFSS, Ansoft Corporation: User's Guide, Version 10—High Frequency Structure Simulator, pp. 220–238. Ansoft Corporation, Pittsburgh, PA (2005)
61. Pozar, D.M.: Microstrip antenna aperture-coupled to a microstripline. Electron. Lett. **21**(2), 49–50 (1985)
62. Cui, X., Yang, F., Gao, M., Zhou, L., Liang, Z., Yan, F.: A wideband magnetoelectric dipole antenna with microstrip line aperture-coupled excitation. IEEE Trans. Antennas Propag. **65**(12), 7350–7354 (2017)
63. Pozar, D.M.: A Review of Aperture Coupled Microstrip Antennas: History, Operation, Development, and Applications. University of Massachusetts at Amherst, pp. 1–9 (1996)
64. Aijaz, Z., Shrivastava, S.C.: Coupling effects of aperture coupled microstrip antenna. Int. J. Eng. Trends Technol. **20**(11) (2011)
65. Kanamaluru, S., Li, M.Y., Chang, K.: Analysis and design of aperture-coupled microstrip patch antennas and arrays fed by dielectric image line. IEEE Trans. Antennas Propag. **44**(7), 964–974 (1996)
66. Targonski, S.D., Pozar, D.M.: Design of wideband circularly polarized aperture-coupled microstrip antennas. IEEE Trans. Antennas Propag. **41**(2), 214–220 (1993)
67. Singh, I., Tripathi, V.S.: Micro strip patch antenna and its applications: a survey. Int. J. Comp. Tech. Appl **2**(5), 1595–1599 (2011)

68. Rahim, M.K.A., Low, Z.W., Soh, P.J., Asrokin, A., Jamaluddin, M.H., Masri, T.: Aperture coupled microstrip antenna with different feed sizes and aperture positions. In: 2006 International RF and Microwave Conference, pp. 31–35. IEEE (2006, September)
69. Croq, F., Papiernik, A.: Large bandwidth aperture-coupled microstrip antenna. Electron. Lett. **26**(16), 1293–1294 (1990)
70. Zhao, C., Wang, C.F.: Characteristic mode design of wide band circularly polarized patch antenna consisting of H-shaped unit cells. IEEE Access **6**, 25292–25299 (2018)
71. Diaz, J.D., Salazar-Cerreno, J.L., Ortiz, J.A., Aboserwal, N.A., Lebrón, R.M., Fulton, C., Palmer, R.D.: A cross-stacked radiating antenna with enhanced scanning performance for digital beamforming multifunction phased-array radars. IEEE Trans. Antennas Propag. **66**(10), 5258–5267 (2018)

Chapter 9
Fabrication Technology for Low-Cost Antennas

9.1 Introduction

Millions of smartphones and other allied products are manufactured every year across the globe. The hardware cost of manufacturing these devices would be a significant portion of the overall cost per unit. This in turn means that manufacturing the 5G and allied antennas within the smartphone would be a reasonable fraction of the overall cost of the hardware unit, typically in the range of 0.5–1.5%. It is pretty evident that if the production cost of the antenna could be reduced, companies could potentially save millions of dollars in the years to come.

Manufacturing antennas is part of the motherboard manufacturing process, and not a stand-alone activity. In this Chapter, cost reduction techniques to realize antennas operating in and around 28 GHz are explored. The cost factor is often ignored in the antenna literature due to many reasons. Most of the articles on antennas operating at high frequencies would be on novel geometries or a variant of the topology of radiating elements [1–10]. Even though some articles and patents discuss alternate fabrication techniques, the cost reduction aspect is often ignored. The scalability and commercial viability is a constraint for new fabrication methods, in spite of a promised cost reduction per unit of the antenna. The other popular genre of antenna articles is on performance enhancement for a given popular industry-standard fabrication process.

Cost reduction could be broadly classified into two groups: innovation in process flow and usage of cheaper materials. Even though easier simplistic, and cheaper process could be realized, commercialization might be challenging. Nevertheless, cheaper process flow is explored in this Chapter without much consideration of the commercial angle of the process. With respect to usage of cheaper materials, one of the cheapest plastics available in the market is used as a dielectric, to realize a 5G antenna system in this Chapter. Various topologies to realize unidirectional antennas and antenna modules are elaborated in the Chapter.

S. K. Koul and K. G. S., *Antenna Architectures for Future Wireless Devices*,
Signals and Communication Technology,
https://doi.org/10.1007/978-981-16-7783-0_9

9.2 What Drives Up the Cost of Manufacturing a Modern Antenna?

Most of the modern antennas, which are integrated with portable devices, are planar in nature. In other words, these antennas would be PCB friendly. These planar antennas would be typically integrated with the motherboard of the portable device. This aspect would restrict the antenna designer to explore the cost reduction options, since the electrical parameters of the PCB board would be usually determined a priori. In some cases, detachable antenna units could be preferred at the cost of increased complexity and transition losses. The only way of cost reduction of a PCB based antenna is to design the antenna on a low-cost substrate.

The choice of metal, used to realize the antenna topology, does not offer any economic advantage. This is because the fabrication of copper traces on a dielectric is a mature technology, thus leaving no option to tweak around with a cheaper metal. It might be argued that Aluminium is way cheaper than copper, but the fabrication process for Aluminium would exponentially ramp up the cost of production. Also, utilization of aluminium in academic and research labs is restricted as the aluminium etchant is expensive and Aluminium clad PCB boards are unavailable in the markets.

Non-planar antennas are usually all-metallic antennas, manufactured by conventional machining techniques. As the surface resolution is a tight requirement, cost of manufacturing these antennas would be high. Also, the engineering man-hours to deliver these products would be relatively high. Cost reduction techniques of both types of antennas are explored in this Chapter.

9.3 A 3D-Printed Slide-On Horn Antenna

Horn antennas are very essential for testing and benchmarking purposes. Hence it is necessary to design horn antennas with minimal expenditure, which is both sustainable and scalable. In this Section, an ultra-low-cost horn antenna is presented along with the experimental results. The low-cost horn antenna also would lead to rapid prototyping, as this technique reduces the lead time for manufacturing, compared to conventional fabrication process. Conventional standard gain antennas are manufactured using precision CNC (Computer numerical control) machines, like the discussion in Sect. 6.4. The whole idea is to take a block of solid metal, such as aluminium or copper, and chisel out the required design. This is a laborious process if the dimension of the antenna is relatively small compared to the tools involved. This manufacturing process also leads to a lot of metal wastage, hence increasing the cost of manufacturing. A simple yet effective fabrication process is explored here.

An exploded view of the proposed antenna is illustrated in Fig. 9.1a. Here the primary structure is a 3D-printed mould, over which a suitable metal sheet is wrapped around. The 3D-printed mould is designed based on the design principles of conventional horn antenna, with a lower cut-off frequency of 24 GHz. The dimensions of the

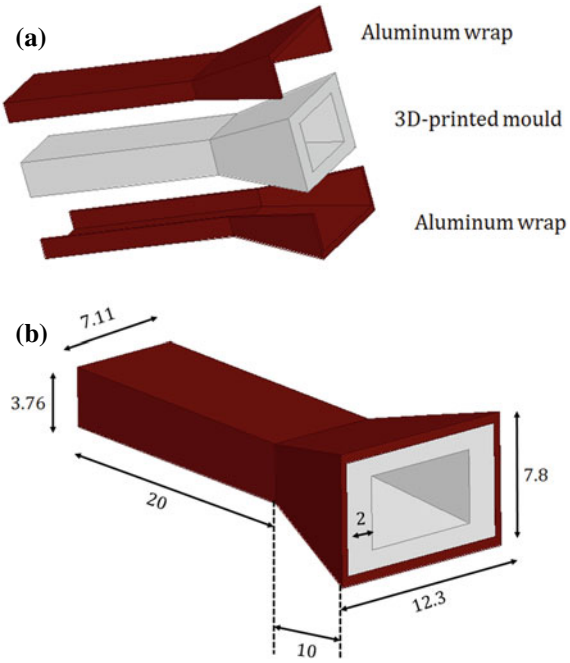

Fig. 9.1 Schematics of the 3D-printed horn construction, **a** break-out view, **b** isometric view with dimensions (All dimensions are in mm)

proposed horn are displayed in Fig. 9.1b. The feeding mouth of the horn is matched with the dimensions of the rectangular waveguide at Ka-band, i.e., WR-28: 7.11 mm $\times$ 3.55 mm. the proposed antenna would be slid into the opening of the waveguide adaptor; hence the 3D-printed mould must be slightly lesser than the length and width dictated by the WR-28 standard. It must also be noted that the 3D-printed dielectric mould would have a non-uniform surface, which further deteriorates the transition between the feed adaptor and the antenna. Several design trials are necessary to accurately fit the metal-clad 3D-printed horn antenna with the waveguide feed.

The fabricated horn antenna is shown in Fig. 9.2a. The 3D-printed mould was designed using Raise 3D-printer with a surface resolution of 50 μm. A conventional CNC machined metal would have a surface resolution in the range of 10-50 μm. PLA (polylactic acid) was used as the 3D-printing material, which has a dielectric constant of 2.75 with a corresponding dielectric loss tangent of 0.01. The thickness of the dielectric mould in the current design is 2 mm, which is a compromise between dielectric loss and mechanical sturdiness for the metal wrap. The entire horn could have been dielectric filled, but the dielectric loss would be significant, hence bringing down the radiation efficiency and the gain. If the thickness is reduced below 1 mm, mechanical sturdiness would be severely compromised. Also, the metal wrapping on a thin dielectric would dent the geometric integrity of the antenna, which would consequently lead to poor coupling of energy from the waveguide feed to the radiating aperture.

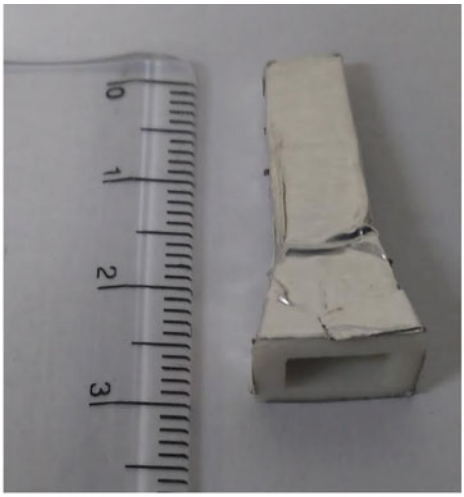

(a)

(b)

Fig. 9.2 **a** Photograph of the fabricated prototype, **b** antenna with the waveguide adaptor

In this example, **aluminium** tape of 100 μm thickness was pasted onto the 3D-printed mould. The pasting was performed manually, leading to fabrication errors. The process of metal wrapping on the dielectric could have been automated, but this would increase the production cost. The cost of the presented antenna is US$3.5 as against a conventional CNC machined all-metallic antenna, which costs around US$350. The antenna mounted with the WR-28 waveguide adaptor is exhibited in Fig. 9.2b; multiple designs were realized with varying dimensions of the feeding portion of the antenna. There were no visible air gaps in the transition of the waveguide adaptor and the antenna feed. Keysight's R281A model was used as the adaptor for measurement purposes. Thinner metal tape would offer flexibility, but the uneven surface of the 3D-printed dielectric would make the metallic wrap to be uneven as well.

The input reflection coefficient of the 3D-printed antenna with Aluminum wrap is showcased in Fig. 9.3. The measured results are like its all-metallic counterpart, the entire Ka-band is covered. The discrepancy between simulated and measured curves could be attributed to the uneven surface finish of the 3D-printed mould. But the

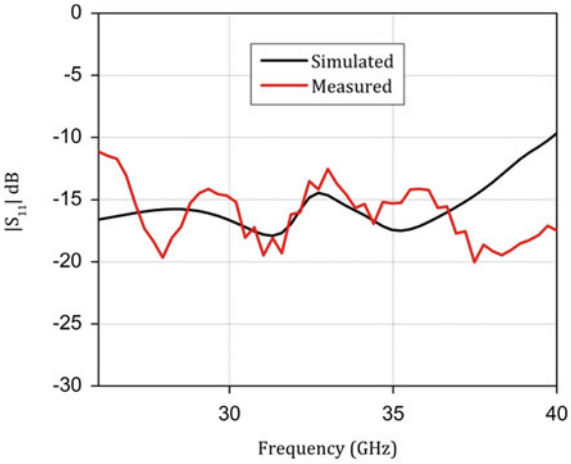

Fig. 9.3 Input reflection coefficient of the 3D-printed horn antenna

measured $|S_{11}|$ is less than 10 dB across the operating spectrum, as expected from a CNC machined horn.

The radiation patterns are shown in Fig. 9.4, the beamwidth shrinks due to the nature of the radiating aperture and its electrical dimensions. Front to back ratio is greater than 25 dB. The patterns at 28 GHz, 32 GHz and 36 GHz are unidirectional, with reasonable variation in beamwidth. The discrepancy between simulated and measured values could be attributed to alignment error, fabrication and assembly errors. The measured patterns prove the utility of the presented ultra-low-cost antenna.

Forward gain variation with frequency is shown in Fig. 9.5. Gain deterioration in the range of 1–2 dB is observed when compared to its all-metallic counterpart.

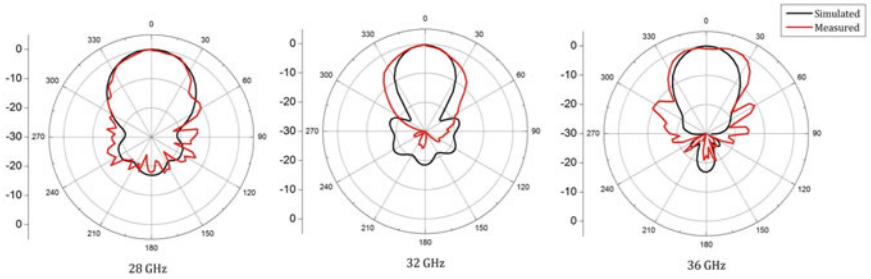

Fig. 9.4 Radiation patterns of the 3D-printed horn

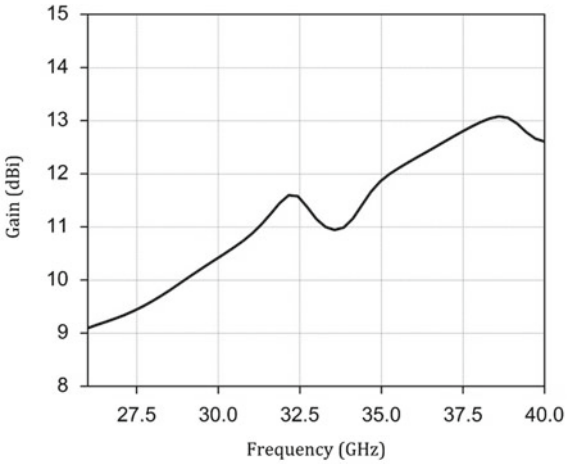

Fig. 9.5 Forward gain of the 3D-printed horn

To compensate for the gain deterioration, a dielectric lens could be integrated with the horn antenna. The entire dielectric mould with the lens could be 3D-printed. The aluminum tape is wrapped around the feed and radiating aperture of the antenna, as illustrated in the schematics of Fig. 9.6. The fabricated prototype is photographed in Fig. 9.7a. The antenna portion alone is metallized, as the 3D-printed lens acts as a gain enhancement structure. The antenna mounted with the WR-28 adaptor is shown in Fig. 9.7b.

The simulated and measured input reflection coefficients of the lens integrated antenna is shown in Fig. 9.8. The impedance bandwidth is like that of the antenna of Fig. 9.1. The integrated lens alters the traveling wave emanating from the antenna and not necessarily the input impedance of the antenna. The radiation patterns are illustrated in Fig. 9.9, the beamwidth is narrower compared to the plain horn element. The narrow beam is observed throughout the operating bandwidth. Forward gain is illustrated in Fig. 9.10. Gain improvement across the band is clearly evident.

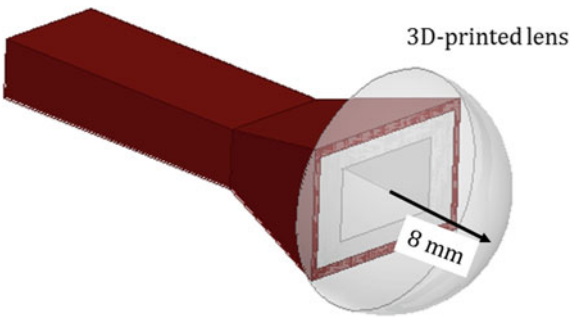

Fig. 9.6 Schematics of the 3D-printed horn integrated with lens

(a)

(b)

Fig. 9.7 **a** Fabricated prototype, **b** antenna with the adaptor

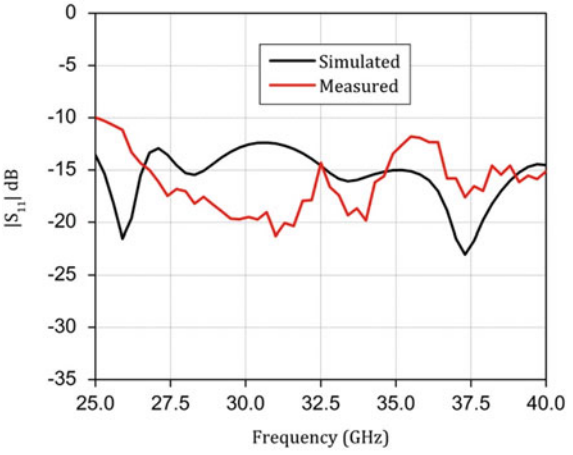

Fig. 9.8 Input reflection coefficient of the 3D-printed horn with lens

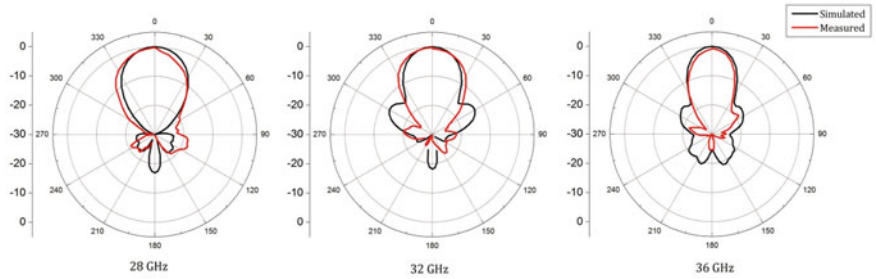

Fig. 9.9 Radiation patterns at various frequencies

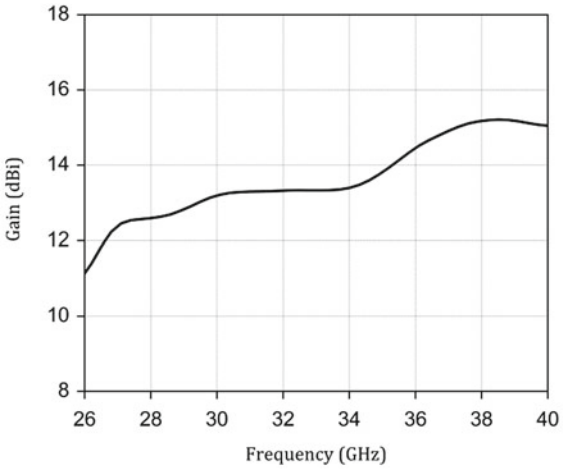

Fig. 9.10 Forward gain of the 3D-printed horn integrated with lens

9.4 Polycarbonate Based Dual-Polarized Antenna System

Dual polarized antenna systems are essential for enhancing the data throughput in high data rate links. The most used approach to achieve dual-polarized feature is to design antennas with orthogonal polarizations. In other words, two different ports would be used to achieve two distinct polarizations. The topology could be two orthogonal polarizations (as in X-polarized and Y-polarized) or two orthogonal circular polarizations (as in left-handed and right-handed circular polarization). Dual polarization in the sub-6 GHz could be achieved by coaxial feeding a shared radiator to invoke orthogonal modes within the antenna. Scaling up this design at mmWave frequencies would be difficult to realize as accommodating two coaxial feeds within 7 mm would be challenging.

The other alternative to achieve polarization diversity is to design two identical linearly polarized broadside radiators that could be placed orthogonally, the problem with this topology is the orthogonal element needs to be redesigned with additional impedance transformers leading to a higher physical footprint. Hence a compact dual-polarized antenna system with unidirectional beams is investigated in this section.

The proposed antenna system is illustrated in Fig. 9.11. It is designed on a low-cost substrate: polycarbonate which has a dielectric constant of 2.9 with a corresponding dielectric loss tangent of 0.01. thickness of the substrate is 500 μm. Polycarbonate is used for illustrative purpose, PET (Polyethylene Terephthalate) or polyimide substrates would also deliver similar performance metrics. The slightly higher dielectric constant aids in size reduction of the effective radiating aperture. The electrically thin substrate facilitates vertical mounting near the smartphone panel. The fabricated prototype with assembled connectors is shown in Fig. 9.12.

Polycarbonate sheet was initially cut according to the desired size. Copper tape of thickness 80 μm was pasted on both the sides of the substrate. The pattern on the top plane was chemically etched. It must be noted that polycarbonate substrate does not support soldering as the dielectric has a lower melting point than conventional PCB dielectrics. Also, the dielectric loss tangent is higher compared to Rogers or Nelco substrates, this feature would lead to a broadside gain reduction of up to 1 dB. Given the economic advantage of the substrate, gain reduction could be overlooked.

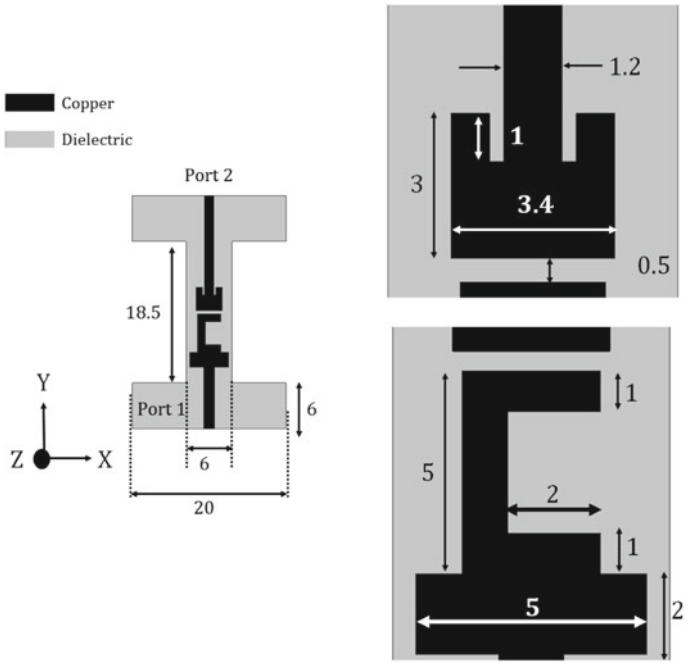

Fig. 9.11 Schematic of the proposed dual polarized antenna (All dimensions are in mm)

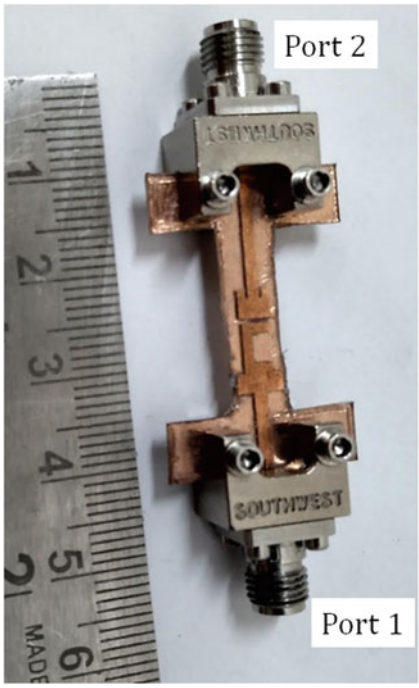

Fig. 9.12 Photograph of the proposed dual polarized antenna

Industrial grade production requires some tweaking of the chemical etching process flow.

The proposed antenna system has two individual ports feeding distinct radiators. Port 1 feeds a 50 Ω line connected to stepped impedance transformer, which in turn is connected to the radiating aperture. The antenna connected to Port 1 is X-polarized, with reference to Fig. 9.11, the overall width of the X-polarized radiator is 6 mm. Similarly, Port 2 is connected to a standard inset-fed patch antenna. Antenna 2 is Y-polarized, hence the two antennas realized on a shared substrate and shared ground achieves dual polarization or polarization diversity. The input reflection coefficients for ports 1 and 2 are shown in Figs. 9.13 and 9.14 respectively. Mutual coupling is less than 20 dB across the band as observed in Fig. 9.15.

The simulated and measured patterns for both the ports are illustrated in Fig. 9.16, both the patterns share a common beamwidth in the broadside orientation proving the dual-polarization action. Both the ports have a reasonable gain for the occupied aperture.

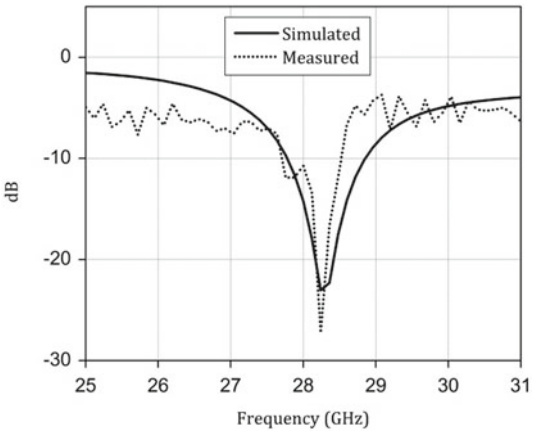

Fig. 9.13 Input reflection coefficient of Port 1

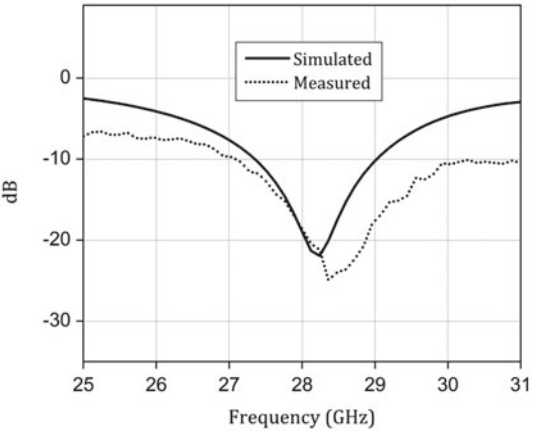

Fig. 9.14 Input reflection coefficient of Port 2

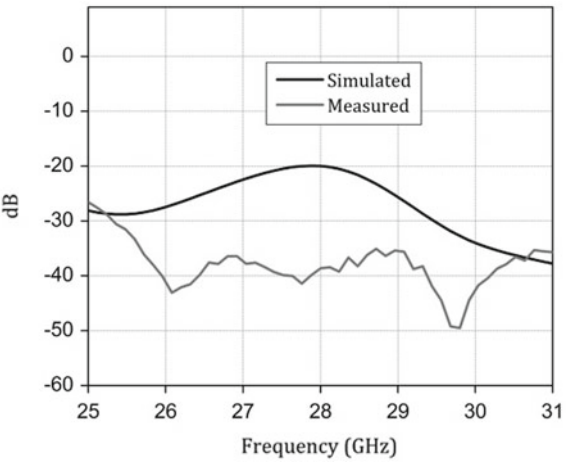

Fig. 9.15 Mutual coupling between the ports

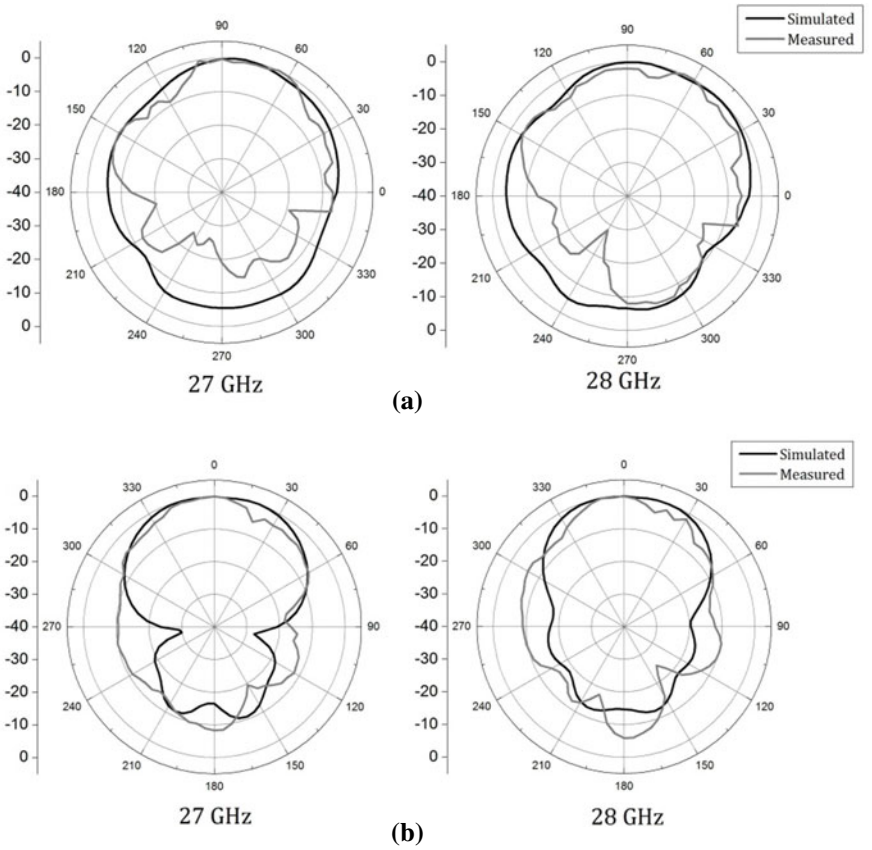

Fig. 9.16 Broadside Radiation patterns when **a** Port 1 is activated, **b** Port 2 is activated

9.5 Conclusion

In this Chapter, need for low-cost antennas was explained in detail. Various aspects of cost reduction of typical antenna were explored. Different planar and non-planar low-cost antenna solutions for 5G applications was investigated in detail.

References

1. Hong, W., Baek, K., Lee, Y., Kim, Y.G.: Design and analysis of a low-profile 28 GHz beam steering antenna solution for future 5G cellular applications. In: 2014 IEEE MTT-S International Microwave Symposium (IMS2014), pp. 1–4. IEEE (June 2014)
2. Przesmycki, R., Bugaj, M., Nowosielski, L.: Broadband microstrip antenna for 5g wireless systems operating at 28 ghz. Electronics **10**(1), 1 (2021)

3. Ullah, U., Al-Hasan, M., Koziel, S., Mabrouk, I.B.: A series inclined slot-fed circularly polarized antenna for 5G 28 GHz applications. IEEE Antennas Wirel. Propag. Lett. **20**(3), 351–355 (2021)
4. Kamal, M.M., Yang, S., Kiani, S.H., Sehrai, D.A., Alibakhshikenari, M., Abdullah, M., Falcone, F., Limiti, E., Munir, M.: A novel hook-shaped antenna operating at 28 GHz for future 5G mmwave applications. Electronics**10**(6), 673 (2021)
5. Aziz, I., Wu, D., Öjefors, E., Hanning, J., Wiklund, E., Dancila, D.: Broadband fan-out phased antenna array at 28 GHz for 5G applications. In: 2020 50th European Microwave Conference (EuMC), pp. 212–215. IEEE (Jan 2021)
6. Srivastava, A.: Dual-cavity backed substrate integrated waveguide slot antenna for 5G applications. In: 2021 5th International Conference on Computer, Communication and Signal Processing (ICCCSP), pp. 1–5. IEEE (May 2021)
7. Hussain, N., Jeong, M.J., Park, J., Kim, N.: A broadband circularly polarized fabry-perot resonant antenna using a single-layered PRS for 5G MIMO applications. IEEE Access **7**, 42897–42907 (2019)
8. Sharaf, M.H., Zaki, A.I., Hamad, R.K., Omar, M.M.: A novel dual-band (38/60 GHz) patch antenna for 5G mobile handsets. Sensors **20**(9), 2541 (2020)
9. Borhani Kakhki, M., Dadgarpour, A., Sebak, A.R., Denidni, T.A.: Twenty-eight-gigahertz beam-switching ridge gap dielectric resonator antenna based on FSS for 5G applications. IET Microwaves Antennas Propag. **14**(5), 397–401 (2020)
10. Kamal, M.M., Yang, S., Ren, X., Altaf, A., Kiani, S.H., Anjum, M.R., Iqbal, A., Asif, M., Saeed, S.I.: Infinity shell shaped mimo antenna array for mm-wave 5G applications. Electronics**10**(2), 165 (2021)

Index

S. K. Koul and K. G. S., *Antenna Architectures for Future Wireless Devices*, Signals and Communication Technology,
https://doi.org/10.1007/978-981-16-7783-0